

**Faculty of Science  
Department of Applied Physics**

**Barium Zirconate Ceramics for Melt Processing of  
Barium Cuprate Superconductors**

**Nigel M. Kirby**

**This thesis is presented for the Degree of  
Doctor of Philosophy  
of  
Curtin University of Technology**

**October 2003**

## **Declaration**

This thesis contains no material which has been accepted for the award of any other degree or diploma in any university.

To the best of my knowledge and belief this thesis contains no material previously published by any other person except where due acknowledgment has been made.

Signature: ..

Date:

.....  
.....17/10/03.....

## ACKNOWLEDGMENTS

When I started this project, I thought science was all about imagination, knowledge, measurement, instrumentation and analysis. By the end of it I also learned something about the importance of people in the progress of science and wish to acknowledge the contribution of the many people who helped make this research feasible.

The 1999 National AXAA conference lead to my introduction to the research staff at Curtin University Materials Research Group (MRG) and a new direction in my work. I'd like to thank the Australian X-ray Analytical Association (AXAA) for their many activities, through which I have gained contact with expert analysts and scientists in this country. I have been privileged to be associated with this organisation.

I'd like to thank Emeritus Professor Brian O'Connor for taking an early interest in my prospective studies at Curtin and the opportunity to join the MRG. I thank him for his technical contribution to the research group, his encouragement throughout the project, for the opportunity of teaching undergraduates XRF, and his staunch support of my applications for external funding and career opportunities.

Dr. Craig Buckley was my Co-Supervisor and the originator of this project through his contacts in England involved in superconductor research. Of the prospective topics in the MRG at the start of my projects, this project caught my attention in part because of the direct benefits which could flow from its successful completion. It has been satisfying to see early signs of this work making a contribution to superconductor research in the U.K., and Craig has been instrumental in establishing these links. His clear, direct, no-nonsense approach to research is one of the things that first attracted me to Curtin, which along with his unwavering support has helped get this project to the stage it finally reached.

Professor Arie van Riessen has been an excellent Principle Supervisor, and I am fortunate to be staying on as a Research Fellow under his supervision through the Australian Synchrotron Research Program. Despite major resource limitations and his many other commitments, Arie has long set an enviable standard in the management of

electron microscope facilities and more recently other equipment, without which projects with such a heavy demand for analytical measurement could not be undertaken. Arie gave me enough rope with this project to hang myself, but just the right amount of advice and guidance to make sure I didn't. To their great credit, Arie and Craig formed the backbone of this research group during the period of this project, and few outside a university environment could appreciate the ability, effort, dedication and sacrifice required to achieve this. Such people help make scientific research and all its challenges and difficulties worthwhile.

Vaughan Wittorff provided frequent advice and assistance almost from the start of the project with his valuable experience at the Interdisciplinary Research Centre in Superconductivity (University of Cambridge). His experience in high temperature superconductivity research helped frame the environment for me to undertake this research, and he helped through financial assistance and supervision of an Honours student who assisted this research.

Dr. Robert Hart joined the research group midway through the project and has provided outstanding support with TEM and other facilities. His versatile expertise has been a great boost to the research group and I thank him for his crucial contribution. I would also like to thank the staff of the Centre for Microscopy and Microanalysis at the University of Western Australia, particularly Dr. Martin Saunders for excellent training courses and assistance with the Jeol 3000F and specimen preparation.

Andrew Trang provided vital assistance as an Honours student in 2002 and the project would have been near impossible to complete to a satisfactory stage without his involvement. Andrew's work provided the capability to get stuck into the solid-state processing system, which helped yield a great deal of the necessary quantitative materials design information required for corrosion resistant crucibles. I owe Andrew a debt of gratitude for the workload he was willing and able to sustain.

The ability to work full time on this project was provided by an Australian Postgraduate Award, and also an Australian Institute of Nuclear Science and Engineering (AINSE) Postgraduate Award which provided a stipend, travel and research



support at the Australian Nuclear Science and Technology Organisation (ANSTO). I wish to acknowledge the efforts of AINSE and its staff in supporting young scientists and for the unique opportunities their activities provides. I can't see how most postgraduate students get by without such opportunities. ANSTO staff who have helped me include Dr. Brett Hunter (ANSTO Supervisor) and the electron microscopy staff who provided initial training on TEM specimen preparation. In particular I wish to thank Dr. David Cassidy who took an active interest in the work and provided great assistance with DTA/TGA and particle characterisation measurements.

Millennium Performance Chemicals (Rockingham, Western Australia) provided crucial support to this project in the provision of zirconium materials throughout the project and some nitrogen adsorption measurements on powders. It has been very helpful to have contact with leading industry professionals, in particular Geoff Carter. Rojan Advanced Ceramics (Henderson, Western Australia) provided vital access to cold isostatic pressing (CIP). Their involvement was crucial as access to CIP in Western Australia is extremely limited. Thanks in particular to Dr. Ioan Alecu.

Thanks also to Andreas Erb (Bavarian Academy of Science) for taking an interest in my work and for personal communications that have been helpful in the progress of the research. It has been invaluable to have contact with the original pioneer of  $\text{BaZrO}_3$  for this application.

Nowhere have I travelled in life without the support of my immediate and extended family. There's not enough you can say to acknowledge all the things parents like mine have given me. The sacrifices they choose to make in support of their sons have not gone unnoticed. My grandfathers taught me at least two things: you only get out of it what you put in, and if it's worth doing, it's worth doing well.

This thesis is for Amanda, for without her I simply could not have done this. You have packed up and moved to the other side of a continent. You have been there day after day to hold the whole show together and chat through all the technical stuff. You have put up with me spending long hours on this project for years. And don't worry, I promise it won't happen again.

## ABSTRACT

---

The widespread use of high temperature superconductors through improved understanding of their underlying physics is in part dependent on the synthesis of large, high quality single crystals for physical research. Crucible corrosion is an important factor hindering the routine synthesis of large, high purity rare-earth barium cuprate superconductor single crystals. Molten  $\text{BaCuO}_2\text{-CuO}$  fluxes required for the growth of such crystals are highly corrosive to substrate materials, and corrosion products may lead to chemical contamination of crystals and other practical difficulties.  $\text{BaZrO}_3$  is known to be inert to  $\text{BaCuO}_2\text{-CuO}$  melts, but its use has remained restricted to a very small number of laboratories worldwide because it is very sensitive to the effects of off-stoichiometric or residual secondary phases which degrade its performance.  $\text{BaZrO}_3$  suitable for sustained melt containment is difficult to produce due to kinetic limitations of phase purity, difficulty in sintering to adequate density, and very narrow stoichiometry tolerances of finished ceramics. The existing literature provided a guide to the production of high quality  $\text{BaZrO}_3$ , but was not sufficiently complete to readily allow production of crucibles suitable for this application.

The two basic aims of this project were:

- To provide a comprehensive and quantitative description of the necessary attributes of crucibles for barium cuprate melt processing and to expand the knowledge of solid-state  $\text{BaZrO}_3$  processing to encourage its widespread application to crucible manufacture;
- To explore the application of solution chemical processes whose potential benefits could lead to routine application of  $\text{BaZrO}_3$  through improved ceramic quality and processing properties.

Based primarily on solid-state processing research, the optimal stoichiometry for corrosion resistant crucibles was observed over the narrow range of  $1.003 \pm 0.003$  Ba : (Zr + Hf) mole ratio. Residual  $\text{ZrO}_2$  must be strictly avoided even at very low levels because severe localized expansion of  $\text{ZrO}_2$  grains during reaction with the melt severely

reduces corrosion resistance. Although the effect of Ba-rich phases are less severe, their abundance must be suppressed as much as allowed by the production process. Solid-state derived crucibles with a large barium excess were unstable and readily attacked by water. TEM analysis clearly showed residual  $\text{ZrO}_2$  was present as discrete grains and not as grain boundary films, and also the prevalence of intragranular defects in Ba-rich ceramics. Quantitative knowledge of the narrow range of required stoichiometry is critical for developing successful solid-state and solution chemical processes. Reliably achieving the required stoichiometry and phase purity is experimentally challenging and beyond the capability of many processing systems.

Systematic investigation revealed sharp changes in physical properties of processed powders across the phase boundary. The resistance of  $\text{BaZrO}_3$  of the desired stoichiometry to grain growth during powder processing has not previously been reported in the available literature. At the desired stoichiometry for corrosion resistance, powder grain growth resistance combined with very precise control over stoichiometry makes the solid-state process more competitive with solution-based processes than previously acknowledged in the literature.

The development of solution processes for  $\text{BaZrO}_3$  precursors is complicated by aqueous chemistry of zirconium compounds. This project developed the first chemically derived precursor process demonstrated to produce a ceramic of adequate quality for sustained barium cuprate melt containment. The barium acetate / zirconium oxychloride / ammonium oxalate system provided control over stoichiometry without requiring elevated solution temperatures, a large excess of barium reagents, or reagents containing alkalis. Despite showing the capability to supersede the solid-state process, the oxalate process still requires further refinement to more reliably achieve high sintered densities.

Although the attributes required for sustained barium cuprate melt containment are now clear, its routine mass production remains reliant on further development of solution chemical techniques or improvements to the kinetics of solid-state processing. This project advanced ceramic design and processing technology in the  $\text{BaZrO}_3$  system and provided new approaches in meeting the challenging analytical needs of research and process control for high quality production of this compound.

## CONTENTS

---

Acknowledgments	ii
Abstract	v
List of Figures	xiii
List of Tables	xxxi
List of Abbreviations used in this Thesis	xxxiii
<b>1.0 INTRODUCTION</b>	<b>1</b>
1.1 Background	1
1.1.1 Crucible materials	2
1.1.2 BaZrO <sub>3</sub> , the “inert” crucible material	3
1.1.3 BaZrO <sub>3</sub> processing	4
1.1.4 Basis for research	4
1.2 Objectives	6
1.3 Study design	6
1.4 Structure of Thesis	7
<b>2.0 LITERATURE REVIEW</b>	<b>9</b>
2.1 Crucible corrosion	9
2.2 Inert BaZrO <sub>3</sub> crucibles	12
2.3 BaZrO <sub>3</sub> processing considerations	15
2.4 Novel processing	16
2.5 Zirconium chemistry	20
2.5.1 Hydrolysis	21
2.5.2 Polymerisation	24
2.5.3 Complex formation	28
2.5.4 Colloid formation	30
2.5.5 Effect of complexing ions on polymerisation	33

2.5.6	Zirconyl ion	35
2.5.7	Oxalates	35
2.5.8	Stability of oxalate complex solutions	38
2.5.9	Complexity	42
2.6	Previous oxalate processing studies	43
2.7	Analysis	47
2.8	Ceramic production	49
2.9	Slurry casting and dispersion	51
2.10	Summary	56
<b>3.0</b>	<b>BACKGROUND AND DESIGN OF EXPERIMENTAL PROGRAM</b>	<b>57</b>
3.1	Experimental aims	57
3.2	Processing implications	57
3.3	Characterisation of powders and ceramics	59
3.4	Experimental overview	60
3.4.1	Solid-state processing considerations	60
3.4.2	Solid-state process development program	61
3.4.3	Chemical process development considerations	63
<b>4.0</b>	<b>EXPERIMENTAL DETAILS</b>	<b>67</b>
4.1	Standardising initial reagents	67
4.1.1	Barium determination	67
4.1.2	Zirconium determination	69
4.2	Qualitative solution tests for detection of barium and zirconium in solution	70
4.3	DTA/TGA analysis	72
4.4	Nitrogen adsorption analysis (BET)	72

4.5	XRF analysis	73
4.5.1	Production and analysis of powders for calibration standards for use on SRS-200 XRF spectrometer	73
4.5.2	Preparation of fusion beads for use on SRS-200 XRF spectrometer	74
4.5.3	Set-up of SRS-200 XRF spectrometer	75
4.5.4	Method as used on Philips PW-1404 spectrometer.	76
4.5.5	Preparation of standards for use on PW-1404	76
4.5.6	Set-up of PW1404 XRF spectrometer	78
4.6.	Transmission electron microscopy	79
4.6.1	Specimen preparation for TEM analysis of powders	79
4.6.2	Specimen preparation for TEM analysis of sintered ceramics.	80
4.6.3	TEM analysis	82
4.7	SEM analysis	82
4.8	X-ray powder diffraction	84
4.8.1	Crystallite size estimation by XRD	85
	<i>Crystallite size estimation using Scherrer equation</i>	85
	<i>Crystallite size and non-uniform strain estimation by Voigt function profile fitting</i>	86
	<i>Crystallite size and particle size considerations</i>	88
4.8.2	Quantitative BaCO <sub>3</sub> determination by XRD	90
4.9	Estimation of Ba-rich phase impurities by ICP-MS analysis of supernatant solutions	91
4.10	Experimental method for solid-state processing development	92
4.10.1	Preliminary experiment	92
4.10.2	Solid-state processing - experiment two	93
4.10.3	Sintered crucible production	94
4.11	Solution processing development	95
4.11.1	Reagents used	95

4.11.2 Barium chloride, zirconyl chloride, oxalic acid system	95
<i>Preliminary experiments</i>	95
<i>Optimisation of oxalate excess in barium chloride, zirconyl chloride, oxalic acid system</i>	95
4.11.3 Barium acetate, zirconyl chloride, ammonium oxalate system	96
4.12 Crucible forming processes	97
4.13 Corrosion resistance testing	97
<b>5.0 BaZrO<sub>3</sub> PROCESSING DEVELOPMENT</b>	98
5.1 Introduction	98
5.2 Solid-state powder processing	98
5.2.1 Phase purity control	98
5.2.2 Interpretation of BaCO <sub>3</sub> levels	102
5.2.3 Solid-state powder processing: determination of calcination times	107
5.2.4 Solid-state processing: crystallite size and non-uniform strain measurement and control	113
5.2.5 Solid-state processing: surface area measurement and control	119
5.3 Oxalate precursor processing	120
5.3.1 Stoichiometry control in the BaCl <sub>2</sub> , zirconium oxychloride, H <sub>2</sub> C <sub>2</sub> O <sub>4</sub> system	120
<i>Introduction</i>	120
<i>Preliminary experiments</i>	121
<i>Optimisation of oxalate excess in barium chloride, zirconyl chloride, oxalic acid system</i>	121
5.3.2 Stoichiometry control in the Ba(CH <sub>3</sub> COO) <sub>2</sub> , zirconium oxychloride, (NH <sub>4</sub> ) <sub>2</sub> C <sub>2</sub> O <sub>4</sub> system	123
5.3.3 Stability of zirconium oxalate solutions	126

5.3.4	Conclusions on oxalate processing chemistry	131
5.3.5	Conversion of oxalate precursors to BaZrO <sub>3</sub>	132
5.4	Comparison between solid-state and oxalate derived powders	144
5.5	Selection of forming processes	146
5.5.1	Slip casting	146
5.5.2	Cold isostatic pressing	151
5.6	Sintering development	153
<b>6.0</b>	<b>SINTERED CERAMICS, MELT CORROSION AND HIGH PURITY CRYSTALS</b>	<b>157</b>
6.1	Introduction	157
6.2	Basic microstructural analysis	157
6.3	Bulk analysis	166
6.3.1	Direct detection of secondary phases by XRD	166
6.3.2	Indirect detection of barium rich phases by XRD	169
6.3.3	Solution analysis by ICP-MS	171
6.3.4	Accuracy of stoichiometry measurement by XRF	177
6.4	Colour	178
6.5	Detailed structural analysis	179
6.5.1	SEM	180
6.5.2	XRD	185
6.5.3	TEM	190
6.5.4	Chemical contamination in oxalate processing	199
6.5.5	Conclusions	204
6.6	Melt Corrosion	205
6.6.1	Corrosion properties	205
6.6.2	Mechanisms of corrosion processes	209
6.7	High purity YBCO single crystals	219



<b>7.0</b>	<b>CONCLUSIONS</b>	222
7.1	Analytical development	223
7.2	Powder processing	226
7.2.1	Solid-state powder processing	226
7.2.2	Oxalate precursor processing	228
7.3	Forming and sintering	230
7.4	Microstructure	231
7.5	Corrosion properties	233
7.6	Overall conclusions	235
7.7	Outlook and recommendations for future research	236
<b>8.0</b>	<b>REFERENCES</b>	239
<b>9.0</b>	<b>APPENDICES</b>	250
9.1	Appendix 1 - Development and assessment of quantitative x-ray analysis methods	251
9.1.1	XRF analysis using a Siemens SRS200 spectrometer	251
9.1.2	XRF analysis using a Philips PW1404 spectrometer	259
9.1.3	BaCO <sub>3</sub> determination by quantitative x-ray diffraction	261
9.2	Appendix 2 – Crystallographic Data	267
9.2.1	ICDD Cards of BaZrO <sub>3</sub> and Related Phases	267
9.2.2	ICSD Data for BaZrO <sub>3</sub>	275
9.3	Appendix 3 – Rietveld Refinement Results	276
9.4	Appendix 4 – Crucible Dimensions	278
9.5	Appendix 5 - Raw Materials Suppliers' Data	279
9.6	Publications Arising from Thesis	292

## List of Figures

---

- Figure 2.1 13  
BaO - ZrO<sub>2</sub> equilibrium phase diagram (Paschoal, Kleykamp and Thuemmler, 1987). T<sub>SS</sub> = tetragonal ZrO<sub>2</sub> solid solution; M<sub>SS</sub> = monoclinic ZrO<sub>2</sub> solid solution.
- Figure 2.2 14  
Calculated secondary phase abundance assuming phase equilibrium. The phases ZrO<sub>2</sub> and Ba<sub>2</sub>ZrO<sub>4</sub> are those indicated on the equilibrium phase diagram (Paschoal, Kleykamp and Thuemmler 1987). Ba<sub>3</sub>Zr<sub>2</sub>O<sub>7</sub> and BaO are calculated simply as other possible phases that may exist under non-equilibrium conditions or as potential phases not detected during the phase diagram determination.
- Figure 4.1 93  
Flow chart of solid-state powder processing development experiment.
- Figure 5.1 100  
The effect of powder processing conditions on BaCO<sub>3</sub> levels for solid-state derived powders calcined at 1300 °C. Powders were analysed by XRD directly after calcination and after >24 hours exposure to air. Uncertainties are ± 2 standard errors.
- Figure 5.2 101  
Effect of air exposure on barium carbonate peak (24 °) for solid-state derived powder produced by single calcination at 1300 °C for one hour with Ba : (Zr + Hf) mole ratio of 0.995. Height of the most intense BaZrO<sub>3</sub> peak at 30.00° 2θ (not shown) was 75 000 counts.

Figure 5.3 102

Effect of air exposure on barium carbonate peak ( $2\theta$ ) in solid-state derived powder produced by triple calcination at  $1300\text{ }^{\circ}\text{C}$  followed by single calcination at  $1420\text{ }^{\circ}\text{C}$  with intermediate re-grinding between all calcinations, with a Ba : (Zr + Hf) mole ratio of 0.987. Height of the most intense  $\text{BaZrO}_3$  peak at  $30.00^{\circ} 2\theta$  (not shown) was 52 000 counts.

Figure 5.4 104

Interpretation of  $\text{BaCO}_3$  levels by investigation of milled sintered ceramic. Ba : (Zr + Hf) mole ratio =  $1.001 \pm 0.002$ . Uncertainties are  $\pm 2$  standard errors.

Figure 5.5 108

Effect of calcination time at  $1300\text{ }^{\circ}\text{C}$  on crystallite sizes of solid-state derived powders with Ba : (Zr + Hf) mole ratio of  $0.995 \pm 0.002$ . Crystallite sizes were determined using Voigt function profile fitting; uncertainties are  $\pm 2\sigma$ .

Figure 5.6 109

Effect of stoichiometry on crystallite size for solid-state derived powders after repeated calcination at  $1300^{\circ}\text{C}$  with intermediate regrinding. Crystallite sizes were determined using Voigt function profile fitting. Crystallite size uncertainties are  $\pm 2\sigma$ .

Figure 5.7 TEM micrograph of solid-state derived powder after three 110  
calcinations with intermediate regrinding and Ba : (Zr + Hf) mole ratio of  $0.995 \pm 0.002$ . Crystallite size by Voigt function profile fitting was  $249 \pm 18\text{ nm}$ , which corresponds to the primary particle size observed by TEM. Scale bar =  $500\text{ nm}$ .

Figure 5.8 111

TEM micrograph of solid-state derived powder after three calcinations with intermediate regrinding and Ba : (Zr + Hf) mole ratio of  $1.025 \pm 0.002$ . Crystallite size by Voigt function profile fitting was  $69 \pm 3$  nm, which corresponds to the primary particle size observed by TEM. Scale bar = 100 nm.

Figure 5.9 112

Detail from Figure 5.7 showing hard agglomeration in a solid-state derived powder with Ba : (Zr + Hf) mole ratio of  $0.995 \pm 0.002$ .

Figure 5.10 114

Effect of stoichiometry on crystallite sizes of solid-state derived powders after three calcinations with intermediate re-grinding. Uncertainties are  $\pm 2\sigma$ .

Figure 5.11 115

Effect of stoichiometry on non-uniform strain of solid-state derived powders after three calcinations with intermediate re-grinding. Random uncertainties are  $\pm 2\sigma$

Figure 5.12 117

The effect of stoichiometry on crystallite sizes determined by Voigt function profile fitting of XRD patterns for solid state derived powders after three calcinations with intermediate re-grinding. TEM images are shown for comparison and verify the results of XRD. Magnifications of images are constant, scale bar = 200 nm. Uncertainties are  $\pm 2\sigma$ .

Figure 5.13 119

Effect of stoichiometry on BET surface area for solid-state derived powders after three calcinations with intermediate re-grinding. Surface areas calculated from crystallite sizes by Voigt function profile fitting and Scherrer equation are shown for comparison.

Figure 5.14	122
Control of powder stoichiometry in the barium chloride / zirconium oxychloride / oxalic acid system.	
Figure 5.15	124
Control of powder stoichiometry in the barium acetate / zirconium oxychloride / ammonium acetate system. All reactions were conducted at $23 \pm 3$ °C.	
Figure 5.16	132
DTA/TGA results for $0.971 \pm 0.002$ Ba : (Zr + Hf) mole ratio powders produced from BaCl <sub>2</sub> , zirconium oxychloride and oxalic acid. Orange and blue curves are for precipitation at 95 °C. Green and black curves are for precipitation at ambient temperature followed by heating to 95 °C before washing.	
Figure 5.17	133
DTA/TGA analysis of precursor synthesised using barium acetate, zirconium oxychloride and ammonium oxalate with either ammonium oxalate or barium acetate in excess. The Ba : (Zr + Hf) mole ratios of the precipitates are indicated in the key.	
Figure 5.18	134
Size control of calcined oxalate derived powders at 0.989 Ba : (Zr+ Hf) mole ratio by variation of calcination temperature. All samples were calcined for 30 minutes.	

Figure 5.19

135

Effect of stoichiometry, calcination temperature and chemical contamination on crystallite size of oxalate-precursor derived powders. Crystallite sizes were determined by Voigt function profile fitting. The samples at Ba : (Zr + Hf) = 0.990 were contaminated with aluminosilicates from process water, and reached large crystallite sizes at calcination temperatures 200 - 300 °C lower than uncontaminated samples.

Figure 5.20

136

Effect of stoichiometry on crystallite size for oxalate-precursor derived powders calcined at 1300 – 1330 °C. Crystallite sizes were determined using Voigt function profile fitting. Uncertainties are  $\pm 2\sigma$ .

Figure 5.21

137

TEM micrograph of oxalate-derived powder with Ba : (Zr + Hf) mole ratio of  $0.989 \pm 0.002$  after calcination at 1350 °C for 60 minutes. Scale bar = 50 nm.

Figure 5.22

137

TEM micrograph of oxalate-derived powder with Ba : (Zr + Hf) mole ratio of  $0.989 \pm 0.002$  after calcination at 1520 °C for 30 minutes. Scale bar = 200 nm.

Figure 5.23

138

TEM micrograph of oxalate-derived powder with Ba : (Zr + Hf) mole ratio of  $0.989 \pm 0.002$  after calcination at 1520 °C for 30 minutes showing hard agglomeration of crystallites (top right of image). Crystallite size by Voigt function profile fitting was  $185 \pm 10$  nm. Scale bar = 100 nm.

Figure 5.24 138

TEM image of oxalate derived powder with Ba : (Zr + Hf) mole ratio of  $0.989 \pm 0.002$  after calcination at 1300 °C for 30 minutes. Large spread in primary particle sizes was presumed to be caused by local composition variation in the precursor, with primary particle size reducing with local Ba : (Zr + Hf) mole ratio. Scale bar = 200 nm.

Figure 5.25 139

TEM of oxalate-derived powder with Ba : (Zr + Hf) mole ratio of  $1.008 \pm 0.002$  after calcination at 1300 °C for 30 minutes. Crystallite size by Voigt profile fitting was  $55 \pm 3$  nm. Scale bar = 100 nm.

Figure 5.26 139

TEM image of oxalate derived powder after calcination at 1300 °C for 30 minutes. Small circular spots on particles near lower half of image are  $\text{ZrO}_2$  (confirmed by STEM-EDS mapping) caused by Ba : (Zr + Hf) mole ratio of  $0.989 \pm 0.002$ . Scale bar = 100 nm.

Figure 5.27 140

TEM lattice image of oxalate derived powder after calcination at 1300 °C for 30 minutes with  $1.008 \pm 0.002$  Ba : (Zr + Hf) mole ratio. Scale bar = 20 nm.

Figure 5.28 141

TEM lattice image of oxalate derived powder after calcination at 1300 °C for 30 minutes. Circular area of Moire fringes is  $\text{ZrO}_2$  (confirmed by STEM-EDS mapping) caused by Ba : (Zr + Hf) mole ratio of  $0.989 \pm 0.002$ . Scale bar = 20 nm.

Figure 5.29 142

Partial XRD pattern of oxalate derived  $\text{BaZrO}_3$  immediately after calcination at 1300 °C for 60 minutes. Sample had Ba : (Zr + Hf) mole ratio of  $0.989 \pm 0.002$ . Note absence of  $\text{BaCO}_3$  peak at 24 °.

Figure 5.30	143
BaCO <sub>3</sub> diffraction peaks for calcined oxalate-derived powders with Ba : (Zr + Hf) mole ratio of $0.986 \pm 0.002$ .	
Figure 5.31	144
BaCO <sub>3</sub> levels of solid-state and oxalate derived BaZrO <sub>3</sub> powders after air exposure with Ba : (Zr + Hf) mole ratios of 0.989 to $0.995 \pm 0.002$ .	
Figure 5.32	145
Approximate estimate of Ba-rich phase impurities of powders with Ba : (Zr + Hf) mole ratio of 0.989 to $0.995 \pm 0.002$ . Powders in blue assumed phase pure to estimate contribution of BaZrO <sub>3</sub> surface area to observed BaCO <sub>3</sub> levels after air exposure.	
Figure 5.33	147
SEM micrograph of fracture surface of slip cast oxalate-derived BaZrO <sub>3</sub> after sintering at 1630 °C for twelve hours. Very high porosity (25 vol.%) was due to poor green density and inadequate sintering temperature. Continuous porosity may make this material suitable for applications such as humidity sensors but totally unsuitable for melt containment.	
Figure 5.34	149
The effect of A40 dispersant level on sintered densities of slip cast BaZrO <sub>3</sub> . The powder used for this study had a crystallite size of $205 \pm 45$ nm.	
Figure 5.35	150
Effect of powder crystallite size and sintering temperature on sintered porosity of slip cast BaZrO <sub>3</sub> . Each slip was prepared so as to minimise viscosity by controlling pH and dispersant levels. All points indicated by blue markers contained aluminosilicate contamination either from process water or porcelain crucibles used during calcination. Crystallite size uncertainties are $\pm 2 \sigma$ .	



Figure 5.36 156

Sintered solid-state derived crucible ready for single crystal growth. Smallest division on ruler is 1 mm.

Figure 6.1 158

Optical micrographs of fractured surfaces of BaZrO<sub>3</sub> pellets with Ba[Zr+Hf] ratio (a) 0.965, (b) 0.988, (c) 0.996, (d) 1.000, (e) 1.002 and (f) 1.010. Scale bar = 500  $\mu$ m.

Figure 6.2 159

Exaggerated grain growth away from external surface (uppermost) in solid-state derived BaZrO<sub>3</sub> with Ba : (Zr + Hf) mole ratio of  $1.002 \pm 0.002$  (same sample as Figure 6.1 e). Scale bar = 500  $\mu$ m.

Figure 6.3 159

SEM micrograph of fracture surface of sintered oxalate-derived BaZrO<sub>3</sub> with Ba : (Zr + Hf) mole ratio of 1.015. Sample isostatically pressed and sintered for 6 hours at 1700 °C. Image taken from centre of cross-section (~ 2 mm from external surface) showing lack of exaggerated grain growth unlike often occurring in Ba-rich solid-state derived ceramics. Scale bar = 10  $\mu$ m.

Figure 6.4 161

Thin sub-surface layer of exaggerated grain growth in solid-state derived BaZrO<sub>3</sub> with Ba : (Zr + Hf) mole ratio of  $1.006 \pm 0.002$ . Scale bar = 1 mm.

Figure 6.5 161

SEM micrograph of fracture surface of sintered ceramic made from solid-state derived powder with Ba : (Zr + Hf) mole ratio of 1.006. Exaggerated grain growth occurred in subsurface layer between ~200 and 650  $\mu$ m from exterior surfaces, but did not extend to the centre of sintered material. External surface is on left side of image. Scale bar = 200  $\mu$ m.

Figure 6.6	162
Fine grain structure of centre region of sample in Figure 6.5.	
Scale bar = 10 $\mu\text{m}$ .	
Figure 6.7	162
Subsurface layer of exaggerated grain growth in solid-state derived $\text{BaZrO}_3$ with Ba : (Zr + Hf) mole ratio of $1.003 \pm 0.002$ . External surface is at bottom of image. Scale bar = 500 $\mu\text{m}$ .	
Figure 6.8	163
Exaggerated grain growth in interior of Ba-rich ceramic mixed with very fine grains. Scale bar = 100 $\mu\text{m}$ .	
Figure 6.9	163
Exaggerated grain growth in interior of Ba-rich solid-state derived ceramic mixed with very fine grains. Scale bar = 50 $\mu\text{m}$ .	
Figure 6.10	164
Large $\text{BaZrO}_3$ grain in fine grained matrix in Ba-rich solid-state derived ceramic where fracture surface has propagated around large grain. Scale bar = 20 $\mu\text{m}$ .	
Figure 6.11	165
SEM micrograph of fracture surface of slip cast Zr-rich oxalate-derived $\text{BaZrO}_3$ containing aluminosilicate contamination after sintering at 1650 $^{\circ}\text{C}$ for twelve hours. Scale bar = 10 $\mu\text{m}$ .	
Figure 6.12	165
Conchoidal fracture surface of same sample as Figure 6.11, i.e. aluminosilicate contaminated oxalate-derived $\text{BaZrO}_3$ sintered at 1650 $^{\circ}\text{C}$ for twelve hours. Density was 99.3 % and Ba : (Zr + Hf) mole ratio was $0.960 \pm 0.002$ . Scale bar = 5 $\mu\text{m}$ .	

Figure 6.13

166

Partly conchoidal fracture surface of uncontaminated oxalate-derived BaZrO<sub>3</sub> after sintering at 1700 °C for 6 hours, indicating conchoidal fracture surface was not caused by aluminosilicate contamination. Sample had Ba : (Zr + Hf) mole ratio of  $0.986 \pm 0.002$  and a density 94.6 % of theoretical. Scale bar = 5 µm.

Figure 6.14

167

Direct detection of ZrO<sub>2</sub> in Zr-rich BaZrO<sub>3</sub> close to phase equilibrium at Ba : (Zr + Hf) mole ratios of 0.965 and 0.988. ZrO<sub>2</sub> could not be detected for solid-state sintered materials ground into powders for analysis with Ba : (Zr + Hf) higher than 0.988. ZrO<sub>2</sub> peaks not overlapped by other phases are 28.1 and 31.5 °. Peak height of BaZrO<sub>3</sub> peak at 30.0 ° was ~ 96 000 counts.

Figure 6.15

169

Phase analysis of Ba-rich BaZrO<sub>3</sub> near phase equilibrium at Ba : (Zr + Hf) mole ratio of  $1.011 \pm 0.002$ . Peaks due to BaZrO<sub>3</sub> are shown in red. All other diffraction peaks are due to BaCO<sub>3</sub>. Peak height of BaZrO<sub>3</sub> at 30.0 ° was 21 000 counts.

Figure 6.16

170

Dependence of BaCO<sub>3</sub> levels after air exposure on stoichiometry and sample preparation. The numbers next to results for powders are the number of calcinations with intermeditate regrinding used during powder processing. Theoretical line assumes phase equilibrium and neglects BaZrO<sub>3</sub> surface area effect. Sintered data at 0.966 includes some overlap from ZrO<sub>2</sub>.

Figure 6.17

171

Raw data from ICP-MS analysis of ceramic. Error bars due to solution concentration measurements of ICP-MS instrument are too small to show. Scatter in data is primarily due to low levels of particulate material in solutions which could not be removed by filtration or centrifugation.

Figure 6.18	172
Dependence of corrected Ba : (Zr + Hf) ratio of dissolved secondary phases(s) on powder stoichiometry.	
Figure 6.19	172
Dependence of calculated total weight percentage of secondary phases(s) on powder stoichiometry calculated from measured supernatant solution concentration.	
Figure 6.20	180
Fracture surface of large grain where fracture has propagated through large grain. Scale bar = 10 $\mu\text{m}$ .	
Figure 6.21	181
Fracture surface of large grain where fracture has propagated through large grain. Scale bar = 5 $\mu\text{m}$ .	
Figure 6.22	181
Intragranular fracture surface within large grain of Ba-rich solid-state derived ceramic. Image is a higher magnification of the central region of Figure 6.20. Scale bar = 2 $\mu\text{m}$ .	
Figure 6.23	182
Intragranular fracture in Ba-rich solid-state derived ceramic including a grain boundary between two large grains. Scale bar = 5 $\mu\text{m}$ .	
	182
Figure 6.24	
Intragranular fracture in Ba-rich solid-state derived ceramic showing fracture morphology which appears to closely conform to an underlying cubic crystal structure. Scale bar = 5 $\mu\text{m}$ .	

Figure 6.25 184

Intragranular fracture surface of large grain in Ba-rich solid-state derived ceramic showing large number of small ( $\sim 1\ \mu\text{m}$ ) circular defects. Orientation of steps in fracture surface shows a rotation about half way through the large grain. Scale bar =  $20\ \mu\text{m}$ .

Figure 6.26 184

SEM of small circular defects within large grains in Ba-rich solid-state derived ceramics. Image is higher magnification of sample shown in Figure 6.25. Scale bar =  $1\ \mu\text{m}$ .

Figure 6.27 188

XRD pattern of solid-state derived sintered ceramic without exaggerated grain growth after brief milling. Ba : (Zr + Hf) mole ratio =  $0.988 \pm 0.002$ . Black points are measured data, red and green lines are calculated and difference plots of Rietveld model. Preferred orientation was minimal.

Figure 6.28 188

XRD pattern of solid-state derived sintered ceramic with exaggerated grain growth showing strong preferred orientation in powder pattern after brief milling: peaks at  $21$  and  $43^\circ$  are much larger than standard patterns from random crystallite orientation. Ba : (Zr + Hf) mole ratio =  $1.015 \pm 0.002$ .

Figure 6.29 189

XRD pattern of solid-state derived ground sintered ceramic with exaggerated grain growth showing strong preferred orientation in powder pattern after brief ring milling (20 seconds). Ba : (Zr + Hf) mole ratio =  $1.011 \pm 0.002$ .

Figure 6.30 191

TEM of defect structure in a large BaZrO<sub>3</sub> grain in Ba-rich solid-state derived ceramic showing consistent defect orientation over a large area of the grain, and characteristic 45 ° angles between defects which may be related to the crystal structure of BaZrO<sub>3</sub>. Scale bar = 1 µm.

Figure 6.31 192

Higher magnification TEM image of Figure 6.30 showing defect structure in more detail. Defect orientation was maintained across the pore shown in the top right of image. Scale bar = 0.5 µm.

Figure 6.32 193

Defect structure in a fine grained Ba-rich solid-state derived ceramic. Defects were rectangular with sharply defined edges (grain in bottom right of image) or had a more diffuse, banded morphology (grain at top of image).

Figure 6.33 194

Detail of typical defect structure in fine grained Ba-rich solid-state derived ceramic. Defects show contrast reversal, rectangular geometry, and some are associated with strain contrast across grain boundaries. Scale bar = 200 nm.

Figure 6.34 195

TEM micrograph of Zr-rich oxalate derived ceramic showing lack of defects within BaZrO<sub>3</sub> grains and segregation of Zr as ZrO<sub>2</sub> grains. Bands across central grain are thickness fringes and not crystal defects. Scale bar = 1 µm.

Figure 6.35 196

Brightfield TEM showing inter- and intragranular ZrO<sub>2</sub> in Zr-rich oxalate derived BaZrO<sub>3</sub>. Strain fields around ZrO<sub>2</sub> are clearly visible. Other dark bands are thickness fringes and not crystallographic defects.

Figure 6.36	197
Bands across BaZrO <sub>3</sub> grains are thickness fringes and strain contours due to ZrO <sub>2</sub> particle. Grain boundaries show Moire fringes due to lattice orientation mismatch between grains but no evidence of grain boundary films.	
Figure 6.37	198
Brightfield STEM image of ZrO <sub>2</sub> grain in sintered Zr-rich ceramic. Scale Bar = 800 nm.	
Figure 6.38	198
Brightfield STEM image of ZrO <sub>2</sub> grain in sintered Zr-rich ceramic. Scale Bar = 80 nm.	
Figure 6.39	200
Bright-field TEM image of grain boundary in kaolin doped sample (Trang 2002). S1 – S4 are sites where EDS analysis was performed. Scale bar = 1 µm.	
Figure 6.40	200
EDS spectrum from site 3 in Figure 6.39 showing aluminosilicate contamination resulted in barium aluminosilicate secondary phases that did not contain zirconium (Trang 2002).	
Figure 6.41	201
EDS spectrum from site 4 in Figure 6.39 confirming detection of barium aluminosilicate phases below ~ 50 nm in size. Zirconium and part of the barium peaks are due to excitation of BaZrO <sub>3</sub> (Trang 2002).	
Figure 6.42	202
Brightfield STEM image of a ~ 5 - 10 nm barium aluminosilicate precipitate at triple point of contaminated sample. Scale bar = 80 nm.	
Figure 6.43	202
EDS Spectrum from triple point shown in Figure 6.42. Cu was due to slot grid on which thin section was mounted (Trang 2002).	

Figure 6.44	203
Brightfield TEM image of a ~ 20 nm barium aluminosilicate precipitate in a triple point of a contaminated sample. Scale bar = 50 nm.	
Figure 6.45	203
EDS Spectrum from triple point shown in Figure 6.44. Cu was due to slot grid on which thin section was mounted.	
Figure 6.46	207
Solid-state derived crucible with Ba : (Zr + Hf) mole ratio of 1.008 after four days corrosion exposure at 1050 °C. The front surface in the photograph was at the front of the furnace during exposure. Smallest division on ruler is 1 mm.	
Figure 6.47	208
Solid-state derived crucible with (Ba : Zr + Hf) mole ratio of 1.002 after four days corrosion exposure at 1050 °C. Smallest division on ruler is 1 mm.	
Figure 6.48	208
Oxalate derived crucible with Ba : (Zr + Hf) mole ratio of ~1.005 after eight days corrosion exposure at 1050 °C. Smallest division on ruler is 1 mm.	
Figure 6.49	211
SEM micrograph showing YBCO grain boundary films after melt corrosion of Zr-rich ceramic. Original SE image (a) and false coloured image (b) indicating locations where YBCO was confirmed by EDS analysis. Scale bar = 2 µm.	
Figure 6.50	212
SEM micrograph confirming YBCO grain boundary films were observed extensively throughout Zr-rich ceramics after melt corrosion. Original SE image (a) and false coloured image (b) indicating locations where YBCO was confirmed by EDS analysis. Scale bar = 2 µm.	



Figure 6.51 213

Distribution of YBCO melt in Ba-rich ceramic in region without exaggerated grain growth. Green regions readily allowed Cu identification by EDS. Red areas with similar morphology and distribution were considered be YBCO melt even though they were too small and/or not accessible to EDS detector to permit Cu identification by EDS. Scale bar = 10  $\mu\text{m}$ .

Figure 6.52 214

Distribution of YBCO melt in Ba-rich ceramic in region without exaggerated grain growth: confirmation that observations made in Figure 6.51 were representative of the sample. Scale bar = 5  $\mu\text{m}$ .

Figure 6.53 216

Optical micrograph of TEM specimen of solid-state derived ceramic with Ba : (Zr + Hf) mole ratio of  $0.999 \pm 0.002$  after melt exposure. Scale bar = 100  $\mu\text{m}$ .

Figure 6.54 217

Cu detection within a sample with exaggerated grain growth with a Ba : (Zr + Hf) mole ratio of  $0.999 \pm 0.002$ . Features 1 and 2 had very low Cu levels, the grain boundary at site 3 had moderate Cu levels, and sites 4 – 6 were clearly YBCO melt with very high Cu levels. Scale bar = 0.5  $\mu\text{m}$ .

Figure 6.55 218

TEM images of the corroded Ba-rich ceramic from Figure 6.53. (a) is a brightfield STEM image and (b) is the corresponding Cu  $K_{\alpha}$  x-ray map. Scale bar = 600 nm.

Figure 6.56 220

The effect of annealing temperature in high purity oxygen and in air on second magnetic moment of a high purity 3.5 mg twinned  $\text{YBa}_2\text{Cu}_3\text{O}_{7-\delta}$  single crystal annealed in high purity oxygen by SQUID magnetometry.

Figure 6.57	221
Relationship between annealing temperature, critical superconducting temperature by SQUID magnetometry and oxygen loss for annealing a high purity 3.5 mg twinned $\text{YBa}_2\text{Cu}_3\text{O}_{7-\delta}$ single crystal annealed in high purity oxygen and in air. (Oxygen loss = $\delta$ in crystal formula $\text{YBa}_2\text{Cu}_3\text{O}_{7-\delta}$ ).	
Figure 6.58	221
Relationship between $T_C$ and oxygen loss for annealing in pure oxygen.	
Figure A1.1	254
Intensity stability on the SRS200 spectrometer. Measurements were taken six to twelve hours apart over four days.	
Figure A1.2	254
Typical repeatability of Ba : (Zr + Hf) mole ratios for a sample with a nominal mole ratio of 1.000 on a single specimen holder in the SRS200 spectrometer. Uncertainties are $\pm 2\sigma$ .	
Figure A1.3	255
The effect of specimen holders on Zr $K_\alpha$ intensities of a single powder and fused bead specimen in the SRS200 spectrometer. The acquisition parameters were fixed for each type of specimen, but the powder and fused specimens were analysed using different instrument settings to produce similar intensities. Error bars from counting statistics are too small to plot: the correlation between the two sets of data shows that the effect of specimen holders was real.	
Figure A1.4	256
BaO : $\text{ZrO}_2$ mole ratio full calibration on SRS200.	
Figure A1.5	257
$\text{HfO}_2$ : $\text{ZrO}_2$ mole ratio full calibration on SRS200.	

Figure A1.6	259
Stability of apparent BaO : ZrO <sub>2</sub> mole ratio of 0.9972 standard without applying new calibrations during a long series of measurements, demonstrating the need for drift correction or frequent re-calibration of the SRS200. Measurements were taken six to twelve hours apart over four days.	
Figure A1.7.	263
Preliminary calibration graph for BaCO <sub>3</sub> assay by quantitative XRD.	
Figure A1.8.	263
Final calibration graph for absolute BaCO <sub>3</sub> assay by quantitative XRD in BaZrO <sub>3</sub> . Uncertainties are $\pm 2\sigma$ .	
Figure A1.9	264
Typical weak BaCO <sub>3</sub> diffraction peaks requiring analysis.	
Figure A1.10	266
BaCO <sub>3</sub> diffraction peaks in solid-state derived powders produced with intermediate re-grinding, at and below the detection limits of the method.	

## List of Tables

---

Table 1.1	2
Record setting superconducting transition temperatures (Elert 1995).	
Table 2.1	23
State of Zr in solution in the absence of complexing ligands at trace concentrations ( $\sim 10^{-9}$ M) (Elinson and Petrov 1969, p27).	
Table 4.1	75
Preparation of XRF specimens for use on SRS200 spectrometer.	
Table 4.2	76
Instrument parameters used on SRS200 spectrometer.	
Table 4.3	78
Preparation of XRF specimens for use on PW1404 spectrometer.	
Table 4.4	78
Preparation of standards for use on PW1404 spectrometer.	
Table 4.5	79
Instrument parameters used on PW1404 spectrometer.	
Table 5.1	121
Stoichiometry of powders following the method of Reddy and Mehrotra (1979).	
Table 5.2	125
Alternative method for production of near stoichiometric BaZrO <sub>3</sub> in the barium acetate, zirconium oxychloride, ammonium oxalate system using an excess of barium acetate at 22 °C.	
Table 5.3	143
Effect of calcination temperature and stoichiometry on BaCO <sub>3</sub> levels in calcined oxalate-derived powders. Errors in crystallite sizes are $\pm 1\sigma$ .	
Table 5.4	154
Sintered porosities of solid-state derived BaZrO <sub>3</sub> ceramics formed using uniaxial or cold isostatic pressing.	

Table 5.5	155
Sintered porosities of uniaxially or isostatically pressed oxalate derived powders.	
Table 6.1	205
Effect of stoichiometry on corrosion resistance of solid-state derived crucibles.	
Table 6.2	207
Effect of stoichiometry on corrosion resistance of oxalate derived crucibles.	
Table A1.1	253
Example of a calibration and analysis of residuals from SRS200. Residuals are the deviation of measured points from the fitted calibration plane and provide an effective basis for determining measurement precision.	
Table A1.2	260
Calibration data from PW1404. Four calibrations were performed over a four hour period and were applied to corresponding batches of unknowns.	
Table A1.3	261
Weights of powders used to produce standards for $\text{BaCO}_3$ in $\text{BaZrO}_3$ for quantitative XRD. Weighing uncertainties were $\pm 0.2$ mg, which contributed a negligible amount to the total measurement uncertainty.	
Table A1.4	262
Intensities of x-ray diffraction peaks from $\text{BaCO}_3$ standards. Standard deviations in this table only include counting statistical errors. All intensities are integrated peak areas.	
Table A3.1	276
Parameters fixed for all Rietveld refinements of solid-state derived sintered ceramics analysed as powders after brief ring milling	
Table A3.2	277
Results of Rietveld refinements of XRD patterns of solid-state derived sintered ceramics analysed as powders after brief ring milling.	

## List of Abbreviations used in this Thesis

---

AAS	Atomic absorption spectroscopy
AR	Analytical reagent
BET	Surface area measurement by nitrogen adsorption using the Brunauer, Emmett and Teller isotherm
CIP	Cold isostatic pressing
DTA/TGA	Simultaneous differential thermal and thermogravimetic analysis
EDS	Energy dispersive x-ray spectroscopy
esd	Estimated standard deviation
FEG	Field emission gun
FWHM	Full width at half maximum
GIF	Gatan image filter
HRTEM	High resolution transmission electron microscopy (i.e. lattice imaging)
ICDD	International Centre for Diffraction Data
HTSC	High temperature superconductor/superconductivity
ICP-MS	Inductively coupled plasma – mass spectroscopy analysis
ICP-OES	Inductively coupled plasma – optical emission spectroscopy analysis
LOI	Loss on ignition
MDI	Materials Data Incorporated (USA)
NIST	National Institute of Standards and Technology (USA)
SE	Secondary electron
SEM	Scanning electron microscope/microscopy/micrograph
SQUID	Superconducting quantum interference device
STEM	Scanning transmission electron microscopy
T <sub>c</sub>	Critical superconducting transition temperature
TEM	Transmission electron microscope/microscopy/micrograph
XRD	X-ray diffraction
XRF	X-ray fluorescence
YBCO	YBa <sub>2</sub> Cu <sub>3</sub> O <sub>7-δ</sub>
[Zr]	Zirconium solution concentration (mol/L)

# CHAPTER 1

## INTRODUCTION

---

### 1.1 Background

The discovery of superconductivity in barium cuprate ceramics by Bednorz and Müller in 1986 led to a significant improvement in the properties of superconductors and sparked a flood of research worldwide into high temperature superconductivity as outlined in Table 1.1 (Elert 2003). Since the discovery of superconductors with critical temperatures above the boiling point of liquid nitrogen (Wu *et al.* 1987), the far reaching potential benefits from the development of high temperature superconductors has spurred attempts to discover and develop the properties of oxide superconductors as well as fundamental and theoretical studies of the physics of high temperature superconductivity (Genoud *et al.* 1997; Gautier-Picard *et al.* 1997; Erb *et al.* 1999). Apart from obtaining high critical temperatures, improvements to properties including critical current density, critical magnetic field and mechanical properties as well as routine industrial fabrication processes are required to facilitate the widespread application of high temperature ceramic superconductors.

In the sixteen years since Wu *et al.* (1987) discovered superconductors with critical temperatures above the boiling point of liquid nitrogen (77K), superconductors have found practical use only in specialised applications. Despite the enormous potential benefit of high temperature superconductors to mankind, they are yet to routinely impact on everyday life. The widespread use of ceramic superconductors requires improved electrical and magnetic properties as well as overcoming processing difficulties in manufacturing and brittle mechanical properties. Development of high performance superconductors requires an understanding of the fundamental physics of high temperature superconductivity. The accuracy of experimental data for physical and magnetisation properties of these materials, and hence theoretical interpretations, has been limited by the quality of the prepared materials. Chemical and structural defects cause uncertainty and error in determining the intrinsic and extrinsic nature of superconductivity (Erb 1999). Research in this field has progressed to the extent where

ultra-high purity and quality single crystals are required to eliminate extraneous effects of chemical and structural defects. Understanding of high temperature superconductivity in single crystals will assist development of applications using polycrystalline materials.

Table 1.1 Record setting superconducting transition temperatures (Elert 1995).

Year	T <sub>c</sub> (K)	Material	Comment
1911	4.154	Hg	Discovery of superconductivity
1913	7.196	Pb	
1932	9.25	Nb	Highest T <sub>c</sub> for element
1932	11.5	NbC	
1941	16.10	NbN	
1952/3	17.1	V <sub>3</sub> Si and NbN <sub>0.7</sub> C <sub>0.3</sub>	
1954	18.05	Nb <sub>3</sub> Sn	
1960	20.7	Nb <sub>3</sub> Al <sub>0.75</sub> Ge <sub>0.25</sub>	
1986	30	La <sub>1.85</sub> Ba <sub>0.15</sub> CuO <sub>4</sub>	High temperature superconductivity discovered
1987	93	YBa <sub>2</sub> Cu <sub>3</sub> O <sub>7</sub>	First superconductivity above liquid nitrogen temperature
1988	115	Bi <sub>2</sub> Sr <sub>2</sub> CaCu <sub>2</sub> O <sub>8</sub>	
1993	133	HgBa <sub>2</sub> Ca <sub>2</sub> Cu <sub>3</sub> O <sub>8</sub>	
1995	138	Hg <sub>0.8</sub> Tl <sub>0.2</sub> Ba <sub>2</sub> Ca <sub>2</sub> Cu <sub>3</sub> O <sub>8.33</sub>	Current record at 1 atmosphere pressure
1994	164*	HgBa <sub>2</sub> Ca <sub>2</sub> Cu <sub>3</sub> O <sub>8</sub>	*At 30 GPa pressure

### 1.1.1 Crucible materials

The crucible material, purity and porosity have been identified as crucial factors in enabling the growth of state-of-the-art high temperature superconductor (HTSC) single crystals. Molten BaCuO<sub>2</sub>-CuO fluxes required for the growth of single crystals are highly corrosive to substrate materials, causing a range of practical difficulties in crystal growth experiments. Common crucible materials (i.e. noble metals and almost all ceramics tested) result in gross chemical contamination of the flux and in most cases



single crystals, preventing study of their intrinsic superconducting properties. Fundamental physical understanding of HTSC materials, and the development of HTSC applications using polycrystalline materials, is therefore dependent on high quality ceramic crucibles, and their corrosion behaviour. BaZrO<sub>3</sub> is known to be inert to BaCuO<sub>2</sub>-CuO melts, but its use has remained restricted to a very small number of laboratories worldwide (University of Karlsruhe, Walther Meissner Institute [Bavarian Academy of Sciences, Munich], University of British Columbia) because of difficulty in its production at the quality required (Huang *et al.* 1999, Liang, Bonn & Hardy 1998, Pfaff 1995, Ubaldini *et al.* 2003).

### **1.1.2 BaZrO<sub>3</sub>, the “inert” crucible material**

Single crystal growth using BaZrO<sub>3</sub> crucibles was first achieved by Erb, Walker & Flükiger (1995) using crucibles fabricated from powders synthesised by calcination of BaCO<sub>3</sub> and ZrO<sub>2</sub> powders. The traditional solid-state method has significant practical difficulties, and requires considerable effort in all processing stages to make acceptable crucibles of low porosity, high chemical and structural purity and a minimum of non-stoichiometric phases.

The desired material is pure, single phase BaZrO<sub>3</sub> with a fine grain size which can only be produced when the mole ratio of BaO:ZrO<sub>2</sub> is unity, and any excess of either oxide remains as undesirable secondary phases that degrade the corrosion resistance of the material (Erb, Walker & Flükiger 1995; Liang, Bonn & Hardy 1998; Paschoal, Kleykamp and Thuemmler 1987). Precise stoichiometry and homogeneity control is crucial for high quality crucible production (Erb, Walker & Flükiger 1995; Liang, Bonn & Hardy 1998). The quality of the ceramic required for melt resistance is such that its characterisation is challenging and easily misrepresented by cursory analysis. For example, the phase purity required for corrosion resistance is in several respects beyond the detection limits of conventional laboratory x-ray diffraction.

### **1.1.3 BaZrO<sub>3</sub> processing**

Reaction of BaCO<sub>3</sub> and ZrO<sub>2</sub> is the most common and straightforward process for producing BaZrO<sub>3</sub>, but may not lead to homogenous, phase pure and contamination free powders suitable for sintering to high density due to poor diffusion kinetics during the solid-state reaction. A large number of processes have been reported for producing BaZrO<sub>3</sub> powders from chemically derived precursors, which typically claim to overcome the limitations of the solid-state process leading to higher quality powders. Most chemical synthesis processes attempt to establish very intimate mixing of reagents, ideally at the atomic level in single-phase precursors, which minimises kinetic limitations on phase formation during calcination. Such methods may allow reduced calcination temperatures leading to reduced agglomeration and improved sintering properties of powders. Despite obvious potential advantages, no public domain literature was available demonstrating successful development of chemically derived precursor processes for fabrication of BaZrO<sub>3</sub> ceramics for molten barium cuprate containment.

### **1.1.4 Basis for research**

Significant literature has been published on barium zirconate, but it was apparent that further public domain research was needed to develop BaZrO<sub>3</sub> as a widely available material suitable for sustained containment of molten barium cuprates. Although very useful information is available, the current literature is not sufficiently complete in its description of processing methods to allow other researchers to readily fabricate adequately corrosion resistant materials. Key pieces of information on characteristics of corrosion resistant BaZrO<sub>3</sub> ceramics requiring quantitative control were described only qualitatively, in particular tolerances on stoichiometry and/or phase purity. Despite numerous papers describing limitations of traditional solid-state processing of BaZrO<sub>3</sub> and claimed improvements for powders derived through solution chemistry, no reports were found demonstrating successful adaptation or implementation of such potentially improved processes for corrosion resistant BaZrO<sub>3</sub> ceramic fabrication. This project attempted to address some of these issues, and support experimental superconductivity research by contributing to crucible technology required for high quality single crystal growth.

Erb (1999) argued that research into the physics of high temperature superconductivity had been compromised by a lack of consideration of the effect of sample quality. His criticism of the lack of effort to characterise and control the effects of crystal quality and contamination from crucibles is noteworthy:

“We have to make better samples and not only assure everyone that the samples are already “high quality single crystals” – a term used in nearly every publication. In most cases this term is unjustified and in the last years a growing number of well-known scientists have realised and criticize the use of this term, when basically no information about the sample was available, since no characterisation had been performed. [From] a detailed study of the process going on during the synthesis of [crystals] and the interaction with crucibles, a really new idea was born...[leading to] the development of a really inert crucible material for the synthesis of the 123-compounds.”

As will be seen in the results presented in this thesis, the use and abuse of the term “high quality” refers equally well to barium zirconate crucibles as it does to  $\text{YBa}_2\text{Cu}_3\text{O}_{7-\delta}$  (YCBO) crystals. The requirements to produce corrosion resistant  $\text{BaZrO}_3$  are particularly stringent, and require careful refinement of all stages of processing methods and analytical techniques.

## **1.2 Objectives**

This project attempted to advance the technology of barium zirconate ceramics for use in the melt processing of barium cuprate superconductors in four main respects:

- Expand the knowledge of solid-state  $\text{BaZrO}_3$  processing to encourage its widespread application in manufacturing crucibles for containment of molten barium cuprates.
- Provide a comprehensive and quantitative description of the characteristics of crucibles required for prolonged containment of molten barium cuprates.
- Explore the application of solution chemical processes whose potential benefits could lead to routine application of  $\text{BaZrO}_3$  through improved ceramic quality and processing properties, and to develop new processing methods where necessary.
- Develop and/or implement analytical methods for process development and ceramic characterisation at the high quality required for this application, and verify interpretation of results.

## **1.3 Study design**

The broad research plan developed to meet the research objectives outlined in Section 1.2 is presented below.

1. Critically review the literature on a wide range of powder synthesis methods and  $\text{BaZrO}_3$  ceramic technology relating to melt processing of barium cuprates.
2. Select candidate processes for high quality  $\text{BaZrO}_3$  powders using chemically derived precursors, and develop and/or implement new processes where appropriate.

3. Investigate and develop the traditional solid-state process from the basic outline available in the literature, and apply this knowledge to alternative processes.
4. Develop analytical methods capable of supporting process development and ceramic characterisation at the high quality required for this application.
5. Evaluate the corrosion performance of ceramics produced to optimise processing methods and ceramic properties and attempt to understand mechanisms affecting the corrosion performance of  $\text{BaZrO}_3$ .

Without a production process one cannot make the ceramic in order to study it, and in any case, processing artefacts may significantly affect the corrosion performance of the ceramic. Without knowing detailed requirements of the ceramic one cannot fully design or assess a production process for making the ceramic. This contradiction lies at the core of the design of the experimental program and added substantially to the complexity of the task at hand. The solution to this problem was to use the traditional solid-state process as a model system, which greatly assisted development of alternative chemically derived precursor processes and provided a yardstick against which to evaluate alternative processes. Progress made in this study in both areas will substantially simplify the task of future development.

#### **1.4 Structure of Thesis**

$\text{BaZrO}_3$  is a challenging ceramic system in which to conduct research, with particularly stringent requirements to achieve corrosion resistance. This thesis has been written for the benefit of the reader rather than the author, and as such attempts to communicate as much of the experience gained through this research on the  $\text{BaZrO}_3$  system to the reader as possible. The thesis contains descriptions of areas where salient difficulties were observed, and describes how full or partial solutions were achieved. Substantial gains in  $\text{BaZrO}_3$  development have been made in this and earlier research, but the technology is still not quite at a level suitable for routine widespread application. The outcomes of this research will substantially simplify future development of the

material and its processing methods, and may hasten its possible routine application. An aim of this thesis is to support such progress with as much relevant information as available. To this end this thesis contains an extensive review to consolidate information on zirconium chemistry and previous BaZrO<sub>3</sub> development as well as reporting original experimentation. This thesis includes results indicating both successful and unsuccessful directions in the current research.

Chapter Two reviews the literature on BaZrO<sub>3</sub> for melt processing of barium cuprates, including traditional and novel processing methods. There is an extensive review of the relevant literature on aqueous zirconium chemistry required for the development of oxalate processing, which was presented because of the fragmented nature of the existing body of literature. Chapter Three provides a comprehensive summary of project design considerations as they relate to the existing literature and the research objectives of the project. The details of the experimental program are provided in Chapter Four. Chapter Five is a comprehensive presentation and discussion of experimental results for powder processing. The analysis and development of corrosion resistant sintered ceramics is presented in Chapter Six. Chapter Seven presents the major conclusion of the project and a summary of the current state of the art and outlook for the future. Key x-ray measurements that required extensive development are discussed in detail in Appendix One.

## CHAPTER 2

### LITERATURE REVIEW

---

#### 2.1 Crucible corrosion

YBa<sub>2</sub>Cu<sub>3</sub>O<sub>7-δ</sub> (123) is the most common of the rare earth cuprates studied, partly because of its well defined cation stoichiometry, variable and easily controlled anion stoichiometry, and the relative ease of crystal growth (Liang, Bonn and Hardy 1998). Single crystals of 123 cannot be grown directly due to incongruent melting (Schneemeyer *et al.* 1987) so are grown by the self flux method. This method involves controlled slow cooling of a molten mixture of Y<sub>2</sub>O<sub>3</sub>, BaO and CuO, where the 123 crystallises out of the approximately eutectic flux mixture of BaCuO<sub>2</sub> - CuO near 1000 °C (Erb 1994). Precipitation and growth of crystals is due to the decreasing solubility of the superconductor crystals in the flux as the temperature is lowered. Unfortunately the barium cuprate flux mixture used to grow YBCO is highly corrosive to commonly available crucible materials. Crucible corrosion results in damage or destruction of crucibles and contamination of the flux with corrosion products (Erb, Walker and Flükiger 1995; Erb *et al.* 1997; Liang, Bonn and Hardy 1998, Erb 1999). Although damage to crucibles is undesirable, flux contamination is the more significant problem because it leads to potential contamination of the growing crystals and/or other undesirable effects on the flux. These problems can cause poor control over crystal growth, poor crystal quality and can preclude the use of advanced crystal growth techniques. As shown in Table 1.1, many other high T<sub>c</sub> compounds contain barium and copper, and hence the corrosion problem will occur for processes where sustained containment of molten barium cuprates is required during processing. Undesirable substrate interaction and contamination also occurs in thin film formation (Huang *et al.* 1999). Crucible corrosion has caused difficulty in accurately determining phase equilibria in the YBCO system (Erb, Biernath and Müller-Vogt 1993; Erb, Walker and Flükiger 1996).

Corrosion products from the crucible that dissolve in the flux can be incorporated into the growing crystal resulting in chemical impurity. For example, corrosion of Al<sub>2</sub>O<sub>3</sub>, Au and SnO<sub>2</sub> crucibles has lead to YBCO crystal impurities of up to 1 wt.% Al, 1.5 at.% Au and 2 - 4 at.% Sn, respectively (Erb, Walker and Flükiger

1995; Tagami *et al.* 1995; Erb *et al.* 1997; Erb 1999). The severity of contamination through the bulk of the crystal can be heterogeneous because the flux composition can change during the growth period. Contamination of the solidified superconductor crystals by corrosion products degrades their superconducting properties and complicates physical explanation of their superconductivity (Schneemeyer *et al.* 1987; Erb, Walker and Flükiger 1995; Erb *et al.* 1997; Liang, Bonn and Hardy 1998; Erb 1999). Crystal contamination has lead to contradicting experimental results because the type and level of impurities in crystals are clearly dependent on the crucible material used for crystal growth, and the presence and effect of impurities in crystals has not always been adequately measured or accounted for in previous research (Erb, Walker and Flükiger 1995; Erb 1999). For example, pure  $\text{PrBa}_2\text{Cu}_3\text{O}_{7-8}$  single crystals cannot be grown in  $\text{Y}_2\text{O}_3$  crucibles because of extensive substitution of Y for Pr in crystals due to crucible corrosion (Tamagi *et al.* 1995).

Flux contamination causes numerous problems even when impurities that are soluble in the flux are not incorporated into the growing crystal. For example  $\text{ZrO}_2$  dissolved from stabilised  $\text{ZrO}_2$  crucibles does not fit into the  $\text{YBa}_2\text{Cu}_3\text{O}_{7-8}$  lattice and remains in the flux (Erb, Walker and Flükiger 1995). However, the reaction of BaO (dissolved in the flux) with  $\text{ZrO}_2$  crucibles to form insoluble  $\text{BaZrO}_3$  continuously reduces the barium concentration of the flux. The composition of the flux can change so significantly that the crystallisation of the desired superconductor ceases or an undesired phase precipitates, in which case controlled crystal growth time is restricted by the corrosion properties of the crucible material crystals (Erb, Walker and Flükiger 1995; Erb *et al.* 1997; Liang, Bonn and Hardy 1998). In the case of  $\text{ZrO}_2$  based crucibles, the restriction of crystal growth time hinders the use of more advanced crystal growth techniques such as top seeded solution growth (Erb *et al.* 1995; Liang, Bonn and Hardy 1998; Erb *et al.* 1996; Erb 1999). An important factor to consider using yttria stabilised  $\text{ZrO}_2$  crucibles is the presence of sintering aids that may have been added to aid production by the manufacturer. Additives such as  $\text{SiO}_2$  may cause leakage and contamination of flux, high flux viscosity and lack of crystal yield, so the quality of yttria stabilised  $\text{ZrO}_2$  crucibles needs to be considered carefully. Calcium stabilised  $\text{ZrO}_2$  has been found to cause calcium contamination of both flux and crystals (Erb 1994).



Contaminants dissolved in the flux may increase its viscosity and hinder crystal growth kinetics. Increased flux viscosity is undesirable as it becomes difficult or impossible to decant the flux from the crystals before cooling to ambient temperature. If the flux cannot be efficiently separated from the crystals whilst still liquid, the mixture must be cooled to ambient temperature, broken into pieces, and any superconductor crystals that are separated must be collected manually. This severely reduces the size of crystals that are recovered because of mechanical damage (Erb, Walker and Flükiger 1995).

The rates of crucible corrosion are not able to be controlled and also vary with the quality of the crucible material. Hence crystal growth experiments in reactive crucibles have been difficult to control and have suffered from poor reproducibility. Crystal growth in non-inert crucibles has been a trial and error process requiring development for each type of crucible material used, and optimisation even for crucibles of the same material type from different manufacturers (Erb, Walker and Flükiger 1996). Flux contamination makes phase diagram determination inaccurate and/or uncertain, such as for the  $\text{BaCuO}_2$  -  $\text{CuO}$  flux system used for  $\text{YBa}_2\text{Cu}_3\text{O}_{7-\delta}$  single crystal growth (Erb, Walker and Flükiger 1995).

In view of these difficulties it is clear that reproducible and controlled melt processing and growth of large, homogeneous, chemically and structurally pure single crystals requires crucibles that are inert to the flux (Erb, Walker and Flükiger 1996; Erb *et al.* 1997). Similar difficulties have also been encountered to some extent in thin film production processes, in which film/substrate reactions have been reported as a problem (Cima, Schneider and Peterson 1988; Huang *et al.* 1999). Large single crystals are desirable because the precision and ease of numerous property measurements increases with crystal size. These measurements include specific heat, thermal conductivity and microwave penetration depth. Some techniques, such as single crystal neutron diffraction, have not been successfully conducted on these materials as the crystals grown to date have been too small to analyse.

## 2.2 Inert BaZrO<sub>3</sub> crucibles

The discovery of BaZrO<sub>3</sub> as a suitable crucible material came about by the observation of the reaction between YBCO films and stabilised ZrO<sub>2</sub> substrates (Cima, Schneider and Peterson 1988) and later between molten flux and stabilised ZrO<sub>2</sub> crucibles (Erb, Walker, and Flükiger 1995). The reaction between YBCO melts and BaZrO<sub>3</sub> powders was first investigated by Stenstrop and Engell (1990). It was observed that YBCO films produced on stabilised ZrO<sub>2</sub> substrates would become depleted of BaO, and a layer of BaZrO<sub>3</sub> would form between the film and the substrate. During single crystal YBCO growth in stabilised ZrO<sub>2</sub> crucibles, a thick layer of BaZrO<sub>3</sub> forms on the surface of crucibles and a sharp interface was observed between the BaZrO<sub>3</sub> layer and the melt (Erb, Walker, and Flükiger 1995). The observed stability of BaZrO<sub>3</sub> in contact with YBCO and molten flux indicated a low solubility of BaZrO<sub>3</sub> with the flux. BaZrO<sub>3</sub> was therefore proposed as a potential candidate material for high temperature YBCO melt processing, and was subsequently verified experimentally (Erb, Walker, and Flükiger 1995).

The first successful crystal growth experiment using essentially inert crucibles was achieved in 1994 by Andreas Erb with BaZrO<sub>3</sub> crucibles fabricated using a traditional ground powder sintering technique from BaCO<sub>3</sub> and ZrO<sub>2</sub> powders (Erb, Walker and Flükiger 1995). These crucibles were then used to grow high quality superconductor crystals. Erb and his co-workers, and more recently other research groups (Liang, Bonn and Hardy 1998), have continued this work and measured many properties of the superconducting crystals, though little further development of the crucible materials has been reported (Huang et al. 1999). The traditional powder sintering method for producing BaZrO<sub>3</sub> crucibles has significant practical difficulties, and requires considerable effort in all processing stages to make acceptable crucibles of low porosity, high chemical and structural purity and a minimum of non-stoichiometric phases.

The desired material is pure, single phase BaZrO<sub>3</sub> with a fine grain size. The BaO - ZrO<sub>2</sub> phase diagram (Figure 2.1) shows single phase BaZrO<sub>3</sub> is only produced when the mole ratio of BaO:ZrO<sub>2</sub> is unity, and any excess of either oxide remains as an undesirable secondary phase (Erb, Walker and Flükiger 1995; Liang, Bonn and

Hardy 1996; Paschoal, Kleykamp and Thuemmler 1987). Even when present in small quantities, any excess of BaO or ZrO<sub>2</sub> reportedly concentrates at the grain boundaries (Erb, Walker and Flükiger 1995). Barium rich phases are readily corroded by flux and unstabilised ZrO<sub>2</sub> can cause cracking, due to phase transformation and thermal expansion mismatch (Erb, Walker and Flükiger 1995). Precise stoichiometry and homogeneity control is crucial for high quality crucible production (Erb, Walker and Flükiger 1995; Liang, Bonn and Hardy 1998). The amounts of secondary phases existing at equilibrium can be calculated from the equilibrium phase diagram and are shown in Figure 2.2 to illustrate the possible susceptibility of BaZrO<sub>3</sub> to secondary phases and provide an initial means of estimating the degree of control that might be necessary.

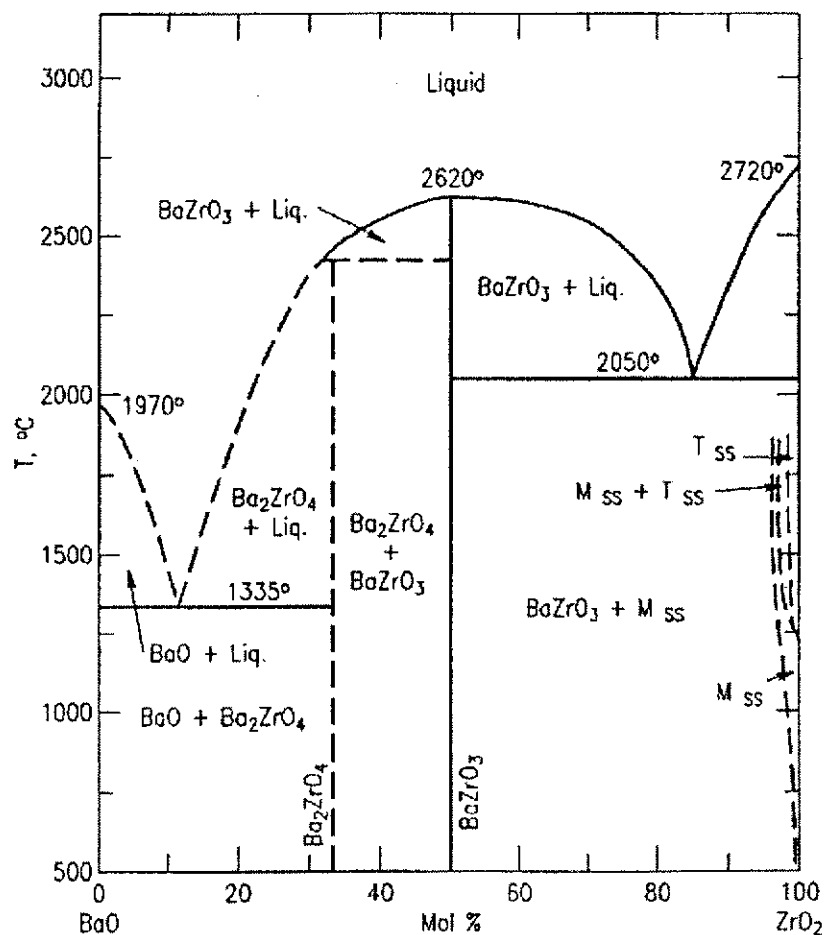


Figure 2.1 BaO - ZrO<sub>2</sub> equilibrium phase diagram (Paschoal, Kleykamp and Thuemmler, 1987). T<sub>ss</sub> = tetragonal ZrO<sub>2</sub> solid solution; M<sub>ss</sub> = monoclinic ZrO<sub>2</sub> solid solution.

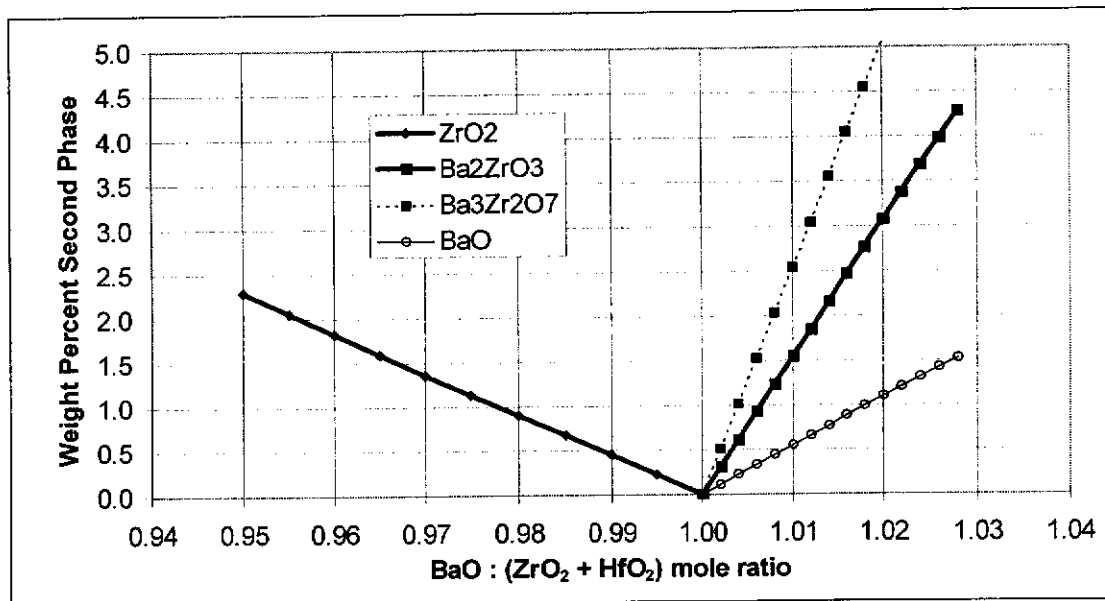


Figure 2.2 Calculated secondary phase abundance assuming phase equilibrium. The phases  $\text{ZrO}_2$  and  $\text{Ba}_2\text{ZrO}_3$  are those indicated on the equilibrium phase diagram (Paschoal, Kleykamp and Thuemmler 1987).  $\text{Ba}_3\text{Zr}_2\text{O}_7$  and  $\text{BaO}$  are calculated simply as other possible phases that may exist under non-equilibrium conditions or as potential phases not detected during the phase diagram determination.

$\text{BaZrO}_3$  is a highly refractory material with a melting point of  $2620^\circ\text{C}$  (Paschoal, Kleykamp and Thuemmler 1987), with a standard heat of formation and standard free energy of formation of  $-1779 (\pm 8) \text{ kJ/mol}$  and  $-1695 (\pm 8) \text{ kJ/mol}$ , respectively (Reznitskii and Guzei 1978). The average bulk thermal expansion coefficient of  $\text{BaZrO}_3$  is  $7.72 \times 10^{-6} ^\circ\text{C}^{-1}$ , which is similar to  $\text{Al}_2\text{O}_3$  ( $8.7 \times 10^{-6} ^\circ\text{C}^{-1}$ ) (Goretta *et al.* 1998; Richerson 1992, p. 152). The Young's modulus of  $\text{BaZrO}_3$  is approximately 220 GPa (Gladysx and Chawla 2001).  $\text{BaZrO}_3$  is difficult to sinter to high density in a pure form from mechanically ground powders without the use of sintering aids. For pressureless sintering, high temperatures of at least  $1700^\circ\text{C}$  are normally required. Sintering temperatures up to  $1700^\circ\text{C}$  in air may be just reached in relatively standard molybdenum disilicide furnaces, but higher temperatures require somewhat specialised heating elements and refractories. The sintering time is ideally limited to a few hours to prevent excessive grain growth, which would degrade the thermal shock resistance of the crucible (Liang, Bonn and Hardy 1998; Erb 1999). The conflicting requirements of densification and grain growth makes high density crucible production difficult and necessitates the use of very fine grained,

homogeneous powders for the production of acceptable crucibles. Producing such powders using mechanical grinding requires repeated firing and re-grinding to achieve adequate phase purity, and careful control of stoichiometry including addition of extra  $\text{BaCO}_3$  to correct for  $\text{ZrO}_2$  contamination from milling media (Erb, Walker and Flükiger 1995; Liang, Bonn and Hardy 1998; Erb 1999). High quality 123 crystals have been grown in  $\text{BaZrO}_3$  crucibles made using this process, but the inherent crucible processing difficulties have restricted their widespread use for high  $T_c$  crystal growth. Despite being the current state of the art material,  $\text{BaZrO}_3$  is used by few research groups worldwide, and the use of stabilised  $\text{ZrO}_2$  and even  $\text{Al}_2\text{O}_3$  crucibles persists despite the inferior results obtained.

### **2.3 $\text{BaZrO}_3$ processing considerations**

Although substantial information on methods used to fabricate suitable crucibles has been published, important details of the crucibles and a complete description of fabrication processes are not available in the literature. In particular, the tolerances on the phase purity required to produce adequate crucibles remains unpublished. Phase purity is determined by three factors:

- \* the accuracy and precision to which bulk stoichiometry is controlled;
- \* the degree to which phase equilibrium is approached (i.e. micro-stoichiometry);
- \* the presence of chemical contaminants which produce stable secondary phases.

According to the  $\text{BaO} - \text{ZrO}_2$  equilibrium phase diagram,  $\text{BaZrO}_3$  is impossible to prepare in an absolutely pure form even under conditions of phase equilibrium, because any excess of  $\text{BaO}$  or  $\text{ZrO}_2$  must produce a second phase. The establishment of stoichiometry may be limited by the accuracy and precision of experimental techniques, such as assaying of starting reagents or the final product, weighing and transfer errors. The production of “phase pure”  $\text{BaZrO}_3$ , even under phase equilibrium conditions, is therefore an approximation, and the deviation from absolute stoichiometry tolerable in the production of acceptable crucibles needs to be established.

In the absence of chemical impurities, phase impurities may occur through at least two factors: non-stoichiometry, and non phase equilibrium. The maximum phase purity possible as determined by stoichiometry occurs at thermodynamic phase equilibrium. For a real sample, kinetic factors limit the actual phase purity according to the extent to which phase equilibrium is established. For example, the completion of solid state reactions in powder processing are controlled by the magnitude and scale of heterogeneity of the powder (a function of effectiveness of milling stages), diffusion kinetics (calcination temperatures) and reaction time (calcination time). The literature gives some information on milling and calcination protocols found to be satisfactory for crucible fabrication. However, some key information, such as calcination times have not been published. Apart from weight loss measurements during calcination stages, there are no published objective means of measuring powder or ceramic characteristics to determine the suitability of a given powder processing protocol for producing corrosion resistant materials. Furthermore, chemical impurities or sintering aids can cause the formation of secondary phases for example by forming binary or ternary compounds (Goretta *et al.* 1998). The literature does not quantify to what extent the inevitable departure from absolute phase purity may be tolerated for materials resistant to corrosion by molten barium cuprates.

## **2.4 Novel processing**

Many novel processes have been reported for the production of alkali-earth zirconates and titanates, predominantly for electronic ceramic applications. Such processes may potentially provide ceramics of a higher quality than the solid-state process, if they are able to simultaneously provide a better combination of :

- stoichiometry control;
- powder phase purity;
- low powder agglomeration state;
- adequately small particle size for sinterability;
- an absence of new defects inherent to that particular process.

Novel processing methods attempt to minimise kinetic barriers to oxide formation, especially solid-state diffusion, in order to minimise reaction times and

temperatures and minimise or eliminate the need for mechanical grinding. Many electronic ceramic applications require tight control of chemical composition, high phase purity and fine grain size to minimise required sintering temperatures, which has justified the extensive process development reported in the journal and patent literature. A further benefit of precursor precipitation methods is that the particle size can potentially be controlled and adjusted by varying the conditions of precipitation and calcination. A major advantage of many chemical processes is the improved scale of mixing which can be achieved compared to the mixing of heterogeneous powders, so phase purity may be reached more readily. When heterogeneous powders are mixed, the reactants are at best segregated on the same scale as the particle size. The degree of heterogeneity is controlled by the achievable particle size, which in the case of mechanically milled powders may be of the order of micrometres. The kinetics of solid-state diffusion during reaction control the extent of reaction and phase purity, and the extent to which phase equilibrium is established. Atomic scale mixing is readily achieved in solution, which under suitable conditions can be maintained during precipitation of a precursor. If a stable single phase precursor can be produced from a homogeneous solution, a phase pure oxide can readily be produced by calcination.

Chemically derived powders can potentially be made considerably finer and more homogeneous than mechanically ground powders, and if so can readily be sintered to very high densities at lower temperatures. For example, the sintering temperature for  $\text{BaZrO}_3$  reportedly can be reduced to as low as 1400 – 1450 °C and still produce densities in excess of 98% of theoretical (Pfaff 1995; Sin, El Montaser and Odier 2002). Reduced sintering temperature may suppress grain growth and make the quality of crucibles significantly higher than those made by the solid-state powder process. Ultra-fine powder methods are yet to be developed for widespread fabrication of large ceramic articles. Given the similar technical requirements of crucibles to those of electronic ceramics, it appears useful to adapt and develop chemical powder processes into methods suitable for producing high quality crucibles for demanding applications such as superconductor melt processing.

The ideal case for precipitated precursors is a stable, single phase compound with a fixed stoichiometry that is relatively insensitive to the conditions of

precipitation, which after calcination produces powders free of aggregation and with very low particle size that are readily sintered. This however, is not readily achieved in practice. Phase segregation may occur during precipitation or a stoichiometric precipitate may not result, and therefore a poly-phase precursor may not yield a phase pure oxide after calcination. For polyphase precursors, the overall stoichiometry depends on the composition and abundance of each phase in the precursor, and heterogeneity depends on the reactivity of the phases during calcination. Chemical processes which produce polyphase precursors may allow adjustment of product stoichiometry, but increase the complexity of controlling the composition or quality of the product. The literature was reviewed to select an appropriate chemical processing method which could be attempted within the time, equipment, and financial resources of this project. The following section is a brief summary of the extensive journal and US patent literature on novel methods of processing alkali-earth zirconates and titanates.

A review of processing methods for the BaO – TiO<sub>2</sub> system by Phulé and Risbud (1990) briefly discusses the problems of the solid-state powder technique and provides an outline of a range of more advanced chemical processes including alkoxide-derived powders, sol-precipitation, sol-gel, hydroxide-, oxalate- and citrate methods, hydrothermal methods, and a freeze-drying process. The earliest report of sol-precipitation methods for BaTiO<sub>3</sub> appears to be by Flaschen (1955). The alkoxide powder process for barium titanate was developed by Mazdiasni, Dolloff and Smith (1969) and Mazdiasni (1984). It consists of reacting a mixture of barium and titanium alkoxides with water to produce a hydrated barium titanate, which is decomposed to ultra-fine barium titanate by vacuum drying at low temperature. Phulé and Risbud (1989) and Chaput and Poilot (1987) also reported detailed organic sol-gel processes for fabricating dense BaTiO<sub>3</sub>. A detailed study of the citrate process has been reported by Mulder (1970), to produce citrate precursors by spraying mixed citrate solutions of inorganic salts into a large excess of alcohol. The drying effect of the alcohol causes precipitation of the mixed citrate, which is calcined to the perovskite powder. Bind *et al.* (1987) described an oxalate-precursor process for BaTiO<sub>3</sub> using TiCl<sub>4</sub> or TiOCl<sub>2</sub>, H<sub>2</sub>C<sub>2</sub>O<sub>4</sub> and BaCl<sub>2</sub>. Other oxalate studies in the barium titanate system were provided by Clabaugh, Swiggard, and Gilchrist (1956)



with further development by Enomoto and Yamaji (1981). A review of oxalate processing for BaTiO<sub>3</sub> was provided by Phulé and Risbud (1990). The thermal decomposition of barium titanium oxalates was studied by Gallagher and Schrey (1963). Numerous hydrothermal processes have been reported for perovskites (Kutty, Vivekanandan and Philip 1990; Inoue and Kawashima 1989; Lilley and Wusirika 1988; Norlund Christensen 1970). A high temperature molten salt technique was reported by Arendt (1981) for titanate, zirconates, and mixtures thereof. A patent has been granted (Matijevic and Her 1999) for the production of crystalline perovskites by adding a mixed aqueous solution of cations to an aqueous base between 70 and 100 °C.

An early report of the production of barium zirconyl oxalate hydrate and its thermal decomposition to BaZrO<sub>3</sub> was produced by Reddy and Mehrotra (1979). Potdar *et al.* (1993) detail a so-called molecular precursor route to BaZrO<sub>3</sub> using a soluble complex formed between sodium oxalate and zirconyl nitrate, from which a barium zirconyl oxalate hydrate was formed and then thermally decomposed to BaZrO<sub>3</sub>. A method for directly producing BaZrO<sub>3</sub> at low temperature without the need for calcination was reported by Phulé and Grundy (1994) using a sol-precipitation method under hydrothermal conditions. A method of producing BaZrO<sub>3</sub> by the decomposition of peroxide pre-cursors was reported by Pfaff (1995) by reacting solutions of barium and zirconyl chloride with hydrogen peroxide and ammonia, then calcining the precipitate at around 900 °C. A patent was granted to Uedaira *et al.* (1986) for the production of BaZrO<sub>3</sub> using hydrolysis of soluble zirconium salts followed by precipitation and aging with barium salts in a high pH environment at elevated temperature. Azad, Subramaniam and Dung (2002) reported a process using barium and zirconium nitrates mixed in a ball mill, followed by calcination to BaZrO<sub>3</sub> at ~ 800 °C.

Only one study has been reported (Robertz *et al.* 2001) attempting the development of solution processed BaZrO<sub>3</sub> for the melt processing of barium cuprate superconductors. In this paper, preliminary results characterising BaZrO<sub>3</sub> powders synthesised using oxalate, citrate, urea, oxalic dihydrazide and solid-state methods were presented, but without results for either sintered ceramics or melt corrosion resistance. One must be careful about the suitability of processes for making BaZrO<sub>3</sub>

articles for use in cuprate melt processing. Characterisation by powder x-ray diffraction (XRD), simultaneous differential thermal and thermogravimetric analysis (DTA/TGA) and scanning electron microscopy (SEM) may be inadequate for predicting the corrosion performance of the ceramic. The corrosion resistance of BaZrO<sub>3</sub> is determined not by the major phase (BaZrO<sub>3</sub>) which when pure may be inert to the melt, but by defects and trace phases which are corroded by the melt. Detection limits for trace phases using bulk techniques such as XRD and DTA/TGA may be inadequate for predicting corrosion performance. Many papers show results from XRD, DTA/TGA and SEM that appear to show a high quality material (Alecú *et al.* 1999; Azad and Subramaniam 2002; Brzezinska-Miecznik, Haberko and Bucko 2002; Pfaff 1995; Robertz *et al.* 2001; Sin, El Montaser and Odier 2002; Taglieri *et al.* 1999) but actual corrosion performance was either not reported or required improvement (Dierickx *et al.* 1996). It is considerably easier to produce a ceramic which on basic analysis may appear to be of high quality than to produce a substrate that is highly resistant to cuprate melt corrosion.

The method selected as most appropriate in this project for chemical processing of BaZrO<sub>3</sub> was the oxalate system. Unfortunately, parts of the literature on the synthesis of barium zirconium oxalates turned out to be incorrect, incomplete and in certain cases misleading. In order to achieve a viable process using oxalate chemistry, very substantial redevelopment was required based on detailed examination of aqueous zirconium solution chemistry. It is appropriate to examine the issues involved in detail, and for this reason a lengthy review of zirconium chemistry is presented below.

## **2.5 Zirconium chemistry**

Chemical processes are inherently more complex to develop than simple solid-state mixed powder methods, because there are many more parameters that must be controlled. The most complex aspect of solution processing is the control of solution chemistry leading to precursor formation, whose difficulty depends on the chemistry of reagents used. Unfortunately, the solution chemistry of titanium, zirconium and hafnium is complex because of the variable state of these ions in aqueous solutions. The state of zirconium ions in solution often has a large influence

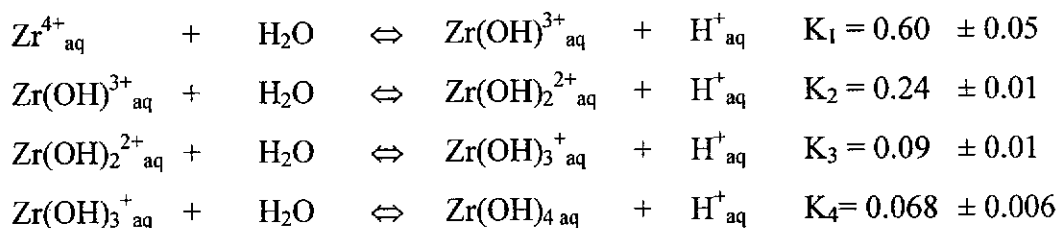
on solution properties (Mukherji 1970, p.1; Elinson and Petrov 1969, p. 15), and the four major phenomena affecting zirconium chemistry are hydrolysis, polymerisation, complex formation and colloid formation (Elinson and Petrov 1969, p. 15,19).

Two outstanding reviews of zirconium chemistry have been presented by Elinson and Petrov (1969) and Solovkin and Tsvetkova (1962). Apart from these major reviews the literature on zirconium chemistry is fragmented, so an extensive summary of the salient aspects relating to  $\text{BaZrO}_3$  precursor production is provided below. The important phenomena affecting zirconium chemistry are complex formation, solution stability, reaction kinetics and hydrolysis which leads to polymerisation and colloid formation. An understanding of zirconium chemistry is required for the development of processing and analytical methods for Zr compounds. The following discussion provides a background upon which the development of oxalate processes suitable for producing high quality  $\text{BaZrO}_3$  was undertaken. Hf behaves chemically almost identically to Zr, and the two co-occur unless Hf has specifically been removed from Zr reagents. For the rest of this chapter, references to Zr also include Hf unless clearly discussed separately. An emphasis is placed on oxalate processes because oxalates, for a number of reasons discussed in Chapter 3, were selected as the primary chemical system for crucible processing development.

### 2.5.1 Hydrolysis

Zirconium ions in aqueous solutions have a strong tendency for hydrolysis due to their high charge and small ionic radius (Elinson and Petrov 1969, p. 20). The hydrolysis of Zr ions in solution plays an important role in the chemical properties of solutions. Simple salts of Zr, for example halides such as  $\text{ZrCl}_4$  and  $\text{ZrOCl}_2 \cdot 8\text{H}_2\text{O}$  do not simply dissolve in water to form  $\text{Zr}^{4+}$  and anions but react with water to form strongly acid solutions (Elinson and Petrov 1969, p. 10).  $\text{ZrCl}_4$  like many other zirconium salts is readily converted to the oxychloride when dissolved in water, which can be recovered by evaporation or treatment with concentrated HCl (Solovkin and Tsevtkova 1962).

A 0.05 M solution of  $\text{ZrOCl}_2 \cdot 8\text{H}_2\text{O}$  has a pH of  $\sim 1$  due to a series of hydrolysis reactions simplified as :



(K is the reaction equilibrium constant at 25 °C) (Elinson and Petrov 1969, p. 21).

The number of hydroxyl groups contained in the hydrolysed Zr ions depends on a number of factors including the concentration of hydrogen ions, and the concentration of Zr (Connick and McVey 1949). The extent of hydrolysis increases with dilution of Zr, aging and heating, and its reversal can be slow (Zaitsev and Bochkarev 1962a; Solovkin and Tsevtkova 1962). Depending on the Zr concentration and presence of complexing ion, Zr may only exist predominately as  $\text{Zr}^{4+}$  in solutions of strong acids, such as  $>2 \text{ N HClO}_4$  and  $>2 \text{ N HCl}$  (Elinson and Petrov 1969, p. 20). The extent of hydrolysis depends on the acidity of the solution, the nature of the acid, the temperature, concentration of Zr and other salts, types of anions in solution, and time. Hydrolysis in perchloric acid is less than in hydrochloric and nitric acids (Solovkin and Tsevtkova 1962). Although initial hydrolysis is rapid, equilibrium in 0.0022 – 0.125 M zirconyl chloride solutions may not be reached for about 10 days (Solovkin and Tsevtkova 1962). Zirconium is considerably hydrolysed at macro concentration even in strongly acid solutions, for example at 0.04 M, hydrolysis of zirconium is observed even in 4 M  $\text{HNO}_3$  (Solovkin and Tsevtkova 1962; Babko and Gridchina 1961; Solovkin and Tsevtkova 1962). However, in very dilute solutions hydrolysis may be avoided if the free acid concentration is above 1 M (Solovkin and Tsevtkova 1962). Recrystallisation of zirconium salts, even from strongly acid solutions is accompanied by some hydrolysis (Elinson and Petrov 1969, p.20). The general solution state of zirconium at very low concentration and without complexing ligands is shown in Table 2.1. However, solution speciation may be considerably more complicated at the higher concentrations required for chemical processing, and in the presence of complexing ligands.

**Table 2.1** State of Zr in Solution in the Absence of Complexing Ligands at Trace Concentrations ( $\sim 10^{-9} \text{ M}$ ) (Elinson and Petrov 1969, p27).

pH	State of Ions and Molecules
< 0	$\text{Zr}^{4+}$ , $\text{Zr}(\text{OH})^{3+}$ (monomers)
0 – 1	$\text{Zr}^{4+}$ , $\text{Zr}(\text{OH})^{3+}$ , $\text{Zr}(\text{OH})_2^{2+}$ , $\text{Zr}(\text{OH})_3^+$ , $\text{Zr}(\text{OH})_4^0$ (monomers)
1.0 – 1.5	$\text{Zr}(\text{OH})^{3+}$ , $\text{Zr}(\text{OH})_4^0$ (monomers)
1.5 – 4.0	$\text{Zr}(\text{OH})_4^0$ (monomer), $[\text{Zr}(\text{OH})_x^{4-x}]$ (polymers, pseudocolloids)
4.0 – 12	$[\text{Zr}(\text{OH})_4]_n$ (true crystals)
> 12	zirconates

The state of zirconium in  $\text{HClO}_4$ ,  $\text{HCl}$  and  $\text{HNO}_3$  solutions prepared at  $\sim 0.4$  M Zr concentration, aged for three weeks and then diluted to 0.05 M Zr concentration prior to analysis was studied by Nabivanets (1961) using electromigration. Below 0.5 M acid concentration, Zr was present only in cationic form, whereas partial combination with anions at higher acid concentrations resulted in a mixture of cationic, neutral and anionic forms. However, the method of detection (colorimetric determination using Alizarin S) may not have been quantitative. Colorimetric methods cannot detect solution species to which the indicator complex are unreactive. Though probably only qualitative, Nabivanets' (1961) detection of a mixture of cationic, neutral and anionic forms of zirconium simultaneously present in solution in the absence of complexing ions appears to be reliable.

Zirconium hydroxide is precipitated from most solutions containing Zr ions by the addition of ammonia or alkali as an amorphous, gelatinous precipitate with very high adsorbent power (Mukherji 1970, pp.3 – 5; Clearfield 1964; Solovkin and Tsevtkova 1962). The solubility of zirconium hydroxide was studied by Kovalenko and Bagdasarov (1961), including the solubility product assuming a formula of  $\text{Zr}(\text{OH})_4$ . However, zirconium hydroxide does not have a definite composition and is typically closer in structure to a hydrated oxide, whose degree of hydration is dependent on many factors (Britton 1925; Singh and Banerjee 1961; Elinson and Petrov 1969, pp. 7 – 8; Zaitsev and Bochkarev 1962a; Solovkin and Tsevtkova 1962). When zirconium hydroxide is precipitated from solutions containing mostly  $\text{Zr}^{4+}$ , such as hot, strongly acidic solutions (i.e.  $>1$  N  $\text{HCl}$ ), its structure and composition is closer to  $\text{Zr}(\text{OH})_4$ , whereas in weakly acid solutions ( $\sim 0.01$  N) where Zr is present chiefly as hydrolysed polymers, zirconium hydroxide precipitates with a

composition closer to  $\text{ZrO}(\text{OH})_2$  (Elinson and Petrov 1969, pp. 7 – 8). The OH content of zirconium hydroxides was determined by Zaitsev and Bochkarev (1962a) using  $\text{F}^-$  titration, which showed that freshly precipitated zirconium hydroxide contained four OH ions per zirconium ion, whereas aging for 2 – 3 days or boiling reduced the rapid reaction of  $\text{F}^-$  to 2 OH ions per Zr ion, with the remaining 2 OH groups taking 10 hours to form by hydration and then react with  $\text{F}^-$ . Drying of zirconium hydroxides, even at room temperature renders them unreactive with  $\text{F}^-$ . Zirconium hydroxide is less soluble when precipitated from a boiling solution than if precipitated in the cold. Dissolution of such hydroxides in acids does not always easily result in a reversal of hydrolysis, and may require acidification to at least 2 N HCl and considerable time to convert polynuclear ions towards  $\text{Zr}^{4+}$ . Some hydroxides, such as  $\text{ZrO}(\text{OH})_2$ , which tends to precipitate from boiling solutions with the addition of alkalis, may only be converted back to zirconyl chloride by prolonged boiling in HCl for in excess of 30 hours. Prolonged heating of weakly acidic Zr solutions reduces the  $\text{Zr}^{4+}$  content in favour of more hydrolysed ions (Elinson and Petrov 1969, pp. 7 – 8).

### 2.5.2 Polymerisation

In very dilute solutions ( $\sim 10^{-5}$  M) of simple zirconium salts at a pH near 1 at 25 °C, Yatsimirskii and Raizman (1961) concluded the predominant speciation of zirconium is  $\text{Zr}(\text{OH})_3^+$ . Other researchers concluded zirconium dimers are present under similar conditions (Connick and Reas 1951). However, when zirconium concentrations are increased to levels pertinent to  $\text{BaZrO}_3$  chemical processing, acid concentrations are reduced or temperatures are increased, zirconium compounds have a strong tendency to polymerise into larger molecules, colloids or sols. The tendency of zirconium to form polynuclear and polymeric solution species of the type  $-\text{ZrO}(\text{X})_2)_n-$  (where  $\text{X} = \text{OH}^-$  or halide ion) is connected with hydrolysis of Zr ions in solution (Elinson and Petrov 1969, p.27). Polymerised forms of zirconium are generally less reactive than monomeric forms, and have a greater tendency for precipitation.  $\text{Zr}^{4+}$  reacts more rapidly than other Zr species and often produces brighter colours with organic indicators, so deliberate methods of minimising the extent of hydrolysis are often employed in analytical techniques (Elinson and Petrov

1969, pp. 20 – 21). To prevent hydrolysis and polymerisation of zirconium solutions, it is recommended that Zr in solution be kept in concentrated acids (such as 10 M HCl) to maintain Zr as a monomeric cation (Elinson and Petrov 1969, p. 27). An acidity of at least 1 – 2 N HCl is required to ensure 0.5 M remains in its most reactive form. The rate of conversion of aged solutions to active ones at ambient temperature is slow and dependent on acid concentration, with equilibrium taking longer than 24 hours in 2 N HCl. To convert solutions that have been heated or aged back to their most reactive state, boiling at 5 N HCl acid concentration has been shown to be effective (Babko and Gridchina 1962).

Polymerisation has been attributed to the processes of olation and oxolation. Olated compounds are complexes in which the metal ions are linked through bridging OH groups. Whether OH groups are present in solid compounds or not, they may be formed to varying extents by hydrolysis reactions. Oxolation is the conversion of bridging OH groups to bridging oxo- groups by the loss of a proton from each bridging OH group. Both of these processes are accelerated or facilitated by heating of solutions, and at increased Zr concentration. Hydrolysis and polymerisation of Zr increases at higher Zr concentrations, at lower acidities, after heating of solutions and at low concentrations of complexing ligands (Elinson and Petrov 1969, p. 24; Clearfield 1964; Babko and Gridchina 1961 and 1962; Zaitsev and Bochkarev 1962a). If a hydroxide formed by ammonia addition to solution is re-dissolved in 1 M HCl, its reactivity with organic indicators is affected by the thermal history of the solution from which the original hydroxide precipitate was formed. If the hydroxide was formed in a solution that had been heated prior to precipitation, the dissolved hydroxide was less reactive to Xylenol Orange than the same zirconium solution that remained cold prior to hydroxide precipitation (Babko and Gridchina 1962). Zirconium has been reported to precipitate hydrolytically, that is merely by boiling the solution, from nitric acid solutions, and possibly from hydrochloric acid solutions if the HCl content is below a few milligrams per litre (Clearfield 1964; Solovkin and Tsevtkova 1962).

Connick and Reas (1951) studied zirconium polymerisation in 2 M and 1 M  $\text{HClO}_4$  using the chelating agent thenoyltrifluoroacetone to perform extraction into benzene. Polymeric ions were mainly dimers containing 3 – 5 hydroxide groups at zirconium concentrations below approximately 0.01 M at 25 °C, however polymerisation was much more extensive at zirconium concentrations between 0.01 and 0.1 M with degrees of polymerisation up to 300 Zr ions/molecule, though experimental precision was a problem at high molecular weights. A continuous series of polymers was concluded to exist, with the extent of polymerisation dependent on zirconium and acid concentrations (Connick and Reas 1951). Kraus and Johnson (1953) reported that 0.1 M Zr in 1.2 N  $\text{HNO}_3$  measured a polymerisation factor of 2, and 0.05 M Zr in 1 N and 3 N acids had factors of 3 and between 2 – 2.6, respectively. Babko and Gridchina (1961) investigated polymerisation of zirconium oxychloride solutions using dialysis. They showed that polymerisation increased with increasing Zr concentration and decreasing acid concentration in perchloric, hydrochloric and nitric acids. HF was also shown to de-polymerise zirconium polymers at low Zr concentrations in 0.05 and 1.0 N HCl solutions, with the polymers more readily broken up at higher acid concentration. Babko and Gridchina (1961) using time dependent dialysis measurements concluded that 0.1 M zirconium oxide chloride in 1 M and 0.1 M  $\text{HClO}_4$  did not contain polymers with a wide range of degrees of polymerisation, but that the degree of polymerisation was narrow and depended on the acid concentration.

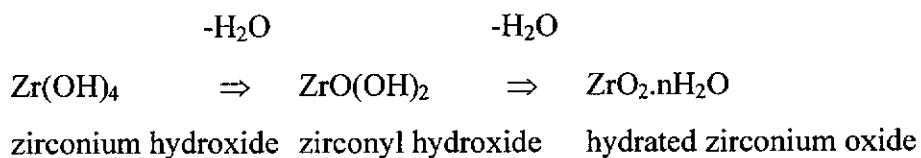
Babko and Gridchina (1962) studied the reactivity of zirconium solutions with organic indicators, particularly Xylenol Orange, as a function of zirconium concentration, acidity, thermal history and time. The sluggish development of colour by reaction between Xylenol Orange and zirconium solutions was interpreted as indicating the decomposition of some polymeric forms of zirconium by formation of complexes with the indicator reagent. This reactivity was not simply dependent on the average degree of polymerisation measured by dialysis – polymeric ions formed in less acid media were observed to decompose more rapidly than those formed in more acid media for the same degree of polymerisation. This was attributed to the presence of different side groups in zirconium polymers: those formed at low acidity would be of the type –  $(\text{ZrO}(\text{OH}_2)_n$  – whereas those formed in more acid media



would be more likely to be of the type  $-(\text{ZrO}(\text{Cl}_2))_n-$ . The latter case would be more reactive with organic indicators because the  $\text{Cl}^-$  ion would be less tightly bound to the zirconium ions than the  $\text{OH}^-$  ion. Whether this interpretation is correct is uncertain – perhaps the dialysis measurements (Babko and Gridchina 1961) have not adequately taken account of the difference in side groups in determining the average degree of polymerisation.

Heating of solutions results in substantial changes in reactivity with Xylenol Orange. Heating solutions containing  $10^{-3}$  M zirconium at  $\text{pH} = 2$  rendered them completely unreactive with Xylenol Orange, whereas an unheated but otherwise identical solution was far more reactive. “Polymeric ions formed in the cold in solutions of low acidity on heating increase to colloidal particles, which are not destroyed even in the presence of Xylenol Orange” (Babko and Gridchina 1962).

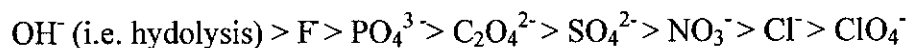
A study of hydrolysed Zr compounds by Zaitsev and Bochkarev (1962a) showed that  $\text{Zr}(\text{OH})_4$  is an unstable compound, and aging or heating leads to dehydration according to the following scheme:



Consequently, most studies which use zirconium hydroxide as a reagent specify its use as a “freshly prepared” compound. Speciation of zirconium in solution is affected by acidity, temperature, time and other conditions (Elinson and Petrov 1969, p. 19). Polymerisation of zirconium hydroxides was reported by Clearfield (1964), in which mixtures of zirconyl chloride and ammonia were refluxed for extensive lengths of time. Refluxing resulted in decreasing solution pH with time and eventual precipitation of crystalline hydrous zirconia phases, which were attributed to hydrolytic polymerisation.

### 2.5.3 Complex formation

Due to high charge, small ionic radius and relatively low ionisation potential, Zr ions are typical complex formers, and the stability of such complexes can be ranked in the following order (Elinson and Petrov 1969, p. 28; Solovkin and Tsevtkova 1962):



Zirconium also forms complexes with numerous other compounds including peroxides, perchlorates, oxalates, certain carboxylic and hydrocarboxylic acids, mandelates, cupferron and EDTA (Elinson and Petrov 1969, pp. 28 – 34). Complex formation is a crucial phenomenon in both the analytical and process chemistry of Zr. In analytical chemistry, complex formation strongly affects the interaction of Zr solutions with reagents for its detection and quantification, and serious errors or missed detection can result from failing to control the speciation and complexation of Zr in solution.

Speciation of zirconium in solution can strongly influence the composition of complexes formed by various ligands. For example, Karlysheva and Sheka (1962) showed the ratio of cupferron to zirconium in cupferron complexes precipitated from sulphuric acid solutions ( $[\text{Zr}] = 0.016\text{M}$ ) decreased with reduced solution acidity and increased aging time of the solution. The same phenomenon occurred in nitric acid solutions even at lower concentration ( $\sim 0.03\text{ M}$ ). The change in complexation with aging and acid concentrations was ascribed to the processes of hydrolysis and polymerisation. Increased acidity was reported to lead to de-polymerisation of zirconium ions, and at ambient temperature, the process of de-polymerisation occurred more rapidly than the original polymerisation.

In process chemistry, the properties of solutions and the structure and properties of precipitates can be influenced by the effects of complex formation on Zr solution speciation. Polymeric forms of Zr are broken up by complexing ions such as fluoride, oxalate,  $\text{H}_2\text{O}_2$  and acetylacetone, with an increasing complex concentration decreasing the degree of polymerisation (Babko and Gridchina 1961). This process occurs either by substitution of bridging OH groups by complexing species, or the prevention of the formation of bridging OH groups. Complexing strength decreases in the following order:

oxalate > citrate > tartrate > glycoate > acetate > formate > sulphate.

(Elinson and Petrov 1969, p. 25)

or

citrate > oxalate > malate > tartrate > glycoate >

succinate ~ malonate ~ malate ~ propionate ~ acetate ~ fumarate > formate >

sulphate > chloride ~ nitrate.

(Solovkin and Tsevtkova 1962)

Speciation of zirconium can be strongly affected by complexing anions. Complexing ions can increase the stability of a solution to polymerisation and precipitation (Elinson and Petrov 1969, p. 8,24,33). For example, zirconium hydroxide precipitates at low pH (~1.8) for solutions of simple zirconium salts such as zirconium oxychloride (Britton 1925; Kovalenko and Bagdasarov 1961), whereas salts such as  $(\text{NH}_4)_2[\text{ZrO}(\text{C}_2\text{O}_4)_2]$  and  $\text{Na}_2[\text{ZrO}(\text{C}_2\text{O}_4)_2]$  do not form a precipitate with addition of KOH until a pH above 10.0 and 9.4 respectively, at zirconium concentrations of ~0.02 M at 25 °C (Zaitsev and Bochkarev 1962b).

The amount of complexing agent added can have a curious effect on the solubility of Zr compounds. Addition of precipitating agents including oxalic acid, alkali oxalates, tartrates and citrates, to freshly prepared solutions of Zr salts such as  $\text{ZrCl}_4$  or  $\text{ZrOCl}_2 \cdot 8\text{H}_2\text{O}$  initially results in an unstable precipitate which rapidly re-dissolves. As more agent is added, the stability of the precipitate increases until a point is reached where it is stable and the amount of precipitate increases with addition of reagent. However, as an excess of the precipitating agent is added, the precipitate re-dissolves and becomes completely soluble in an excess of the reagent (Mohanty, Singh and Murty 1955; Elinson and Petrov 1969, p. 25). In the case of old or previously boiled solutions, the precipitate may not be soluble in an excess of reagent (Elinson and Petrov 1969, p. 25). As outlined previously, zirconium hydroxides precipitated from cold but previously boiled or aged solutions often differ in composition to those from fresh solutions. Clearly the reactivity, composition and/or structure of the precipitated complex, including oxalates, can be influenced by the solution speciation of zirconium at the time of reaction. Excesses of certain

complexing reagents can affect the product stoichiometry by preventing Zr from precipitating in the desired amounts in the product. Processing methods which use complexing species may need to control the potentially solubilising effects of an excess of complexing reagents, and also may need to consider Zr speciation to control the structure and composition of the precipitate.

#### 2.5.4 Colloid formation

The process of polymerisation, at high levels, leads to the formation of colloidal particles or sols. Britton (1925) first proposed that basic zirconium salt solutions were “essentially colloidal despite the fact that many of the solutions are perfectly clear”, and that “the process of precipitation is one which involves formation of a colloidal solution which subsequently precipitates”. Sols can be stable in moderately concentrated acid solutions. The sol may have positive or negative charge due to adsorption of cations or anions from the solution and may have a wide range of zirconium : anion weight ratios of 6.6 – 16.2 to up to 40 : 1 (Solovkin and Tsvetkova 1962). The variable charges of these species because of adsorption is considered by Solovkin and Tsvetkova (1962) to account for the mis-identification of non-existent compounds which were once believed to have unusual composition.

Sols can be sensitive to the action of electrolytes and in some cases can be completely precipitated by pH-neutral salts such as KCl, KBr. It has been pointed out that addition of AgNO<sub>3</sub> to an aqueous solution of a sol may not give a AgCl precipitate unless boiled for a prolonged period with concentrated acid (Solovkin and Tsvetkova 1962), indicating extraordinary stability of either Cl<sup>-</sup> or much more likely Ag<sup>+</sup> adsorption by the sol. Increased temperature causes an increase in the concentration of the sol, and its aggregation and conversion to a gel. Furthermore, the pH below which zirconium hydroxide dissolves has been observed to decrease with increased ionic strength (solution concentration) of neutral ionic compounds such as NaNO<sub>3</sub> (Kovalenko and Bagdasarov 1961).

Colloid stability is an important phenomenon for chemical processing for three reasons. Firstly, preferential precipitation of one component of the solution as a particulate is a form of phase segregation. For example, the formation of

zirconium-rich colloids must subsequently be reversed by solid-state diffusion during calcination in order to form a phase pure calcined product, the ease of which is determined by the scale and magnitude of segregation. Secondly, if the mechanism of precipitation is one of de-stabilisation of a charge-stabilised colloidal phase by adsorption of dissolved ions, the structure and chemistry of the colloid may influence the chemistry (especially mole ratio) and ultra-structure (phase segregation) of the precipitated product, and hence colloid properties must be controlled to produce the desired product. Finally, if the precipitate is of a very fine particle size (which is desirable for producing a highly sinterable product), the colloid must not be too highly dispersed during filtration and washing stages, otherwise the process may not be feasible because of particle loss through filtration media and poor filtration rates. The dispersion state is controlled by the surface chemistry of the precipitate, particularly its surface charge. The suitability of a system to adjustment of surface chemistry, such as by additional reagents or pH change, depends on the responsiveness of the system and the level of contamination tolerable in the product.

Aging and boiling of sols causes decreased hydration and structural rearrangement in the sol, and a pH drop of the solution by liberation of free acid (Solovkin and Tsvetkova 1962). Colloid formation at high acidities is more reversible than that at low acidity or zirconium concentration, or for aged or boiled solutions. The difference in properties has been related to colloid particle size, and the process of oxolation by Thomas (Solovkin and Tsvetkova 1962). For 0.1 M zirconium solutions in 6 M nitric acid solutions, on the basis of ion exchange data, Lister and MacDonald (cited in Solovkin and Tsvetkova 1962) concluded the size of zirconium polymers is of the order of 4 – 6 Å, and the molecular weight of polymers increases approximately six fold with a decrease in HNO<sub>3</sub> concentration to 0.02 M. The ions present contained NO<sub>3</sub><sup>-</sup> in addition to OH. It has also been shown using ion exchange that 0.1 M zirconium nitrate is colloidal and does not have a clearly defined cationic character. At the same concentration in 1.5 M HNO<sub>3</sub>, zirconium nitrate was cationic and remained that way for one month (Solovkin and Tsvetkova 1962).

X-ray diffraction on solutions was used by Muha and Vaughan (1960) to show that HfOCl<sub>2</sub>·8H<sub>2</sub>O and HfOBr<sub>2</sub>·8H<sub>2</sub>O in solution over the concentration range 0.5 – 2 M best matched the complex ion [Hf<sub>4</sub>(OH)<sub>8</sub>(H<sub>2</sub>O)<sub>16</sub>]Cl<sub>8</sub> (i.e. without the Cl<sup>-</sup>

ion attached directly to the zirconium ion), with good agreement for  $\text{ZrOCl}_2 \cdot 8\text{H}_2\text{O}$  as  $\text{Zr}_4(\text{OH})_8(\text{H}_2\text{O})_{16}\text{Cl}_8$  at 2 M concentration. This data is in agreement with the ion exchange data of Lister and MacDonald who found polymers of similar size containing OH and anions (cited in Solovkin and Tsvetkova 1962).. Zirconium fluorescence, which is very intense for Mo  $K_\alpha$  x-radiation because of the relative energies of characteristic Mo emission and the Zr K absorption edge, prevented measurements below 2 M for zirconyl chloride, and there was not quite as good a match of experimental and calculated results as for Hf salts. The structures for the Hf and Zr salts were clearly very similar, though the Zr salt was thought to possibly be more highly polymerised than the Hf salt in agreement with a previous study. The great problem with the study of Muha and Vaughan (1960) is that their conclusions do not account for the acidity of solutions of zirconium and hafnium oxyhalides. If the metal is present as the same ion,  $[\text{Me}_4(\text{OH})_8(\text{H}_2\text{O})_{16}]^{8+}$ , in the solid and in the solution, then dissolution of the solid in water could not affect pH. However, the strong acidity of these salts in water shows that considerable hydrolysis still occurs. Muha and Vaughan (1960) failed to fully disclose raw experimental data and commented that a large, concentration dependent peak was removed from the data shown in their paper. Their assertion that this peak did not arise from intermolecular scattering was not explained. The increase in scattering intensity with increased concentration could be due to the formation of polymers or colloids probably consisting of clusters of the  $[\text{Me}_4(\text{OH})_8(\text{H}_2\text{O})_{16}]^{8+}$  ions which might explain the remainder of the diffraction pattern. This unresolved possibility may account for the missing hydrolysis in the conclusions of the x-ray investigation.

The literature relating to zirconium chemistry at concentrations high enough to be useful for chemical processing is scant compared to analytical chemistry literature on dilute solutions. Yuranova, Komissarova and Plyuschchev (1962) studied the aqueous solubility of zirconium and hafnium oxide nitrate hexahydrates. The solubility of such compounds (and presumably all related, non-highly polymerised oxide halide salts) increased as a function of temperature, quite markedly between 30 and 35 °C, and then fell substantially above ~35 to 80 °C (the maximum temperature measured). The reduced solubility above 35 °C was attributed to hydrolysis and polymerisation, which is favoured by increased temperature.

Correspondingly, the recovered salt after heating became continuously more basic in composition (lower nitrate : zirconium ratio) with increased temperature. Yuranova, Komissarova and Plyuschchev's results (1962) clearly show simple zirconium salts can be of indefinite composition (i.e. fractional mole ratios of ions in molar formulae) which is dependent on the conditions under which they were prepared, and their results infer that zirconium solutions are subject to hydrolysis and polymerisation at high concentration, particularly at elevated temperature.

### **2.5.5 Effect of complexing ions on polymerisation**

Polymerisation is influenced by the processes of hydrolysis and complex formation (Nabivanets 1961). The tendency for hydrolysis and polymerisation even in weakly acidic solutions can be reduced or negated by complexation, which can be exploited in both processing and analytical chemistry. Weak organic complexing agents such as acetylacetone have been used in analytical chemistry to ensure efficient extraction by completely preventing the formation of slow reacting polynuclear cation of zirconium or zirconium hydroxide (Kuznetsov and Fang Ming-o 1962). Sulphate ions can be used to break up some polymeric zirconium species to significantly increase their reactivity with other compounds, for example with organic indicators for analytical chemistry. Sulphate ions when present in a large excess, substantially reduce polymerisation of 0.01 M zirconium even when heated, particularly if the acid concentration is above 1 M (Babko and Gridchina 1962).

Babko and Gridchina (1961) used dialysis to show that the degree of polymerisation of zirconium in perchloric acid is dependent on the zirconium and perchloric acid concentrations. High zirconium (0.001 to 0.1M) and low acid concentrations favour polymerisation. Complexing agents such as  $F^-$ , oxalate, hydrogen peroxide and acetylacetone were claimed to destroy polymeric forms of zirconium. Their results showed for 0.01 M zirconium concentration, a HF:Zr ratio of 1 or more resulted in the destruction of polymeric zirconium in 1 M  $HClO_4$ , as did HF : Zr ratios of 4 or more in 0.05 M  $HClO_4$ . The solutions were prepared by dissolving freshly prepared hydroxide in acid. However, previously aged or heated reagents would be unlikely to be as easily de-polymerised by complexing agents.

There is little information on the stability of zirconium salts at high concentration in the presence of complexing ligands, as a function of thermal history.

Of particular interest to this study is the effect of oxalate complexation on polymerisation. The presence of oxalates interferes with polymerisation of zirconium, or in some cases can de-polymerise zirconium in solution (Babko and Gridchina 1961; Elinson and Petrov 1969, p. 24) or solubilise precipitated oxalates (Mohanty, Singh and Murty 1955; Elinson and Petrov 1969, p. 25). Elinson and Petrov (1969, p. 40) stated “the oxalate complex of zirconium  $[\text{Zr}(\text{C}_2\text{O}_4)_4]^{4-}$  is so strong that it is impossible to prepare the hydroxide from it. However, that comment has been shown likely to be incorrect in the current study as hydroxide precipitation was observed from solutions containing a large excess of oxalic acid, though confirmation of  $[\text{Zr}(\text{C}_2\text{O}_4)_4]^{4-}$  speciation of zirconium prior to OH addition was not attempted. As mentioned above, oxalate complexation can suppress the precipitation of zirconium from pH above ~1.8 in simple zirconium salt solutions such as zirconium oxychloride (Britton 1925; Kovalenko and Bagdasarov 1961), to above pH 10.0 and 9.4 for  $(\text{NH}_4)_2[\text{ZrO}(\text{C}_2\text{O}_4)_2]$  and  $\text{Na}_2[\text{ZrO}(\text{C}_2\text{O}_4)_2]$ , respectively (Zaitsev and Bochkarev 1962b).

One reason for the effect of complexing ions on polymerisation is that replacement of OH groups by complexing ligands may prevent or reverse olation. The degree of substitution is determined by the concentrations of reagents (especially Zr), the relative concentrations of the reagents (i.e. both Zr and complexing ion concentrations), the coordinating power of the complexing species, and the nature of zirconium species present (Elinson and Petrov 1969, pp. 24 - 25). As discussed above, there are many factors affecting the speciation of zirconium, and therefore their reactivity with complexing species. Addition of oxalate salts to previously boiled zirconium solutions can produce precipitates that are insoluble in an excess of oxalate, whereas precipitates formed from fresh, cold solutions can be re-dissolved by excess oxalate to form perfectly clear solutions (Elinson and Petrov 1969, p. 25). Hence the effect of complexing ions on zirconium polymerisation is also dependent on the other factors controlling zirconium speciation.



### 2.5.6 Zirconyl ion

It is often mistakenly assumed that compounds written as  $\text{ZrO-X}$  (e.g.  $\text{ZrOCl}_2 \cdot 8\text{H}_2\text{O}$ ) contain a zirconyl ion, i.e. a  $\text{Zr=O}$  double bond, either as a solid compound or when dissolved in solution (Mukherji 1970, p.1; Elinson and Petrov 1969, pp. 15 - 20). The  $\text{Zr=O}$  double bond only exists in a small fraction of instances, and there has been considerable disagreement in the literature as to the existence of the zirconyl ion.  $\text{ZrOCl}_2 \cdot 8\text{H}_2\text{O}$  has been shown by XRD to have the structure of the tetramer  $[\text{Zr}_4(\text{OH})_8 \cdot 16\text{H}_2\text{O}]^{8-}$  (Clearfield and Vaughan 1995; Clearfield 1964). Many solutions of “zirconyl” compounds including  $\text{ZrOCl}_2 \cdot 8\text{H}_2\text{O}$  have been shown by techniques such as vibrational spectroscopy, XRD, electromigration, electrometric titration, ion exchange etc. to contain no  $\text{Zr=O}$  double bonds as solids or in solution. Solovkin and Tsevtkova (1962) concluded “from an examination of the properties of aqueous and acidic solutions of, for the most part, the chlorides and nitrate, that there is no justification for the zirconyl theory.” Some compounds do contain the zirconyl group, such as zirconium oxyfluorides, certain alkali zirconium hydroxy thiocyanate hydrates and  $\text{Zr}_4\text{F}_{10}\text{O}_3$  (Elinson and Petrov 1969, pp. 15 - 20; Mukherji 1970, p. 1). One cause of disagreement over the ionic state of zirconium compounds in solution is variation of conditions under which they were determined, particularly acid concentrations (Zaitsev and Bochkarev 1962a).

### 2.5.7 Oxalates

There is considerable uncertainty in the speciation of zirconium oxalate complexes in solution. The speciation of zirconium compounds can depend on the method by which they were prepared and the conditions under which they are analysed. Yatsimiskii and Raizman (1961) concluded only  $[\text{Zr}(\text{OH})(\text{C}_2\text{O}_4)]^+$  with a  $\text{Zr:oxalate}$  ratio of 1:1 was formed between  $\sim 3 \times 10^{-5}$  M zirconium oxychloride dissolved and  $\sim 3 \times 10^{-5}$  M oxalic acid at 25 °C. Using ion exchange, Marov and Ryabchikov (1962) concluded 1:1 and 1:2 zirconium:oxalate complexes form in solutions containing  $5 \times 10^{-6}$  M zirconium,  $5 \times 10^{-6}$  to  $10^{-4}$  M oxalic acid and 2 - 4 M acid solutions. Such results may be of interest to analytical chemistry but are of limited interest here because it is not feasible to operate a chemical process for  $\text{BaZrO}_3$  production as dilute as  $\sim 10^{-5}$  M. Connick and McVey (1949) noted 0.001 M zirconium in oxalic acid produced only 0.36 % as much extractable zirconium

compared with zirconium in perchloric acid, indicating strong oxalate complex formation. This is still too low a zirconium concentration for efficient chemical processing. Grinberg and Asatpovich (1961) determined that the instability constant of a zirconium oxalate complex ion,  $[\text{Zr}(\text{C}_2\text{O}_4)_4]^{4-}$  at 0.002 M Zr concentration, between pH 3.02 and 4.50, was approximately  $10^{-4}$ . Although not stated explicitly, this study infers that zirconium oxalates are present under these conditions in monomeric form rather than as polymers, if prepared from alkali zirconium oxalate compounds using the methods given.

Zaitsev and Bochkarev (1962a) discounted Vinogradov and Sphinel's (1961) conclusion that zirconyloxalic acid contains no zirconyl groups, claiming that in strongly acid solutions of oxalic and hydrochloric acid, zirconyl groups are converted to zirconium ions, whereas at more neutral pH where their own measurements were taken, limited reaction with  $\text{F}^-$  was interpreted as indicative of zirconyl groups. The existence of negatively charged ions has been observed in the presence of strongly acidic media and complexing agents. In the presence of oxalic acid and soluble oxalates, zirconium forms soluble complexes containing no zirconyl groups including  $\text{Zr}(\text{C}_2\text{O}_4)^{2+}$ ,  $\text{Zr}(\text{C}_2\text{O}_4)_4^{4-}$  (or possibly  $[\text{Zr}_4(\text{C}_2\text{O}_4)_{16}]^{16-}$ ) and  $\text{Zr}(\text{C}_2\text{O}_4)_5^{6-}$  as the concentration of oxalate is increased (Elinson and Petrov 1969, p. 17, 32, 39 - 40). Using potentiometric titration of sodium oxalate to 0.1 M zirconium nitrate, Mohanty, Singh and Murty (1955) observed the formation of insoluble  $\text{Zr}(\text{C}_2\text{O}_4)_2$  which dissolved upon further addition of sodium oxalate to form 3 soluble complexes:  $\text{Zr}(\text{C}_2\text{O}_4)_2 \cdot 2\text{Na}_2\text{C}_2\text{O}_4$ ,  $\text{Zr}(\text{C}_2\text{O}_4)_2 \cdot 4\text{Na}_2\text{C}_2\text{O}_4$  and  $\text{Zr}(\text{C}_2\text{O}_4)_2 \cdot 6\text{Na}_2\text{C}_2\text{O}_4$ . Presumably it is the formation of these complexes which results in the solubility of zirconium salts in excesses of oxalate salts. In a sufficient excess of oxalate, it is claimed that it is impossible to precipitate the zirconium as the hydroxide, but this remark was made without qualification, such as stating a range of zirconium concentration or extent of polymerisation or oxolation (Elinson and Petrov 1969, p. 40). There must be a structural or compositional difference between precipitates formed by oxalate addition to previously boiled solutions compared to fresh, cool solutions because of the large differences in solubility in excess oxalate. The state of Zr ions in oxalate complexes, particularly at high Zr concentrations, remains under studied and somewhat unclear.

Earlier studies by Zaitsev and Bochkarev (1962a+b) using the  $F^-$  determination of  $OH^-$  investigated the structures of relevant Zr compounds including Zr-hydroxides,  $ZrOC_2O_4 \cdot 4H_2O$ ,  $Ba[ZrO(C_2O_4)_2]$ ,  $(NH_4)_2[ZrO(C_2O_4)_2]$ ,  $Na_2[ZrO(C_2O_4)_2]$ ,  $K_2[ZrO(C_2O_4)_2]$ , and  $ZrOCl_2 \cdot 8H_2O$  (where no attempt was made to account for bound water in the formulas except for  $ZrOCl_2 \cdot 8H_2O$ ). Zaitsev and Bochkarev (1962a) concluded that  $F^-$  substitutes for OH groups of zirconium compounds, with the liberated OH detected by acid/base titration. The reaction was considered to occur in two steps: compounds containing OH in the solid reacted rapidly with  $F^-$ , whereas reaction of  $F^-$  with zirconyl ions required prior hydration of zirconyl ion. The hydration of zirconyl ions from the solid was the rate limiting step, with reaction taking more than 24 hours for certain compounds.

The observed OH : Zr mole ratio of these oxalate compounds depended on the solution conditions under which the measurements were made. For zirconyl oxalate,  $Ba[ZrO(C_2O_4)_2]$ ,  $(NH_4)_2[ZrO(C_2O_4)_2]$ ,  $Na_2[ZrO(C_2O_4)_2]$ ,  $K_2[ZrO(C_2O_4)_2]$ , and  $ZrOCl_2 \cdot 8H_2O$ , the observed OH:Zr ratio was 2.0 when measured with HCl added to the solutions, and for  $(NH_4)_2[ZrO(C_2O_4)_2]$  and  $Na_2[ZrO(C_2O_4)_2]$  between approximately 1.4 and 1.7 when in water alone. The compounds precipitated under alkaline conditions apart from the ammonium and sodium salts, in which case the observed Zr:OH ratios were between 1.0 and 1.3 at pH 9.0; the reduction in OH content was concluded to be due to condensation reactions. In many cases, the apparent release of  $OH^-$  by substitution with  $F^-$  was slow, often taking in excess of 24 hours to approach equilibrium. Significant approximations in the results are ignored rather than explained (e.g. Zr:OH = 1.78 for the ammonium salt was rounded to 2 without justification or consideration), and possible causes such as reaction kinetic limitations in the method, polymeric solution speciation or failures in the technique are not explored. Conclusion on degrees of polymerisation, such as dimers for the ammonium, barium and sodium salts, are tenuous at best since they relied on untested assumptions and unverified interpretations. Applying the same assumptions and interpretations to the data for  $ZrOCl_2 \cdot 8H_2O$  would predict a dimeric solution complex (though the paper does not explicitly state the degree of polymerisation for  $ZrOCl_2 \cdot 8H_2O$ ), whereas structures at least as large as tetramers were measured by Muha and Vaughan (1960) using x-ray scattering. The effect of increased pH on

complex structure was interpreted as due to condensation reactions between coordinated OH groups, either on the same Zr ion or between two (and not more than two) Zr ions. This is a useful interpretation, as coordination of higher numbers of OH groups might be expected at higher pH, whereas the opposite was observed using the F<sup>-</sup> technique. The interpretation was based on condensation reactions which seem to occur in Zr(OH)<sub>4</sub>, leading to ZrO(OH)<sub>2</sub> and eventually ZrO<sub>2</sub>.nH<sub>2</sub>O. The condensation reactions were reported to produce H<sub>2</sub>O, and would therefore not result in a pH change. This is in contrast to the hydrolysis and oxalation reactions reviewed by Solovkin and Tsvetkova (1962), which were reported to produce free acid and therefore reduce pH. Leaving aside the possible limitations in the authors' interpretations, the study shows apparent effects of pH and cation type on the structure of Zr-oxalate complexes.

#### **2.5.8 Stability of oxalate complex solutions**

Zirconium may form highly stable solution complexes under certain conditions. However, it is also apparent that under certain conditions, zirconium oxalate complexes have a significant tendency to precipitate or aggregate into colloids. The stability of these complexes is of critical importance to the optimal performance of the oxalate process in terms of phase purity and particle size. A useful case to illustrate this behaviour has been investigated in the present study using a mixed solution of zirconium oxychloride and oxalic acid in the mole ratio of 1:2.2 at a zirconium concentration of 0.1 M, made by slowly adding the zirconium solution to oxalic acid. If the rate of addition of the zirconium is low enough, a clear solution can be made at room temperature. As the solution is heated it becomes opalescent due to the formation of a visible amount of colloid at 74 °C which increases to the point where by 85 °C the slurry becomes strongly opaque. After boiling for a few minutes, the solid phase is stable at room temperature for a period exceeding one week, possibly indefinitely, and is not readily soluble in hydrochloric acid.

The formation of clear solutions is favoured at low temperatures, probably because the complexing anion replaces some hydroxo-groups to form the complex ion thereby restricting the ability for polymerisation. During heating, polymerisation

overcomes this process, possibly by the process of oxolation, which is the conversion of bridging hydroxo-groups to much more stable oxo-groups by the loss of a proton to solution. Oxolation is favoured by high pH, heating and increased zirconium concentration. The reversal of oxolation reactions is reported to be very slow. The observed precipitation of zirconium by oxalic acid, whatever the exact mechanism, may be a central cause of observed phase segregation in the attempted formation of stoichiometric barium zirconyl oxalate hydrates using barium chloride and oxalic acid. The effectively irreversible precipitation of zirconium or zirconium rich oxalate colloids at high temperature (~ 90 - 95 °C) may prevent the necessary reaction with barium ions that might otherwise result in a single phase stoichiometric compound.

Zirconium oxalate sols were used by Ju *et al.* (2000) in a sol-gel method for forming  $\text{ZrO}_2$  membranes. Zirconyl oxalate sols were prepared by mixing 0.25 M oxalic acid solution with 0.5 M  $\text{ZrOCl}_2 \cdot 8\text{H}_2\text{O}$  solution in a 1:8 mole ratio at 90 °C. After 30 minutes, a transparent blue coloured sol was formed, which was used to form coatings on an  $\text{Al}_2\text{O}_3$  support. Etienne *et al.* (1994) prepared hydrated zirconyl oxalate sols by mixing 0.25 M oxalic acid and 0.5 M  $\text{ZrOCl}_2 \cdot 8\text{H}_2\text{O}$  in a 1 : 1 mole ratio at ambient temperature. The sol was stabilised by HCl formed by hydrolysis of  $\text{ZrOCl}_2 \cdot 8\text{H}_2\text{O}$ . Gellation occurred during drying at 30 – 40 °C, but the dried material could be re-dispersed in water as a sol unless dried above 60 °C. The reaction of zirconium with oxalates has also been used in microemulsion techniques (Fang *et al.* 1997). The formation of zirconium oxalate colloids under these conditions proves that oxalate complexing is unable to fully suppress zirconium polymerisation at high concentrations at high temperatures under acidic conditions. It is therefore very likely that at high zirconium concentrations, polymerisation may not be prevented by oxalate complexing, and the lack of an observable colloid may not be indicative of monomeric or even molecular zirconium speciation.

A similar or identical effect occurs in titanate systems. US Patent 5009876 (Hennings and Schreinemacher, 1991) reports a process for producing  $\text{BaTiO}_3$  using an oxalic acid derived precursor. Solutions containing  $\text{TiOCl}_2$  and oxalic acid were found to be unstable when heated above  $60^\circ\text{C}$ , with only 30 minutes of stability at  $80^\circ\text{C}$ . Presumably the term “unstable” refers to the formation of precipitates, which would be expected to be colloidal in nature and consistent with the observations in this study. Because of solution instability, processing temperatures between  $20$  and  $60^\circ\text{C}$  were recommended, preferably between  $50$  and  $60^\circ\text{C}$ , and optimally at  $55^\circ\text{C}$ . At temperatures higher than the recommended range, an undesirably high degree of  $\text{TiO}_2$  precipitation was observed, though by what means it was detected and at what stage (i.e. before or after calcination) was not reported. If the reaction temperature was too low, the reaction rate was reported to be strongly reduced. What detrimental effects this may have had (other than reduced production rates) were not reported, though reaction kinetics commonly impact on precipitate size. Instability in the oxalic acid / Zr system was also reported by Clabaugh, Swiggard, and Gilchrist (1956).

The instability of solutions containing oxalic acid and zirconium salts may be minimised or avoided by using alkali or ammonium oxalates instead of oxalic acid. This possibility may represent a substantial improvement in process chemistry by allowing more flexibility in process temperatures and the potential to use significantly higher temperatures to suppress the precipitation of  $\text{Ba}(\text{C}_2\text{O}_4) \cdot 0.5\text{H}_2\text{O}$  as a stable or intermediate phase. This possibility was briefly investigated by Clabaugh, Swiggard, and Gilchrist (1956).  $\text{BaCl}_2$  solutions were added to solutions of alkali (Na, K, and  $\text{NH}_4$ ) zirconium oxalate solutions, where the pH of the alkali zirconium oxalate solution was 5-6, and the solution mole ratio of barium : zirconium : oxalate was 1 : 1 : 2. The compounds formed all had a slight deficiency of barium, with the mole ratio of barium : zirconium ranging between 0.888 and 0.994. The ratio of  $\text{C}_2\text{O}_4$  : Zr varied only very slightly between 2.001 and 2.005, which was less than the limit of experimental determination. The variation of Ba:Ti ratios in repeated experiments was small though significant, and one might infer from the results of Gangadevi, Subba Rao and Kutty (1980) that this could have been due to variations in pH. The calcined compounds were dissolved in HCl. Samples prepared with the potassium

reagent showed potassium in solution, and the sample prepared using the ammonium salt left an insoluble residue asserted to be  $\text{TiO}_2$ . Clabaugh, Swiggard and Gilchrist (1956) concluded that some of the barium was replaced in the compound by the alkali ion, which formed acid soluble alkali oxides during calcination. The ammonium compound was stated to form  $\text{TiO}_2$  during calcination which would explain the acid insoluble residue. The use of barium : zirconium : oxalate ratios of  $>1 : 1 : 2$  to achieve stoichiometry has been explored by Gangadevi, Subba Rao and Kutty (1980). Presumably the  $\text{Zr}:\text{C}_2\text{O}_4$  ratio was fixed at 2 to prevent the formation of highly soluble poly-oxalate complexes, and/or barium oxalates.

In the oxalate process reported by Robertz *et al.* (2001), basic zirconium carbonate was dissolved in dilute nitric acid and added to a solution of ammonium oxalate which was 10% in excess with respect to barium and zirconium. A solution of  $\text{BaNO}_3$  was added under constant stirring to cause precipitation. The precipitate was separated by centrifugation, and the solution was found to be free of barium ions. The thermal decomposition of the product was studied by DTA/TGA, XRD and IR. No  $\text{ZrO}_2$  was observed by XRD in decomposition products, though  $\text{BaCO}_3$  was found to be an intermediate calcination product by IR. The count statistics shown in the XRD data suggest the detection limits for  $\text{ZrO}_2$  may be relatively poor, and no measurement of the stoichiometry of the product was reported. The next paper by these researchers is awaited, hopefully showing useful progress towards a high quality product.

The stability of alkali zirconium oxalates and instability of zirconium/oxalic acid complexes contrasts with the method of Clabaugh, Swiggard, and Gilchrist (1956) for producing  $\text{BaTiO}_3$  by adding a mixed solution of  $\text{BaCl}_2$  and  $\text{TiOCl}_2$  to oxalic acid at  $80^\circ\text{C}$  which resulted in highly repeatable Ba : Ti ratios of 0.998 to 1.008. The order of additions and temperatures are different to that of Gangadevi, Subba Rao and Kutty (1980) and Hennings and Schreinemacher (1991). The temperature used by Clabaugh, Swiggard, and Gilchrist was sufficiently high that the stability of the zirconium oxalic acid complex would be low, resulting in precipitation of Zr-rich phase(s) in the absence of Ba, at least if given sufficient time for reaction. In the presence of Ba, the situation may be somewhat different, for as Clabaugh Swiggard and Gilchrist (1956) reported, the stability of titanium oxalate

complexes are increased by the presence of ions such as K, Na,  $\text{NH}_4$  and Ba. This raises the possibility that precursor phase purity might be improved by adding the Zr-containing solution to a mixed solution of oxalate and barium. The inclusion of Ba in this list is somewhat curious, since the object of oxalate processing is to precipitate the barium rather than leave it remaining in stable solution complexes.

### 2.5.9 Complexity

Not all zirconium reagents can be ascribed a definite composition. For example, zirconium oxychloride does not necessarily have a constant Zr : Cl ratio, and readily loses water and HCl even at low temperature (Solovkin and Tsevtkova 1962). The state of zirconium ions in solution may be very complicated and is dependent on the relative predominance of hydrolysis, complex formation, polymerisation and colloid formation (Elinson and Petrov 1969, p. 15,19; Marov and Ryabchikov 1962). The composition and method of preparation of the solution may be important because in certain cases, zirconium in solution can take an abnormally long time to come to its equilibrium state, sometimes weeks, and in certain cases even months or years (Elinson and Petrov 1969, p. 19-20; Solovkin and Tsevtkova 1962). The kinetics of establishing equilibrium can explain why certain results may be difficult to reproduce, and why the detailed method of reaction, such as the history of the solution and the order of addition of reagents can affect the outcomes of reactions. In this light it is considered appropriate and necessary to criticise much of the existing literature on solution processing of zirconium based ceramic precursors for failing to meet the high standards required for proper experimental reporting of zirconium solution chemistry.

A characteristic of zirconium is the formation of salts with indefinite composition, partly because the mechanism of formation is the interaction of precipitating species with a range of zirconium species that may be simultaneously present in a given solution. This is true of both sparingly soluble compounds as well as readily soluble chlorides and nitrates. Often it is only possible to prepare compounds with a well defined composition by strictly controlling experimental conditions such as acidity, temperature, time, order of addition etc. It is clear that the chemistry of zirconium is a complex interaction of the effects of hydrolysis,



polymerisation, colloid formation and stability, solution complexation and kinetics, and considerable uncertainty and ambiguity is present in the literature.

## 2.6 Previous oxalate processing studies

One process which attempts to form a strictly stoichiometric phase is the oxalate process for the production of perovskites including barium titanate and barium zirconate. One of the early studies producing barium zirconium oxalates was by Grinberg and Astapovich (1961) who produced  $\text{Ba}_2[\text{Zr}(\text{C}_2\text{O}_4)_4] \cdot 7\text{H}_2\text{O}$  by reaction of a solution of potassium zirconium oxalate with barium chloride solution, then washing and drying the precipitate. For the production of the  $\text{BaTiO}_3$  or  $\text{BaZrO}_3$ ,  $\text{BaTiO}(\text{C}_2\text{O}_4)_2 \cdot 4\text{H}_2\text{O}$  or  $\text{BaZrO}(\text{C}_2\text{O}_4)_2 \cdot 4.5\text{H}_2\text{O}$  may be formed, respectively, which is then calcined in air to the pure perovskite. In the case of  $\text{BaTiO}_3$ ,  $\text{BaTiO}(\text{C}_2\text{O}_4)_2 \cdot 4.5\text{H}_2\text{O}$  can be synthesised by reacting  $\text{TiCl}_4$ ,  $\text{BaCl}_2 \cdot 2\text{H}_2\text{O}$  and oxalic acid solutions under controlled conditions which are described in considerable detail by Clabaugh, Swiggard and Gilchrist (1956). The same compound can be made by digesting  $\text{BaTiO}_3$  formed by solid-state processes with a small excess of oxalic acid at 90 °C for 24 hours.

In the case of  $\text{BaZrO}_3$ , a method of producing  $\text{BaZrO}(\text{C}_2\text{O}_4)_2 \cdot 4.5\text{H}_2\text{O}$  by reacting  $\text{ZrOCl}_2 \cdot 8\text{H}_2\text{O}$ ,  $\text{BaCl}_2$  and oxalic acid solutions under controlled conditions was reported by Reddy and Mehrotra (1979). It is worth quoting and examining the entire description of their process as reported in their original paper:

“All the reagents used in the present study were of BDH AnalaR quality. The zirconium oxychloride octahydrate was of Fluka AG (Buchs SC, Switzerland) and was recrystallised twice before use. The IR spectrum of the recrystallised compound compared well with that of zirconium oxychloride octahydrate reported in the literature. The BZO [barium zirconyl oxalate hydrate] was prepared as follows: equimolar (0.5 M each) aqueous solutions of barium chloride and zirconium oxychloride were added to the hot solution of oxalic acid (1.0M) which was 10% in excess. The precipitate was digested on a waterbath for 30 minutes, cooled and filtered, then washed with distilled water and acetone and air dried. Wet chemical analysis showed the ratio of barium to zirconium was 1:1.”

Several ambiguities in their paper relevant to the current application should be pointed out. Although reagents concentration are provided, no information on the mole ratio of reagents is provided, either explicitly or able to be calculated from relative volumes of reagents used. The temperature of the reaction is not given clearly: how hot is “hot”? The sequence and timing of mixing of reagents is also not clear. The statement on the mole ratio of the product comes with neither an experimental uncertainty nor a description of the method used to measure it, and is a standard of reporting inadequate for an application where very accurate control over mole ratio may be required. There is also little evidence of phase purity of the calcined product other than the lack of carbonate impurity for more highly calcined samples, and no attempt to report evidence or otherwise of zirconia or other non-carbonate secondary phases in the calcined product.

The paper by Reddy and Mehrotra (1979) forms a possible basis from which to develop a method for high quality BaZrO<sub>3</sub> production but not a finished process ready to implement for the current demanding application. The journal literature displays a preoccupation of many authors in claiming high quality reaction products, incomplete disclosure of experimental details, and few systematic studies of the conditions under which the desired compounds are formed. The consequences of such substandard experimental reporting for the present study have been that attempts to reproduce numerous previous experiments failed to produce the claimed experimental outcomes, and considerable effort was expended on experiments and review of the chemical literature to understand why the reactions did not proceed as claimed.

The production of BaZrO<sub>3</sub> using oxalic acid and barium chloride solutions is reported by Potdar *et al.* (1993) to have numerous experimental difficulties including the control of complexes in solution, the stability and sensitivity of complexed species as a function of pH, and the control of microstoichiometry, but details of these difficulties are not reported. Much of the problems need to be inferred from the chemical literature, rather than from papers which deal directly with processing methods. A modification of the oxalic acid method is reported by Potdar *et al.* (1993) which claims to overcome these difficulties using sodium oxalate instead of oxalic acid.

A related method used by Gangadevi, Subba Rao and Kutty (1980) to prepare  $\sim\text{BaZrO}(\text{C}_2\text{O}_4)_2 \cdot 7\text{H}_2\text{O}$  converted a solution of  $\text{H}_2\text{ZrO}(\text{C}_2\text{O}_4)_2 \cdot 3\text{H}_2\text{O}$  to  $(\text{NH}_4)_2\text{ZrO}(\text{C}_2\text{O}_4)_2 \cdot 3\text{H}_2\text{O}$  in solution using dry ammonia, which was added to a solution of barium acetate. The reaction temperature was not reported, so is inferred as ambient temperature. Gangadevi, Subba Rao and Kutty (1980) showed some of the difficulties of preparing a stoichiometric compound: the stoichiometry of the precipitate was found to be dependent on the pH of the solution, the ratio of Ba:Zr in solution, and the soluble barium salt used for precipitation. A large excess (100%) of barium was required to produce the stoichiometric compound. In the method described by Potdar *et al.* (1993), the Ba:Zr solution ratio might be inferred (though was not stated) to be unity, whereas in the Gangadevi, Subba Rao and Kutty (1980) study, the ratio was explicitly stated as two. Reddy and Mehrotra (1979) described their experimental procedure so poorly that actual mole ratios of the reagents cannot be determined. Gangadevi, Subba Rao and Kutty (1980) provided a valuable insight into the conditions under which stoichiometric oxalate precursors are achieved. It is one of very few reports which deal with conditions under which stoichiometric precipitates are not achieved or provide information on the effect of pH in the zirconium oxalate system at high zirconium concentration. The Ba : Zr ratio was observed to be dependent on the pH values of the starting solutions, though the mechanism of the chemistry was not considered.

There is considerable uncertainty, ambiguity or differences in the literature regarding the structure and composition of barium zirconyl oxalate hydrates, which appear to be a somewhat poorly defined or complicated series of materials rather than a single compound with a definite composition and structure. The structure and composition of these precipitates, as for other zirconium complexed solids, may be dependent on the speciation of the zirconium in solution prior to the precipitation stage, the conditions of the precipitation reaction, such as temperature, concentrations, speciation etc., and the method of drying.

The XRD pattern of the precursor reported by Gangadevi, Subba Rao and Kutty (1980)  $\text{BaZrO}(\text{C}_2\text{O}_4)_2 \cdot 7\text{H}_2\text{O}$  shows significant differences to that reported for  $\text{BaZrO}(\text{C}_2\text{O}_4)_2 \cdot 4.5\text{H}_2\text{O}$ , particularly at high d-spacings. Vinogradov and Sphinel (1961) propose conflicting conclusions to Zaitsev and Bochkarev (1962a) on the

composition of zirconium oxalates. Uncertainty in the structure and composition of the zirconyl oxalate hydrates adds to the complexity of designing a reliable process for producing them. The analysis of precursor structure is therefore complicated, such as when determining whether a given product is a single phase or a polyphase mixture, because the reference patterns available are low in number and poor in quality. Approximate XRD patterns (d-spacings, approximate intensities etc.) are available in the literature for certain barium zirconyl oxalate hydrates, but no detailed structural analysis, even pattern indexing, has been reported. There are no barium zirconium oxalate hydrates in the Inorganic Crystal Structure Database and only one XRD result. Reddy and Mehrotra's  $\text{BaZrO}(\text{C}_2\text{O}_4)_2 \cdot 4.5\text{H}_2\text{O}$  has been accepted into the Powder Diffraction File published by the International Centre for Diffraction Data (ICDD-PDF), with a poor quality ranking due to poor intensity data and a lack of peak indexing.

Given that zirconium oxalate complex ions are reported to contain no zirconyl groups in solution (Zaitsev and Bochkarev 1962a), it is optimistic to expect solid barium zirconium oxalate hydrates to contain them as may appear at first glance from the molecular formula. The infrared spectra reported by Reddy and Mehrotra (1979), and Gangadevi, Subba Rao and Kutty (1980) do not display  $\text{Zr}=\text{O}$  absorption bands in the range  $830 - 900 \text{ cm}^{-1}$ . The structure may contain polymers such as the tetramers of  $\text{ZrOCl}_2 \cdot 8\text{H}_2\text{O}$ , and by analogy to the oxychloride, it is probable that the  $\cdot \text{H}_2\text{O}$  as written may be present as hydroxide groups.

Low temperature dehydration, between  $25$  and  $120^\circ\text{C}$ , is reported for  $\text{BaZrO}(\text{C}_2\text{O}_4)_2 \cdot 7\text{H}_2\text{O}$ , and hence the method of drying needs to be considered prior to structural and chemical analysis. In most published studies, the precipitates were washed in water to remove unwanted soluble compounds, washed in acetone, then dried in air or over a desiccant such as concentrated  $\text{H}_2\text{SO}_4$ .

## 2.7 Analysis

Methods used for chemical analysis of the reaction products must be called into question and carefully verified experimentally. The gravimetric determination of barium as sulphate is notorious for interference by other elements (Kolthoff *et al.* 1969, p. 603). In the present study, gravimetric analysis for Ba using sulphate precipitation from a mixed solution of  $\text{BaCl}_2$  and  $\text{ZrCl}_4$  resulted in serious contamination of the  $\text{BaSO}_4$  precipitate with zirconium and an overestimation of the Ba content in excess of 30%, and hence gravimetric methods for mixed solutions was abandoned in favour of quantitative x-ray fluorescence (XRF) determinations.

In the study by Gangadevi, Subba Rao and Kutty (1980) the reaction products were decomposed by heating and then dissolved with hydrochloric acid. Ba was analysed gravimetrically by precipitation as the sulphate, and Zr was precipitated using cupferron (ammonium salt of nitrosophenylhydroxylamine) (Kolthoff *et al.* 1969, p. 270), and weighed as  $\text{ZrO}_2$  after ignition. Unless precautions are taken to prevent zirconium co-precipitation by solution complexation (i.e. masking agents), or by prior removal of solution zirconium by precipitation, errors in gravimetric barium determinations may result. Complexation has been conducted using an excess of EDTA for  $\text{BaTiO}_3$  analysis (Clabaugh, Swiggard, and Gilchrist 1956). The problem could also be avoided by removing the Zr prior to  $\text{BaSO}_4$  precipitation, using reagents such as cupferron or mandelic acid. In other papers such as Clabaugh, Swiggard, and Gilchrist (1956) on barium titanyl oxalate hydrate, the use of EDTA to prevent Ti interference in the  $\text{BaSO}_4$  determination was stated explicitly and the basis for the analytical method explained. In such cases, the results are credible. It was not clear whether Gangadevi, Subba Rao and Kutty (1980) conducted cupferron precipitation of zirconium prior to barium sulphate precipitation and hence whether their results were correct. However, their TGA results and permanganate titrations strongly support the compositions of the compounds reported. Supporting evidence for correct analytical results could have been provided by an XRD result of the calcined material. A single phase stoichiometric powder would be expected to readily produce phase pure  $\text{BaZrO}_3$ , and although the end product is stated to be crystalline barium metazirconate ( $\text{BaZrO}_3$ ), results are not presented to support or quantify this claim. The XRD analysis of an intermediate decomposition product was claimed to

be crystalline  $\text{Ba}_2\text{Zr}_2\text{O}_5\text{CO}_3$ , and this result was used to assert that  $\text{BaZrO}_3$  is formed directly and not formed by solid-state reaction between  $\text{BaCO}_3$  and  $\text{ZrO}_2$ . The basis on which the authors can claim that the XRD patterns was  $\text{Ba}_2\text{Zr}_2\text{O}_5\text{CO}_3$  is uncertain: such a compound does not appear as a reference in the ICDD-PDF or ICSD files. In the author's view, to what degree the precipitated compound was stoichiometric remains uncertain.

In most zirconium determinations in the processing literature, there has been no measurement of, or correction for, any hafnium content of the zirconium salt used in the experiments. Because of the similar chemistry of Zr and Hf, and the natural occurrence of  $\sim 1 - 2$  wt.% Hf in Zr mineral deposits, Zr salts normally contain Hf unless they have been specifically processed to remove the Hf. Because of the almost identical chemistry of Zr and Hf, determination of Hf in Zr compounds is difficult other than by spectroscopic methods. For  $\text{BaZrO}_3$  the important stoichiometry is not Ba:Zr but Ba:[Zr+Hf]. Although Ba should not interfere with Zr precipitation in an acid medium when using precipitates such as cupferron and mandelic acid, the molar weight used for accurately calculating the Ba:Zr mole ratio using gravimetric methods normally requires a small correction, simply because these compounds precipitate both Hf and Zr and the atomic weights of hafnium and zirconium are significantly different. Precisions quoted in many zirconate studies are unjustified given the inaccuracy from errors caused by unquantified Hf levels. Many suppliers neglect to identify Hf in their reagents or to supply quantitative analysis of Hf contents, and this effect is overlooked or unstated in most papers. Salts such as  $\text{ZrCl}_4$  are commercially available which have had all but traces ( $\sim 50$  ppm) of Hf removed. Because Hf has a much higher thermal neutron absorption cross section than Zr, specially purified Zr compounds are produced to supply the demands of the nuclear industry. These reagents can save the effort of performing the rather difficult separation of Hf from Zr in the laboratory and can be used to prepare accurate standards for zirconium determinations. Wet chemical determinations, such as gravimetric methods, of Hf : Zr ratios are generally poor and laborious, though excellent determinations can be made spectroscopically using XRF and other techniques (Elinson and Petrov 1969 pp. 161, 166, 189; Mukherji 1970, p. 226).

## 2.8 Ceramic production

Much of the above discussion relates to the production of powders. However, the main goal of this study was to make high quality ceramics and specific aspects of ceramic processing require review. The goal of powder processing is to produce powders with suitable characteristics for fabrication into high quality ceramic articles. The ideal  $\text{BaZrO}_3$  powder can be summarised as phase pure, chemically pure, of a small particle size to maximize sinterability but suitable for the specific forming technique used to shape the article, and of a low degree of agglomeration.

Calcination conditions during powder processing are a key factor affecting the phase purity, particle size and agglomeration state of  $\text{BaZrO}_3$  powders. Agglomeration in powders normally leads to poor green microstructure and therefore poor sintered microstructure. The irregular shape of agglomerates causes poor particle packing, and chemical segregation may interfere with densification and the final microstructure. Agglomeration may directly occur during precipitation of precursors as a result of nucleation and growth processes. All small particles are mutually attracted to each other as a result of van der Waals forces, but may also be attracted by electrostatic attraction, liquid bridging, capillary forces or polymer bridging (Roosen and Hausner 1988). Mutual attraction of small particles in liquid dispersions increases with reduced particle size and increased volume fraction of solid, and is pronounced in submicron- and nano- powders. Soft agglomerates may form due to poor dispersion stability, particularly during processing stages where the volume fraction of solids is increased such as in filtration and in particular, drying. Agglomeration of ultrafine precursors can be a significant problem because soft agglomerates may readily fuse into hard agglomerates during calcination. If these hard agglomerates are not broken by milling or compaction during forming, they may rapidly densify into pore free regions early during sintering, reducing the contact with the surrounding partially sintered material and forming pores which cannot be removed during the remainder of the sintering operation. Local density gradients caused by agglomeration may also cause crack formation (Brzezinska-Miecznik, Haberko and Bucko 2002).

There are a number of approaches with the potential to reduce powder agglomeration and thereby maximize the quality of the final ceramic. Direct agglomeration during precipitation may be minimised by optimisation of nucleation and growth kinetics. The washing conditions used to treat precipitated precursors may influence agglomeration because the forces between particles can be strongly affected by the type and amounts of surface absorbed anions. Washing with organic liquids rather than water may substantially reduce agglomeration during drying because the reduced surface tension and dispersion properties of many organic solvents reduce the capillary forces between particles. In freeze drying, capillary forces are eliminated because the liquid phase is frozen and then removed by sublimation, so dried powders are generally unagglomerated. The temperature and humidity at which powders are dried can also influence agglomeration (Roosen and Hausner 1988).

As will be shown in the results of this study, phase purity and particle size increase with increasing calcination temperature and calcination time. Solid state diffusion during calcination also causes the formation of “hard agglomerates” by formation of solid bridges between particles, particularly those already agglomerated from previous processing operations, especially drying (Roosen and Hausner 1988). Given that this type of agglomeration occurs by solid state diffusion, it would clearly be increased by excessive calcination temperatures or times. Hard agglomerates are those with sufficient mechanical strength to interfere with particle packing during green forming, thus relatively weak agglomerates that are mechanically crushed by uniaxial or isostatic press forming may still be a problem for casting operation such as slip casting. To a limited extent, the effects of hard agglomeration after calcination can be reduced by milling and/or sedimentation to physically remove large particles.

Apart from affecting densification by its impact on green microstructure, residual secondary phases after incomplete calcination may also affect densification. Most authors consider that residual carbonates hinder the sinterability of perovskites. The energy changes due to chemical reactions between non-equilibrium phases are often larger than surface energy changes during densification. Chemical reactions thus cause the formation of larger particle and pores of lower coordination number, which hinder densification during sintering. Attempts to remove secondary phases



prior to green forming have therefore been attempted, such as chemical dissolution of carbonates, for example in dilute acids, or extra thermal treatment to remove carbonates by solid state reaction (Sin, El Montaser and Odier, 2002; Hérard, Faivre and Lemaître 1995a+b). However, thermal pretreatments cannot be conducted without affecting the particle size and agglomeration state of powders. The optimum calcination cycle (time and temperature) which produces the highest density ceramic with the desired microstructure is a balance between increased phase purity with increased agglomeration and the corresponding degradation of green microstructure (Brzezinska-Miecznik, Haberkowicz and Bucko 2002). The highest density ceramic may potentially be produced using calcination conditions insufficient to produce a phase pure powder, depending on the relative effects of phase purity on sintering kinetics and the effects of powder calcination on green microstructure. The optimum calcination temperature for a given system and processing method can readily be found experimentally.

Particle size control is necessary to ensure powders are suited to the particular forming method used to shape green ceramic articles, and to ensure an adequate green microstructure is established. Relative to casting operations, pressing is ideally suited to ultrafine powders. For a powder of adequate particle size and shape distribution and low agglomeration state, establishing a good green microstructure simply requires the application of sufficient localised compressive stress to overcome inter-particle friction to ensure efficient particle packing. The use of liquids and solids of low shear strength as lubricants can substantially reduce both inter-particle and die wall friction to assist green forming, and assist in establishing uniform green density. Although friction losses increase as the particle size is reduced, pressing operations can readily be developed for ultrafine powders with appropriate powder pretreatment.

## **2.9 Slurry casting and dispersion**

Casting operations can be much more complicated than press forming for ultrafine powders. Poor dispersions produce green bodies with poor green density and microstructure due to poor particle packing, which leads to poor sintered microstructure, in particular, greater difficulty producing high sintered density. Optimal slip casting requires slurries which are as highly dispersed as possible, and

with high solids loading. The complexity of casting ultrafine powders lies in the difficulty in establishing high stability liquid dispersions of ultrafine particles at high solids loadings. A good review of colloidal processing of ceramics was provided by Lewis (2000).

All small particles, such as those dispersed in a fluid, mutually attract each other through van der Waals forces, the magnitude of which rapidly increases as the spatial separation of their surfaces decreases. The interparticle potential energy  $V$ , due to van der Waals attraction can be approximated by the Hamaker expression. For spherical particles of equal size  $r$ , van der Waals attraction exhibits a power law dependence whose strength depends on

- the properties of the interacting colloidal particles and the intervening fluid, both of which influence the Hamaker constant  $A$ ,
- the minimum separation of the particle surfaces  $d$

$$V \approx -\left(\frac{A}{6}\right)\left(\frac{2}{s^2-4} + \frac{2}{s^2} + \ln \frac{s^2-4}{s^2}\right) \quad (2.1)$$

$$\text{where } s = \frac{2r+d}{r} \quad (\text{Lewis 2000})$$

Equation 2.1 is only accurate at very small separation distances and becomes highly inaccurate at separations greater than about 10% of the particle radii, but this limitation is not a serious problem because van der Waals attraction is only significant at close approach of particles. Other corrections can be applied to improve the calculation at greater separation.

The Hamaker constant for a given solid/fluid pair can be estimated from their dielectric constants and the characteristic frequencies of the media which can be obtained from optical refraction data. Values of Hamaker constants for common ceramic materials in vacuum and water at 25 °C was provided by Lewis (2000), which shows the van der Waals attraction is substantially weaker in water compared to vacuum. It is possible to negate van der Waals attraction by using a fluid index matched to the solid, in which case the dispersion is described as having hard sphere behaviour. However, given the high index of refraction of typical ceramics this is of limited practical importance though it may be far more useful in biological and polymer systems.

Unless the ubiquitous attractive van der Waals forces are balanced by repulsive forces such as electrostatic, steric, electrosteric, and depletion forces, small particles in a liquid dispersion inherently stick together. Since the average separation of very small particles at high solids loading may be extremely small, van der Waals attraction may be strong enough to overcome repulsive forces, causing agglomeration and possibly flocculation. Brownian motion causes constant deviation from the average separation, while reduced particle size and increased solids loading move the entire separation distribution to smaller values. For a fixed volume fraction of solid material, the average distance between spherical particles is approximately proportional to their average diameter (Richerson 1992, p. 447), and hence the difficulty of maintaining highly stable concentrated dispersions increases as the particle size diminishes.

Electrostatic repulsion can be used to partially or fully overcome van der Waals attraction to produce stable dispersions. Most particle surface in aqueous dispersions carry a surface charge due to ionisation of surface groups or the specific surface adsorption of ions including  $\text{H}_3\text{O}^+$ ,  $\text{OH}^-$  from water or other ionic species in solution. The “distributions of ions around a charged particle is determined by the electric interaction with the charged surface and the randomising tendency of thermal motion.” Gregory (1993, p. 63). Oppositely charged ions (counterions) are electrically attracted to the surface, and the distribution of the electrical double layer formed influences the interaction between charged particles. At low ionic strength, the double layer is diffuse and extends a considerable distance from the particle surface, whereas at high ionic strength, the diffuse layer is compressed. Particles of like charge repel each other when their diffuse layers begin to overlap, so repulsion occurs at higher particle separation for lower ionic strengths.

Electrostatic particle interaction is affected by electrical potential at the Stern layer, which is the inner boundary of the diffuse layer just outside a layer of closely associated counterions. The potential at the Stern layer cannot be measured directly but is commonly estimated as being the same as the zeta potential, which can be measured experimentally using a number of techniques but most commonly by electrophoresis (Gregory 1993, p 64).

For identical particles (same material and radii), the electrostatic interaction reduces to (Gregory 1993, p. 64):

$$V_E = 32 \pi \epsilon_r (kT / ze)^2 \lambda^2 \exp(-\kappa d) \quad (2.2)$$

where  $\epsilon$  is the permittivity of the fluid,  $r$  is the radius of the particles,  $k$  is Boltzmann's constant,  $T$  is the temperature in Kelvin,  $z$  is the valency of the counterions,  $e$  is the elementary charge of the electron,  $\lambda$  is a dimensionless function of the zeta potential:  $\lambda = \tanh(z e \xi / 4 k T)$ ,  $\kappa$  is the Debye-Hückel parameter which is a function of ionic strength (Lewis 2000)

$$\kappa = \left( \frac{F^2 \sum N_i z_i^2}{\epsilon_r \epsilon_0 k T} \right)^{1/2} \quad (2.3)$$

where  $F$  is the Faraday constant,  $N_i$  and  $z_i$  are the number density and valency of counterions, respectively.  $\epsilon_r$  and  $\epsilon_0$  are the relative dielectric constant and permittivity of free space, respectively.

The Debye-Hückel parameter for aqueous dispersions at 25 °C from is given by

$$\kappa = 2.3 \times 10^9 \left( \sum c_i z_i^2 \right)^{1/2} \quad (2.4)$$

where  $c_i$  is the molar concentration and  $z_i$  is the valency of ions of type  $i$ , the sum of which is taken over all the ions in solution (Gregory 1993).

Increasing ionic strength has two effects on electrostatic repulsion of particle dispersions. Increased ionic strength decreases  $1/\kappa$ , often called the decay length or screening length, and hence particles approach each other more closely before electrostatic repulsion becomes significant. Also, increased ionic strength causes a decreased zeta potential, which for a given separation reduces interparticle repulsion. These effects, as shown in Equations 2.3 and 2.4 are more pronounced for counterions of high valency. Apart from increasing ionic strength, the electrostatic contribution of aqueous dispersion can also be de-stabilised by adjusting the pH towards the isoelectric point (IEP). The IEP is the pH at which surface charge is reduced to a minimum (zero) due to balanced adsorption of  $H_3O^+$  and  $OH^-$ . Aqueous dispersions are normally created at a pH significantly below the IEP to create positive surface charge (positive zeta potential) by greater  $H_3O^+$  adsorption than  $OH^-$  adsorption, or at a pH higher than the IEP to create negative surface charge (negative zeta potential) by increased  $OH^-$  adsorption relative to  $H_3O^+$  adsorption.

In practice it is often difficult to produce stable ceramic dispersions suitable for casting operations using only electrostatic repulsion to overcome van der Waals attraction. If the energy barrier formed by electrostatic repulsion is not of sufficient magnitude, it may be overcome by Brownian motion or external forces which push the particles over the potential barrier and result in flocculation. The kinetics of flocculation are dependent on the magnitude of the energy barrier produced by electrostatic repulsion, though electrostatic dispersion can greatly decrease the rate of flocculation. Particle chemistry may restrict the working range of pH, and large double-layer thickness can cause excessive drying shrinkage.

Steric forces are typically used, often in conjunction with electrostatic forces, to produce optimal dispersion. For steric dispersion, adsorbed organic molecules, often polymers, aid dispersion by adsorbing onto particle surfaces with sufficient thickness and density to provide a steric barrier to flocculation, making sure not to produce bridging flocculation. Bridging flocculation is the adsorption of the same polymer molecules on two or more particles. The strength of steric dispersant adsorption needs to be strong enough to avoid desorption during particle collision, and produce a suitable layer structure at the particle surface under the conditions used for casting. The layer structure (conformation) of the adsorbate is dependent on its molecular structure, solvent properties, density of active adsorbing groups, the density of active surface sites on the particle, and the adsorbate and particle concentrations.

Electrosteric dispersion employs an ionisable steric dispersant, which provides dispersion by a combination of electrostatic and steric forces. Electrosteric dispersants contain at least one ionisable functional group, with molecular structures ranging from homopolymers to the various types of copolymers. Adsorption of electrosteric dispersants is strongest when the ionic charge of the dispersant is of opposite sign to the surface charge of the particles, though in such cases the adsorption of an incorrect amount of adsorbate can neutralise surface charge and promote flocculation. For a given dispersant and solvent such as water, adsorption and dispersion characteristics can be adjusted by variation of the solids content of the slurry, the concentration of the dispersant, pH, ionic strength and temperature.

## 2.10 Summary

Considerable basic information was available in the published literature on  $\text{BaZrO}_3$  for use in melt processing of molten barium cuprates. Corrosion resistant crucibles could not be fabricated directly from published information because of a lack of sufficient detail on powder processing and the characteristics of ceramics required for adequate corrosion resistance. Such details were significant because of the high quality required to achieve corrosion resistance. Specific aspects of solid-state and solution processing that required investigation are discussed in Chapter 3.

No studies have been reported demonstrating successful development of chemically derived  $\text{BaZrO}_3$  suitable for molten barium cuprate containment. Although novel processes typically claim to produce high quality powders with improved properties compared to solid-state processing, the suitability of solution chemical processes for corrosion resistant  $\text{BaZrO}_3$  required verification and/or further process development. Results of oxalate processing based on previous literature showed that considerable redevelopment was required to produce crucibles of adequate quality. Because of the complexity of zirconium solution chemistry, information gathered from a large body of chemical literature was required to enable this research.

No literature could be found on the aqueous slip casting of  $\text{BaZrO}_3$ . Progress was made using literature on slip casting of  $\text{BaTiO}_3$  (Blanco López, Rand and Riley 2000a+b), and general literature on colloid dispersions and ceramic slurry processing used to support current efforts to slip cast  $\text{BaZrO}_3$  was reviewed.

## CHAPTER 3

# BACKGROUND AND DESIGN OF EXPERIMENTAL PROGRAM

---

### 3.1 Experimental aims

Much of the remainder of this thesis outlines work conducted in order to establish the three basic considerations for fabricating  $\text{BaZrO}_3$  resistant to molten barium cuprate corrosion:

- establish precise details of process(es) to produce corrosion resistant  $\text{BaZrO}_3$ ;
- investigate characteristics of the ceramic required for corrosion resistance;
- develop and/or implement analytical methods required for process development and ceramic characterisation.

### 3.2 Processing implications

When researching new ceramics, one needs to understand two important contributions to the properties of a material: the intrinsic properties of the material, and the effects of defects due to processing limitations. In the case of  $\text{BaZrO}_3$ , residual processing defects may have a significant impact on its corrosion resistance. Processing artefacts can be assessed using available analytical methods, but conclusions that can be drawn are restricted by the performance of analytical methods. For  $\text{BaZrO}_3$ , the quality of ceramic required for corrosion resistance places severe demands on analytical methods. At the opposite end of the spectrum one may erroneously conclude that  $\text{BaZrO}_3$  has poor corrosion resistance to molten barium cuprates without knowing that the samples studied were of inadequate quality. This would clearly be erroneous because other researchers have already shown corrosion resistance is high for samples made under carefully controlled conditions as already discussed.

Fabrication processes vary in control over stoichiometry and establishment of phase equilibrium, and may have an impact on grain size, chemical purity and density of the ceramic. Some or all of these characteristics may affect corrosion resistance. This may apply both to variations arising from different types of processes, or to

variation within stages of processing for any given type of process. The traditional solid-state process is reputed to have certain limitations, some or all of which could potentially be overcome by using solution chemical processes. However, simply because a process uses solution chemistry for producing the powder provides no certainty in its quality, and may impose new difficulties in meeting the objective (Taglieri *et al.* 1999). Other researchers have professed the potential advantages of chemical processes, but it is a much a more demanding task to achieve those gains, and then to make objective and quantitative comparisons. This study has shown that converting the potential advantages of chemical processing into realised improvements can be an arduous task, primarily because the chemical processes that were feasible to undertake with the resources available to this study were inadequately specified in the literature, and/or did not function as reported.

Chemical processing literature pointed to limitations in the attainable phase purity of the solid-state process, so the literature was reviewed to select the most appropriate chemical process for fabrication of high quality crucibles considering the resources available to the project. Processes were assessed in terms of reagents costs, cost and complexity of required processing equipment, the need to maintain specialised reaction conditions such as a controlled gas environment, elevated pressure or constant temperature, and yield efficiency. Many potential processes were not feasible within the resources of the project. For example, organic sol-gel processes were immediately rejected on the basis of high reagent costs and the need for reactions to be performed in a glove box. Furthermore, the developmental stage of processes were of major importance: the project originally aimed to use an already mature process ready to implement and did not intend major redevelopment of existing processing or the development of an entirely new process. As will be clear from Chapters 4 and 5, considerable processing development and modification was required to devise a useful solution chemical process using the resources available.

In developing a new chemical process, even in a single chemical system, there are many available experimental variables, such as the selection of reagents used, solution concentrations, reaction temperatures, order of mixing of reagents, mixing rates, pH of reaction, as well as washing, filtering, drying, calcination, packing and



sintering protocols. With this large number of variables there are an enormous number of combinations, most of which will not produce the desired outcome. In dealing with such complexity, it was necessary to develop a strategy with which to begin and to proceed.

### **3.3 Characterisation of powders and ceramics**

The complexity and difficulty of investigating the characteristics of the ceramic required for corrosion resistance arise from:

- the sensitivity of the finished ceramic to defects which degrade its corrosion performance;
- the suitability of analytical methods for characterising the specific ceramic of interest, e.g. practical difficulties in the application of analytical techniques to the BaZrO<sub>3</sub> system;
- the precision, accuracy and detection limits of analytical methods.

As will be seen in the results of this research, BaZrO<sub>3</sub> can be fabricated to have good resistance to molten barium cuprates but is very sensitive to defects which restrict its performance. When using direct analytical methods to discern the requirements for corrosion resistance, the high sensitivity of the ceramic to defects places severe demands on the analytical methods used to characterise the ceramic. In certain cases, direct measurements were needed very close to or even beyond detection, precision and accuracy limits achievable. There are numerous substantial difficulties inherent to the analysis of BaZrO<sub>3</sub>, such as difficulty in dissolution for solution trace element analysis, poor detection limits imposed by fusion/dissolution preparation, peak overlap in XRD analysis, poor sensitivity to light trace elements using XRF analysis, and specimen preparation difficulties for TEM. These considerations impose limitations on what information can be gathered by direct methods, and in certain cases, indirect observations were needed to support the understanding and improvement of the corrosion resistance of the material.

### **3.4 Experimental overview**

As outlined in Section 3.1, the experimental design of this project can be considered as having two major, though dependent aspects: to determine the requirements of corrosion resistant  $\text{BaZrO}_3$ , and to develop processes for fabricating such a ceramic. In this project, two major process types were pursued, solid-state and oxalate processing. Research was required on the solid-state system to overcome the gaps in published research and to guide the optimisation of oxalate process development. Oxalate processing was conducted in order to attempt to overcome the processing limitations of the traditional process and provide ceramics of superior performance.

#### **3.4.1 Solid -state processing considerations**

The purpose of conducting research using solid-state processing, was primarily to understand and quantify the requirements of the ceramic for corrosion resistance. Solid-state processing offers three important advantages over most other processes when exploring the requirements of the ceramic:

1. The process has already been established as feasible if performed to adequate standards. At the outset it was uncertain as to whether other processes are capable of producing suitable crucibles, hence a reliable process was needed as a starting point or model system from which other processes could be investigated.
2. The solid-state process was the most straightforward system in which to develop a complete processing system for all stages of processing.  $\text{BaZrO}_3$  is a difficult ceramic to fabricate to high density and phase purity at high chemical purity, and experience was required to learn how it can be achieved. Solid-state processing is amongst the easiest of processes to carry out in the laboratory, and facilitated the scope of experimentation needed for completion of the research.
3. The stoichiometry of the product can be readily and reliably controlled to high precision, and to a lesser degree, high accuracy, by adjusting the mass of reagents used. Solid-state processing was therefore the most convenient and

reliable process for studying the effects of stoichiometry. Weighing and transferring errors in the process are low, whereas solution processes have a number of stages where control over stoichiometry may be compromised, for example in initial precipitation reactions or variable losses during washing stages.

The aim of processing development in the solid-state system was to quantify the inherent requirements for a corrosion resistant material, using samples as free of residual processing artefacts as could be achieved. Minimising processing artefacts required refinement of the solid-state method to suit the specific equipment and raw materials available to the project. Process development work was conducted predominately to provide access to high quality ceramics in order to study the characteristics required for corrosion resistance, but also provided insight into processing properties of  $\text{BaZrO}_3$  which could be applied to other processes. Residual processing defects may remain which are close to or below detection limits, and hence the results of this study remain an approximation within the limits imposed by the kinetics of the system and the analytical techniques used to study it.

### **3.4.2 Solid-state process development program**

Considerable detail is available on the method used to fabricate corrosion resistant crucibles using solid-state powder processing (Erb, Walker & Flükiger 1995; Liang *et al.* 1998). The current development was undertaken to determine key aspects of the processes that had not been described quantitatively, and to devise an adequate process using raw materials, processing and analytical equipment different from the original. As well as developing the production process, analytical procedures were developed to characterise the products and optimise processing. Although the principle of solid-state processing is very simple, each stage of the process must be conducted carefully in order to obtain the maximum quality of the end product.

Decisions needed to be made about each of the following specific aspects of the process:

1. Mixing of starting reagents. No guidance was provided in the literature. Clearly the greater the degree of mixing, the more reactive is the mixture during solid-state reaction. The mill available for the project was a ring mill rather than a ball mill as used by other researchers. Also the  $\text{ZrO}_2$  available to the project came from a different manufacturer from that used in the original research (Erb, Walker and Flükiger 1995).
2. Calcination temperatures. Quite specific information was reported by Erb on suitable calcination temperatures, specifically 1200 and 1300 °C. Most calcination was performed at 1300 °C in this project on the basis of XRD results.
3. Calcination times. No specific information on calcination times was available, and they had to be determined experimentally.
4. Regrinding/re-calcining protocols. Erb published general information on re-grinding and re-calcination protocols, but did not specify regrinding or re-calcination times. The assertion that re-grinding improved phase purity was also tested.
5. Final grinding requirements. Fine particle size is well known to be required to achieve adequate sintering properties to achieve sufficient density at attainable sintering temperatures. Erb (1995) stated a final ball mill for up to 24 hours was required, and that an average particle size of 0.3  $\mu\text{m}$  with no particles larger than 1  $\mu\text{m}$  as measured by a Cilas particle size analyser was adequate. Given the different milling characteristics of ring mills and ball mills and potential differences in the agglomeration state and strength after final calcination, a grinding time needed to be established. However, it is not clear whether Erb's particle size figures describe the size of discrete un-agglomerated particles or the size of agglomerates. The relationship between results obtained from this instrument compared to other particle sizing instruments or other methods of analysis such as microscopy or XRD analysis was not known, so a practical method was needed using available equipment.

6. Powder phase purity. Little information was available on the required phase purity of the powder. The existing method for determining completion of the solid-state reaction was by following weight losses attributed to carbonates. However, a more direct approach was desirable, despite the challenges of achieving detection limits suitable for this application.
7. Shape forming and particle packing. Erb describes in good detail his shape forming procedure. However, Erb's ability to isostatically press crucible shapes without adding a lubricant to the powder could not be replicated, and possible difficulties caused by lubricant use could not be eliminated. The effect of lubricant addition on grain growth was evaluated and found to be insignificant.
8. Sintering conditions. Erb clearly described his sintering procedure: 4 to 24 hours at 1730 °C, generally at or close to the lower end of this range. In this study, sintering temperatures were chosen at essentially only two levels considering previous literature and the limitations of available furnace equipment: 1650 and 1700 - 1710 °C. The furnaces routinely available to this project were molybdenum di-silicide muffle furnaces capable of routine operation at 1650 °C. At higher temperature, degradation of elements, refractory linings and Pt-Rh control thermocouples increases rapidly, and 1710 °C was the upper limit beyond which risk of furnace damage was severe. The rates of furnace degradation still required the number of firings to be kept to a minimum. One group of samples was sintered at 1750 °C using an alternative furnace to confirm corrosion problems were not simply attributable to inadequate sintering temperatures.

### **3.4.3 Chemical process development considerations**

The purpose of oxalate chemical process development was to try to reduce defects caused by reputed limitations of the solid-state process, guided by the required attributes of the ceramic learned from the literature and from the current study. Ideally this could provide a ceramic of improved performance, and a process for fabricating it on a routine or industrial basis.

When developing a viable chemical process, there are many potential variables as outlined in Section 3.2, even when confining development to the oxalate system. Therefore the experimental program had to be constrained to a feasible set of starting variables. Furthermore, a strategy was needed to investigate only certain combinations of these variables, because studying all combinations would be inefficient and possibly unnecessary, and in any case impossible within the resources of the project. The following discussion outlines the basis on which reaction conditions were chosen for study, and is presented essentially in the sequence of the production process. The scope of the project was necessarily limited to finding a viable process, rather than a comprehensive study of combinations of variables unlikely to yield a useful product.

Previous literature provided a basis of restricting the reagents of interest to a short list comprising oxalic acid, ammonium oxalate, barium chloride, barium acetate, zirconium oxychloride, zirconium tetrachloride, mineral acids such as hydrochloric acid, and ammonia. Other reagents containing metallic cations, such as sodium oxalate as used by Potdar *et al.* (1992) were optional but largely avoided due to potential cation contamination by partial co-precipitation or incomplete removal during precipitate washing. To minimise deionised water consumption, initial solution concentrations were generally confined to reasonably high values, such as 0.1 - 1 M for very soluble reagents or just below solubility limits imposed by less soluble reagents such as ammonium oxalate. Mole ratios of solutions were limited bearing in mind efficiency and disposal concerns: for example, barium to zirconium solution mole ratios were constrained between one and two, with a clear preference for ratios close to one. Ba : Zr mole ratios higher than one simply mean the excess barium is washed out of the product after precipitation, which represents a cost disadvantage, but also a containment and disposal problem of toxic barium salts. Oxalate salts, not being such a cost or disposal problem, could be readily used in excess if necessary, and the mole ratio of oxalate to zirconium was constrained between two and three since a larger excess was observed to be unnecessary or detrimental to the product.

Orders of mixing of reagents and rates of addition of reagents were studied for only a few cases. One pattern noticed in many aqueous processes for alkali-earth zirconates, for example oxalate, peroxide and citrate methods, is that these reagents form solution complexes with zirconium salts. Given the stabilising effect of complexing ligands against hydroxide or polymer formation, it appeared to be an obvious approach to zirconium complex formation prior to addition of other reagents where appropriate. The formation of solution complexes formed the primary basis for selecting the order of addition of reagents. The aim was to produce a coprecipitate, ideally a single phase, rather than a mixture of phases precipitated sequentially, thus mixing of any two solutions which formed a precipitate prior to the addition of the third solution was avoided where possible. Preference was given to mixing the zirconium and oxalate solutions to produce a stable zirconium solution complex prior to addition of barium, though as the results show, stable zirconium solution complexes form only under certain conditions. If these goals could not be met, barium and zirconium solutions were mixed, then the mixed solution added to the oxalate solution.

Precipitation temperature was known to be important from previous studies, and experimentally could be continuously varied between 22 and 95 °C for small quantities of solutions up to approximately 2.5 L, using a hotplate stirrer. The decision of what temperatures to investigate was carefully considered to avoid adding an unsustainable level of complexity to the experimental program. One might wish to study reactions at numerous incremental temperature changes, for example 10 °C increments. Studying eight temperature levels for all reactions would immediately lead to an impracticably large number of experiments. In the oxalate system, the study of the binary interaction of zirconium oxychloride with oxalate salts lead to a much more strategic choice of temperatures: ambient, approximately 70 °C (which was just below the temperature at which zirconium oxychloride observably formed a precipitate with oxalic acid), and close to boiling at 90 - 95 °C. There was advantage in using ambient temperature reactions, not only to simplify process control, but also to allow for scale up of reaction volumes without dedicated temperature control equipment.

Washing volumes were chosen to reduce unreacted reagents or supernatant ions such as chloride to acceptable levels. Drying was generally conducted using a laboratory oven at 110 - 120 °C as solvent washing was impractical for the number of samples produced.

A key parameter for forming and sintering properties of powders is particle size, and the effect of calcination conditions on particle size was studied extensively. Temperatures were selected between 1000 and 1500 °C on the basis of establishing reasonable powder phase purity as measured by XRD, and producing a particle size suitable for shape forming processes. Considerable scope was given to evaluating the feasibility of slip casting as a forming process, and the particle size demands of this process required a wide range of temperatures to be evaluated. Maximum calcination temperature was presumed to be restricted by the permissible level of hard agglomerate formation.



## CHAPTER 4

### EXPERIMENTAL DETAILS

---

#### 4.1 Standardising initial reagents

Standardisation of reagents used for precipitation was necessary to accurately control solution ratios of reagents in developing chemical methods for  $\text{BaZrO}_3$  production. Rather than relying on suppliers' data, independent and repeatable methods for assaying barium and zirconium salts were developed. In summary:

- barium salts were assayed gravimetrically by quantitative precipitation as barium sulfate using sulfuric acid;
- zirconium salts were precipitated as zirconium mandelate using mandelic acid, allowing gravimetric determination of Zr + Hf after calcination to the oxide.

The detailed procedures used are outlined in Sections 4.1.1 and 4.1.2.

##### 4.1.1 Barium determination

A quantity of barium salt (either  $\text{BaCl}_2$ ,  $\text{BaCO}_3$  or  $\text{Ba}(\text{CH}_3\text{COO})_2$ ) containing 0.025 mol Ba was weighed to  $\pm 0.1$  mg into the container in which the precipitation was to be performed, preferably a 400 mL conical beaker. A single container was used to eliminate the potential for transferring errors. The salt was dissolved in approximately 100 mL of high purity de-ionised water (e.g. Milli-Q) and acidified with 1M HCl. Nitric acid must not be used for dissolution as it was observed to cause a systematic loss of approximately 1.0 wt.% in the assay of  $\text{BaCO}_3$ .

The solution needs to be acidic to ensure that the barium sulfate precipitated will have a suitable particle size for quantitative gravimetry. This objective was achieved by the following processes:

- For  $\text{BaCO}_3$ , the powder was wet with 100 mL water, then 75 mL of 1.0 M HCl was added without stirring. The excess acid ensured the powder dissolved completely and formed a suitably acidic solution. The powder was left to dissolve with only

occasional slow swirling, preventing spattering out of the conical beaker by bubbles of carbon dioxide bursting at the surface of solution. The dissolution process took several hours, and was usually left to complete overnight without disturbance.

- For  $\text{Ba}(\text{CH}_3\text{COO})_2$ , HCl was added in slight excess, e.g. 2.4:1 HCl to Ba mole ratio, that is, 60 mL of 1.0 M HCl. If no HCl is added, the precipitate that forms is too fine for quantitative determination, causing severe filtration loss on even the finest grades of paper filters, adhesion of the precipitate to glassware, and poor washing of the precipitate.
- For  $\text{BaCl}_2$ , only a small amount of HCl needed to be added to acidify the solution: 0.01 mole (i.e. 10 mL of 1.0 M HCl) was found to be sufficient.

Once the barium solution was prepared, it was heated on a hotplate stirrer, along with 100 - 120 mL of 0.30 M  $\text{H}_2\text{SO}_4$ . Once both solutions reached 85 – 95 °C, the  $\text{H}_2\text{SO}_4$  was added to the barium solution while maintaining magnetic stirring. Precipitation was observed to occur instantaneously, though the suspension was allowed to stir at 85 - 90 °C for 5 - 10 minutes to ensure complete reaction. As a safety precaution, there must be no interruption to stirring of barium sulfate slurries on hotplates, as the precipitate has a strong tendency to settle out of suspension causing explosive boiling at the bottom of the vessel, which can easily break glass containers. Once taken off the hotplate, the suspension was allowed to cool to room temperature without stirring, then the precipitate was isolated using cellulose nitrate membrane filters with a pore size of 0.45  $\mu\text{m}$  or less to prevent filtration loss. The 47 - 55 mm glass membrane filtration units made by Millipore, Whatman or Sartorius are ideally suited for this purpose. Care must be taken to ensure complete transfer of the precipitate to the filter funnel, without excessive use of water. The amount of water used to affect transfer was kept under 200 mL. Once precipitate transfer was completed, a small quantity of water was used to wash all precipitate to the bottom of the filter funnel. After all water had been removed, 100 mL of 0.03 M  $\text{H}_2\text{SO}_4$  was used to wash the precipitate.

Porcelain crucibles (30 - 50 mL) were used for calcining the precipitate. All crucibles were prepared for use by heating to 1000 °C for 30 - 60 minutes, furnace cooling to around 100 - 200 °C then to ambient temperature in a desiccator containing dry silica gel, then weighed to  $\pm 0.1$  mg. The precipitate and filter membrane was transferred to a pre - weighed porcelain crucible, taking care to ensure complete transfer. Using the clean side of the filter membrane to remove the bulk of precipitate adhering to the filter funnel, and a small amount of de-ionised water to wash the last traces of precipitate into the crucible was found to be a highly effective technique. The crucibles were dried at 100 °C, ignited at 1000 °C for an hour, and cooled as before in a desiccator to ambient temperature. The weight of each crucible was measured to  $\pm 0.1$  mg, and the assay for each reagent calculated from the mass of BaSO<sub>4</sub>. The procedure, followed carefully, has been observed to allow a precision as high as  $\pm 0.02$  % ( $\pm 1$  standard deviation) for barium acetate.

Depending on the quality of the reagent, barium salts usually contain strontium in varying amounts depending on the level of specific purification. No corrections for slight errors due to strontium were applied in this measurement. The procedure for barium assay was useful for standardising barium reagents, but not for analysing barium in solutions also containing zirconium due to co - precipitation of zirconium in the sulphate. An assay of a solution made with known amounts of BaCl<sub>2</sub> and ZrCl<sub>4</sub> containing a 1 : 1.00 mole ratio of BaCl<sub>2</sub> and ZrCl<sub>4</sub> resulted in the calcined precipitate 37 % heavier than attributable to the known barium content. For this reason, all quantitative determinations for samples containing both barium and zirconium were conducted using XRF.

#### **4.1.2 Zirconium determination**

Zirconium oxychloride was standardised by precipitation with mandelic acid and assayed gravimetrically after calcination to ZrO<sub>2</sub>. There are numerous gravimetric procedures to assay zirconium solutions including precipitation as hydroxides or hydrates (using alkali hydroxides, ammonia or organic bases), selenious acid, cupferron, phosphates, organic acids (including mandelic) and potassium iodate (Elinson and Petrov 1969, p. 46-47, Mukherji 1970, p. 18-20). The mandelate acid

route was chosen as mandelic acid is a highly specific precipitant for zirconium and hafnium, that is, it leaves contaminants largely in solution. For this reason the mandelate route was also used to make  $\text{ZrO}_2$  from high purity  $\text{ZrCl}_4$  for standards for XRF analysis. Mandelic acid provides a quantitative and a readily washable and filterable precipitate under the conditions used, and is a relatively inexpensive and non-toxic reagent. Furthermore, the gravimetric assay after calcination to the oxide makes this process insensitive to variable or uncertain precipitate composition, unlike other processes such as  $\text{KIO}_3$ .

Approximately 5.5 g of the salt was weighed to  $\pm 0.1$  mg and dissolved in 200 mL of de-ionised water, to which 50 mL of concentrated HCl (37 wt.% assay) was added. A solution of mandelic acid was prepared by dissolving 15.0 g of DL-Mandelic Acid (Fluka Chemika, >99%) in 200 mL of de-ionised water. Both solutions were heated to 90 °C on a hotplate stirrer, then the mandelic acid was added to the stirred zirconium oxychloride solution. The slurry was digested at 90 °C for approximately 15 minutes, cooled to ambient temperature and filtered. The precipitate was washed using 200 mL of 2% mandelic acid solution in 2% HCl, re-filtered and dried. The precipitate was calcined in porcelain crucibles for 2 hours at 1000 °C and the  $\text{ZrO}_2 + \text{HfO}_2$  content determined assuming a pure oxide. Transfer and weighing details were as for the barium assay procedure. A repeat analysis using 7 specimens produced a standard error of  $\pm 0.03$  % for a sample containing 36.82 wt.% ( $\text{ZrO}_2 + \text{HfO}_2$ ).

#### **4.2 Qualitative solution tests for detection of barium and zirconium in solution**

During development of chemical processing, it is very helpful in understanding basic process chemistry to have a qualitative or quantitative measure of solution composition at various stages of processing. This could be facilitated by access to analytical laboratory instruments, including AAS, AES and their many derivatives, or solution XRF. However, this was neither available nor strictly necessary for this research, as qualitative solution tests were sufficient. Analytical techniques for

measuring the speciation of ions in solution would have been very useful for determining and controlling the precise nature of process chemistry, especially considering the widely observed importance of zirconium speciation on its chemical properties. The literature lists numerous techniques for determining zirconium speciation including wet chemical, ion exchange, electrochemical, dialysis, and ultracentrifuge techniques (Elinson and Petrov 1969, p 38-45). However, such methods were considered too indirect and involved to warrant serious effort unless no alternative could be found, particularly given the contradictory results and interpretation present in the literature, and the limited aims of the current research.

A standard and sensitive test for barium in solution is precipitation as sulphate, often using dilute sulphuric acid, and this was adopted for this project. Zirconium forms soluble complexes with sulphates under most conditions, so interference from zirconium, though observed as significant in quantitative gravimetric precipitations, was not regarded as a severe problem. A relative test useful in approximate comparison of different solutions was readily achieved by adding controlled amounts of each solution to a fixed and excess volume of acid or vice versa. In most cases, precipitation was rapid and obvious. However, in some cases where concentrations were low precipitation was slow, taking up to a minute to become visible. Therefore several minutes were allowed to confirm non - detection.

The simplest and most useful solution test for zirconium was the addition of solution to an excess of 1 M NaOH, checking for precipitation, and for a pH in excess of 12. The difficulties of other qualitative tests for zirconium are a requirement to ensure zirconium speciation allows reaction with the indicator, and that the stability of the indicator exceeds that of competing complexing agents under the conditions used. Without detailed knowledge of the limitations of such tests, using organic indicators appeared rather uncertain. In the case of mandelic acid used for quantitative precipitations of raw zirconium reagents, the stability of complexes formed with oxalates often prevented detection with mandelic acid that were readily detected by NaOH precipitation so mandelic acid for qualitative tests was quickly abandoned in favour of NaOH. Zirconium salts are readily precipitated by strong alkalis in most cases.

For the purposes of a simple qualitative test, the H<sub>2</sub>SO<sub>4</sub> and NaOH approaches appeared satisfactory, given that results of qualitative testing were consistent with XRF analysis of the reaction products and the known quantities of reagents used in the process.

#### **4.3 DTA/TGA analysis**

Differential thermal and thermogravimetric analysis (DTA/TGA) was conducted on a Setaram TAG24 instrument. Samples were analysed in platinum crucibles in air with a heating rate of 10 °C/minute up to 1300 °C using alumina as a reference. The nominal sample mass was 50 mg ( $\pm$  10mg). The principle purpose of DTA/TGA analysis was to measure the temperature at which calcination of oxalate precipitates was complete in order to estimate appropriate calcination temperatures in powder processing.

#### **4.4 Nitrogen adsorption analysis (BET)**

Apparent surface areas of powders were measured using an ASAP 2400 or Gemini 2360 surface area analyser (Micromeritics Inc.) using N<sub>2</sub>. Samples were dried at 120 °C in air, then de - gassed under vacuum at 200 °C for at least three hours in the case of the ASAP 2400, and under flowing dry nitrogen at 200 °C at ambient pressure for the Gemini. The surface area was determined by a BET fit to at least five points (typically at least ten points) of the N<sub>2</sub> adsorption isotherm at -195.8 °C. The correlation coefficients of the BET adsorption isotherms of all measurements were greater than 0.999, which was considered acceptable for surface area determination.

Primary particle sizes were estimated from BET surface areas assuming a single phase with a density of 6.229 g/mL (PDF 06 - 0399) and monodisperse size distributions of cubes or spheres. The specific surface area of cubes and spheres with the same edge length and diameter are identical.

## **4.5 XRF analysis**

X - ray fluorescence spectroscopy (XRF) was used to determine the mole ratios of Ba : (Zr +Hf) for powder samples in this project. Since the potential phase purity of the ceramic was known to be dependent on the stoichiometry of the ceramic, an accurate, precise and reliable means of measuring stoichiometry was crucial to the progress of this research. Refinement of the XRF method formed a major component of the project because the accuracy and precision needed to optimise stoichiometry demanded a method close to the limits of current technology. For optimisation of the measurement, it was necessary to determine and minimise the various contributions to measurement errors, such as sample preparation, and the numerous sources of instrument error. A key requirement for XRF analysis was quantification of the accuracy and precision of the measurement in practice, so that a justifiable and reliable experimental error could be defined. The importance of quantifying accuracy and precision levels becomes obvious from corrosion testing results: the tolerances on stoichiometry of corrosion resistant ceramics were only slightly larger than the error of the best XRF measurement achieved.

The procedure was based on the fusion bead technique developed for geological samples by Norrish and Hutton (1969). Fusion beads provided relatively simple and accurate calibrations by reducing potential particle size and inter-element effects to negligible or manageable levels through the effects of dilution and/or a heavy-absorber. Furthermore, the use of fusion beads allowed the relatively straightforward production of stable calibration standards from assayed powder reagents without potential contamination from grinding or calcination. A heavy absorber flux was needed to produce beads of infinite thickness for the Zr-  $K_{\alpha}$  line.

### **4.5.1 Production and analysis of powders for calibration standards for use on SRS - 200 XRF spectrometer**

BaCO<sub>3</sub> was prepared by precipitation from solution of BaCl<sub>2</sub> (Sigma Chemicals, AR grade) and ammonium carbonate (Sigma Chemicals, AR grade). The precipitate was repeatedly washed by filtering the solids from a dilute slurry and re-dispersing with de-ionised water. After 5 washings, the solids were dried at 110 °C

and calcined for two hours at 520 °C. The calcined powder was equilibrated in air for 15 hours to ensure any moisture gain from air reached equilibrium to allow highly stable weighing of the powder for gravimetric analysis. The barium content of the powder was determined using sulfate precipitation as described in Section 4.1.1. Analysis in triplicate samples gave the BaCO<sub>3</sub> content as 99.63 wt.% (standard error ± 0.04%).

High purity zirconia was prepared from ZrCl<sub>4</sub> (Aldrich, product number 221880) purified to <50 ppm Hf. The manufacturer's batch analysis showed a purity of 99.995 % based on trace metal analysis. The ZrO<sub>2</sub> was precipitated with DL - mandelic acid (Fluka Chemika, product number 63470, purity 99.9 %, ignition residue of 0.05 %). The precipitate was repeatedly washed with de - ionised water, and calcined to ZrO<sub>2</sub> at 1000 °C for 120 minutes. The calcined powder was lightly ground in an agate mortar and pestle. Since mandelic acid is a highly specific precipitant for zirconium and hafnium in solution (i.e. does not precipitate other cations), the purity of the ZrO<sub>2</sub> produced was assumed to be at least 99.95%.

HfO<sub>2</sub> (98%, Aldrich product number 202118) was lightly ground by mortar and pestle and calcined at 1000 °C for one hour. The manufacturer's batch analysis shows a loss on ignition of 0.7% and 0.65 wt.% oxide impurities when converted from trace element data. The powder was assumed to contain 99.0 wt.% HfO<sub>2</sub> after calcination. This approximation was considered adequate given the low abundance of HfO<sub>2</sub> in the analyte.

#### **4.5.2 Preparation of fusion beads for use on SRS - 200 XRF spectrometer**

Powders were weighed as per Table 4.1 on a 4 decimal balance or a 6 decimal microbalance for HfO<sub>2</sub> into 10 mL Pt-Au crucible, gently stirred with a spatula and transferred to an electric muffle furnace at 1100 °C. After 10 minutes, the crucible was briefly removed to allow agitation and tilting to assist fusion and homogenising the bead composition. Total fusion time was 25 minutes (± 5 minutes), after which time the beads were formed by manual press - quenching using an aluminium plunger onto



a graphite disk placed on an electric hotplate. The beads were covered by aluminium cups and annealed on the hotplate for at least 4 hours. Synthetic standards were observed to produce a substantially clear melt after approximately 15 minutes, whereas BaZrO<sub>3</sub> powders fully dissolved in approximately 5 - 10 minutes. SiO<sub>2</sub> was added to eliminate bead cracking. Al<sub>2</sub>O<sub>3</sub> was also found to be useful in this regard, but SiO<sub>2</sub> appeared to be more effective. KBr was an effective non-wetting agent and in most cases, cleaning of crucibles between specimens was not required. The bead size was 2.5 mm ( $\pm$  0.3 mm) thick and 27 mm diameter. Beads have been stored in a desiccator without signs of hydration or cracking for over 12 months. The dilution of the sample is about as low as can be readily achieved, because using a higher sample : flux ratio causes difficulty in dissolving the synthetic standard powders in less than 30 minutes. Inter-element effects were readily managed at low dilution because of absorption buffering by La<sub>2</sub>O<sub>3</sub>. The dilution indicated above yielded results adequate for this project and suited the sensitivity of the spectrometer.

Table 4.1 Preparation of XRF specimens for use on SRS200 spectrometer.

Material	Mass (g)
Standard Norrish Flux (16.3 wt.% La <sub>2</sub> O <sub>3</sub> , 36.7 wt.% LiCO <sub>3</sub> , 47 wt.% Li <sub>2</sub> B <sub>4</sub> O <sub>7</sub> , Sigma Chemicals, W.A.)	3.000 $\pm$ 0.001
Analyte (BaO, ZrO <sub>2</sub> and HfO <sub>2</sub> assuming BaCO <sub>3</sub> decomposes to BaO during bead formation)	0.400 $\pm$ 0.001
SiO <sub>2</sub> (99.99 wt.%, Sigma Chemicals W.A.)	0.200 $\pm$ 0.001
KBr (BDH AR - grade)	0.030 $\pm$ 0.002

#### 4.5.3 Set - up of SRS - 200 XRF spectrometer

##### Global Parameters:

- Molybdenum (Mo) x-ray tube operating at 40 kV, 60 mA
- 20 mm mask, no filter.
- Analysis medium: vacuum.
- Specimen spinner: on
- Instrument maintained at 25 °C ( $\pm$  1 °C) with a temperature control unit
- Flow counter pressure controlled using a manostat.

Table 4.2 Instrument parameters used on SRS200 spectrometer.

Parameter	Ba - $L\alpha_1$	Zr - $K\alpha_{1,2}$	Hf - $L\beta_1$
Wavelength (Å)	2.776	0.788	1.374
Crystal	LiF 200	LiF 220	LiF 200
Peak position ( $2\theta$ °)	87.080	32.110	39.910
Background point ( $2\theta$ °)	89.200	33.300	42.500
Incident aperture (mm)	20	20	20
Collimator	0.4 °	0.15 °	0.4 °
Detector	flow counter (P10 gas)	NaI scintillator	flow counter (P10 gas)
Detector bias	1730 V	1125 V	1730 V
Linear amplifier gain	128	128	128
Discriminator window	0.5 - 1.6 V	0.4 - 1.6 V	0.3 - 1.3 V
Approximate net count rate (counts/second)	16 000	48 000	500
Peak and background count times (seconds)	300	180	300

#### 4.5.4 Method as used on Philips PW1404 spectrometer

Towards the end of the project, the SRS - 200 spectrometer was withdrawn from service and a new set of standards and instrument parameters were created to suit analysis on a Philips PW1404 spectrometer. New standards were required as the specimen cassettes were designed for specimens of larger diameter (40 mm) than could be made using the 27 mm press - quench facilities available. The new fusion beads standards and specimens were prepared using a casting process rather than press - quenching, resulting in a much improved surface finish and flatness.

#### 4.5.5 Preparation of standards for use on PW1404

Barium carbonate (Fluka Chemika, >99 %) was used to prepare a new set of standards because of its relatively low strontium content. Because it was used as a reagent in other parts of the project, the strontium content of certain samples must match the standard. The reagent was standardised gravimetrically as per Section 4.1.1.  $ZrO_2$  and  $HfO_2$  were prepared as per Section 4.3.1. Three standards were prepared at constant  $ZrO_2:HfO_2$  ratio using the average result of previous XRF analyses, with nominal Ba: (Zr+Hf) mole ratios of 0.9, 1.0 and 1.10. Each reagent, including Norrish

formula x-ray flux, SiO<sub>2</sub> and KBr was weighed to  $\pm 0.1$  mg directly into a 40 mL Pt - Au crucible. The powder was gently mixed, then fused in an electric muffle furnace at 1050 °C for a total of 30 ( $\pm 2$ ) minutes. At 8 - 10 minute intervals during the fusion, the crucible was removed from the furnace and agitated strongly for approximately 20 seconds to aid fusion and to ensure a homogenous bead composition. After 30 minutes of fusion, the melt was poured into a pre - heated Pt - Au casting mould (40 mm diameter), which was left in the furnace for a further 2 minutes. The mould was then lifted out of the furnace and allowed to cool in air. During cooling, the melt solidified into a clear bead without signs of crystallisation, and the bead ( $4 \pm 0.5$  mm thick) was removed from the mould when cool enough to handle without gloves. Two important aspects of this procedure were observed to be:

1. Considerable agitation was required during fusion. A brief ( $< 5$  second) agitation at eight minute intervals was enough to ensure complete melt, but on a large bead was insufficient to homogenise the bead composition and produce repeatable results. One indicator of insufficient melt agitation was a slight visible colour difference in the melt at full temperature as the casting mould was removed from the furnace. Parts of the melt glowed slightly more red or brightly whilst still at furnace temperature and produced  $\sim \pm 1\%$  repeatability when analysed on the spectrometer. Well agitated beads displayed a featureless melt in the casting mould at full furnace temperature and produced a repeatability of approximately  $\pm 0.1\%$ , close to the instrument repeatability.
2. Moulds were cooled to near ambient temperature before removing specimens, which produced a low cracking rate ( $\sim 1\%$ ). Specimen removal too soon after solidification caused increased cracking problems.

Table 4.3 Preparation of XRF specimens for use on PW1404 spectrometer.

Material	Mass (g)
Standard Norrish Flux (16.3 wt.% $\text{La}_2\text{O}_3$ , 36.7 wt.% $\text{LiCO}_3$ , 47 wt.% $\text{Li}_2\text{B}_4\text{O}_7$ , Sigma Chemicals, W.A.)	$10.000 \pm 0.001$
Analyte ( $\text{BaO}$ , $\text{ZrO}_2$ and $\text{HfO}_2$ assuming $\text{BaCO}_3$ decomposes to $\text{BaO}$ during bead formation)	$1.350 \pm 0.001$
$\text{SiO}_2$ (99.99 wt%, Sigma Chemicals W.A.)	$0.700 \pm 0.001$
KBr (BDH AR - grade)	$0.100 \pm 0.002$

Table 4.4 Preparation of Standards for use on PW1404 spectrometer.

Nominal [Ba:Zr+Hf] mole ratio	$\text{BaCO}_3$ Wt. (g) $\pm 0.0001\text{g}$	$\text{ZrO}_2$ Wt. (g) $\pm 0.0001\text{g}$	$\text{HfO}_2$ Wt. (g) $\pm 0.0001\text{g}$	Calculated Ba:[Zr+Hf] mole ratio $\pm 0.0008$
0.9	0.9181	0.6274	0.0125	0.8997
1.0	0.9652	0.5918	0.0126	1.0019
1.1	1.0069	0.5620	0.0118	1.1008

#### 4.5.6 Set - up of PW1404 XRF spectrometer

The PW1404 operating with a new x-ray tube provided a significant improvement over the considerably older SRS - 200 in terms of instrument stability, sensitivity and speed of analysis. A set of instrument parameters yielding repeatable, stable and fast analysis was readily found:

##### Global Parameters:

Philips PW - 1404 XRF Spectrometer

Rhodium (Rh) x-ray tube operating at 45 kV, 60 mA

27 mm mask, no filter.

Analysis medium: vacuum.

Specimen spinner: on

Table 4.5 Instrument parameters used on PW-1404 spectrometer.

Parameter	Ba - $L\alpha_1$	Zr - $K\alpha_{1,2}$	Hf - $L\beta_1$
Wavelength (Å)	2.776	0.788	1.374
Crystal	LiF 200	LiF 220	LiF 200
Peak position ( $2\theta$ °)	87.190	32.040	39.880
Background point(s) ( $2\theta$ °)	84.690, 89.190	34.540	37.380, 42.380
Incident aperture (mm)	27	27	27
Collimator	coarse	coarse	fine
Detector	flow counter (P10 gas)	scintillator only	flow counter + scintillator (P10 gas)
Discriminator window	35 - 68%	23 - 78%	28 - 57%
Approximate net count rate (counts/second)	60 000	240 000	650
Peak, background count time(s) (seconds)	120, 20, 20	46, 16	30, 6, 6

## 4.6 Transmission electron microscopy

TEM was used for two purposes:

1. to measure particle size of powders during processing;
2. to characterise microstructure, and in particular, grain boundary structure of sintered ceramics, in order to check phase purity of samples and to help understand corrosion processes. For one sample, TEM was used to determine the microstructural distribution of aluminosilicate contamination that had been caused by inadequately purified wash water during early oxalate process development.

### 4.6.1 Specimen preparation for TEM analysis of powders

Specimen preparation for powders was essentially very simple: a droplet of very dilute aqueous dispersion of the powder was applied to a holey-carbon TEM grid and allowed to dry under a mild infra-red heating lamp. The dilute dispersion added to the grid was prepared by double dilution to assist representative sampling. After drying, the specimen was ready for insertion into the microscope. Dispersions were generally

prepared by adding an ammonium polyacrylate dispersant (Dispex - A40, Allied Colloids) pre - dissolved in water to approximately 1 g of powder. The amount of dispersant used was 2 - 4 wt.% of the powder in the as supplied concentration. Samples were ring milled for the five minutes to aid dispersion and remove agglomerates within the capability of such milling conditions. Two stages of dilution in high purity de - ionised water were used to prepare the final slurry, which was applied to holey-carbon TEM grids (ProsciTech Australia) using a 1 mL syringe with a 25-gauge needle. A few samples were ring milled for up to 30 minutes to study the effect of extended milling, but no obvious change was observed.

#### **4.6.2 Specimen preparation for TEM analysis of sintered ceramics**

Preparation of thin sections of bulk ceramics remains a laborious task using typical preparation equipment. Many researchers avoid TEM altogether or compromise their results by avoiding proper specimen preparation, but analysis at a resolution only accessible to TEM was a key requirement for progress in this research.

The technique used for sectioning can be summarised into 4 main stages with nominal thickness indicated:

- resin mounting and preliminary bulk sectioning (1 mm);
- hand polishing of flat section (70  $\mu\text{m}$ );
- dimple grinding (20  $\mu\text{m}$ );
- ion milling (electron transparency).

Samples were glued inside brass tubes (3.0 - 3.1 mm outer diameter) to aid handling of sections during preparation. The bulk sample was sliced and rounded into a cylinder using 400 grit sand paper, to fit into the brass tubes. The samples were then glued inside the brass tubes using Araldite™ epoxy adhesive, being careful to ensure complete filling of the space between the specimen and the tube and a minimum of bubbles in the adhesive. After curing at least overnight at 40° C, the tubes were then sliced into approximately 1.0 mm thick discs using a Struers Minutome diamond saw. Mounting specimen inside metal tubing improved ease of handling thinned specimens. However, specimens were also prepared from 1 mm sections cut using a diamond saw,

then to 3.05 mm diameter discs using a Gatan ultrasonic disc cutter. Unmounted specimens were sufficiently robust for thin sectioning if handled with care.

Manual grinding of rough thinned sections was done by a Gatan Disc Grinder. The grinder was used on 400, 600, 800, 1200, 2000 and 4000 grit SiC paper. For specimens with a mole ratio less than one, where water soluble phases were absent, flowing water was used as the lubricant. For samples close to or above unity mole ratio, the possibility or known presence of water soluble phases required a non-aqueous lubricant. In this study kerosene was used. This method was used to produce  $\sim 70\ \mu\text{m}$  sections, finished to 4000 grit on at least one side. The  $70\ \mu\text{m}$  thickness derives from the geometry of the 15 mm dimple wheel used in the next step, and the subsequent geometry of low angle ion milling used for final thinning.

The flat pre - thinned section was dimpled on the last side of polishing using a Gatan dimple grinder, operating at 20 g load, using a 15 mm bronze dimpling wheel running at a medium rotation speed. Either 0.25 or  $1\ \mu\text{m}$  diamond paste was used for dimple grinding to the target thickness of  $20\ \mu\text{m}$  at the centre of the dimple. Dimpled thickness was controlled using the dial - gauge on the dimple grinder.

Electron transparency was achieved using a Gatan Precision Ion Polishing System (PIPS) to thin the dimpled sample from  $20\ \mu\text{m}$  to its final thickness. It was found that at the average operating conditions of 4 kV and  $\sim 10\ \text{mA}$  in each gun, the centre of the specimen thinned at approximately  $3 - 4\ \mu\text{m/hr}$ . Ion milling time proved to be the limiting factor in the rate at which specimens could be produced.

Control of the end point of ion milling was possible only with the low - powered optical microscope fitted on the PIPS. Samples would invariably perforate in some areas before other evidence of an approaching end point became visible. Thinning was continued just past the first sign of perforation, with analysis conducted in the thin areas close to perforations. It was also clear that decreasing the gun voltage of the ion mill from 4 kV to 3 kV and especially 2 kV at the end of polishing (just after the earliest indication of perforation at 4 kV) markedly improved the available transparent area. A final low voltage polish was used for most specimens despite the

significant increase in ion milling time caused by low gun efficiency and low milling rates at low operating voltage. Where possible, specimens were examined mounted inside the section of brass tube. For samples where the adhesive failed during very late stages of thinning, recoverable sections were mounted on slotted grids using minute droplets of epoxy adhesive applied to the grid with a fine fibre such as an eyelash, followed by carefully positioning the section using vacuum tweezers.

#### **4.6.3 TEM analysis**

The bulk of analysis was performed using a Jeol JEM 2011 TEM fitted with a LaB<sub>6</sub> filament and operated at 200 kV. The instrument was equipped with an Oxford Instruments Link EDS spectrometer controlled using Oxford Instruments Inca EDS software, a Gatan CCD camera and a Jeol scanning TEM (STEM) unit capable of 2 dimensional EDS elemental mapping.

A Jeol JEM 3000F was used to determine aluminium and silicon distributions in a sample known to be contaminated by aluminosilicates during processing. This high performance microscope was fitted with a field emission gun (FEG) operating at 300 kV, an identical Oxford Instruments Link EDS spectrometer controlled using Oxford Instruments Inca EDS software, an identical Jeol STEM unit, as well as a Gatan Image Filter (GIF) capable of electron energy loss spectroscopy and imaging. The high brightness and small probe sizes available with a FEGTEM provided significantly improved STEM x-ray analysis and particularly two dimensional mapping performance over the 2011.

#### **4.7 SEM analysis**

Scanning electron microscopy was used to analyse the basic microstructure of sintered samples, for approximate grain size, pore size and distribution of observable secondary phases. Fracture surfaces were preferred over polished surfaces, because there was evidence of removal of ZrO<sub>2</sub> from cut and polished sections from x-ray diffraction analysis. Samples were fractured at ambient temperature, mounted on aluminium stubs with double sided adhesive carbon tape and painted on the sides with



carbon paint to eliminate possible charging problems. All samples were coated with a conductive coating, typically a light sputter coating with gold. Some samples were evaporatively coated with carbon where interference by gold in EDS analysis could not be tolerated.

The instrument used was a Philips XL-30 SEM using a tungsten filament electron source, fitted with an Everhart-Thornley type secondary electron detector, a solid state backscatter detector, and an Oxford Instruments Link EDS spectrometer controlled using Oxford Instruments Inca EDS software. The fully computerised instrument was fitted with a conventional motor driven 5-axis goniometer stage, and digital microscope control and image acquisition using proprietary Philips software. Most imaging and EDS analysis was conducted at 20 to 30 kV as the sintered samples were not affected by beam damage or significant charging difficulties. Image resolution at higher accelerating voltages was not adversely affected by excessive specimen interaction volumes because of the relatively high average atomic number of  $\text{BaZrO}_3$ . Higher accelerating voltages produced significantly higher gun brightness and therefore improved signal to noise ratios and acquisition speed in imaging, as well as higher resolution and lower instrument aberrations compared to operation at low voltages such as 5kV. Furthermore, high accelerating voltages gave the most favorable EDS analysis conditions due to high gun brightness and sufficient over - potential for efficient excitation of x-ray emission for characteristic spectral lines of interest.

SEM was most useful in providing initial determination of the process of melt percolation, due to clear image contrast and rapid EDS differentiation between yttrium barium cuprates and  $\text{BaZrO}_3$  structures. Evaluation of secondary phase distributions by SEM were somewhat disappointing, as little contrast in secondary and backscatter images could be obtained even under the most favourable instrument conditions.  $\text{ZrO}_2$  could be identified as a secondary phase, but only where substantial segregation and high local phase abundance was present, for example at the "as sintered" surfaces of certain samples.

#### 4.8 X-ray powder diffraction

X-ray powder diffraction analysis was performed using a Siemens D500 Bragg - Brentano diffractometer using a Cu tube operating at 25 - 40 mA and 40 kV,  $K_{\alpha 1,2}$  radiation (1.54060 and 1.54439 Å), fixed slit optics with 1 ° incident beam divergence, 0.15 ° receiving slit, graphite post - diffraction monochromator and NaI scintillation detector using pulse height selection. Two - theta step sizes were 0.02 ° for peak shape analysis, or 0.04 ° for maximum intensity. Count times were between 1 and 16 seconds per step depending on the counting statistics required.

Powder samples were prepared by de-agglomeration in an agate mortar and pestle and side packed into aluminium sample holders. Samples were either analysed soon after calcination treatments, or after exposure to air in order to allow carbonation (reaction with atmospheric humidity and carbon dioxide) which appeared to significantly increase XRD sensitivity to barium - rich secondary phases which could not be detected directly. Bulk analysis of sintered samples was conducted by grinding a representative piece of ceramic into a powder and performing standard powder diffraction. A sintered sample known to contain approximately 2.0 wt.%  $ZrO_2$  (based on XRF analysis of stoichiometry), was sectioned using a laboratory diamond saw and the cut surface analysed by laboratory x-ray and synchrotron radiation diffraction. Synchrotron radiation diffraction detected only very weak  $ZrO_2$  peaks despite TEM analysis showing considerable  $ZrO_2$  throughout the interior of the ceramic. The sensitivity for  $ZrO_2$  by bulk diffraction is poor, but  $ZrO_2$  may also have been removed from the analysis surface during cutting. Bulk analysis of sintered samples was therefore performed after grinding to ensure representative sampling.

The grinding time had a definite effect on peak profiles for sintered materials. For ring milling times between a few seconds and five minutes, increased milling time caused continuously increasing peak widths and reduced peak heights. Clearly there was no way to eliminate effects of grinding observed in the diffraction patterns, and the need for representative sampling to compare phase abundance was of greater priority. Grinding times were fixed where comparisons are made in the results.

#### 4.8.1 Crystallite size estimation by XRD

Crystallite size was estimated from specimen broadening of diffraction peaks using two different approaches: the simple Scherrer equation, and Voigt function profile fitting.

##### *Crystallite size estimation using Scherrer equation*

The simplest method of estimating crystallite size is to use the Scherrer equation (4.1) and assume all specimen broadening is due to size effects with negligible non-uniform strain broadening :

$$t = \frac{0.9\lambda}{B \cos \theta} \quad (4.1)$$

where  $t$  = average column length of particles in the direction of the lattice used for analysis

$\lambda$  = wavelength of x-radiation used (1.541838 Å for Cu  $K_{\alpha}$  ave)

$\theta$  = Bragg angle

$B$  = specimen broadening of full width at half maximum intensity (FWHM), in units of radians

$$= [B_{\text{observed}}^2 - B_{\text{instrument}}^2]^{1/2}$$

where  $B_{\text{observed}}$  = total FWHM of diffraction peak of specimen

$B_{\text{instrument}}$  = FWHM contribution from instrument, measured with a reference sample considered to produce negligible specimen broadening.

Instrument broadening was determined using the NIST certified reference material 660a (LaB<sub>6</sub> powder), a certified line position and line shape standard for powder diffraction. The (110) diffraction peaks of BaZrO<sub>3</sub> and LaB<sub>6</sub>, both at approximately 30 ° (2θ) for Cu  $K_{\alpha}$  radiation, were used for broadening analysis as they were the most intense peaks. The  $K_{\alpha 1}$  and  $K_{\alpha 2}$  components of these peaks were not resolved. For Scherrer equation calculations, total FWHM values were obtained on raw peaks including combined  $K_{\alpha 1}$  and  $K_{\alpha 2}$  components using Traces V5.0 (Diffraction Technology, Australia). The (110) diffraction peak of LaB<sub>6</sub> had an observed FWHM at 30.38 °2θ. There was no evidence of significant preferred

orientation in any of the large number of processed BaZrO<sub>3</sub> powders analysed in this study. High resolution TEM analysis showed in many cases, the primary particles were crystals of cubic morphology whose surfaces were <100> planes.

The Scherrer equation method is a useful approach for samples where specimen broadening was dominated by particle size effects without substantial specimen broadening from other microstructural features. This simple approach can often be a reasonable approximation for brittle materials analysed as loose powders, especially where corroborating evidence confirms specimen broadening can be ascribed to particle size effects. There are numerous reasons why strong non-uniform strain effects were not expected in processed powders. BaZrO<sub>3</sub> is a brittle ceramic, not a ductile metal. Samples were analysed after calcination treatments allowing diffusion processes to minimise crystal faults. For calcined powder there was no significant mechanical milling between calcination and analysis to introduce new defects into crystal structures.

The results of crystallite sizes calculated using the Scherrer equation were less accurate than those from Voigt profile fitting because non-uniform strain was not negligible. Some results from the Scherrer equation have been included for comparison, and could be adequate for process control of oxalate processing if more sophisticated methods of XRD data analysis are not available. TEM observations of primary particle sizes agreed more closely to Voigt profile crystallite sizes, but such comparisons are limited because they measure different particle characteristics.

#### ***Crystallite size and anisotropic strain estimation by Voigt function profile fitting***

Analysis of crystallite size and non-uniform strain broadening was also conducted using a Voigt function profile fitting method (de Keijser *et al.* 1982). Voigt function peak profiles were fitted using Shadow v4.2 (MDI, USA 1999) to BaZrO<sub>3</sub> powder samples and the LaB<sub>6</sub> line position and profile standard. The contribution of random errors to the measurement of instrument broadening was minimised by using a multiple peak method across a wide angular range of the observed diffraction pattern of the line profile standard. Crystallite size and non-uniform strain of BaZrO<sub>3</sub> were

determined from the (110) diffraction peak after removal of instrumental broadening at  $30^\circ 2\theta$ .

The software fitted separate peak profiles to each (hkl) reflection of measured XRD patterns taking into account the  $K\alpha_1$  and  $K\alpha_2$  components of the incident radiation (with the  $K\alpha_1 : K\alpha_2$  intensity ratio set at 2:1). To maximise the quality of fitted profiles for the profile standard, peak profiles were refined individually for each reflection rather than simultaneously on all reflections. Rietveld asymmetry was also refined. Each refined reflection produced a fitted peak equivalent to monochromatic  $K\alpha_1$  radiation. Shadow has the capacity both to report fitted peak profiles data (e.g. peak position, intensities, two theta position, observed Gaussian and Lorentzian integral breadth ( $B_{hL}$  and  $B_{hG}$ ) etc.) as well as being able to fit curves to profile shape parameters as a function of  $2\theta$  or  $\tan(\theta)$ . The curve fitting functions for shape parameters (e.g.  $B_{hL}$  and  $B_{hG}$ ) allow parameterisation of instrument profiles using the standard Caglioti function (U,V,W) and also with a modified Caglioti function which can have up to two additional  $\cot(\theta)$  dependent terms if necessary (*Shadow: A system for X-ray Powder Diffraction Pattern Analysis* 1998, p. 114-5). A  $\cot(\theta)$  term was included because the standard Caglioti function was not adequate to describe the instrument profile, particularly at theta values of most interest to broadening analysis ( $\sim 30^\circ 2\theta$ ). Furthermore, the modified Caglioti function of the instrument profile was "intensity - weighted", that is, weighted according to the relative intensity of fitted  $LaB_6$  peaks in order to minimise random error contributions from peaks of very low intensity, although the use of intensity weighting was most significant at high  $2\theta$  angles. The best estimate of the instrument function was therefore taken as an intensity weighted modified Cagliotti fit of  $B_{gL}$  and  $B_{gG}$  as a function of  $\tan(\theta)$  using one  $\cot(\theta)$  dependent term. The use of a fitted curve to calculate the instrument profile at any required two - theta point provided the most reliable results by minimising random errors from fitting uncertainties for individual peaks, particularly since the fitted curve was intensity weighted.

Specimen - only integral breadths were deconvoluted from observed integral breadths according to:

$$\begin{aligned}\beta_{fL} &= \beta_{hL} - \beta_{gL} \\ (\beta_{fG})^2 &= (\beta_{hG})^2 - (\beta_{gG})^2\end{aligned}$$

where  $\beta_{fL}$ ,  $\beta_{hL}$  and  $\beta_{gL}$  refer to the specimen - only, observed, and instrument - only Lorentzian integral breadths, and  $\beta_{fG}$ ,  $\beta_{hG}$  and  $\beta_{gG}$  refer to the specimen - only, observed, and instrument - only Gaussian integral breadths, respectively.

An average crystallite size,  $D$ , was calculated assuming

$$\beta_{fL} = \frac{\lambda}{D \cos(\theta)} \quad (\text{where } \beta_{fL} \text{ is in radians}) \quad (4.2)$$

Root - mean - square (RMS) non - uniform strain,  $\epsilon$ , can be calculated assuming

$$\beta_{fG} = 4 \epsilon \tan \theta \quad (\text{where } \beta_{fG} \text{ is in radians}) \quad (4.3)$$

Uncertainties were calculated by combining estimated standard deviations provided by Shadow for BaZrO<sub>3</sub> and LaB<sub>6</sub> samples.

### ***Crystallite size and particle size considerations***

It is important to consider what attributes of particle size were of importance to the project, and therefore which need to be considered and if necessary, measured. Primary particle size is important to processing properties, because primary particle size provides the dominant contribution to specific surface area, and therefore the surface energy driving solid state densification during sintering. Hard agglomerates are clusters of primary particles which are not broken up during milling operations and persist in the formed green article, causing increased green porosity and green pore size leading to sintering difficulties. Soft agglomerates are clusters of primary particles due to poor dispersion of primary particles during analysis, for example in TEM analysis or laser diffraction particle size measurement, but do not cause problems in particle packing and therefore are not of great importance to processing properties. Soft agglomerates are not necessarily an intrinsic property of the powder but a consequence of the state of dispersion. Primary particle size and hard agglomerate size were therefore the aspects of particle size important to this project.

It was necessary to consider how to measure all three types of sizes, and in particular, how to differentiate between hard and soft agglomerates. Laser diffraction analysis of specimens dispersed in a fluid typically treats agglomerates as single particles, and size distributions include contributions from agglomerates and dispersed primary particles. Differentiating the contribution of primary particles, soft agglomerates and hard agglomerates requires a degree of interpretation. If a specimen is measured in what is regarded as a well dispersed state, in which agglomeration is caused by strong particle bonding and not by poor dispersion, agglomerates could be interpreted as hard agglomerates. However, this requires a judgment about the magnitude of dispersion problems during measurement. In these experiments, there was not sufficient evidence to discount dispersion problems during measurement at the scale of primary particles, and hence quantitative conclusions on the hard agglomeration state of powders could not be made.

XRD crystallite size can be determined largely independently of agglomeration state, particularly if strain contributions to peak broadening can be separated. Crystallite size is the correct term to describe the structural unit contributing to size broadening. Broadening analysis fundamentally provides a measurement of crystallite size, which can only be converted to particle size if the number of crystallites per particle is known. Primary particle size was readily observed by TEM. XRD crystallite size results closely and consistently agreed with primary particle sizes observation by TEM, for a large number of samples over a wide range of sizes. XRD crystallite size was therefore considered equivalent to primary particle size.

The benefit of XRD primary particle size estimates over TEM analysis was a much larger sampling volume and a faster and more cost effective measurement. XRD provided a simple and routine method of quantitative analysis while avoiding dependence on quantitative microscopy, in which image analysis methods have significant problems in analysing poorly dispersed specimens.

The range of measurement by broadening analysis, approximately 35 - 500 nm, conveniently covered the range of crystallite sizes encountered throughout the project. From Equation 4.1, the experimental error of crystallite size estimates increases as the

magnitude of size broadening decreases, and the method was only able to provide size estimates up to  $\sim 500$  nm with acceptable precision, above which specimen broadening was too small to resolve from the instrument profile. However, it was quite clear from TEM analysis that this very simple approach consistently provided primary particle size estimates quite adequate for process development, control and optimisation.

#### **4.8.2 Quantitative BaCO<sub>3</sub> determination by XRD**

To optimise powder processing methods and ceramic performance, it was critically important to be able to assess their phase purity, ideally by quantitative methods. Previous researchers limited their assessment of powder processing to measurement of weight loss due to CO<sub>2</sub> liberation during calcination, or basic laboratory XRD methods often stating samples that appear “phase pure” by XRD but without quantification of detection limits.

The procedure used for quantitative XRD analysis was based on the method of standard additions (Jenkins and Snyder 1996, pp. 369 - 70). A sample of reasonably pure BaZrO<sub>3</sub> was prepared by solid - state synthesis from BaCO<sub>3</sub> and ZrO<sub>2</sub> in a mole ratio of  $1.008 \pm 0.002$  using three repeated calcinations at 1300 °C with intermediate re - grinding. The method was derived for quantitative analysis by spiking and does not require a phase pure powder for preparation of standards. Empirical standards were made by addition of BaCO<sub>3</sub> powder ( $> 99$  wt.%) to the BaZrO<sub>3</sub> in known amounts up to 14 wt.%. Samples were analysed on a Siemens D500 using a step size of  $0.04^\circ 2\theta$  and  $0.3^\circ 2\theta/\text{minute}$  scan rate with all other instrument parameters as above. Data was acquired over at least the range  $20 - 35^\circ 2\theta$ . Calibration and measurement of BaCO<sub>3</sub> was carried out using the ratio of the net areas of the BaCO<sub>3</sub> and BaZrO<sub>3</sub> peaks at  $24^\circ 2\theta$  and  $30^\circ 2\theta$  respectively. The background was estimated by fitting a quadratic function through points between  $20.00 - 20.50$ ,  $21.80 - 23.00$ ,  $25.00 - 26.50$ , and  $32.50 - 33.00^\circ 2\theta$ . Peak areas were determined between  $23.00 - 25.00^\circ 2\theta$  for BaCO<sub>3</sub> and  $28.00 - 32.00^\circ 2\theta$  for BaZrO<sub>3</sub>. Curve fitting and calculations were conducted using a spreadsheet.

The methods allowed determination of the amount of BaCO<sub>3</sub> in the original powder from which the standards were prepared, and therefore the absolute BaCO<sub>3</sub>



content of standards and unknowns. Detection limits were calculated as three standard deviations of the counting error of the net peak intensity, which includes contribution from counting errors of both background and raw peak areas. Counting and curve fitting errors in background intensities have an important effect on detection limits, so specimens must be presented to the diffraction equipment in such a way as to minimise background intensity. Glass capillaries may be used to prevent air exposure during analysis but substantially increase relative background intensities and provide poor detection limits relative to flat plate powder diffraction.

#### **4.9 Estimation of Ba - rich phase impurities by ICP - MS analysis of supernatant solutions**

It was observed that a sintered sample with a bulk Ba : (Zr + Hf) mole ratio of 1.025 disintegrated within hours of submersion in water. A qualitative test of the supernatant solution with sulphuric acid indicated substantial dissolved barium levels. All samples whose Ba : (Zr + Hf) mole ratio was less than  $\sim 1.005$  were not observably affected by water submersion, even for extended periods of up to at least a year. It was hypothesised that barium - rich secondary phases are water soluble, or more specifically, substantially more water soluble than  $\text{BaZrO}_3$ . This hypothesis was used to attempt a prospective method to determine phase purity from analysis of dilute HCl supernatant solution. Acidic conditions were used to assist retention of dissolved zirconium because neutral or alkaline conditions are considerably more likely to cause precipitation of zirconium as its hydroxide.

Sintered ceramic samples with bulk Ba : (Zr + Hf) mole ratios between 0.965 and 1.010 (determined by XRF) were ground in a  $\text{ZrO}_2$  ring mill for 1 minute, then 1.000 g of ground powder was added to 110.0 mL of 0.1 M HCl. Slurries were allowed to react for 24 hours with regular vigorous agitation, centrifuged at high speed to maximize the efficiency of particle/supernatant separation, then diluted 100-fold. These solutions and a blank were submitted for barium and zirconium determination by ICP-MS. The undiluted supernatant had a very slight but observable turbidity, indicating it contained a low level of particulate material which could not be removed centrifugally.

## 4.10 Experimental method for solid-state processing development

### 4.10.1 Preliminary experiment

$\text{BaCO}_3$  (Fluka, > 99%, Catalog No. 11729) was assayed using the barium assay procedure in Section 4.1.1 and  $\text{ZrO}_2$  (Z-Tech SF-Ultra > 99.5%) was estimated by measuring its loss on ignition (LOI) for one hour at 1100 °C and assuming the residue was pure Hf/ $\text{ZrO}_2$ .  $\text{BaCO}_3$  (assayed at  $99.58 \pm 0.02$  %) and  $\text{ZrO}_2$  (LOI =  $1.20 \pm 0.02$  %, effective mole weight correcting for Hf content  $124.25 \text{ gmol}^{-1}$ ) were weighed and mixed using a  $\text{ZrO}_2$  ring mill in ethanol for five minutes, to yield approximately 50 g of  $\text{BaZrO}_3$  with a Ba : (Zr + Hf) mole ratio of  $0.996 \pm 0.002$ . The ethanol was then evaporated in an oven at 75 °C, then the sample was divided into representative portions, loaded into stabilised zirconia crucibles, and put through a series of calcination and regrinding protocols as shown in Figure 4.1. Calcination was conducted in still air inside a molybdenum disilicide resistance muffle furnace. Heating and cooling rates of 5 °C/minute were used, as close to the maximum which could be sustained by the zirconia crucibles without undue thermal shock problems. The aim of this experiment was to establish a basic solid state processing method, investigate effects of regrinding between calcination stages, and establish useful calcination times. One aspect of the experiment was to determine if the packing density of the powder could influence solid state reaction products: samples prepared for initial calcination were either loosely packed or firmly compacted by hand into crucibles and compared after calcination under identical conditions.

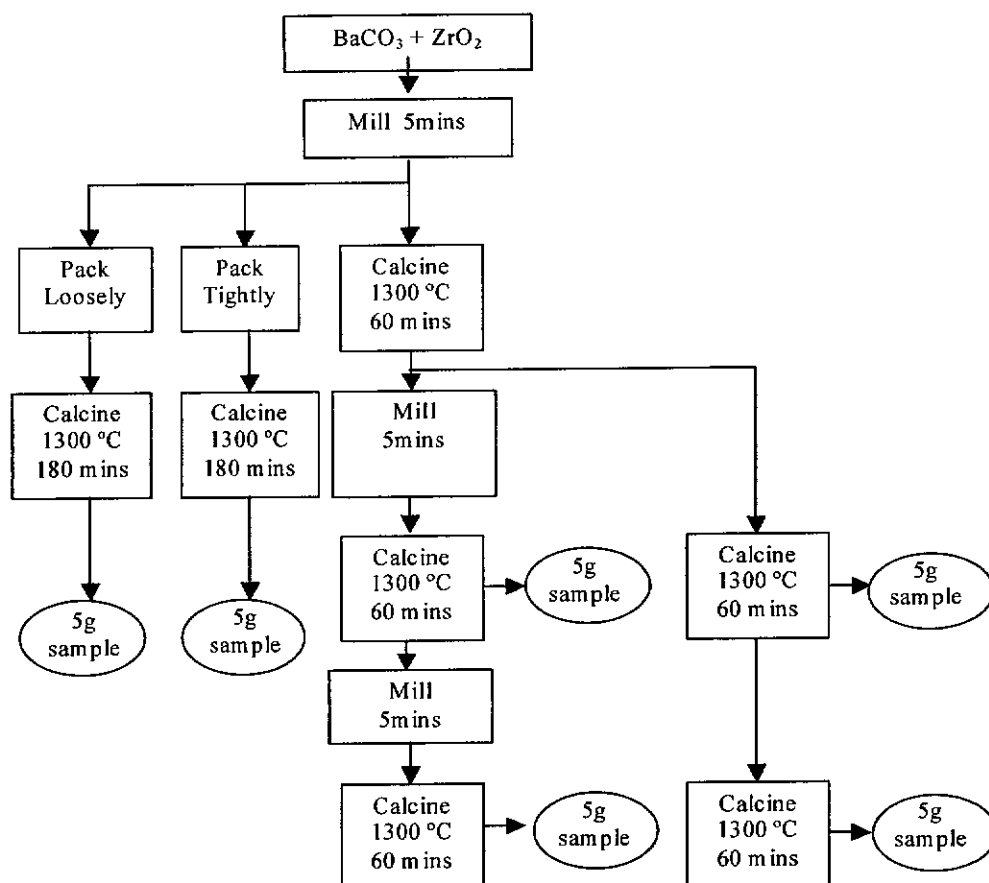


Figure 4.1 Flow chart of solid - state powder processing development experiment.

Samples were analysed by XRD to determine secondary phases and primary particle size using the methods described in Section 4.6. XRD analysis was also conducted on selected samples after exposure to air for at least 24 hours to detect barium rich phases that were undetectable immediately after calcination, but which formed barium carbonate after air exposure as described in Section 4.6.5. Selected samples were also studied by TEM.

#### 4.10.2 Solid -state processing - experiment two

Once the preliminary experiment had been completed and the basic processing routine established, a second series of experiments was conducted to optimise product stoichiometry. This experiment investigated the effects of stoichiometry on processing properties of powders and characteristics of sintered ceramics. Samples were prepared from BaCO<sub>3</sub> and ZrO<sub>2</sub> weighed at different ratios to produce powders and ceramics with Ba : (Zr + Hf) mole ratios between 0.945 and 1.025.

The powder process sequence for this experiment was:

1. five minutes ring milling of  $\text{BaCO}_3$  and  $\text{ZrO}_2$  reagents in 99.8% ethanol
2. calcination at 1200 °C for 5 hours
3. five minutes regrinding in 99.8% ethanol
4. calcination at 1300 °C for 3 hours
5. five minutes regrinding in 99.8% ethanol
6. calcination at 1300 °C for 1 hour
7. five minutes regrinding in 99.8% ethanol.

Finished powders with nominal mole ratios between 0.965 and 1.010 were uniaxially pressed at 150 MPa into circular pellets without addition of lubricants. The pellets were sintered in air using a furnace cycle comprising heating at 200 °C/hr to 450 °C, 60 minutes isothermal at 450 °C, heating at 300 °C/hr to 1700 °C, 6 hours isothermal at 1700 °C, then cooling to ambient temperature at 360 °C/hr. To avoid reaction with furnaceware at such elevated temperatures, all samples were raised above the furnaceware by a 3 mm thick layer of  $\text{BaZrO}_3$  powder and/or a 3 mm thick pre-sintered disk of  $\text{BaZrO}_3$ .

Powders were analysed by XRF, XRD, BET  $\text{N}_2$  adsorption and TEM, and sintered pellets were analysed using optical microscopy using a Nikon ME600 microscope.

#### **4.10.3 Sintered crucible production**

Sintered crucibles were produced using powders with Ba : (Zr + Hf) mole ratios of 0.961 - 1.025. Powders were prepared using the protocol described in Section 4.8.2, with the following alterations to maximise the phase purity achieved in the samples:

- the initial calcination severity was increased by increasing the temperature to 1300 °C for three hours, and
- typical milling times were extended to approximately twenty minutes.

Fully calcined powders were lubricated with 2.5 to 3.0 wt.% cetyl alcohol and pressed into green crucibles as described in Section 4.12.

## 4.11 Solution processing development

### 4.11.1 Reagents used

- zirconium oxychloride, Millennium Performance Chemicals, Rockingham, Western Australia, gravimetric assay 36.8 wt.%  $\text{ZrO}_2 + \text{HfO}_2$
- $\text{ZrOCl}_2 \cdot 8\text{H}_2\text{O}$ , Riedel - de Haën 99.5%+
- $\text{BaCl}_2 \cdot 2\text{H}_2\text{O}$ , AR - grade, Sigma Chemicals, Balcatta, Western Australia
- oxalic acid dihydrate, AR - grade, Sigma Chemicals, Balcatta, Western Australia
- $\text{Ba}(\text{CH}_3\text{COO})_2$ , Riedel - de Haën 99%+, gravimetric assay 99.46 wt. %
- $(\text{NH}_4)_2\text{C}_2\text{O}_4 \cdot \text{H}_2\text{O}$ , Riedel - de Haën 99.5%+

### 4.11.2 Barium chloride, zirconyl chloride, oxalic acid system

#### *Preliminary experiments*

Preliminary experiments were performed following the method of Reddy and Mehrotra (1979) in which “equimolar (0.5 M each) aqueous solutions of barium chloride and zirconium oxychloride were added to the hot solution of oxalic acid (1.0 M) which was 10% in excess”. In the current study, solutions of approximately 0.5 M  $\text{BaCl}_2$ , 0.5 M zirconium oxychloride and 1 M oxalic acid were mixed using different orders of addition at temperatures of 80 to 95 °C at solution mole ratios of 1.00:1:2.20 Ba:[Zr+Hf]: $\text{C}_2\text{O}_4$ . The precipitate was stirred at constant temperature for 30 minutes, cooled to ambient temperature, filtered using Whatman #6 filter paper, washed with deionised water and dried at 120 °C. The dried precipitate was calcined in yttria-stabilised  $\text{ZrO}_2$  crucibles in air at 1150 °C.

#### *Optimisation of oxalate excess in barium chloride, zirconyl chloride, oxalic acid system*

Results from preliminary experiments presented below showed that a severely barium deficient product was produced at solution mole ratios of 1.00 : 1 : 2.20 Ba : Zr :  $\text{C}_2\text{O}_4$ . A second series of experiments was performed to investigate the use of additional oxalic acid with a fixed 1.00:1 Ba:Zr solution mole ratio, at both 25 ° and 95 °C. A freshly prepared equimolar solution of zirconium oxychloride (0.25 M) and

barium chloride (0.25 M) solution was added dropwise to 1 M oxalic acid solution maintained at 95 °C under constant stirring. The volume of oxalic acid used was varied to study the above system with solution mole ratios of Ba : (Zr+Hf) : C<sub>2</sub>O<sub>4</sub> over the range 1.00 : 1 : 2.50 to 1.00 : 1 : 3.00. The slurries were cooled to ambient temperature, filtered using Whatman #6 filter paper, washed twice with de - ionised water, dried at 100 °C in air, and calcined in air at 1000 °C for two hours. For comparison, the same procedure was used to confirm whether similar results would be obtained using Riedel de Haën ZrOCl<sub>2</sub>.8H<sub>2</sub>O over the solution mole ratio range 1.00 : 1 : 2.20 - 2.60. Precipitation was also studied at 25 °C for Millennium zirconium oxychloride over the range 1.00 : 1 : 2.20 - 2.80. The effect of rapid addition of mixed barium zirconium solution to oxalic acid at 95 °C at a solution Ba : (Zr+Hf) : C<sub>2</sub>O<sub>4</sub> mole ratio of 1.00 : 1 : 2.60 was also studied.

#### **4.11.3 Barium acetate, zirconyl chloride, ammonium oxalate system**

The effect of variation of solution oxalate content on product stoichiometry was investigated for the barium acetate, zirconium oxychloride and ammonium oxalate system over the mole ratio range of 2.00 : 1 : 2.00 - 3.00 respectively. Zirconium oxychloride and ammonium oxalate solutions were mixed until a clear solution was formed at 25 °C (0.075 M Zr, ~0.15 M NH<sub>4</sub>C<sub>2</sub>O<sub>4</sub>), then 0.25 M barium acetate was added rapidly at ambient temperature under vigorous stirring. The slurry was stirred for 90 minutes then the precipitate was filtered using Whatman #6 filter paper, washed twice in de - ionised water, dried at 100 °C and calcined in air between 1000 and 1500 °C. The same procedure was used for solution mole ratios 1.027 : 1 : 2.4 and 1.027 : 1 : 3.00.

#### **4.12 Crucible forming processes**

Finished powders were formed into green crucibles either using slip casting or cold isostatic pressing (CIP). For crucibles formed by CIP, calcined powders were ring milled in a solution of cetyl alcohol in ethanol for a period of between five and twenty five minutes, then dried at 140 °C. Cetyl alcohol was fully dissolved in ethanol before addition to the powder, and added between 1 and 3 wt.% of the powder. A controlled amount of ethanol was used to produce a flowable paste after milling, but not a dilute fluid which risked settling out of the solid and segregation of the lubricant after drying. The mass of ethanol used was typically 80 % of the mass of dry powder and never larger than 100 %. The lubricated powder was lightly ground in a mortar and pestle then packed into a mould comprising a stainless steel inner mandrel, a flexible plasticised PVC outer case, and a rubber stopper positioned after powder filling and steel hose clamps used to close the ends of the mould. Isostatic pressing was conducted for 60 seconds at 140 or 200 MPa with controlled compression and decompression rates. The green body was removed from the mould and hand fettled using SiC papers to radius external and internal corners.

#### **4.13 Corrosion resistance testing**

The corrosion resistance of sintered crucibles during YBCO single crystal growth was evaluated by isothermal exposure at 1000 - 1050 °C. Seven millilitre crucibles were filled with a mixture of  $Y_2O_3$ ,  $BaCO_3$  and  $CuO$  in a mole ratio of 1 : 32 : 90 respectively, packing as much powder into the crucibles as possible. Crucibles were heated to 1000 - 1050 °C and held isothermally in air in a muffle furnace, with the rate of leakage observed visually.

Inspection of the outer surface of crucibles required the door of the muffle furnace to be opened briefly. To check the level of the melt inside crucibles required them to be picked up using pre - heated steel tongs and removed from the furnace for a few seconds. Thermal shock during inspection of crucibles was observed to degrade their performance, because in almost all cases, the initial sign of any leakage of melt was observed at the front facing surface, where thermal shock was most severe.

## CHAPTER 5

### BaZrO<sub>3</sub> PROCESSING DEVELOPMENT

---

#### 5.1 Introduction

The aim of the work presented in this chapter was to design effective fabrication methods for high quality crucibles using solid-state and oxalate derived powders. The purpose of developing oxalate precursor processes was to attempt to improve the quality of ceramics through the potential benefits of solution based processing. Each complete process required optimisation of powder processing, green forming and sintering stages. Powder processing required control over the effects of calcination time, calcination temperature, regrinding between repeated calcination (intermediate regrinding) and stoichiometry. Forming and sintering processes were optimised with respect to the physical and chemical properties of powders.

As with any experimental study, the quality of conclusions drawn depend on the quality of measurements and interpretation of results. This chapter describes attempts to overcome the significant experimental difficulties encountered in the BaZrO<sub>3</sub> system, and detailed explanation of steps taken to verify the interpretation of key measurements made in this study.

#### 5.2 Solid-state powder processing

##### 5.2.1 Phase purity control

The phase purity of solid-state derived materials has been reported to be limited by solid-state reaction kinetics. Powder process development was focussed on optimisation of phase purity and methods for its assessment.

Unfortunately XRD has poor sensitivity to directly observe nearly all of the secondary phases most likely to occur in BaZrO<sub>3</sub> including ZrO<sub>2</sub>, Ba<sub>2</sub>ZrO<sub>4</sub>, Ba<sub>3</sub>Zr<sub>2</sub>O<sub>7</sub> and BaO. Detection limits for these phases were totally inadequate for directly assessing the phase purity of processed powder samples after a single calcination treatment. Poor sensitivity to secondary phases was due to severe peak overlap with BaZrO<sub>3</sub>, low diffraction intensities of secondary phases relative to BaZrO<sub>3</sub> (partly due to lower crystal symmetry), and reduced peak definition due to crystallite size



broadening. Crystallite size broadening (cf. Section 4.8.1) was expected for unreacted  $\text{ZrO}_2$  according to the shrinking-core model of solid-state reaction proposed by Ubaldini *et al.* (2003). The initial crystallite size of the  $\text{ZrO}_2$  reagent was  $\sim 50$  nm, and it would have been reduced to such a small size after extensive solid state reaction that size broadening would severely reduce XRD sensitivity to  $\text{ZrO}_2$ . For example, from geometry one can readily calculate that the average  $\text{ZrO}_2$  particle size would be reduced from its initial size of 50 nm to less than 10 nm after 99% completion of the solid-state reaction. The particle size distribution of  $\text{ZrO}_2$  starting reagent may be critical to the quality of  $\text{BaZrO}_3$  produced by solid-state reaction. A critical  $\text{ZrO}_2$  particle size will exist above which restricted solid-state reaction kinetics will prevent their removal. This project benefited from close collaboration with one of the leading international  $\text{ZrO}_2$  manufacturers (Millennium Performance Chemicals), whose production process is able to control particle size distributions.

The challenge of XRD analysis was to extract useful information on powder phase purity despite low sensitivity to  $\text{ZrO}_2$ ,  $\text{Ba}_2\text{ZrO}_4$ ,  $\text{Ba}_3\text{Zr}_2\text{O}_7$  and  $\text{BaO}$ . The only impurity phase in processed powders detectable by XRD was  $\text{BaCO}_3$ . Some researchers suggest that detection of  $\text{BaCO}_3$  indicates phase impurity (Robertz *et al.* 2001; Taglieri *et al.* 1999).  $\text{BaCO}_3$  is obviously not  $\text{BaZrO}_3$  and hence detection of  $\text{BaCO}_3$  by definition indicates less than 100%  $\text{BaZrO}_3$  in the specimen at the time of measurement. The most intense diffraction peak of  $\text{BaCO}_3$  is sufficiently well resolved from those of other relevant phases (with the important exception of monoclinic  $\text{ZrO}_2$ ) to allow useful phase identification and quantification by XRD as described in Section 6.3.1. Positions of diffraction peaks are given in Appendix 2.

Low XRD sensitivity to  $\text{ZrO}_2$  assisted quantitative determination of  $\text{BaCO}_3$ . The most intense  $\text{BaCO}_3$  peak used for quantitative analysis at  $\sim 24^\circ 2\theta$  is overlapped by the minor (110) and (011) diffraction peaks of monoclinic  $\text{ZrO}_2$ . Without substantial preferred orientation of  $\text{ZrO}_2$ , the contribution of  $\text{ZrO}_2$  to the  $\text{BaCO}_3$  peak is negligible if the much more intense ( $\bar{1}11$ ) peak is below detection. The  $\text{ZrO}_2$  ( $\bar{1}11$ ) peak was not observed in any of the diffraction patterns used for quantitative  $\text{BaCO}_3$  analysis except where explicitly stated.

Figure 5.1 compares  $\text{BaCO}_3$  levels for various processing routes, for samples analysed immediately after calcination and also after exposure to air.  $\text{BaCO}_3$  was detected at low levels in all samples produced without intermediate re-grinding. Increasing calcination time above one hour had little impact on the apparent completion of the solid-state reaction, particularly if judged on XRD analysis immediately after calcination. The apparent improvement of solid-state reaction kinetics due to intermediate regrinding might be explained by the shrinking core model proposed by Ubaldini *et al.* (2003). The reaction kinetics are controlled by poor diffusion kinetics of reactants through  $\text{BaZrO}_3$  that grows on the surface of  $\text{ZrO}_2$  particles during reaction. These results suggest that mechanical milling was effective in exposing unreacted  $\text{ZrO}_2$  to subsequent reaction in the next calcination treatment, thereby significantly improving reaction kinetics in each subsequent calcination. Irrespective of the actual mechanism of this effect, all solid-state derived powders used for crucible fabrication in this project were calcined three times with intermediate regrinding to maximise the apparent phase purity of powders. No statistically significant  $\text{BaCO}_3$  peaks were detected after two and three calcinations with intermediate re-grinding for samples immediately after calcination (Figure 5.1).

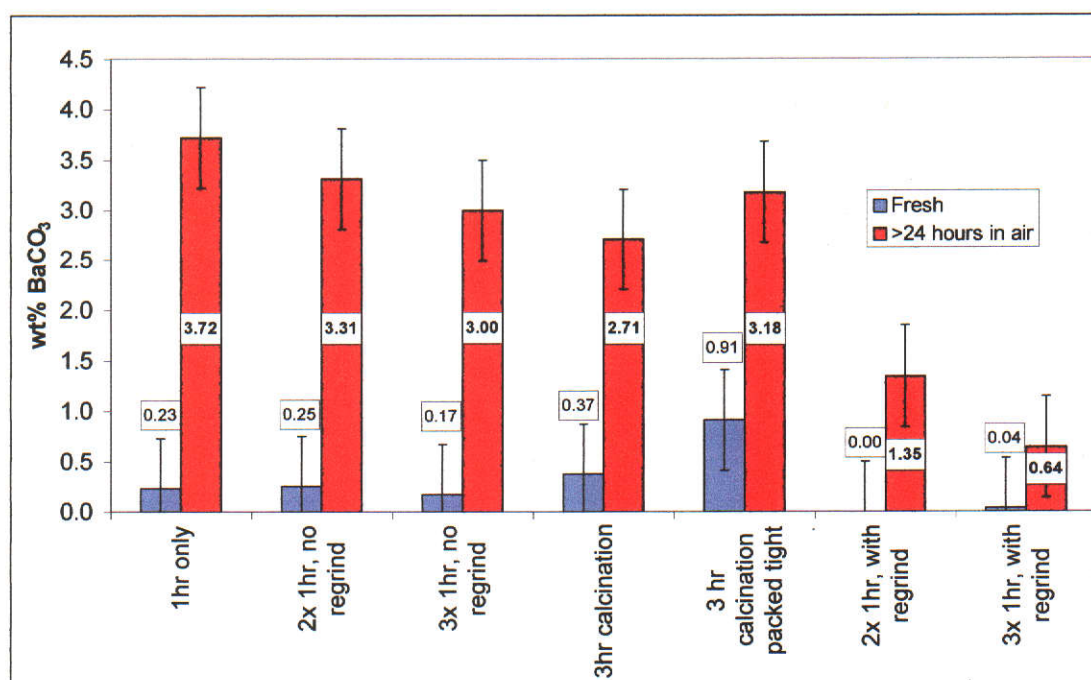


Figure 5.1 The effect of powder processing conditions on  $\text{BaCO}_3$  levels for solid-state derived powders calcined at 1300 °C. Powders were analysed by XRD directly after calcination and after >24 hours exposure to air. Uncertainties are  $\pm 2$  standard errors.

It was noticed that samples which had initially shown no detectable secondary phases after calcination showed detectable  $\text{BaCO}_3$  within a few hours exposure to air (Figure 5.2). This was more pronounced for samples likely to contain barium-rich phases such as those with  $\text{Ba} : (\text{Zr} + \text{Hf})$  mole ratios higher than one, or with poorly completed solid-state reactions. The intensity of  $\text{BaCO}_3$  peaks observed in powders after processing increased with duration of air exposure, reaching a maximum within approximately 24 hours and without further increase over eight weeks. Specimens expected to have very low or perhaps no barium-rich secondary phases displayed much less increase in  $\text{BaCO}_3$  diffraction intensity, such as the Zr-rich sample produced using an extended calcination procedure as shown in Figure 5.3. These initial observations suggested there was a relationship between  $\text{BaCO}_3$  levels after air exposure and phase purity of powders. The quantitative XRD test for  $\text{BaCO}_3$  was developed partly to try to exploit the observed large increase in possible sensitivity to barium-rich secondary phases by air exposure, and thereby provide a more sensitive though indirect means of assessing phase purity.  $\text{BaCO}_3$  is often the only impurity phase which can be detected by XRD, and has been considered by some researchers as an indicator of phase purity of  $\text{BaZrO}_3$ , particularly during powder processing (Robertz *et al.* 2001; Taglieri *et al.* 1999).

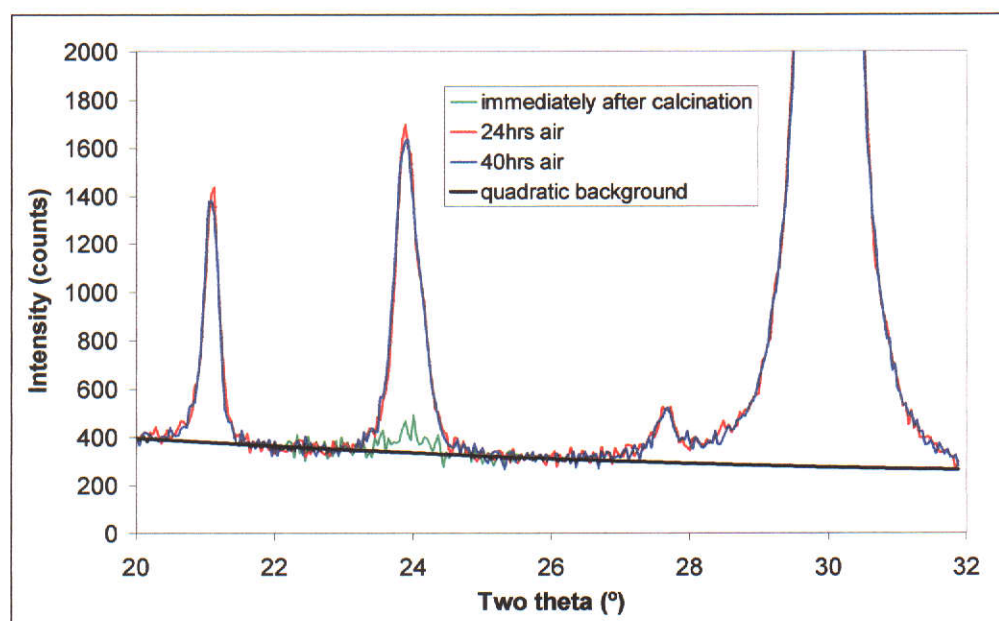


Figure 5.2 Effect of air exposure on barium carbonate peak ( $24^\circ$ ) for solid-state derived powder produced by single calcination at  $1300^\circ\text{C}$  for one hour with  $\text{Ba} : (\text{Zr} + \text{Hf})$  mole ratio of 0.995. Height of the most intense  $\text{BaZrO}_3$  peak at  $30.00^\circ 2\theta$  (not shown) was 75 000 counts.



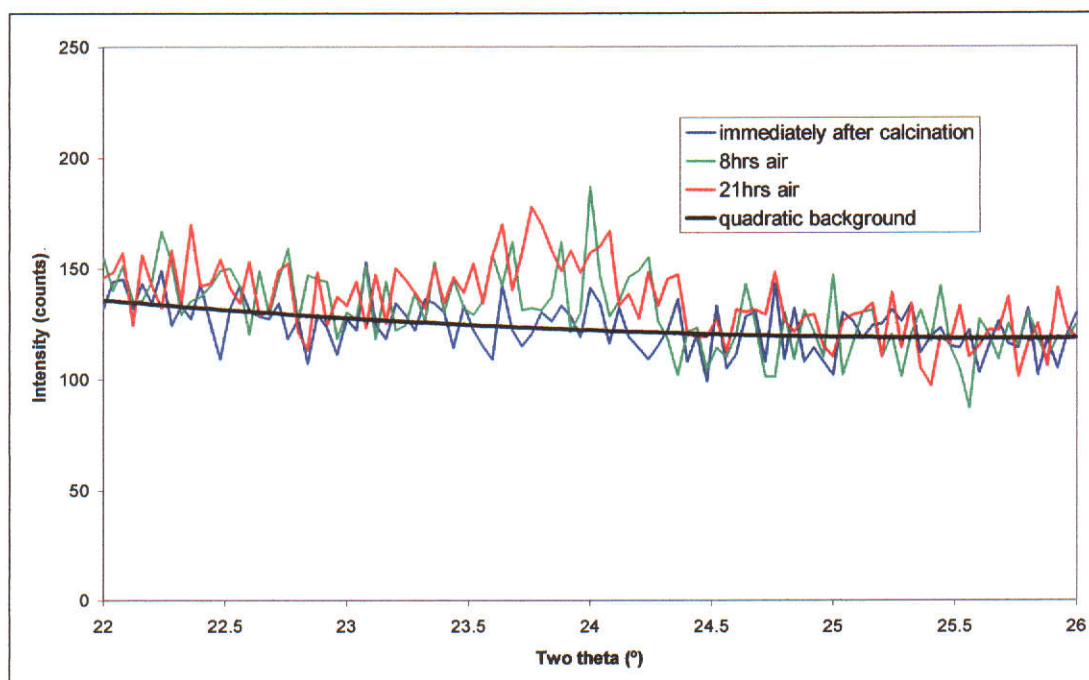


Figure 5.3 Effect of air exposure on barium carbonate peak (24 °) in solid-state derived powder produced by triple calcination at 1300 °C followed by single calcination at 1420 °C with intermediate re-grinding between all calcinations, with a Ba : (Zr + Hf) mole ratio of 0.987. Height of the most intense BaZrO<sub>3</sub> peak at 30.00 °2θ (not shown) was 52 000 counts.

The amount of BaCO<sub>3</sub> increased substantially after exposure to air in all samples as shown in Figure 5.1, with the greatest increase for samples prepared without intermediate re-grinding. Intermediate re-grinding reduced the amount of BaCO<sub>3</sub> detected after air exposure by a factor of approximately 4.5. Figure 5.1 suggests intermediate re-grinding was effective in improving the extent of solid-state reaction. This conclusion is consistent with those of Erb, Walker and Flükiger (1995) and Liang, Bonn and Hardy (1998) albeit based on different methods of assessment.

### 5.2.2 Interpretation of BaCO<sub>3</sub> levels

There are substantial difficulties in assessing the phase purity of BaZrO<sub>3</sub> through BaCO<sub>3</sub> levels. Accurate quantitative analysis of phase impurity levels in BaZrO<sub>3</sub> based on BaCO<sub>3</sub> measurement after air exposure requires knowledge of the phase(s) from which BaCO<sub>3</sub> formed. The possible Ba-rich phases such as BaO, Ba<sub>2</sub>ZrO<sub>4</sub> or Ba<sub>3</sub>Zr<sub>2</sub>O<sub>7</sub> have different ratios of reactant to BaCO<sub>3</sub> produced, and because none of them can be adequately detected directly by XRD, the total mass

fraction of Ba-rich phases may be difficult to determine with any certainty. An estimate might be attempted assuming that  $\text{Ba}_2\text{ZrO}_4$  is the most likely Ba-rich phase near the completion of the solid-state reaction (it is the equilibrium secondary phase close to unity Ba : (Zr + Hf) mole ratio) combined with an independent measure of bulk stoichiometry, for example by XRF, to calculate residual  $\text{ZrO}_2$  by mass balance.

Estimation of phase purity by  $\text{BaCO}_3$  analysis also requires confirmation that  $\text{BaZrO}_3$  does not react with air to produce  $\text{BaCO}_3$ . In principle, this could be directly achieved using fine  $\text{BaZrO}_3$  powder with an abundance of Ba-rich phases too low to produce observable  $\text{BaCO}_3$  after air exposure, and therefore any observed  $\text{BaCO}_3$  must be due only to  $\text{BaZrO}_3$ . In practice this was not possible. With no means of measuring the abundance of trace Ba-rich phases, one cannot assume  $\text{BaCO}_3$  observed after air exposure is solely due to barium-rich phases. Making  $\text{BaZrO}_3$  completely free of Ba-rich residual phases by solid-state powder synthesis is made difficult by kinetic limitations of the solid-state reaction. The kinetics of barium consumption can be improved by synthesis with an excess of  $\text{ZrO}_2$ , but  $\text{BaCO}_3$  detection by XRD is compromised because of overlap by  $\text{ZrO}_2$  peaks.  $\text{ZrO}_2$  peak overlap in powders near completion of the solid-state reaction was often negligible as discussed in Section 6.3.1. However, this was not the case for samples made with a large excess (e.g. 10 - 20%) of  $\text{ZrO}_2$  added to avoid residual barium-rich secondary phases. In summary, it was not possible to produce  $\text{BaZrO}_3$  powders definitely free of Ba-rich phases by using an excess of  $\text{ZrO}_2$ , without interfering with  $\text{BaCO}_3$  determination by XRD because of peak overlap. An experimental approximation or alternative procedure was required.

Investigation of the effects of grinding time, air exposure and regrinding on the level of  $\text{BaCO}_3$  provided an empirical solution to the problem of  $\text{BaCO}_3$  interpretation which avoided dependence on access to completely phase pure samples. A specimen of  $\text{BaZrO}_3$  with high (although undetermined) phase purity was made by three repeated calcinations of  $\text{BaCO}_3$  and  $\text{ZrO}_2$  at 1300 °C at a mole ratio of 1.001 ( $\pm 0.002$ ) with intermediate regrinding followed by sintering to high density at 1700 °C for six hours. The sintered material was milled for between 20 seconds and 15 minutes in a  $\text{ZrO}_2$  ring mill, then exposed to air for 30 days to ensure complete



reaction. Samples were exposed over the same period of time to avoid potential effects of changes in relative humidity.  $\text{BaCO}_3$  levels measured by quantitative XRD analysis were compared to samples which were ring milled for 10 minutes followed by repeated two day air exposures with one minute intermediate regrinding. All specimens were divided from one sample to minimise sampling errors, and results were compared as a function of total grinding time. The concept behind this experiment was to determine whether brief repeated ring milling would expose fresh surfaces of  $\text{BaZrO}_3$  to carbonation and thereby increase  $\text{BaCO}_3$  levels, compared to samples ground for identical milling times where the reaction products inhibited further reaction of the  $\text{BaZrO}_3$ .

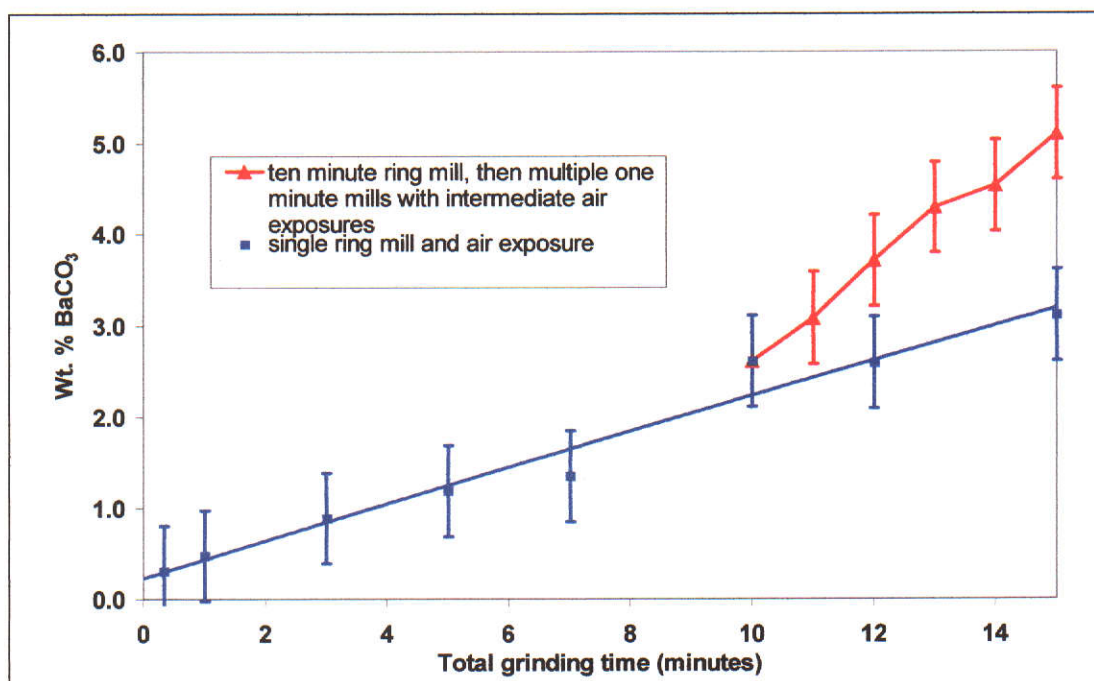


Figure 5.4 Interpretation of  $\text{BaCO}_3$  levels by investigation of milled sintered ceramic. Ba : (Zr + Hf) mole ratio =  $1.001 \pm 0.002$ . Uncertainties are  $\pm 2$  standard errors.

Figure 5.4 shows an increase in  $\text{BaCO}_3$  levels for powders repeatedly exposed to air between ring milling compared to those with a single exposure to air after equivalent total milling times. The results of this experiment are interpreted as confirming that  $\text{BaZrO}_3$  reacts with air to a limited extent to produce low levels of  $\text{BaCO}_3$ , and that repeated milling exposes fresh  $\text{BaZrO}_3$  surfaces for further reaction. There are several considerations supporting this conclusion. It is implausible that the

initial phase purity of the BaZrO<sub>3</sub> used in this experiment was sufficiently low to produce 5.0 wt.% BaCO<sub>3</sub> from Ba-rich secondary phases alone, given the Ba : (Zr + Hf) mole ratio of  $1.001 \pm 0.002$  and the extensive calcination/regrinding protocol and sintering treatment used to make the starting specimen. The powder used to produce the sintered ceramic produced  $2.0 \pm 0.5$  wt.% BaCO<sub>3</sub> after air exposure. The significant increase in phase purity due to sintering for six hours at 1700 °C means that any barium-rich phases present after sintering could only account for substantially less than 2.0 wt.% BaCO<sub>3</sub> after air exposure, whereas  $5.0 \pm 0.5$  wt.% BaCO<sub>3</sub> was observed after repeated grinding and air exposure, with no indication of the divergence between the curves in Figure 5.4 tailing off. The probability of observing five points in a row above the lower curve in Figure 5.4 due to random error is not statistically significant, and indicates a systematic change in BaCO<sub>3</sub> levels due to the change in sample treatment. Furthermore, repeated air exposure and regrinding was performed after the sample had already been milled for 10 minutes, and differences in surface areas of the two groups because of altered milling properties appears unlikely to account for the observed affect on BaCO<sub>3</sub> levels. The ring mill is able to reduce the particle size of the powder to less than the grain size of the sintered ceramic within about one minute, so all of the Ba-rich phases should be accessible to react well before fifteen minutes of ring milling. The sharp transition in crystallite size near the phase boundary (Figure 5.12) would be spread over a much wider range of Ba : (Zr + Hf) mole ratios or occur much further from the phase boundary, if the phase purity of processed powders or ceramics were low enough to account for BaCO<sub>3</sub> derived only from Ba-rich phases. Further data is presented in Section 6.3.2 showing the combined effects of phase impurity (due to bulk non-stoichiometry) and grinding time on BaCO<sub>3</sub> levels of milled sintered ceramics. The most plausible conclusion from this experiment is that BaZrO<sub>3</sub> is not inert in humid air. Robertz *et al.* (2001) observed this effect using infrared spectroscopy. Surface reaction of BaTiO<sub>3</sub> was reported by Hérard, Faivre and Lemaître (1995).

The mechanism of the apparent reaction between weak carbonic acid dissolved in adsorbed water films clearly must occur at particle surfaces. Dissolution of BaZrO<sub>3</sub> in HCl (Section 6.3.3) supports the hypothesis that it reacts with carbonic acid. The reactivities of Ba-rich phases are likely to be far higher than BaZrO<sub>3</sub> since

they are more alkaline and are readily attacked by water (Sections 4.9 and 6.3.3.). Although profile refinement instability did not allow accurate crystallite sizes to be measured from the overlapping (111) and (102) peaks,  $\text{BaCO}_3$  diffraction peaks were too narrow to arise from  $\text{BaCO}_3$  present as thin surface films, showing that barium diffuses from surface reaction sites and precipitates as larger crystals, possibly as a result of precipitation kinetics or surface energy minimisation. Investigation of details of this process, and the mechanism(s) which slow or terminate the reaction after a few days of air exposure are not clear and beyond the scope of this project, but may well be due to amorphous zirconium hydroxide surface films which do not migrate away from surface sites due to the very low solubility of zirconium hydroxides at neutral or alkaline pH. These surface zirconium hydroxide films (not detectable by XRD) may restrict further hydrolysis of  $\text{BaZrO}_3$  and therefore terminate the carbonation reaction.

The current results raise serious doubt that  $\text{BaCO}_3$  levels are purely an indicator of phase impurity. It is concluded that  $\text{BaCO}_3$  levels are a combined result of phase impurity, powder surface area and duration of air exposure. The results of this experiment showed that although quantitative XRD can determine the phase abundance of  $\text{BaCO}_3$ , it does not appear to provide an independent measurement of secondary phase impurity abundance for fine  $\text{BaZrO}_3$  powders at levels adequate for the current application. Apart from various potential barium-rich phase impurities,  $\text{BaCO}_3$  appears to form directly from  $\text{BaZrO}_3$  in amounts dependent on the powder surface area. Fine  $\text{BaZrO}_3$  powders appeared to inherently react with atmospheric  $\text{CO}_2$  at ambient humidity to form  $\text{BaCO}_3$ , and therefore detection of  $\text{BaCO}_3$  in a powder is not an independent measure of its phase purity but is convoluted with a surface area effect.

The relatively high surface areas achievable using the oxalate process, and all powders produced with an excess of barium make such powders prone to reaction with air after calcination. Reaction with air could be prevented by inert gas blanketing, but this was impractical during both powder processing and analysis on a



conventional diffractometer. The phase abundance of  $\text{BaCO}_3$  can be minimised (in some cases to below detection limits of laboratory XRD) by analysis of the powder after minimal exposure to humid air, i.e. removal of calcined powder while still hot and cooling to ambient temperature in a desiccator, followed immediately by XRD analysis. Powders with low surface area (such as due to  $\text{ZrO}_2$  excess and/or very high calcination temperatures) produced only very minor  $\text{BaCO}_3$  levels after air exposure. Storage of powder samples in screw-top bottles did not prevent air reaction, and hence it was impossible to re-analyse old samples in the later part of the project for fresh  $\text{BaCO}_3$  levels. Archiving of samples requires careful procedures not found in the literature and unknown until late in the project. It may be feasible to devise a method to correct for the surface area effect to allow accurate phase purity determination. However, a comprehensive attempt to develop a surface area correction was not attempted due to limited access to surface area instrumentation, and because of concerns over whether sufficiently low experimental uncertainties could have been achieved. In order to compare the relative phase purities achieved by each powder process, a comparison of  $\text{BaCO}_3$  levels after air exposure of oxalate and solid-state derived powders at equivalent Ba : (Zr + Hf) mole ratio as a function of surface area is presented in Section 5.9 despite the very limited amount of BET data available.

### **5.2.3 Solid-state powder processing: determination of calcination times**

Appropriate calcination times and heating/cooling rates required selection to achieve a suitable compromise between powder phase purity, particle size and agglomeration. Maximum heating and cooling rates were determined by the thermal shock resistance of the home-made ~ 100 – 200 mL fully stabilised Y- $\text{ZrO}_2$  crucibles used to contain powders during calcination. With a full load of powder these crucibles could reliably withstand heating and cooling rates of 5 °C/min, and any substantial increase in cooling rate lead to cracking problems. Selection of calcination times was more complicated and more ambiguous because of the combined effects of stoichiometry and regrinding on crystallite size.

As shown in Figure 5.5, intermediate regrinding had a significant effect on crystallite size at a fixed mole ratio (0.995), whereas an increase in initial calcination time from one to three hours caused only a moderate increase in crystallite size. The initial calcination time was chosen to be three hours as the slight increase in apparent phase purity (Figure 5.1) was considered to justify the moderate increase in crystallite size (Figure 5.5).

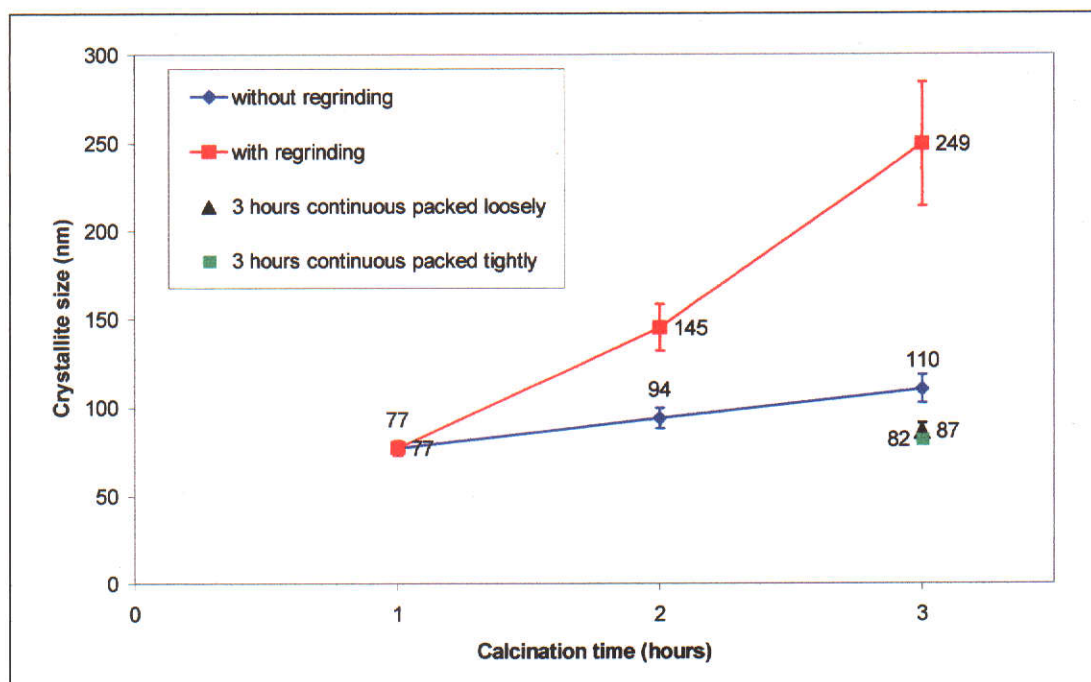


Figure 5.5 Effect of calcination time at 1300 °C on crystallite sizes of solid-state derived powders with Ba : (Zr + Hf) mole ratio of  $0.995 \pm 0.002$ . Crystallite sizes were determined using Voigt function profile fitting; uncertainties are  $\pm 2 \sigma$ .

Selection of the second and third calcination times also required consideration of the effect of Ba : (Zr + Hf) mole ratio. As shown in Figure 5.6, the crystallite size of powders processed using two calcinations for three hours followed by calcination for one hour at 1300 °C with intermediate re-grinding was strongly dependent on the stoichiometry of the powder. As shown in Section 6.6.1, the stoichiometry which produced maximum corrosion resistance was slightly on the barium-rich side of the phase boundary. Powders with the desired stoichiometry were highly resistant to grain growth, and a large increase in calcination temperature (to  $\sim 1500$  °C) was required to significantly increase crystallite sizes of slightly Ba-rich powders compared to those in Figure 5.6. Calcination times were therefore selected primarily

on the basis of phase purity considerations rather than grain growth effects. Based on the information above, the powders for crucible fabrication were produced using two calcinations for three hours followed by one calcination for an hour, with intermediate regrinding. The effects of powder processing stages on crystallite size are shown in Figure 5.6. The final calcination was kept to one hour to restrict grain growth, particularly on the zirconium-rich side of the phase boundary whilst still achieving high phase purity.

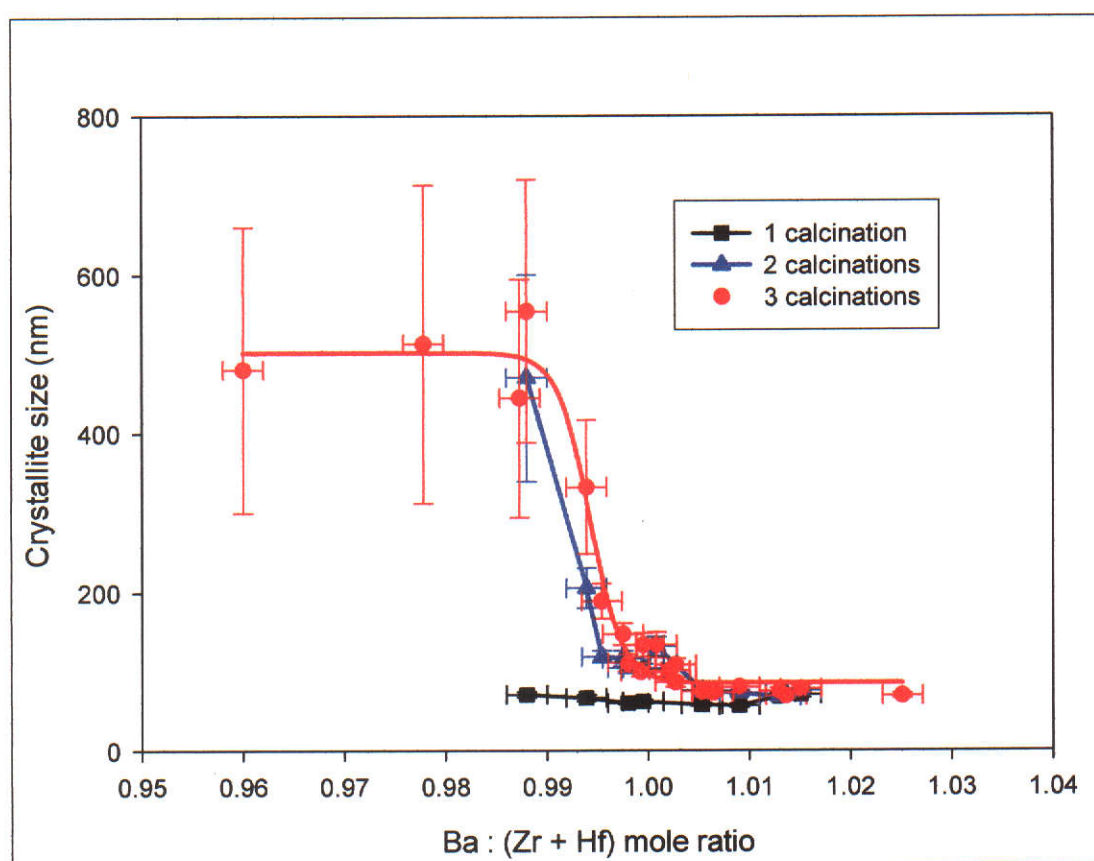


Figure 5.6 Effect of stoichiometry on crystallite size for solid-state derived powders after repeated calcination at 1300 °C with intermediate regrinding. Crystallite sizes were determined using Voigt function profile fitting. Crystallite size uncertainties are  $\pm 2\sigma$ .

The microstructure of solid-state derived powders are shown in Figures 5.7 to 5.9. Powders produced by three calcinations with intermediate re-grinding and a Ba : (Zr + Hf) mole ratio of 0.995 or below typically produced large and somewhat rounded primary particles, whereas those with Ba : (Zr + Hf) mole ratios above  $\sim 1.002$  produced much smaller and typically cuboid shaped primary particles. A mixture of particles sizes for solid-state derived powders after three calcinations was observed between these limits. Primary particle sizes observed by TEM were in good agreement with crystallite sizes calculated from XRD using Voigt function profile fitting.

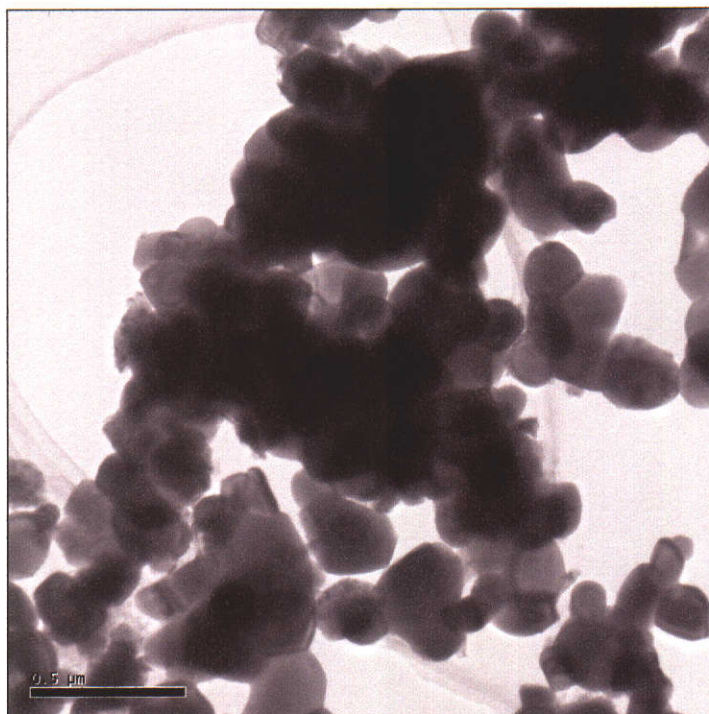


Figure 5.7 TEM micrograph of solid-state derived powder after three calcinations with intermediate regrinding and Ba : (Zr + Hf) mole ratio of  $0.995 \pm 0.002$ . Crystallite size by Voigt function profile fitting was  $249 \pm 18$  nm, which corresponds to the primary particle size observed by TEM. Scale bar = 500 nm.



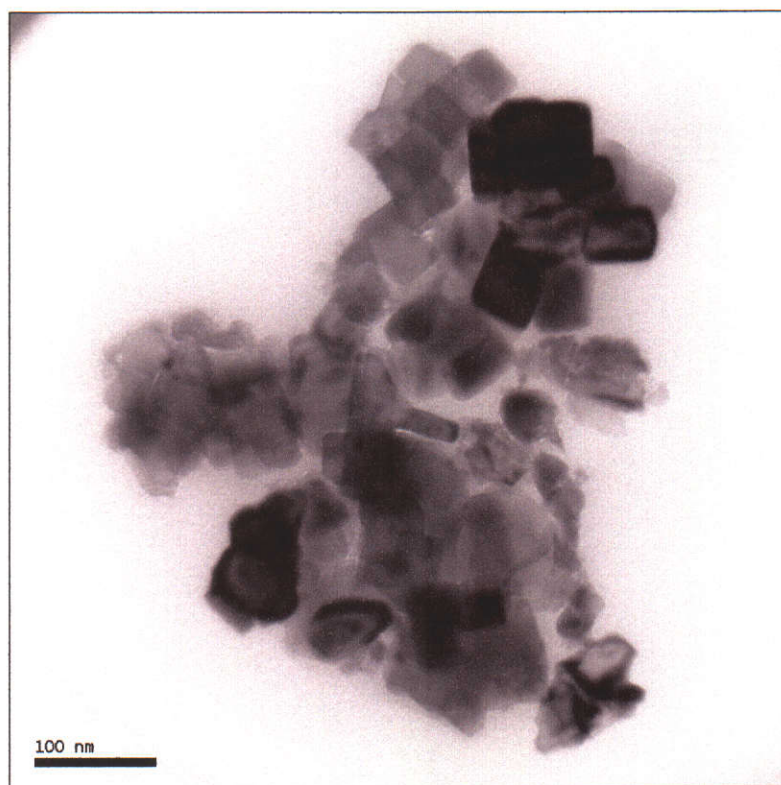


Figure 5.8 TEM micrograph of solid-state derived powder after three calcinations with intermediate regrinding and Ba : (Zr + Hf) mole ratio of  $1.025 \pm 0.002$ . Crystallite size by Voigt function profile fitting was  $69 \pm 3$  nm, which corresponds to the primary particle size observed by TEM. Scale bar = 100 nm.

In some areas of specimens there was clear evidence of hard agglomeration between primary particles which can be observed from closely fitting grain boundary shapes as shown in Figure 5.9. Hard agglomeration is strong bonding between particles that occurs during heat treatment of powders, where particles are partially fused or sintered together. The qualitative distinction between hard and soft agglomeration is based on how easily such agglomerates are broken apart by subsequent mechanical processing such as milling and/or pressing. An accurate interpretation from TEM of the overall degree of agglomeration is difficult because of uncertainty over the stability of dispersion of the particles during specimen preparation. Primary particles were typically distributed in clusters on amorphous carbon support films, but unlike the clear evidence of hard agglomeration shown in Figure 5.9, it was less clear whether primary particles were bonded together or simply clustered due to inadequate dispersion during sample preparation. Although the dispersant used for TEM specimen preparation was reasonably effective (based

on its properties when used for slip casting) it was not known to what extent dispersion was maintained during TEM specimen preparation, that is until complete drying of the specimen grid. This was particularly important for particles less than approximately 100 nm diameter, where inter-particle attraction makes dispersion particularly difficult. Clusters of primary particles observed in TEM were typically much wider than they were thick, suggesting that much of the observed agglomeration was a result of surface interactions between particles and amorphous carbon support films during specimen preparation, rather than severe hard agglomeration during powder synthesis.

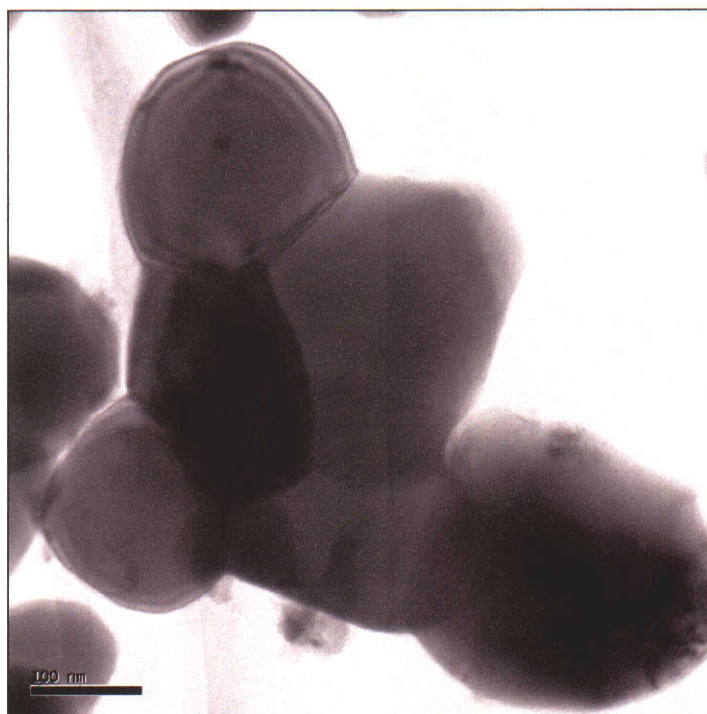


Figure 5.9 Detail from Figure 5.7 showing hard agglomeration in a solid-state derived powder with Ba : (Zr + Hf) mole ratio of  $0.995 \pm 0.002$ .

The interpretation of the agglomeration state of  $\text{BaZrO}_3$  particles from TEM observation remained somewhat ambiguous, but what could be readily interpreted by TEM observations of powders were the typical sizes of the primary particles from which observed agglomerates were formed. High magnification and high resolution imaging showed these particles were frequently single crystals. Observed primary particle sizes agreed closely and consistently with estimations of crystallite size from XRD.



#### 5.2.4 Solid-state processing: crystallite size and non-uniform strain measurement and control

Figure 5.10 shows that close to the phase boundary, stoichiometry had a large effect on the crystallite size (or particle size by BET) of solid-state derived powders produced using three calcinations with intermediate re-grinding. This conclusion was supported by three independent measurements (XRD, BET and TEM) and two approaches to XRD data analysis (Voigt function profile fitting and Scherrer equation). Particle growth during powder processing at the correct stoichiometry for corrosion resistance was heavily suppressed. The physical properties of particles (especially particle size and degree of agglomeration) has a significant bearing on their processing properties, particularly on their suitability for shape forming by slurry casting techniques, packing efficiency in dense green bodies and their densification behaviour during sintering (Section 5.9). The low particle size of solid-state derived powders at the optimum stoichiometry for corrosion resistance prevented the use of aqueous slip casting because of difficulty in maintaining strong dispersion of ultra-fine particles at high solids loadings. Poor green density in castings resulted in increased drying shrinkage and minor cracking problems, but most significantly restricted densification at 1700 °C to levels less than required for reliable melt tightness.

Crystallite sizes determined by Voigt profile fitting were consistently larger than those calculated by the Scherrer equation, particularly for powders with Ba : (Zr + Hf) mole ratios below 0.995 (Figure 5.10). In general, Gaussian and Lorentzian integral breadths of refined Voigt profile functions were of similar magnitude indicating that for most samples, line broadening was due approximately equally to non-uniform strain and crystallite size. All powders with Ba : (Zr + Hf) mole ratios larger than 0.995 displayed statistically significant strain broadening (at 99 % confidence levels). The magnitude of non-uniform strain of solid-state derived powders after three calcinations with intermediate regrinding was dependent on stoichiometry as shown in Figure 5.11. Despite showing similar trends as Voigt profile fitting and BET measurements, crystallite sizes calculated using the Scherrer equation were inaccurate because the assumption of negligible non-uniform strain broadening proved to be invalid. Systematic error of the Scherrer equation method

was greatest for powders with Ba : (Zr + Hf) less than 0.990, because non-uniform strain broadening was larger than crystallite size broadening in these specimens, although experimental uncertainties were large because the peak profiles were very close to the instrument profile as estimated by LaB<sub>6</sub>. Scherrer equation results were presented for comparison with Voigt profile refinements, and despite their limited accuracy, the Scherrer equation may still be useful for process control if more sophisticated data analysis methods are unavailable and where limited accuracy may be tolerated.

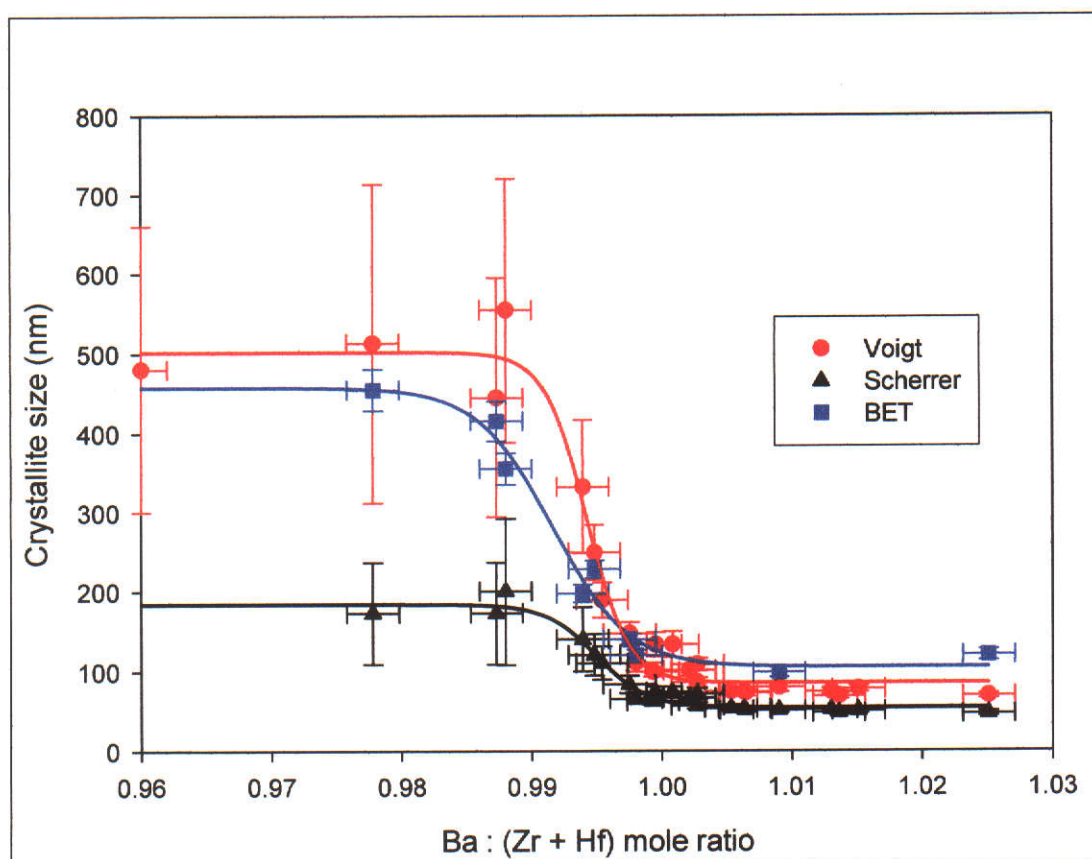


Figure 5.10 Effect of stoichiometry on crystallite sizes of solid-state derived powders after three calcinations with intermediate re-grinding. Uncertainties are  $\pm 2\sigma$ .

Crystallite sizes of solid-state derived powders calculated from Voigt profile analysis of XRD patterns were remarkably similar to particle sizes calculated from BET surface area measurements. Direct comparison of these results is complicated



by the fact that crystallite sizes calculated using the XRD methods are volume weighted averages, whereas conversion of the BET measurements would yield area weighted average sizes. Area weighted average crystallite sizes can be determined using XRD, but require high quality diffraction patterns to be acquired over a large angular range, which was neither practicable nor of sufficient importance for this project.

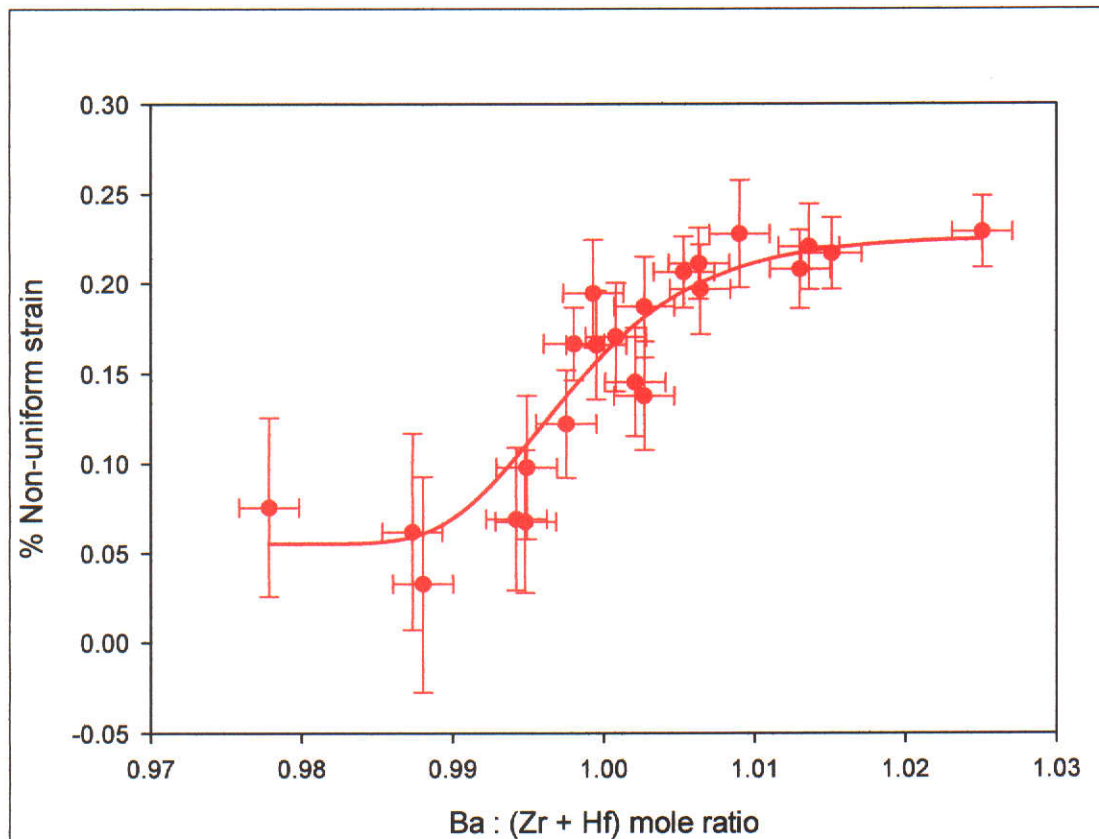


Figure 5.11 Effect of stoichiometry on non-uniform strain of solid-state derived powders after three calcinations with intermediate re-grinding. Random uncertainties are  $\pm 2\sigma$ .

The high slope of the curve in Figure 5.6 at Ba : (Zr + Hf) mole ratios near 0.995 would make particle size control difficult at that stoichiometry. The importance of experiment design during processing development is also inferred from Figure 5.6. Had all samples at Ba : (Zr + Hf) mole ratio of 0.995 not been taken from a single well mixed stock of powder, slight variations in mole ratio would have compromised repeatability and interpretation of results.

Figure 5.12 shows there was very good agreement between primary particle sizes observed by TEM with crystallite sizes estimated by Voigt function profile fitting over a wide size range. Representative TEM micrographs were readily obtained on powder samples because for most samples there was a relatively narrow distribution of particle sizes, and the differences in particle sizes and shapes between samples on either side of the phase boundary were distinct. Particle size distributions were widest for specimens adjacent to the phase boundary, presumably due to variations in local stoichiometry during processing. Because the effect of stoichiometry on crystallite size near the phase boundary is very strong (Figure 5.12), it would be difficult to achieve sufficient precision to verify the effect of local stoichiometry variation on local crystallite size by microanalysis.

Uncertainties quoted for crystallite size measurements from Voigt profile fitting of XRD patterns were based on estimated standard deviations calculated by Shadow. Calculated two sigma uncertainties were quoted even though they typically underestimated the observed repeatability of crystallite size measurement by XRD. The agreement between crystallite sizes by Voigt profile fitting of XRD patterns with large primary particle sizes observed by TEM was closer than inferred by  $2\sigma$  crystallite size uncertainties. For example, the primary particle sizes of specimens with Ba : (Zr + Hf) mole ratios less than 0.99 shown in Figure 5.12 did not differ from the mean crystallite size estimated by Voigt profile fitting by as much as  $\pm 2\sigma$ . Using  $2\sigma$  crystallite size uncertainties, the difference in results for samples with Ba : (Zr + Hf) mole ratios below 0.99 with the sample at 0.995 would not be statistically significant. However, a clear difference in primary particle sizes was observed by TEM. As discussed in Section 4.8.1, the most important size characteristic of powders for processing properties was considered to be primary particle size. Crystallite size measurement by XRD was used primarily to estimate powder processing properties rather than for accurate measurement of crystallite sizes.

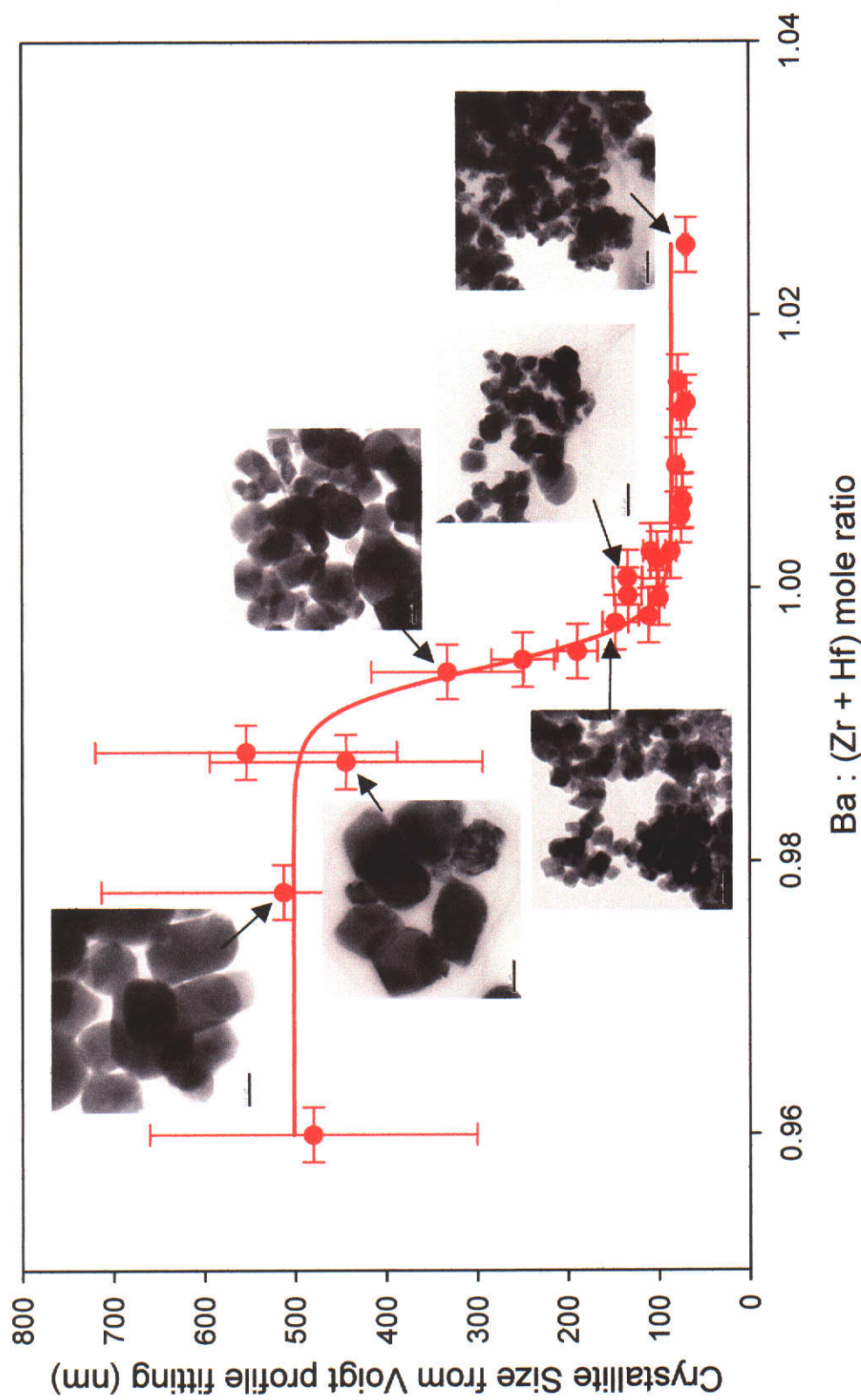


Figure 5.12

The effect of stoichiometry on crystallite sizes determined by Voigt function profile fitting of XRD patterns for solid state derived powders after three calcinations with intermediate re-grinding. TEM images are shown for comparison and verify the results of XRD. Magnifications of images are constant, scale bar = 200 nm. Uncertainties are  $\pm 2\sigma$ .



The statistical confidence of non-uniform strain broadening was poor for powder specimens with a crystallite size larger than ~350 nm. Due to limitations of Shadow's Voigt profile fitting algorithm, meaningful results could not be obtained if  $\beta_{hG}$  was constrained. For example  $\beta_{hG}$  could not be constrained to  $\beta_{gG}$ , that is, the software would not allow non-uniform strain broadening to be constrained to zero or near zero values for specimens where non-uniform strain broadening was not statistically significant. This meant that non-zero non-uniform strain broadening had to be included in profile refinements, regardless of its physical basis. Closer agreement between particle sizes observed by TEM and crystallite sizes estimated from Voigt profile fitting than the Scherrer equation towards the upper limit of XRD measurements may suggest slight non-uniform strain broadening is present despite the low statistical confidence of the Gaussian component of these Voigt profile refinements.

An alternative approach to the determination of crystallite size and strain is by the angular dependence of peak broadening using various forms of the Williamson-Hall plot (Young 1993, p. 113 – 126). The full width at half maximum of diffraction peaks due to size and isotropic non-uniform strain vary according to

$$\beta_{size} = \frac{\lambda}{\tau} \sec \theta \quad \beta_{strain} = k\epsilon \tan \theta \quad (5.1)$$

and there are several graphical methods of measuring and separating size and non-uniform strain effects (Young 1993, p. 113 – 126). This popular approach was not used because it requires collection of either full diffraction patterns or at least diffraction peaks over wide angular ranges, which significantly extends data collection times and cost of analysis, and because the simple single peak Voigt profile analysis was shown to be adequate for this research.

Investigation of crystallite domain size by HRTEM was not successful for particles larger than ~100 nm, because lattice images for these larger particles could not be obtained probably due to electron energy loss and multiple scattering. TEM analysis of thin sections from sintered ceramics clearly showed that intragranular defects were prevalent and readily observed in sintered Ba-rich ceramics, and grains in sintered Zr-rich ceramics were nearly free of observable internal defects. However, defects observed in sintered ceramics were not observed in powders, and so the

origin of non-uniform strain derived from Voigt profile fitting of XRD patterns of processed powders was not determined.

### 5.2.5 Solid-state processing: surface area measurement and control

A ubiquitous and industry standard technique for measurement of surface areas of fine powders is nitrogen gas adsorption, and such measurements in this project were considered accurate based on the correlation coefficients of BET isotherms. Surface areas calculated from Voigt profile fitting compared more closely to BET surface areas than Scherrer equation estimates as shown in Figure 5.13.

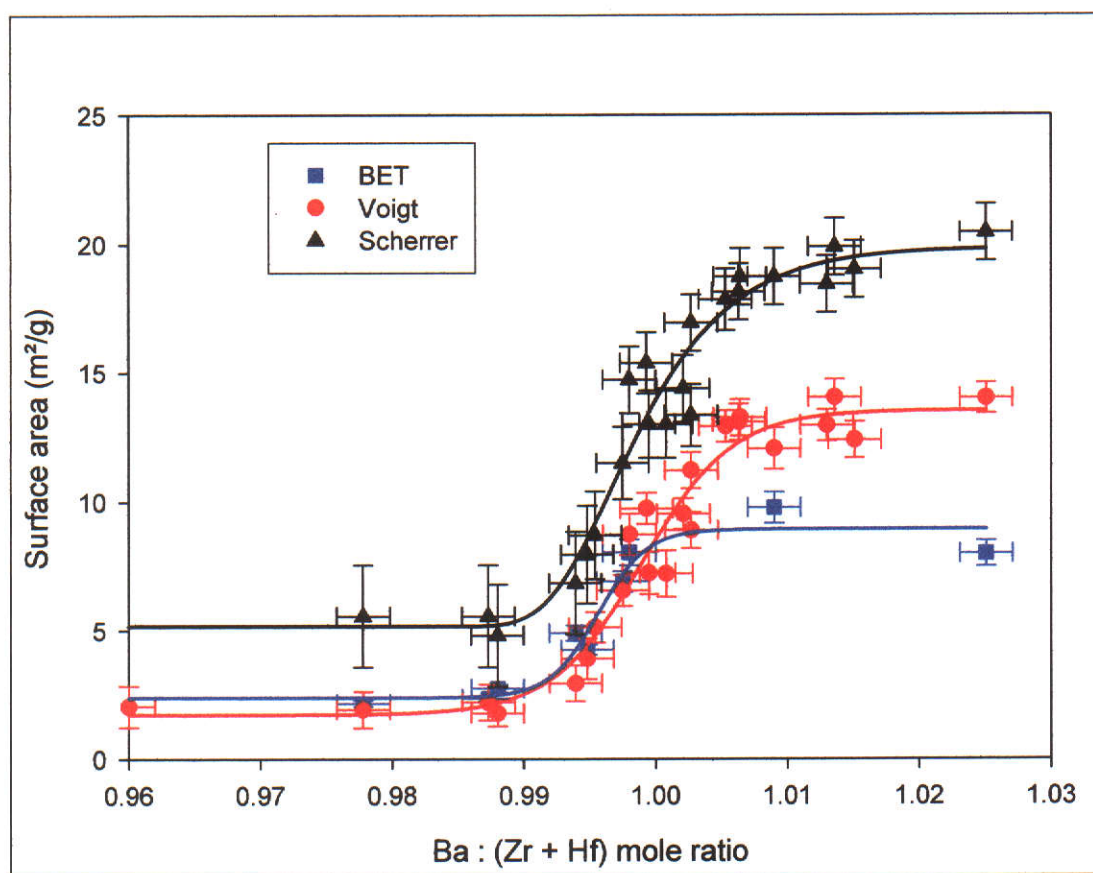


Figure 5.13 Effect of stoichiometry on BET surface area for solid-state derived powders after three calcinations with intermediate re-grinding. Surface areas calculated from crystallite sizes by Voigt function profile fitting and Scherrer equation are shown for comparison. Uncertainties are  $\pm 2\sigma$ .

Surface areas estimated from accurate crystallite size measurements could be expected to be equivalent to BET measurements for powders composed only of single crystallites. However, in the normal case where particles are not single crystallites but agglomerates, surface areas calculated from crystallite sizes would be expected to overestimate BET surface areas because crystallite boundaries which are not at particle surfaces may not be accessible to N<sub>2</sub>. However, quantitative estimation of crystallite agglomeration from this data is not feasible, partly because of the difficulty of comparing volume-weighted and area-weighted size averages. Low crystallite size was due to the effects of stoichiometry and/or calcination procedure (Figure 5.6). Reduced diffusion kinetics through low calcination temperatures (and possibly barium excess) may inhibit free energy minimisation through progressive elimination of crystallite interfacial area.

### **5.3 Oxalate precursor processing**

#### **5.3.1 Stoichiometry control in the BaCl<sub>2</sub>, zirconium oxychloride, H<sub>2</sub>C<sub>2</sub>O<sub>4</sub> system**

##### ***Introduction***

As outlined in Section 4.9, two main chemical systems were investigated for their potential to provide a viable process for corrosion resistant crucible fabrication: the barium chloride / zirconium oxychloride / oxalic acid system and the barium acetate / zirconium oxychloride / ammonium oxalate system. As for solid-state processing, solution processing development requires control over powder phase purity, particle size and agglomeration state, but considerable experimentation was required to establish control over stoichiometry. Powder stoichiometry by solid-state processing is readily controlled by weight ratios of reagents because there are no preferential losses of reagents during processing. However, oxalate processing requires control over precipitation chemistry because precipitations are not necessarily quantitative for either zirconium or barium. Control over stoichiometry was one of the most challenging aspects of oxalate processing and is presented first.

##### ***Preliminary experiments***

Preliminary experiments were conducted in order to devise a viable process based on the method of Reddy and Mehrotra (1979). As shown in Table 5.1, samples

produced in preliminary experiments using BaCl<sub>2</sub>, zirconium oxychloride and oxalic acid with a solution mole ratio of 1.00 : 1 : 2.20 Ba : [Zr+Hf] : C<sub>2</sub>O<sub>4</sub> were severely barium deficient irrespective of reaction conditions. Other combinations of reagent addition rate, reaction temperature (including ambient temperature), order of reagent addition and zirconium oxychloride supply (Millennium or Riedel-de Haën) were investigated, but none could be found that produced BaZrO<sub>3</sub> with anything like unity mole ratio. The DTA curve reported by Reddy and Mehrotra (1979) is not consistent with results from this project shown in Figure 5.16 for powders with Ba : (Zr + Hf) mole ratios close to unity (e.g. 0.970) produced from BaCl<sub>2</sub>, zirconium oxychloride and an excess of oxalic acid. The method of Reddy and Mehrotra (1979), as far as could be interpreted from their very brief description, did not work.

Table 5.1 Stoichiometry of powders following the method of Reddy and Mehrotra (1979).

Order of mixing of reagents	Precipitation Temperature (°C) (± 3 °C)	Ba : (Zr +Hf) mole ratio (± 0.002)
Zr added to mixture of BaCl <sub>2</sub> and oxalic acid	95	0.695
Zr added to mixture of Ba and oxalic acid	80	0.709
mixture of Ba and Zr added to oxalic acid	95	0.703
oxalic acid added to mixture of Ba and Zr	90	0.737

***Optimisation of oxalate excess in barium chloride, zirconyl chloride, oxalic acid system***

The initial method used to increase the mole ratio of the precipitate compared to the process of Reddy and Mehrotra (1979) was to use a significantly larger excess of oxalic acid. The logic behind increasing oxalic acid addition was to increase the available oxalate ion concentration for barium precipitation, because excessive zirconium complexation of oxalate ions may have left insufficient oxalate ions for

adequate precipitation of barium. The use of greater than 10% excess oxalic acid was useful in controlling product stoichiometry in the  $\text{BaCl}_2$ , zirconium oxychloride, oxalic acid system both at ambient and elevated temperature for a 1 : 1 Ba : (Zr + Hf) solution mole ratio as shown in Figure 5.14.

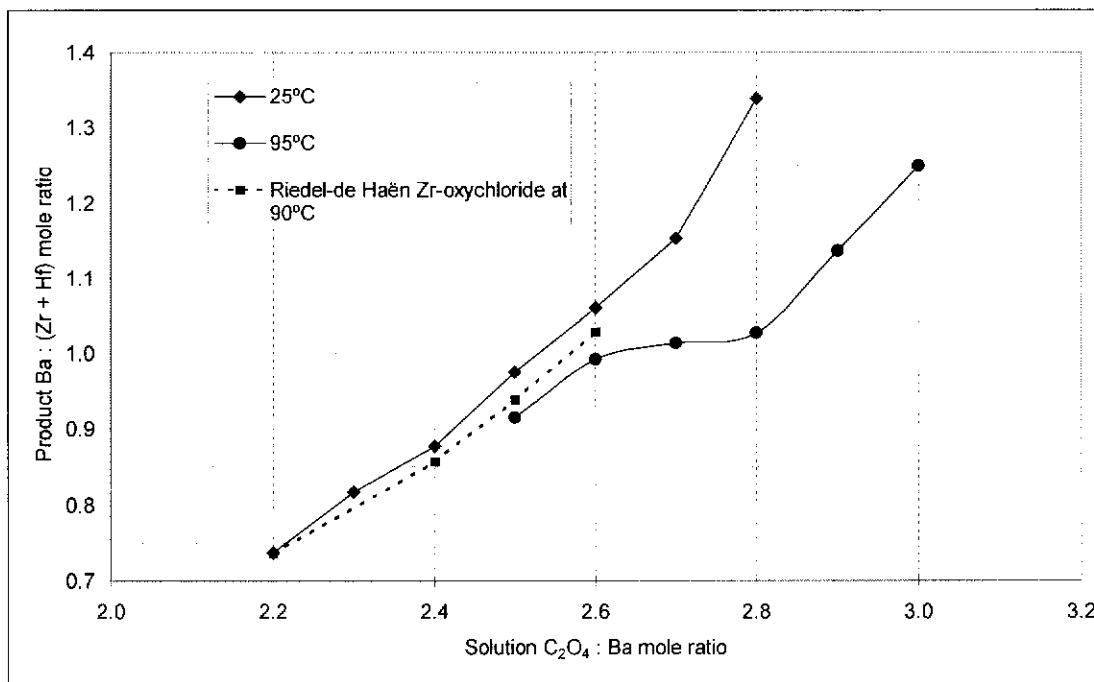


Figure 5.14 Control of powder stoichiometry in the barium chloride / zirconium oxychloride / oxalic acid system.

In the three systems indicated in Figure 5.14, product stoichiometry was dependent on the mole ratios of solutions used for precipitation. The barium chloride, zirconyl chloride and oxalic acid system was not ideal for controlling product stoichiometry, due to the relationship between product stoichiometry, solution ratios and temperature. Unless the ratio of  $\text{H}_2\text{C}_2\text{O}_4$  : Zr was approximately 2.6 : 1 and not 2.2 : 1 as specified by Reddy and Mehrotra (1979), a stoichiometric product could not be obtained at any temperature without a significant excess of barium or the addition of ammonia. The sensitivity of product composition to solution ratios at ambient temperature makes the barium chloride, zirconyl chloride and oxalic acid system unsuitable for high quality process control. The system was also sensitive to acid/base additions: addition of HCl and  $\text{NH}_3$  caused reduced and increased product Ba : (Zr + Hf) mole ratios, respectively.



At near boiling temperature, the flatter region of the curve in Figure 5.14 shows that the system may be capable of stable production at 95 °C. However, the requirement for elevated temperature control adds undesired complexity to the process, particularly for scaling up production. Rapid addition of reagents in the barium chloride, zirconium oxychloride, oxalic acid system at elevated temperature caused difficulties in filtration and washing. Precipitates formed by rapid reagent addition were considerably slower to settle and had much more severe particle losses during filtration, leading to poor repeatability of product stoichiometry. Slow rates of reagent addition were required in this system to produce a washable product, adding inefficiency and complexity to process control.

Qualitative testing showed that as the  $\text{H}_2\text{C}_2\text{O}_4$  : Ba solution mole ratio increased, the barium and zirconium concentrations of the supernatant solutions decreased and increased, respectively. Under such conditions, zirconium was solubilised by an excess of oxalic acid, resulting in a zirconium deficient precipitate above a 2.60 : 1  $\text{H}_2\text{C}_2\text{O}_4$  : Zr solution mole ratio. Barium-rich precipitates were formed at excessive oxalic acid levels not because of increased barium precipitation, but by the lack of precipitation of zirconium.

### **5.3.2 Stoichiometry control in the $\text{Ba}(\text{CH}_3\text{COO})_2$ , zirconium oxychloride, $(\text{NH}_4)_2\text{C}_2\text{O}_4$ system**

The barium acetate, zirconyl chloride, ammonium oxalate system proved to be far more suitable for high quality production because the product composition could be precisely controlled by the Ba : Zr solution mole ratio, at ambient temperature and with low sensitivity to excess oxalate addition above a 2.4 : 1  $\text{C}_2\text{O}_4$  : Ba solution mole ratio. Other than correcting for minor scale-up effects, product stoichiometry was controlled simply by the Ba : [Zr+Hf] solution ratio in the presence of a suitable excess of ammonium oxalate as shown in Figure 5.15. A  $(\text{NH}_4)_2\text{C}_2\text{O}_4$  : barium acetate mole ratio of 2.4 was used for routine production of  $\text{BaZrO}_3$ , although a greater excess of oxalate can be used if desired because excess ammonium oxalate does not solubilise zirconium under the conditions studied.

Scaling up the size of production by a factor of 10 caused a minor drop in product Ba : (Zr + Hf) mole ratio, but this could be corrected by reduced zirconium oxychloride addition and/or increased oxalate addition.

Alternatively, near stoichiometric product can be produced using a large excess of barium acetate instead of an excess of ammonium oxalate, as shown in Table 5.2. However, the waste barium causes unnecessary disposal problems, and this method, although viable, is not recommended.

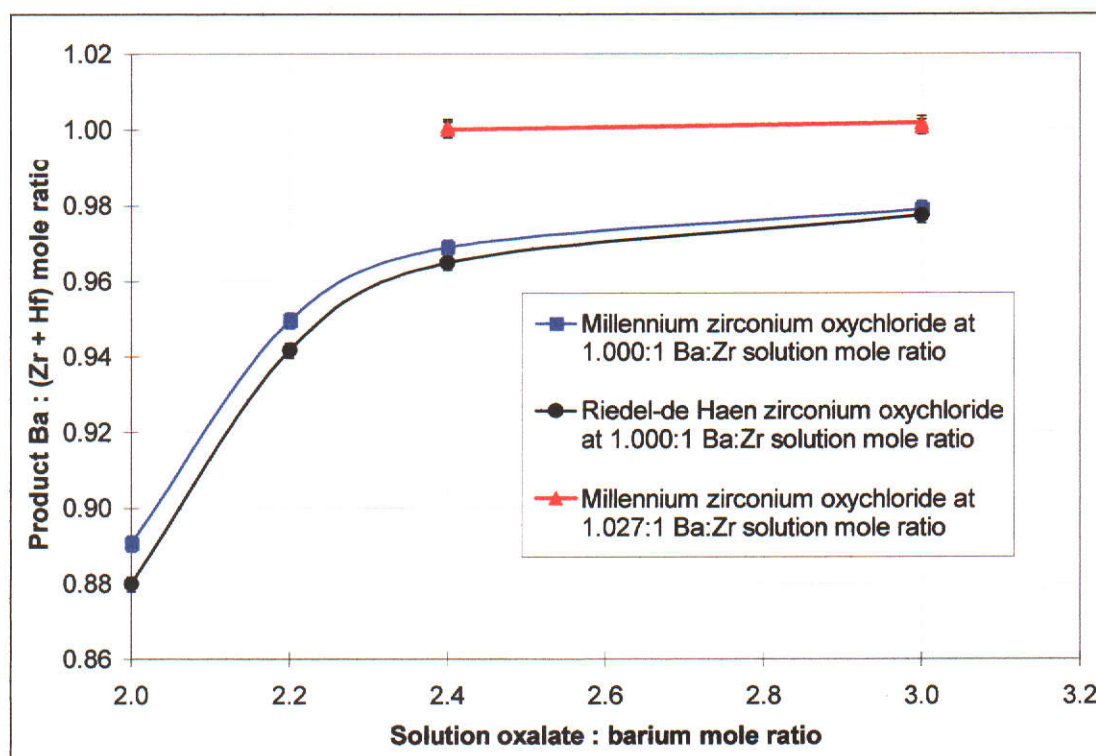


Figure 5.15 Control of powder stoichiometry in the barium acetate / zirconium oxychloride / ammonium acetate system. All reactions were conducted at  $23 \pm 3$  °C.

Table 5.2 Alternative method for production of near stoichiometric BaZrO<sub>3</sub> in the barium acetate, zirconium oxychloride, ammonium oxalate system using an excess of barium acetate at 22 °C.

Ba(CH <sub>3</sub> CO <sub>2</sub> ) <sub>2</sub> : ZrOCl <sub>2</sub> : (NH <sub>4</sub> ) <sub>2</sub> C <sub>2</sub> O <sub>4</sub> Solution Mole Ratio	Order of Reagent Mixing	Precipitate Ba : (Zr + Hf) Mole Ratio (±0.002)	Batch Size (L)
2.00 : 1 : 2.00	Zr to AmmOx, then Ba added rapidly	0.975	2
2.00 : 1 : 2.00	Zr to AmmOx, then Ba added rapidly	0.970	15
2.00 : 1 : 2.00	Zr to AmmOx, then Ba added slowly	0.988	1
2.03 : 1 : 2.03	Zr to AmmOx, then Ba added rapidly	0.990	20
2.03 : 1 : 2.01	Zr to AmmOx, then Ba added rapidly	0.960	20
2.03 : 1 : 2.01	Zr to AmmOx, then Ba added rapidly	0.966	20
2.03 : 1 : 2.01	Zr to AmmOx, then added slowly to Ba	0.961	20
2.01 : 1 : 2.05	Zr to AmmOx, then Ba added rapidly	0.994	20
2.00 : 1 : 2.05	Zr to AmmOx, then Ba added rapidly	1.000	20
2.00 : 1 : 2.05	Zr to AmmOx, then Ba added rapidly	0.962	20

Comparison with the oxalic acid system (Section 5.6) shows that stoichiometric BaZrO<sub>3</sub> production required less oxalate addition using ammonium oxalate compared to oxalic acid. The results of this study showed the Ba : (Zr + Hf) mole ratio of precipitates increased with basicity of reagents at equivalent oxalate levels and Ba : (Zr + Hf) solution ratios, consistent with the conclusions of Gangadevi, Subba Rao and Kutty (1980). Ammonium oxalate is more basic than oxalic acid, and a brief experiment using sodium oxalate resulted in an even more Ba-rich precipitate at equivalent oxalate levels. Clearly, the stoichiometry of precipitates is influenced by acidity and alkalinity of reagents used. Gangadevi, Subba Rao and Kutty (1980) reported that precipitation “in strongly acidic media will

be deficient in zirconium ... giving rise to barium carbonate as one of the decomposition products.” This was only observed at excessive oxalic acid levels as shown in Figure 5.14. Solubilisation of zirconium by excess oxalate did not occur up to at least a 50% excess of ammonium oxalate, which would presumably also apply to alkali oxalates. Addition of HCl and NH<sub>3</sub> to the oxalic acid system resulted in Ba-deficient and Ba-rich precipitates, respectively.

### 5.3.3 Stability of zirconium oxalate solutions

Direct assessment of the speciation of zirconium in oxalate solutions remained well beyond the scope of this project. Analysis of zirconium speciation is a challenging task in analytical chemistry typically requiring specialised knowledge and techniques such as dialysis, ultra centrifugation, various electrochemical techniques and colorimetric methods. It was not feasible to even begin this task, nor were necessary resources available. The study of zirconium chemistry during this project was limited to application of understanding gained from literature, visual observations of reactions between solutions, qualitative analysis of supernatant solutions, investigations of the stabilities of zirconium oxalate solutions and the stoichiometry of precipitates by XRF. Studying the stability of zirconium oxalate solutions under a range of conditions provided patterns of observations which were valuable in understanding oxalate processing chemistry and the suitability of different reagents and reaction conditions to produce stoichiometric precipitates. The available information allows only approximate working hypotheses regarding the mechanism of precipitation upon addition of barium to zirconium oxalate solutions, but these ideas were still useful for controlling the oxalate system. The following discussion describes a series of experiments performed to improve the understanding of zirconium oxalate solution chemistry for stoichiometric barium zirconium oxalate precipitation.

Freshly prepared 0.25M zirconium oxychloride solution was added slowly from a burette to stirred 0.65M oxalic acid solution to form a clear solution with [Zr] = 0.1 M and a Zr : C<sub>2</sub>O<sub>4</sub> mole ratio of 1 : 2.60 at ambient temperature. The solution was stirred for ten minutes then heated slowly on a hotplate to 90 °C and the

temperature at which precipitation occurred was measured. This experiment was also conducted for a solution with a Zr : C<sub>2</sub>O<sub>4</sub> mole ratio of 1 : 2.20.

If the rate of addition of the zirconium was low enough, a clear solution could be made at room temperature. As the solution was heated it became opalescent due to the formation of a visible amount of colloid at 74 °C which increased to the point where by 85 °C the slurry became strongly opaque. After boiling for a few minutes, the solid phase was stable at room temperature for a period exceeding one week, possibly indefinitely, and was not readily soluble in hydrochloric acid. A 2.20 : 1 H<sub>2</sub>C<sub>2</sub>O<sub>4</sub> : Zr mole ratio solution was cloudy at ambient temperature, and the quantity of precipitate increased as the slurry was heated. The precipitation of zirconium oxalates under acidic conditions at elevated temperatures may make such solutions undesirable for barium zirconate processing.

The stability of zirconium oxychloride / Na<sub>2</sub>C<sub>2</sub>O<sub>4</sub> solutions as a function of temperature was also investigated. Zirconium oxychloride solution was added to 0.2 M Na<sub>2</sub>C<sub>2</sub>O<sub>4</sub> while stirring to form a solution with Zr : C<sub>2</sub>O<sub>4</sub> mole ratio of 1 : 2.0 and [Zr] = 0.05 M. During addition of Zr, a rapidly re-dissolving precipitate was observed, but by the end of addition of Zr the solution was slightly cloudy. After dilution to [Zr] = 0.025 at ambient temperature the solution became completely clear, and remained clear after boiling for several minutes. This experiment was repeated using 1 : 2.2 Zr : C<sub>2</sub>O<sub>4</sub> mole ratio at [Zr] = 0.05 M and [C<sub>2</sub>O<sub>4</sub>] = 0.11 M producing a cloudy solution at ambient temperature which was still cloudy after three hours. Instead of diluting this solution, it was heated on a hot-plate stirrer, becoming clear above 50 °C and remained clear to at least 90 °C.

The stability of zirconium oxychloride / ammonium oxalate solutions was tested by addition of 0.5 M zirconium oxychloride to 0.33 M (NH<sub>4</sub>)<sub>2</sub>C<sub>2</sub>O<sub>4</sub> and dilution to [Zr] = 0.09 M. A rapidly re-dissolving precipitate was formed at the contact between the solutions but a completely clear solution was produced soon after complete addition of Zr. The solution was left for 15 minutes, then heated on a hotplate stirrer to 97 °C over 45 minutes. The solution remained completely clear during heating and for 10 minutes at 97 °C, but became very slightly opaque after

cooling to ambient temperature. The pH before and after heating was  $7.02$  and  $6.45 \pm 0.03$ , respectively.

A sample of the heated zirconium oxychloride / ammonium oxalate solution was taken and titrated with  $1\text{ M HCl}$ . Once the pH was reduced to below  $0.9 \pm 0.1$ , the slightly opaque solution became very cloudy and was opaque after 2 minutes without further addition of  $\text{HCl}$ . The slurry was allowed to settle overnight, which allowed the gelatinous precipitate to settle to the bottom of the beaker leaving a nearly clear supernatant solution with  $\text{pH } 1.18 \pm 0.05$ . The precipitate was stirred into suspension, and then titrated with  $0.1\text{ M NH}_3$ . Once the pH was raised above  $4.6 \pm 0.1$ , the suspension started to become clear and was completely transparent by  $\text{pH } 5.0$ . To check the stability of this solution,  $\text{NaNO}_3$  was added, which caused the solution to become very cloudy again and the pH dropped to  $4.65 \pm 0.05$ .

Another mixed solution of zirconium oxychloride and ammonium oxalate was prepared at ambient temperature with a  $\text{Zr} : \text{C}_2\text{O}_4$  mole ratio of  $1 : 2.4$  with  $[\text{Zr}] = 0.087\text{ M}$ . Without subsequent heating, the solution was aged for 90 minutes at ambient temperature and then titrated with  $1\text{ M HCl}$ . This clear solution became very cloudy at  $\text{pH } 3.1 \pm 0.1$ , a significantly higher pH than the previously boiled solution described above.

From the above observations, precipitate stoichiometry and qualitative supernatant solution measurements reported earlier, it is appropriate to speculate about the speciation of zirconium oxalate solutions to conceptualise rough working models to assist the control of oxalate precipitation chemistry. The above observations of the properties of zirconium oxalate solutions are more readily understood if one considers zirconium oxalates as negatively charged colloids or macromolecules rather than simple ionic solutions. The idea of zirconium existing as colloids despite solutions appearing completely clear was first proposed by Britton (1925). For example, the addition of a neutral electrolyte ( $\text{NaNO}_3$ ) to cause both gelation from a clear solution and a substantial drop in pH may be accounted for by assuming zirconium oxalate is present as a dispersed colloid, and that exchange of surface adsorbed  $\text{H}^+$  for  $\text{Na}^+$  causes the observed pH drop and flocculation of the colloid so that it becomes visible. Slight cloudiness after boiling ammonium

oxalate/zirconium oxychloride solutions and strong cloudiness above 74 °C for oxalic acid/zirconium oxychloride indicated that structural changes in zirconium oxalates occurred which were pH and temperature dependent. Heating of zirconium solutions or increasing their pH is typically associated with increased hydrolysis and polymerisation and normally results in less stable solutions (Solovkin and Tsvetkova 1962). However, heating of ammonium oxalate/zirconium oxychloride solutions suppressed gelation by HCl addition to lower pH. Increasing pH through NH<sub>3</sub> addition caused cloudy suspensions to clear. Neither of these observations can be readily explained by zirconium in an ionic form, but are more consistent with the existence of zirconium oxalate colloids or at least macromolecules, particularly after heating.

If zirconium oxalates existed as colloids under the conditions studied, the experimental observations show these would have negatively charged surfaces. Flocculation by addition of H<sup>+</sup> or Na<sup>+</sup> (and Ba<sup>2+</sup>) is consistent with surface charge neutralisation of negatively charged colloids. Negative surface charge could be restored by increased pH, and would result in re-dispersion when enough surface charge was induced to overcome interparticle van der Waals attraction within flocs. Flocculation and dispersion of the colloid could be repeatedly reversed until the solution electrolyte concentration became too high, above which flocculation would be irreversible. The ability to alternatively flocculate and disperse the colloid several times was observed experimentally during this study. The pH at which re-dispersion was observed after NH<sub>3</sub> was added was significantly higher (pH ~5) than the pH at which flocculation occurred due to HCl addition (pH ~1). A higher surface charge (i.e. higher pH) would be expected to be required to overcome the increased attraction between flocculated particles than to maintain stable dispersions (Malmsten 1998, p. 21), because particles in flocs are much closer together than their average separation whilst dispersed.

The observed properties of zirconium oxalate solutions are not well explained by zirconium speciated as monomeric ions. Precipitation and resolubilisation by pH change or the addition of pH neutral electrolytes are not consistent with reported trends associated with changes in polymerisation or hydrolysis for monomeric species. Increased pH for zirconium solutions normally reduce solution stability

through increased hydrolysis and polymerisation, whereas in the current experiments increasing pH caused gelatinous precipitates to disappear. Zirconium polymerisation, and certainly its reversal are not caused by addition of neutral electrolytes, and hence precipitation of gelatinous precipitates by  $\text{NaNO}_3$  addition was not due to increased polymerisation or hydrolysis. The formation of gelatinous precipitates upon HCl addition was not consistent with increased polymerisation because high acid concentrations are normally used to suppress zirconium polymerisation (Elinson and Petrov 1969, p. 27). The significant drop in pH upon addition of  $\text{NaNO}_3$  (which is itself pH neutral) may be caused by liberation of adsorbed  $\text{H}^+$  by exchange with added  $\text{Na}^+$ . This may also apply to ion exchange of coordinated cations for zirconium oxalates speciated in molecular form.

These observations of zirconium oxalate solution properties may also be consistent with zirconium present in molecular form rather than colloids. However, the stability of the dispersion of such molecules may be interpreted in much the same way as for colloids. Molecular structure is determined by Zr concentrations, temperature and pH effects and not by neutral electrolytes. For example, the structure of zirconium oxalate molecules can be changed by boiling, which was evidenced by a small drop in pH after boiling of zirconium oxychloride/ammonium oxalate solution. All reports in previous literature reviewed in this thesis associated heating with increased polymerisation. Dispersion stability appears to be provided by negative charge, which can be neutralised by coordination of cationic species such as  $\text{H}^+$  and  $\text{Na}^+$  (and perhaps most importantly for this study by  $\text{Ba}^{2+}$ ) to induce precipitation. Potdar *et al.* (1993) described zirconium oxynitrate / sodium oxalate solutions as “molecular precursors” although without experimental evidence on zirconium speciation, but the existence of molecular or colloidal structures depends on many factors. Precipitation by adsorption of cations to colloids or coordination of cations with molecules may be useful models for understanding the behaviour of zirconium oxalate solutions so that their precipitation may be directed towards the desired outcome. Determination of the speciation of zirconium oxalates (e.g. either as colloids or molecules) remained beyond the scope of this Thesis, but the existence of colloidal particles could be investigated using small angle x-ray or neutron scattering which are routinely used to provide nanoscale structural information on colloids.



#### 5.3.4 Conclusions on oxalate processing chemistry

Zirconium speciation control appears to be the most important consideration in the barium zirconium oxalate system for production of stoichiometric product. The solution speciation of zirconium compounds is far more complex than that of other reagents studied in this project. Speciation of zirconium oxalates in solutions is dependent on many factors outlined in Chapter 2, and in the current experiments was adjusted by variation of solution concentration, solution mole ratios, temperature and pH. For processing at ambient temperature, pH was the most important experimental variable affecting product stoichiometry and the ease with which it could be controlled. The effect of pH on product stoichiometry appeared to be through changes in zirconium speciation rather than simply through oxalate ion acid-base equilibria. The speciation of zirconium oxalates under acidic (oxalic acid) and near neutral conditions (ammonium oxalate) are distinctly different as shown by the marked difference in solution stabilities at elevated temperature, and the lack of solubilisation of zirconium at elevated oxalate concentrations at neutral pH.

Direct analysis of zirconium solution speciation is a challenging exercise in analytical chemistry and well beyond the scope of this project. Review of the literature suggests solubilisation of zirconium by excessive oxalate levels under acidic conditions may have occurred by the formation of solution complexes containing large amounts of oxalate ligands (Elinson and Petrov 1969, pp. 39-40). This did not occur under neutral conditions, and formed the basis of the barium acetate process.

Understanding the speciation of zirconium in solution is of great importance in the control of oxalate processing. Precipitation of a single phase stoichiometric precursor with atomic scale mixing of barium and zirconium may require the formation of molecular solution precursors with optimised molecular structure for maximum solution stability and quantitative coordination of  $\text{Ba}^{2+}$ . Precipitation of barium zirconium oxalates from colloidal zirconium oxalate precursors would result in phase segregation in precursors and greater difficulty in producing phase pure  $\text{BaZrO}_3$  relative to molecular precursors, but may still be better than the traditional solid-state process. Processing performance appears to depend on the control of zirconium speciation, which can be adjusted according to thermal history, solution concentrations and ratios, ligand complexing properties, and in particular, pH.

### 5.3.5 Conversion of oxalate precursors to BaZrO<sub>3</sub>

DTA/TGA was used as an initial guide for determining appropriate calcination conditions for conversion of oxalate precursors to BaZrO<sub>3</sub>. TGA results in Figures 5.16 and 5.17 show that decomposition of oxalate precursors in air neared completion by 1100 °C, with very little further weight loss up to 1300 °C. Based on DTA/TGA results, calcination temperatures were investigated between 1000 to 1500 °C, with most powders calcined at approximately 1300 °C.

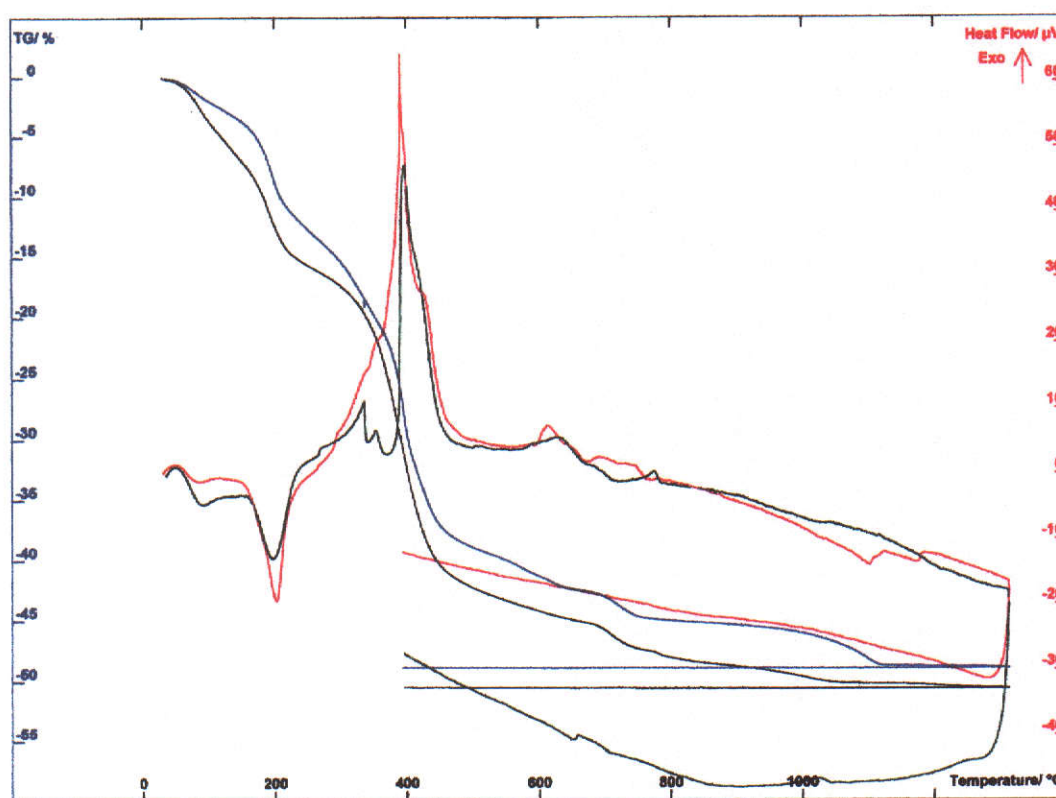


Figure 5.16 DTA/TGA results for  $0.971 \pm 0.002$  Ba : (Zr + Hf) mole ratio powders produced from BaCl<sub>2</sub>, zirconium oxychloride and oxalic acid. Orange and blue curves are for precipitation at 95 °C. Green and black curves are for precipitation at ambient temperature followed by heating to 95 °C before washing.

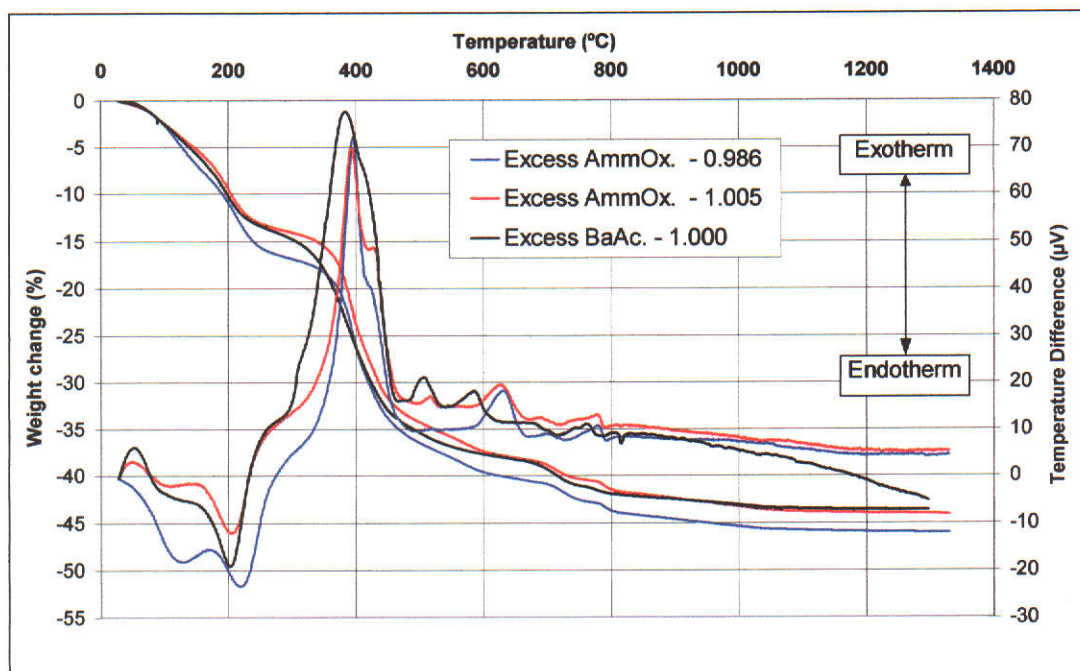


Figure 5.17 DTA/TGA analysis of precursor synthesised using barium acetate, zirconium oxychloride and ammonium oxalate with either ammonium oxalate or barium acetate in excess. The Ba : (Zr + Hf) mole ratios of the precipitates are indicated in the key.

Comparison of Figures 5.16 and 5.17 showed that weight loss of near stoichiometric oxalate derived powders was complete at approximately the same temperature irrespective of the reagents used for its production. The DTA/TGA curves for each system were consistent with those of Potdar *et al.* (1992) and Gangadevi, Subba Rao and Kutty (1980) but not with the DTA curve reported by Reddy and Mehrotra (1979).

Figure 5.18 shows the effect of calcination temperature on crystallite size at a Ba : (Zr + Hf) mole ratio of 0.989 for powder derived from barium acetate, zirconium oxychloride and ammonium oxalate. For a fixed stoichiometry, calcination temperature can be an effective means of controlling the crystallite size and surface areas of calcined powders to suit later stages of processing.

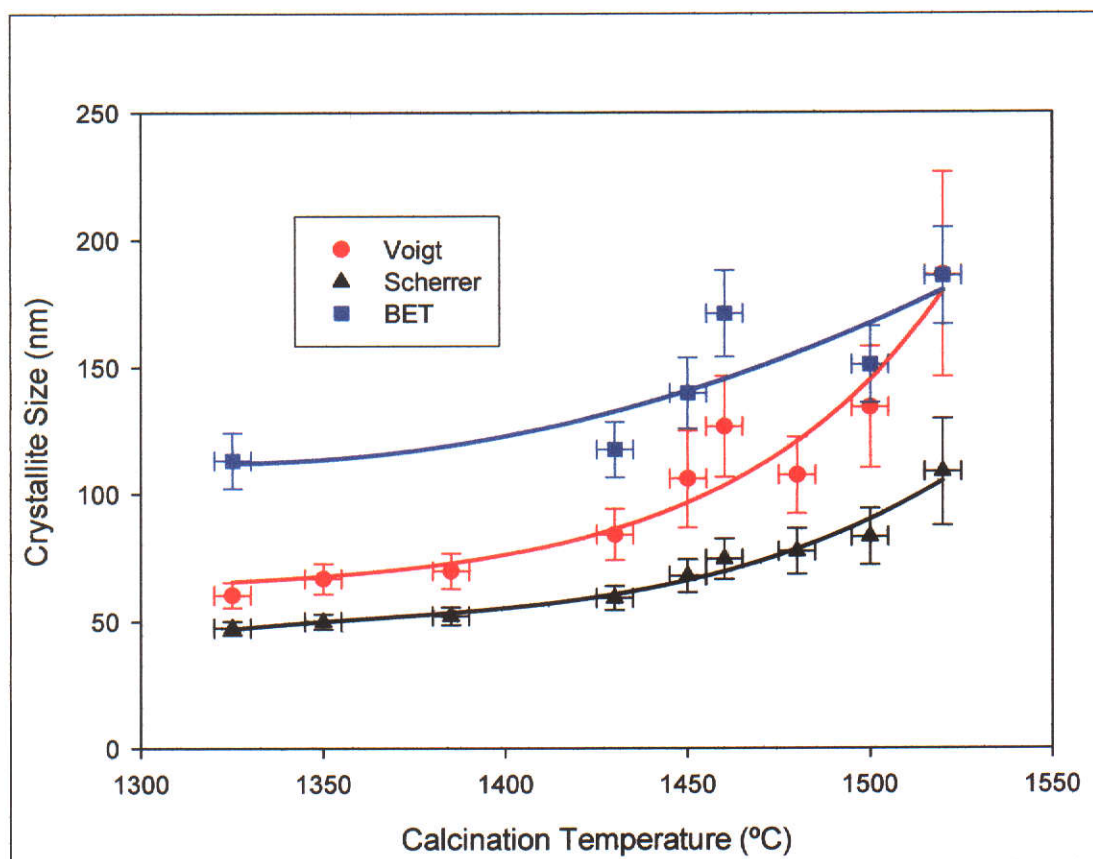


Figure 5.18 Size control of calcined oxalate derived powders at 0.989 Ba : (Zr + Hf) mole ratio by variation of calcination temperature. All samples were calcined for 30 minutes.

Crystallite size was dependent on stoichiometry, chemical contamination and calcination temperature as shown in Figures 5.18 to 5.20. Grain growth in powders was pronounced in powders with Ba : (Zr + Hf) mole ratios below 0.985, but minimal in stoichiometric powders at calcination temperatures of up to 1500 °C. As for the solid-state system, production of slip castable powders with optimal stoichiometry for corrosion resistance was not possible using oxalate precursor processing.



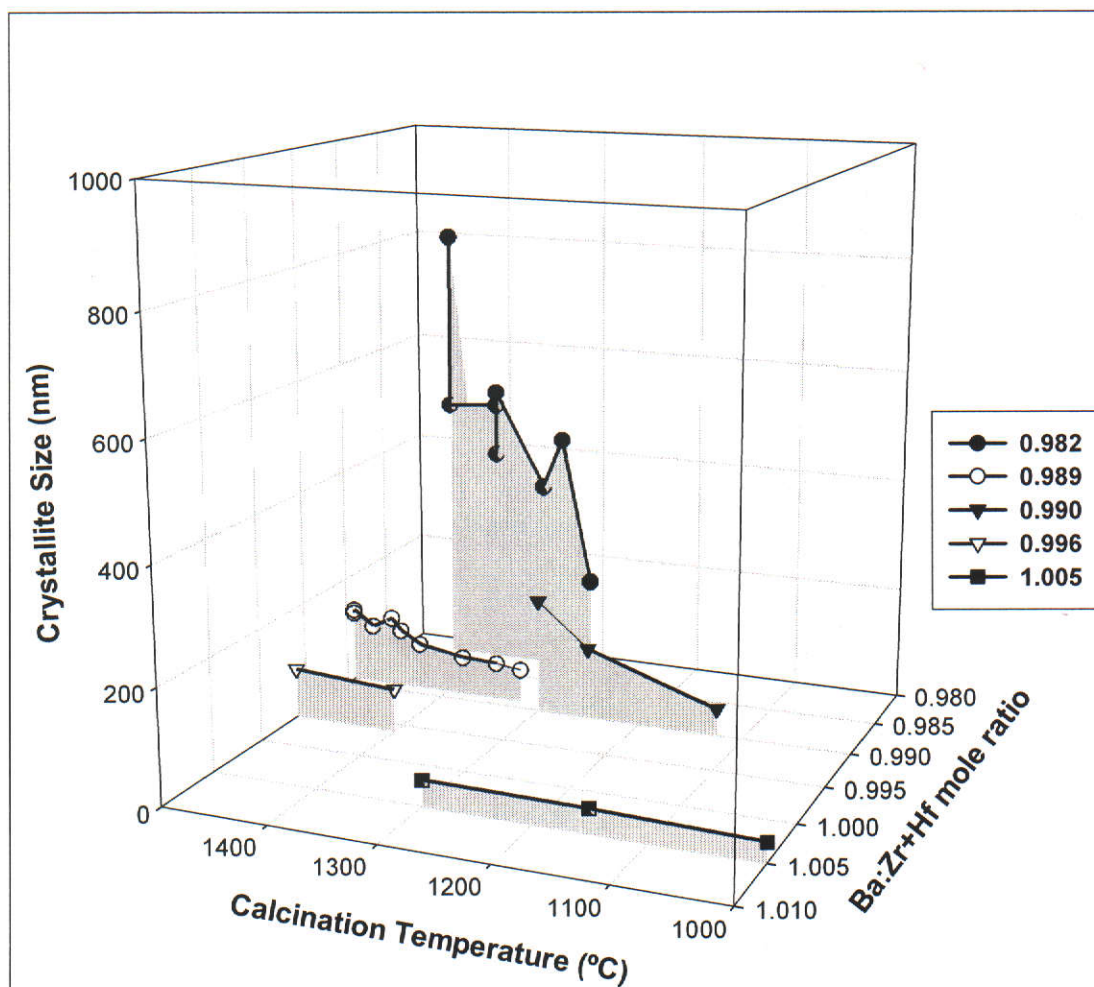


Figure 5.19 Effect of stoichiometry, calcination temperature and chemical contamination on crystallite size of oxalate-precursor derived powders. Crystallite sizes were determined by Voigt Function profile fitting. The samples at  $\text{Ba} : (\text{Zr} + \text{Hf}) = 0.990$  were contaminated with aluminosilicates from process water, and reached large crystallite sizes at calcination temperatures 200 - 300 °C lower than uncontaminated samples.

The position of the sharp transition of crystallite size across the phase boundary for solid-state processing (Figures 5.6 and 5.12) may be indicative of high phase purity, or more specifically, that powder grain growth may occur after removal of Ba-rich residual phases. The sharp transition in the solid-state system occurred very close to unity mole ratio but not until after two calcinations with intermediate re-grinding. The transition in the oxalate system occurred after a single calcination but at a low  $\text{Ba} : (\text{Zr} + \text{Hf})$  mole ratio (0.985, Figure 5.20), suggesting that oxalate derived  $\text{BaZrO}_3$  after a single calcination may not be as phase pure as solid-state derived  $\text{BaZrO}_3$  after two or more calcinations at 1300 °C with intermediate

regrinding. This conclusion is consistent with greater difficulty in sintering oxalate derived powders compared to solid-state derived powders as described in Section 5.6. These observations imply that the oxalate precursors produced in this study were not single phase compounds, which would be expected to decompose to very high phase purity  $\text{BaZrO}_3$  far more readily than solid-state diffusion controlled reactions. A comparison between solid-state and oxalate derived powders is made in Section 5.9.

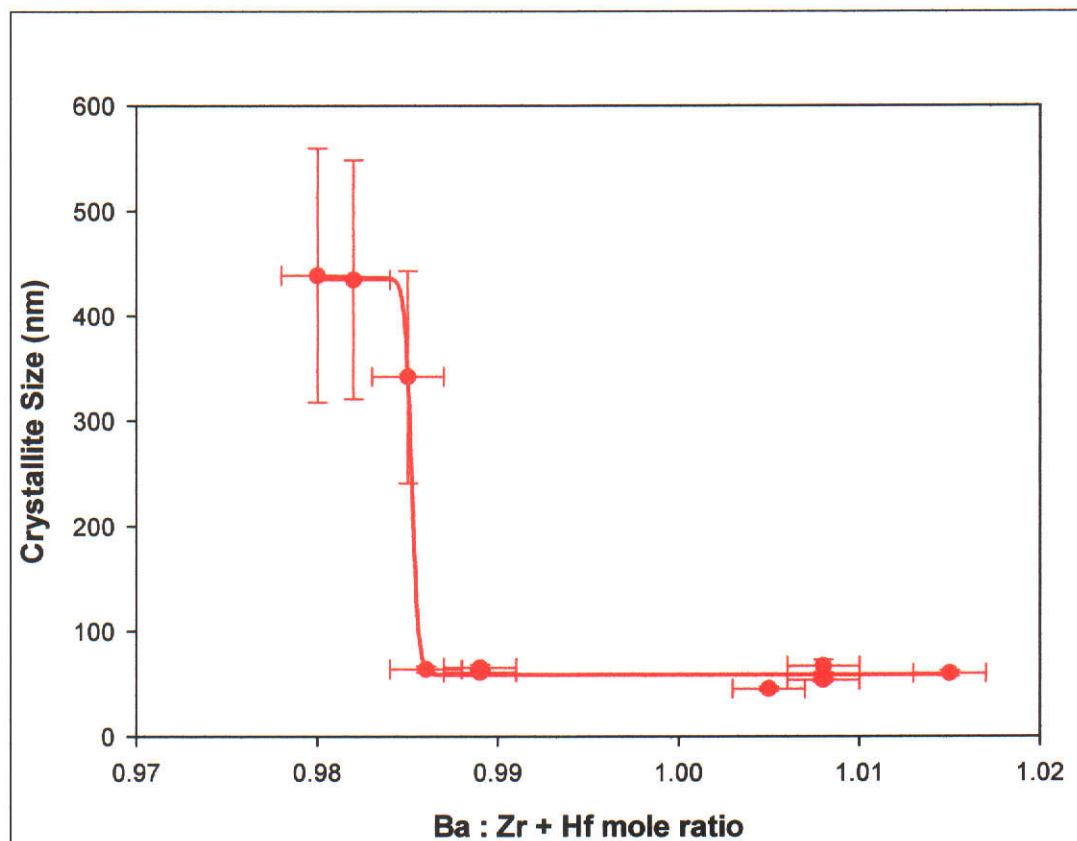


Figure 5.20 Effect of stoichiometry on crystallite size for oxalate-precursor derived powders calcined at 1300 – 1330 °C. Crystallite sizes were determined using Voigt function profile fitting. Uncertainties are  $\pm 2\sigma$ .

The microstructure of calcined oxalate derived powders was affected by the same major factors as solid-state derived powders: calcination temperature and stoichiometry. As shown in Figures 5.21 to 5.28, the primary particle size was in agreement with crystallite sizes determined by XRD. Powders with a Ba : (Zr + Hf) mole ratio below  $\sim 0.985$  produced large, rounded primary particles and those above  $\sim 1.000$  produced small cuboid shaped primary particles. Lattice images (Figures 5.27 and 5.28) show that primary particles were predominantly single crystals.



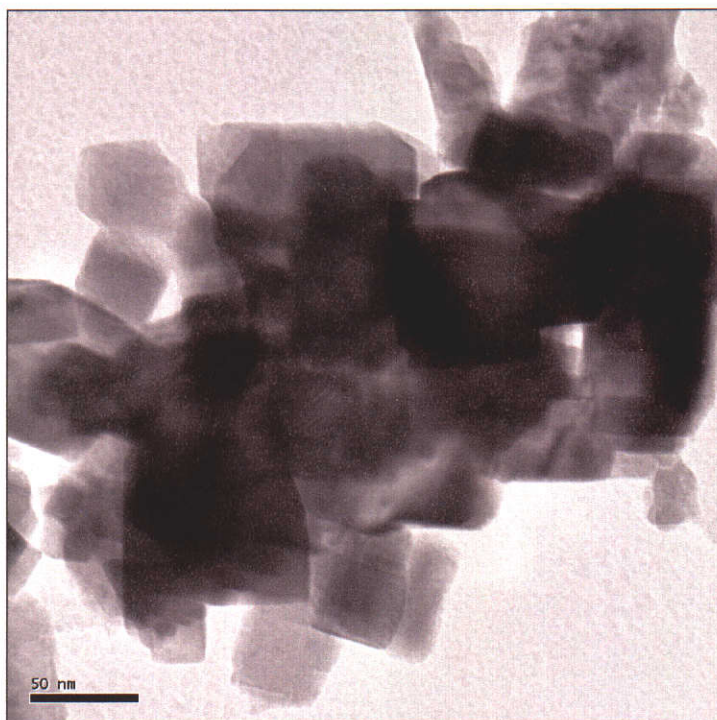


Figure 5.21 TEM micrograph of oxalate-derived powder with Ba : (Zr + Hf) mole ratio of  $0.989 \pm 0.002$  after calcination at 1350 °C for 60 minutes. Scale bar = 50 nm.

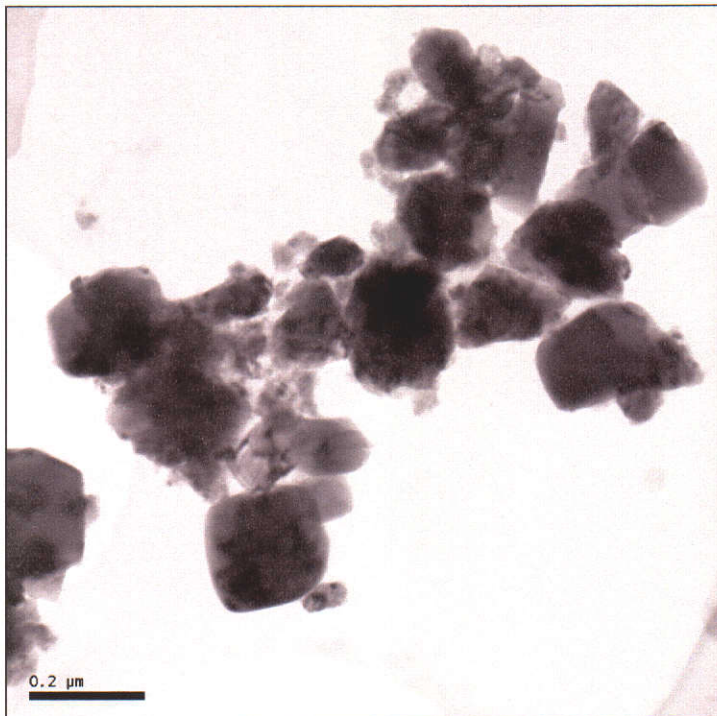


Figure 5.22 TEM micrograph of oxalate-derived powder with Ba : (Zr + Hf) mole ratio of  $0.989 \pm 0.002$  after calcination at 1520 °C for 30 minutes. Scale bar = 200 nm.

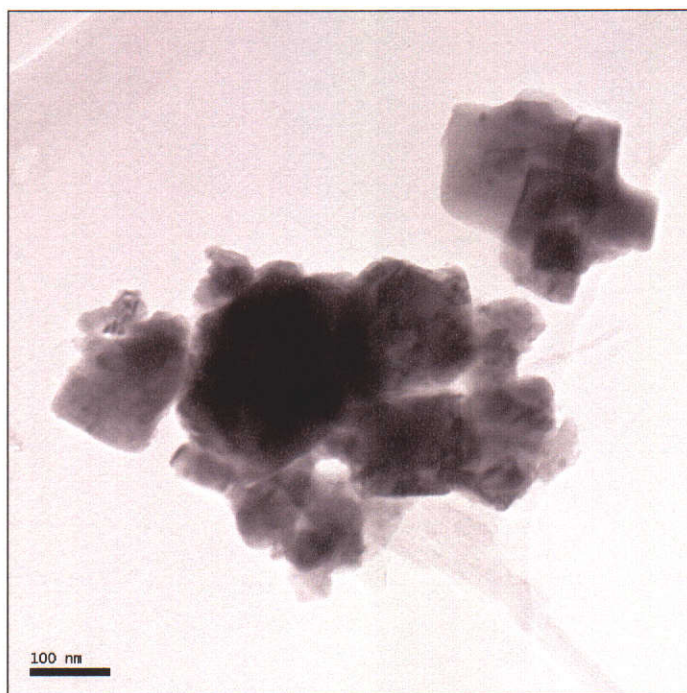


Figure 5.23 TEM micrograph of oxalate-derived powder with Ba : (Zr + Hf) mole ratio of  $0.989 \pm 0.002$  after calcination at 1520 °C for 30 minutes showing hard agglomeration of crystallites (top right of image). Crystallite size by Voigt function profile fitting was  $185 \pm 10$  nm. Scale bar = 100 nm.

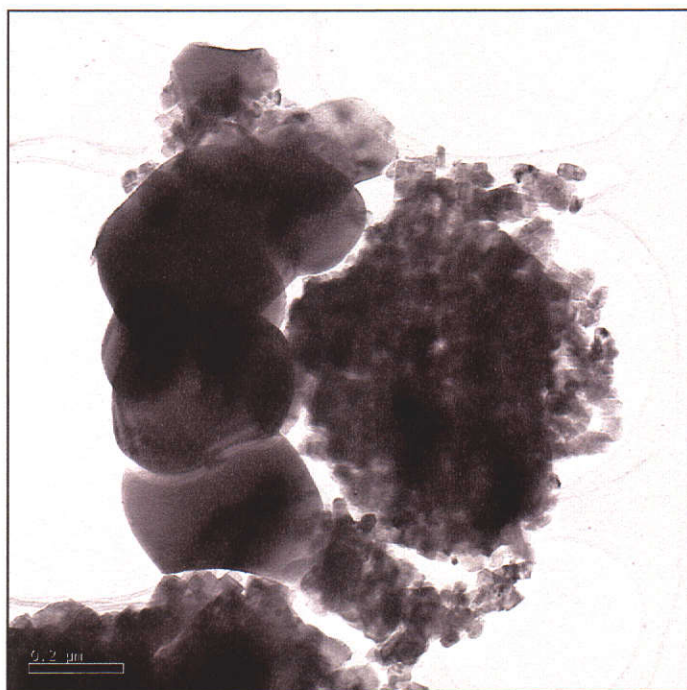


Figure 5.24 TEM image of oxalate derived powder with Ba : (Zr + Hf) mole ratio of  $0.989 \pm 0.002$  after calcination at 1300 °C for 30 minutes. Large spread in primary particle sizes was presumed to be caused by local composition variation in the precursor, with primary particle size reducing with local Ba : (Zr + Hf) mole ratio. Scale bar = 200 nm.



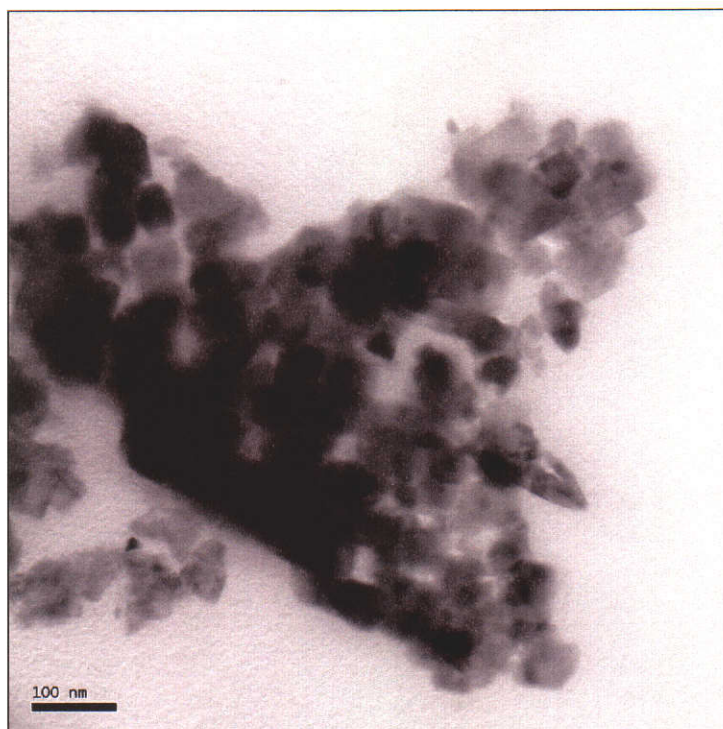


Figure 5.25 TEM of oxalate-derived powder with Ba : (Zr + Hf) mole ratio of  $1.008 \pm 0.002$  after calcination at 1300 °C for 30 minutes. Crystallite size by Voigt profile fitting was  $55 \pm 3$  nm. Scale bar = 100 nm.

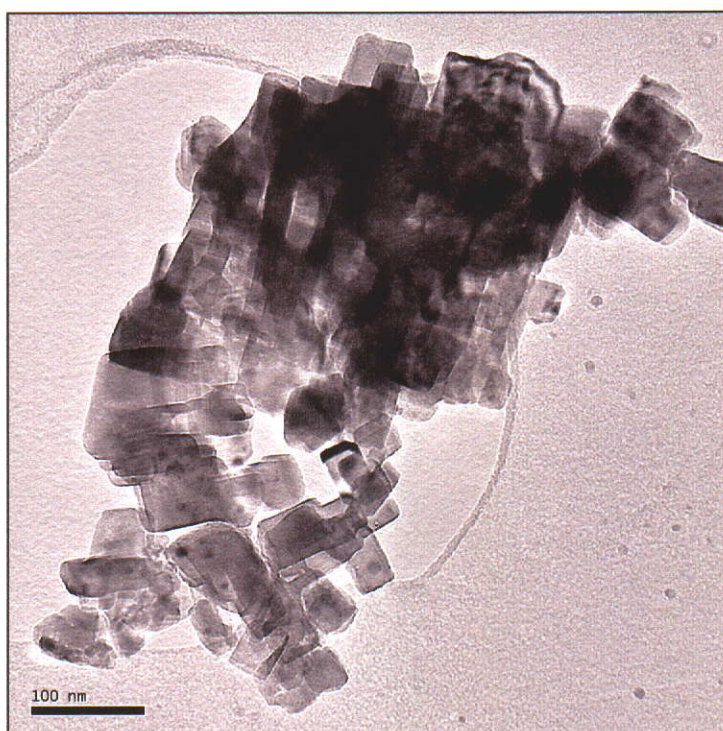


Figure 5.26 TEM image of oxalate derived powder after calcination at 1300 °C for 30 minutes. Small circular spots on particles near lower half of image are  $\text{ZrO}_2$  (confirmed by STEM-EDS mapping) caused by Ba : (Zr + Hf) mole ratio of  $0.989 \pm 0.002$ . Scale bar = 100 nm.



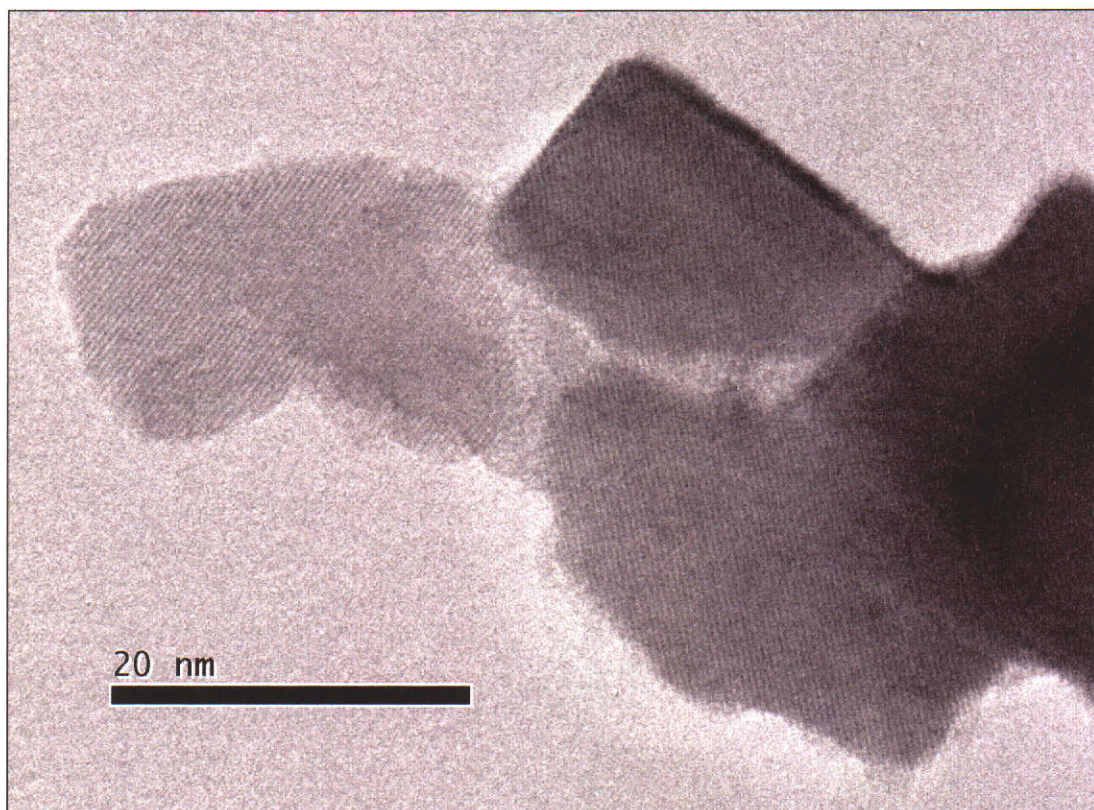


Figure 5.27 TEM lattice image of oxalate derived powder after calcination at 1300 °C for 30 minutes with  $1.008 \pm 0.002$  Ba : (Zr + Hf) mole ratio. Scale bar = 20 nm.

Agglomeration definitely occurred in calcined oxalate derived powders, particularly for zirconium rich powders. Powder samples prepared for XRD analysis were briefly ground using a mortar and pestle. Zirconium rich powders were considerably more difficult to grind than barium-rich powders and contained large hard agglomerates which required quite a lot of pressure to crush by hand. Aggregation was almost certainly exacerbated by simply drying filter cakes of precipitate in an oven. Improved drying processes, such as washing with volatile organic solvents before drying, spray drying or freeze drying may be required to overcome this problem but were not feasible during this project.



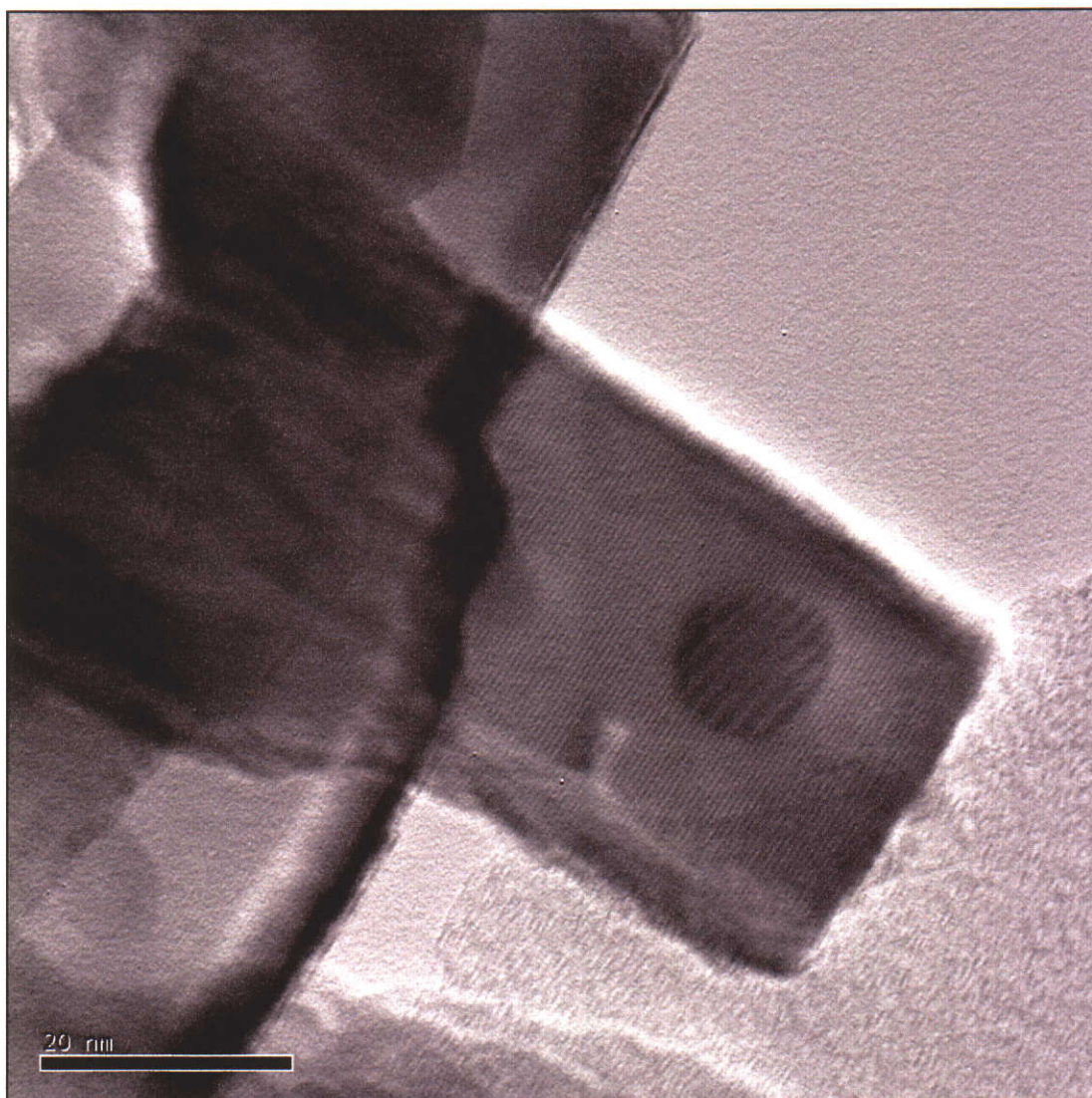


Figure 5.28 TEM lattice image of oxalate derived powder after calcination at 1300 °C for 30 minutes. Circular area of Moiré fringes is  $\text{ZrO}_2$  (confirmed by STEM-EDS mapping) caused by Ba : (Zr + Hf) mole ratio of  $0.989 \pm 0.002$ . Scale bar = 20 nm.

As for the solid-state system, grain growth in calcined powders was observed as an increase in crystallite sizes measured by XRD and the formation of large, rounded primary particles observed by TEM. Rates of grain growth during powder processing are clearly increased by excess unreacted  $\text{ZrO}_2$ . Grain growth at or above 1300°C clearly occurs by solid-state diffusion since decomposition of the oxalate is complete by approximately 1100°C as shown by the TGA data in Figures 5.16 and 5.17, a process inevitably leading to agglomeration. As for other processes, the calcination temperature should be kept to the minimum required to achieve adequate phase purity for the application if forming is conducted using CIP.

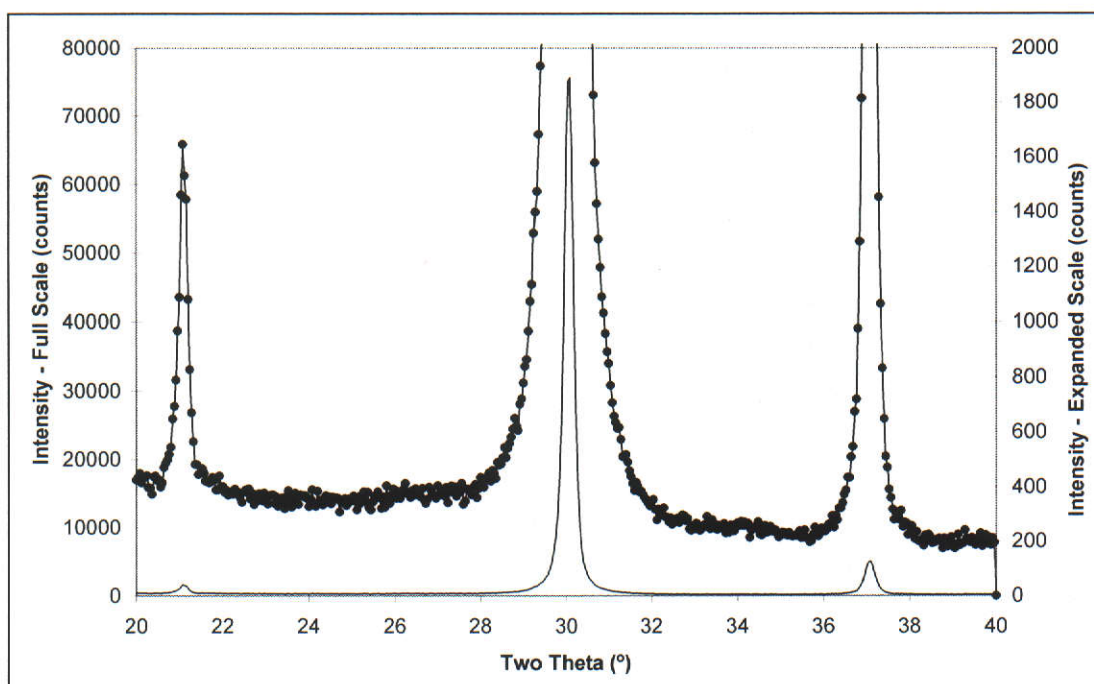


Figure 5.29 Partial XRD pattern of oxalate derived  $\text{BaZrO}_3$  immediately after calcination at  $1300^\circ\text{C}$  for 60 minutes. Sample had Ba : (Zr + Hf) mole ratio of  $0.989 \pm 0.002$ . Note absence of  $\text{BaCO}_3$  peak at  $24^\circ$ .

Near phase-pure  $\text{BaZrO}_3$  was produced at temperatures of  $1300^\circ\text{C}$  or higher. The most intense diffraction peaks of potential secondary phases  $\text{BaCO}_3$  or  $\text{ZrO}_2$  (at  $24.0^\circ$  and  $28.2^\circ$ , respectively) were absent from freshly calcined powder with Ba : (Zr + Hf) mole ratio of 0.989 shown in the expanded view in Figure 5.29 and Figure 5.30.  $\text{BaCO}_3$  was detected in calcined samples after exposure to air, particularly for samples with an excess of barium or with low calcination temperatures as shown in Table 5.3. As discussed in Section 5.2, the amount of  $\text{BaCO}_3$  formed after air exposure depends on the phase purity and surface area of powders. Without surface area measurements and a quantitative correction for the effect of surface area on  $\text{BaCO}_3$  formation it is difficult to accurately assess the relative phase purity of powders as a function of calcination treatment. There was some inconsistency between  $\text{BaCO}_3$  levels of freshly calcined powder due to scheduling delays between calcination cycles and XRD measurement as well as variations in humidity, but the trends for  $\text{BaCO}_3$  levels after air exposure were quite clear.



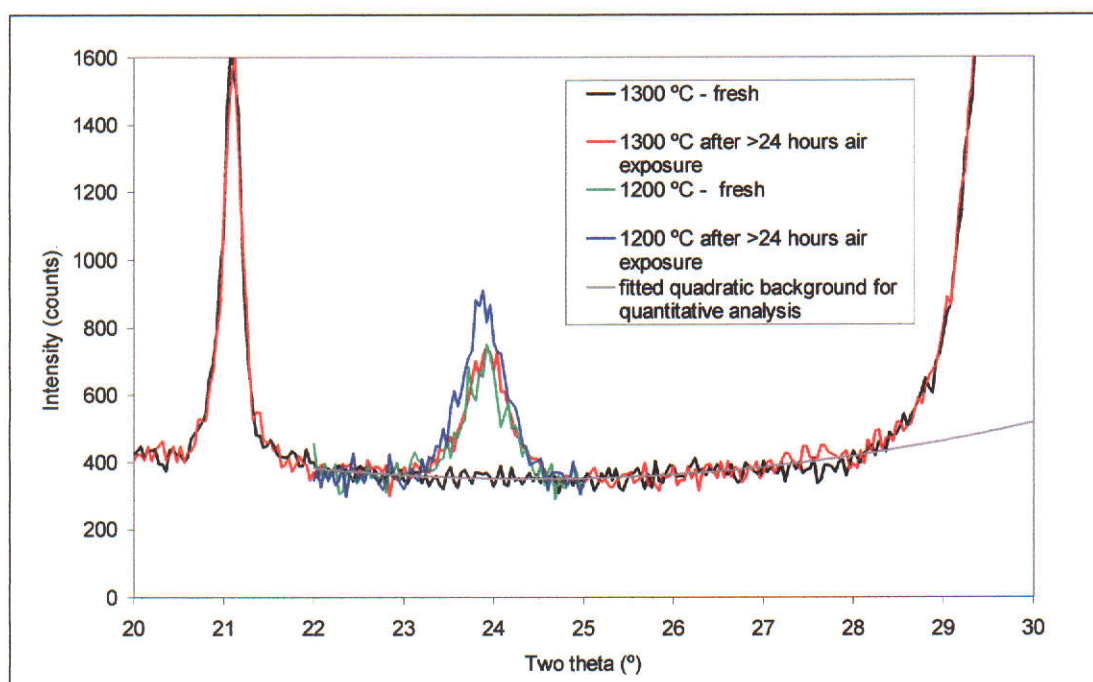


Figure 5.30  $\text{BaCO}_3$  diffraction peaks for calcined oxalate-derived powders with Ba : (Zr + Hf) mole ratio of  $0.986 \pm 0.002$ .

Table 5.3 Effect of calcination temperature and stoichiometry on  $\text{BaCO}_3$  levels in calcined oxalate-derived powders. Errors in crystallite sizes are  $\pm 1\sigma$ .

Ba : (Zr + Hf) mole ratio	Calcination Temperature (°C)	Crystallite Size (Voigt) (nm $\pm \sigma$ )	Wt.% $\text{BaCO}_3$ before air exposure ( $\pm 0.5$ )	Wt.% $\text{BaCO}_3$ after > 24 hours air exposure ( $\pm 0.5$ )
0.986	1200	49 ( $\pm 1$ )	4.3	6.5
0.986	1300	63 ( $\pm 2$ )	undetected (i.e. $< 0.15$ )	1.0
1.005	1000	35 ( $\pm 1$ )	3.8	10.7
1.005	1150	42 ( $\pm 1$ )	undetected (i.e. $< 0.15$ )	4.1
1.005	1300	45 ( $\pm 2$ )	1.0	4.0
1.008	1300	53 ( $\pm 5$ )	1.2	6.3

#### 5.4 Comparison between solid-state and oxalate derived powders

Figure 5.31 shows there was little difference between solid-state and oxalate derived  $\text{BaZrO}_3$  powders when compared as a function of BET surface area. Surface areas of solid-state derived powders were varied using different regrinding and calcination procedures, and oxalate derived powder surface areas were controlled by varying calcination times. A more comprehensive analysis (e.g. over a range of stoichiometry) was not possible due to limited access to BET instrumentation.

Comparison of phase purity requires consideration of surface areas because as discussed in Section 5.2,  $\text{BaCO}_3$  levels after air exposure are affected by phase purity and surface area. The driving force for sintering is the reduction of surface energy, hence ideal powders for high quality ceramics should have high phase purity and high surface area. Both solid-state and oxalate processing require a compromise between phase purity and surface areas of powders.

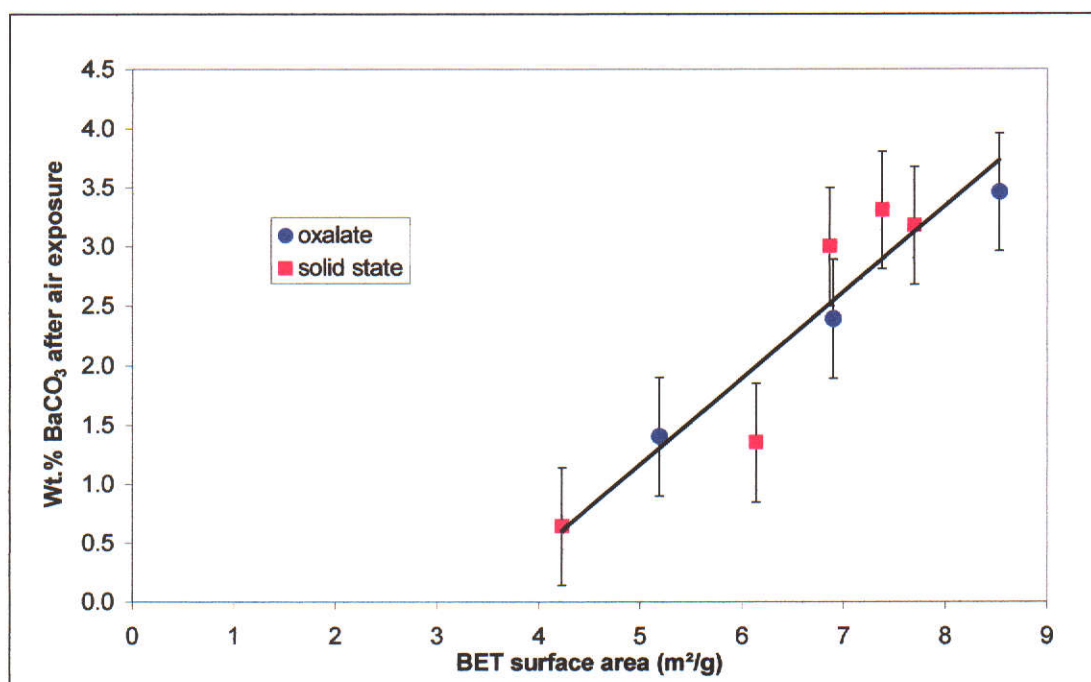


Figure 5.31  $\text{BaCO}_3$  levels of solid-state and oxalate derived  $\text{BaZrO}_3$  powders after air exposure with Ba : (Zr + Hf) mole ratios of 0.989 to  $0.995 \pm 0.002$ .

Unfortunately, a quantitative analysis of the effect of surface area on  $\text{BaCO}_3$  levels after air exposure was not possible because of limited access to BET instrumentation. This could be attempted using powders of very high phase purity without Ba-rich residual phases produced by repeated calcination and sintering of Zr-rich powder, with BET surface areas and  $\text{BaCO}_3$  levels measured as a function of ring milling time. Any increase in  $\text{BaCO}_3$  levels of unknown powders could be quantitatively attributed to Ba-rich phase impurities. The nearest approximation to this approach with the available data is shown in Figure 5.32. If the most highly processed powders are assumed to contain no Ba-rich residual phases, and the amount of  $\text{BaCO}_3$  formed during air exposure is assumed proportional to surface area, the slope of this line can be applied to other powders to estimate the amount of  $\text{BaCO}_3$  formed from Ba-rich phases. The accuracy in this data set is poor, but illustrates the concept and a possible method by which quantitative analysis of Ba-rich phase impurity may be attempted in further research.

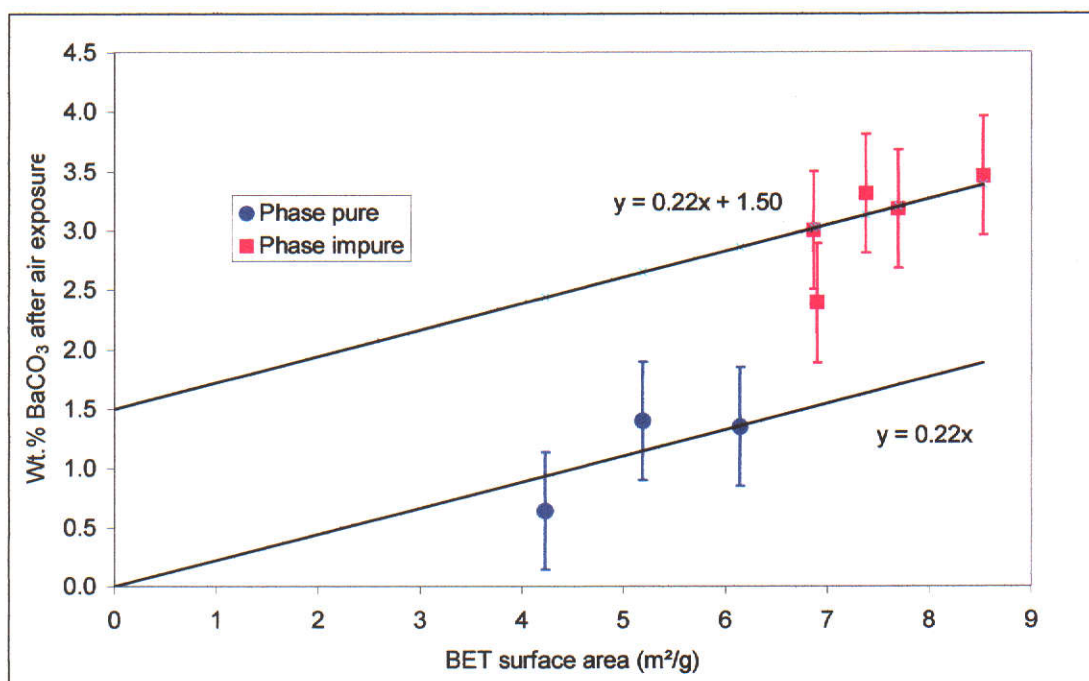


Figure 5.32 Approximate estimate of Ba-rich phase impurities of powders with Ba : (Zr + Hf) mole ratio of 0.989 to  $0.995 \pm 0.002$ . Powders in blue are assumed phase pure to estimate contribution of  $\text{BaZrO}_3$  surface area to observed  $\text{BaCO}_3$  levels after air exposure.



## 5.5 Selection of forming processes

### 5.5.1 Slip casting

The two available options for forming green ceramics were slip casting and cold isostatic pressing (CIP). Slip casting is a technique where a powder is dispersed in a fluid, usually water to form a dispersion termed "slip". The slip is poured into a porous mould typically made of Plaster of Paris. As capillary suction from the mould dewateres the slurry, a layer of green ceramic is deposited at the surface of the mould. Once the desired thickness has been allowed to deposit, excess slip is poured out of the mould, and the green-form is dried under controlled conditions (Richerson 1992). Slip casting was attempted because if successful, it would offer a ready means of mass production. Moulds can easily be made from Plaster of Paris in large numbers in a wide range of shapes and sizes to suit particular applications.

The aim of successful slip casting is to produce a high density casting to control shrinkage during drying and promote densification during sintering. Slip casting is only successful where a stable liquid dispersion can be produced at high solids content. Inadequate dispersion permits inter-particle attraction to cause poor particle packing in the slip and cast body and increased slip viscosity. The casting properties of slips are affected by the stability of the dispersion and particle size distribution of the powder. A large number of variables influence the stability of a dispersion, including the adsorption, charge and steric properties of dispersant(s) used, the amount of dispersant added, dielectric properties of the fluid, particle surface properties, particle size distribution and agglomeration state, pH, surface composition, impurities and volume fraction of solids in the slip.

High sintered density requires high green density at low particle size presenting conflicting demands for casting of fine particle slips. For well packed green bodies, reduced particle size increases sintered density due to increased surface energy available for densification. A maximum particle size exists above which the very high sintered densities required for this application cannot be achieved without sintering aids. However, as particle size is reduced, it becomes increasingly difficult to produce a dispersion at high solids loading sufficiently stable for slip casting. At fixed solids loading, reduced particle size causes reduced average separation between particles and increased secondary attraction between particles, which favours



aggregation of particles into porous clusters known as flocs. Flocculation causes increased slip viscosity, but most importantly causes poor particle packing in the casting. Poor particle packing causes increased green porosity leading to increased drying shrinkage, greater tendency for cracking, and increased sintered porosity. A minimum particle size exists for a fixed set of slip casting conditions, below which dispersion problems are too great to allow casting of an adequate green body. Figure 5.33 shows a ceramic with very high porosity despite 12 hours sintering, partly because the particle size used for slip casting failed to produce adequate green structure. The challenge of establishing a slip casting process is to find a set of stable dispersion conditions in which a slip can be prepared at high solids loading which casts into a sufficiently dense green body using a particle size low enough to allow densification during sintering.

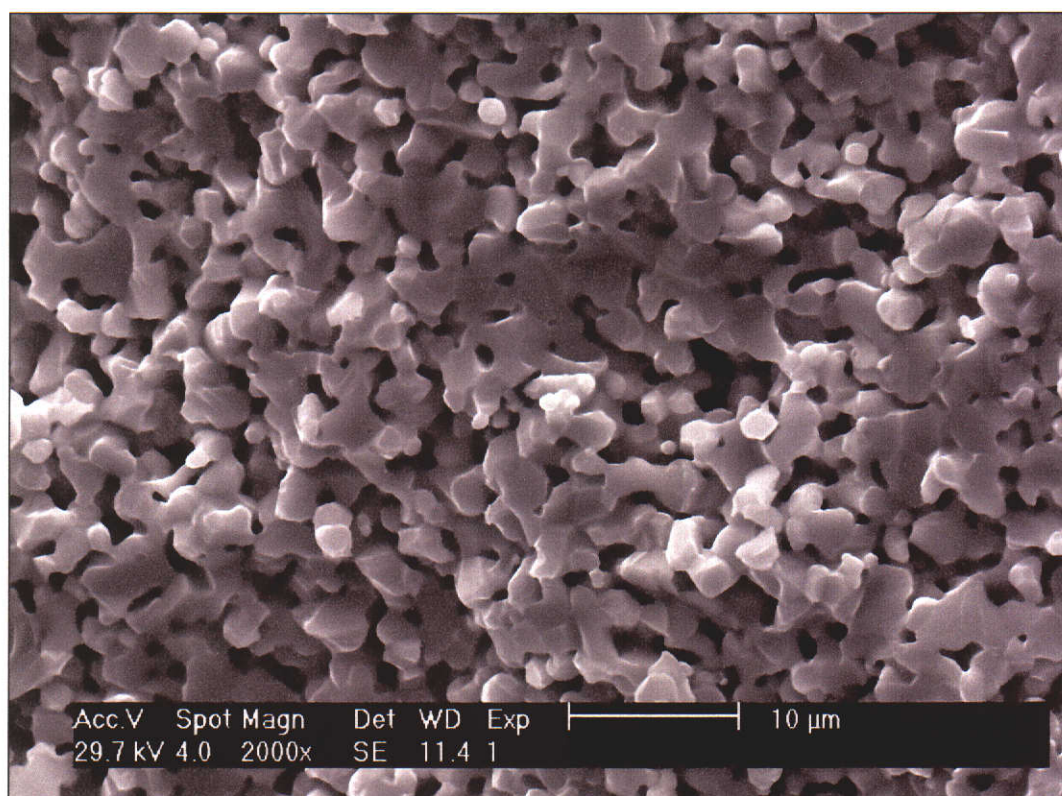


Figure 5.33 SEM micrograph of fracture surface of slip cast oxalate-derived  $\text{BaZrO}_3$  after sintering at 1630 °C for twelve hours. Very high porosity (25 vol.%) was due to poor green density and inadequate sintering temperature. Continuous porosity may make this material suitable for applications such as humidity sensors but totally unsuitable for melt containment.

The sintered highest density achieved for slip cast crucibles was 99.3 % of theoretical, using a powder with a Ba : (Zr + Hf) mole ratio of  $0.960 \pm 0.002$  and sintered for 12 hours at 1650 °C. The casting properties of this slip were assisted by larger particle sizes ( $190 \pm 25$  nm) accessible at Ba : (Zr + Hf) mole ratios below one. This density result was artificially high due to aluminosilicate contamination from poor quality de-ionised process water used for early batches of oxalate precursors. These contaminants lead to greatly improved sintering kinetics and barium aluminosilicate precipitates ( $\sim 30$  nm) as shown in Section 6.5.4, at approximately 5 % of the triple points in the ceramic. After contamination was eliminated by changing to high purity de-ionised process water, a great deal of effort was needed to produce sintered densities above 90 % of theoretical and required sintering temperatures of at least 1700 °C (Figure 5.35). Greatly improved sintering properties are possible through doping with chemical impurities to cause crystallographic defects which increase diffusion rates during solid-state sintering (Richerson 1992, p. 529). Deliberate addition of impurity elements may be an important method of overcoming the significant processing difficulties of relatively high purity BaZrO<sub>3</sub> encountered in this project, and may provide a means of routine high quality crucible fabrication not otherwise readily achieved at high chemical purity. High purity water was used for all oxalate processing of ceramics used for corrosion resistance studies.

Numerous trials were conducted attempting to develop an adequate slip casting process. Of the many variables affecting slip casting, this project focused on particle size (as controlled by stoichiometry and processing conditions), dispersant levels and pH. Dispersant levels had a significant effect on sintered densities as shown in Figure 5.34. The powder used for that experiment had a crystallite size of  $190 \pm 15$  nm, but optimal dispersant levels were dependent on particle size and pH. Particles smaller than  $\sim 100$  nm required increased dispersant levels (between 2.0 - 3.0 wt.%) to produce low slip viscosities. As suggested by Figure 5.34, high dispersant levels adversely affected green and therefore sintered density. Although the weight percentages of dispersant used may appear to be quite low, the dispersant actually occupies a significant volume fraction of the green body because of the large difference in densities of the two phases. Addition of dilute ammonia solution

slightly reduced the viscosities of most slips, but adequate sintered densities could not be routinely achieved.

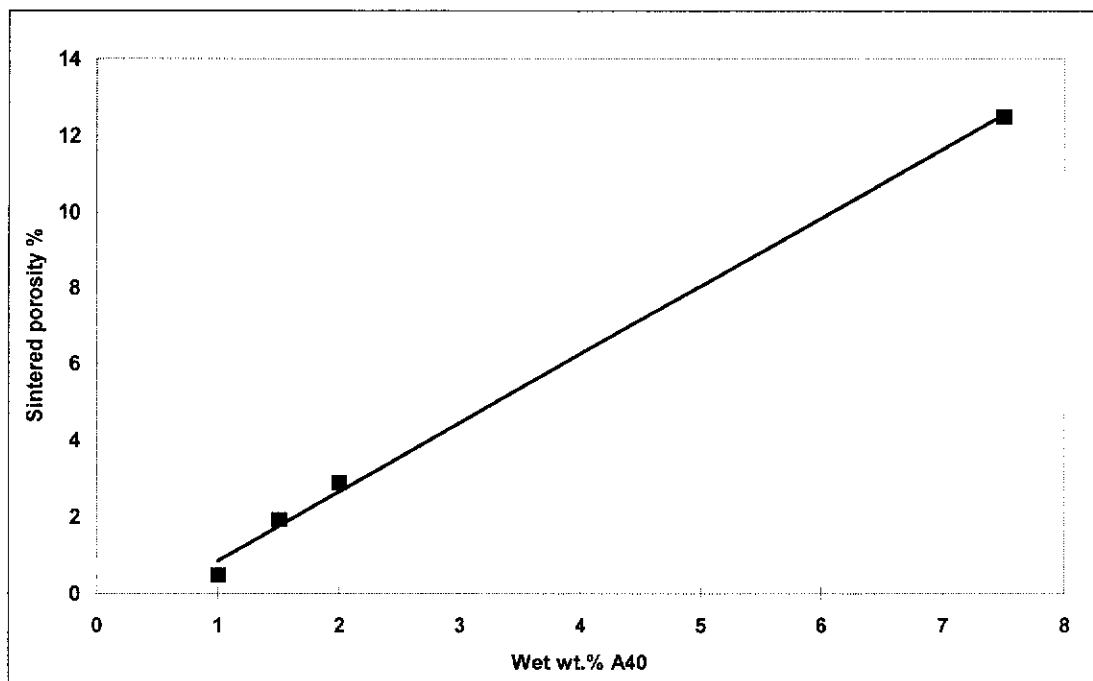


Figure 5.34 The effect of A40 dispersant level on sintered densities of slip cast  $\text{BaZrO}_3$ . The powder used for this study had a crystallite size of  $205 \pm 45$  nm.

Figure 5.35 shows the effect of powder crystallite size on the sintered porosity of slip cast  $\text{BaZrO}_3$ . The optimal crystallite size of  $\sim 150 - 200$  nm for slip cast articles represents the best compromise between poor sintering properties of particles larger than  $\sim 300$  nm and poor dispersion of particles smaller than  $\sim 100$  nm under the conditions used in these experiments. The samples indicated with blue markers in Figure 5.35 contained aluminosilicate contamination either from process water or porcelain crucibles used during calcination, which may have produced an artificially low porosity. Uncontaminated samples indicated by black or pink markers in Figure 5.35 were much more difficult to sinter.

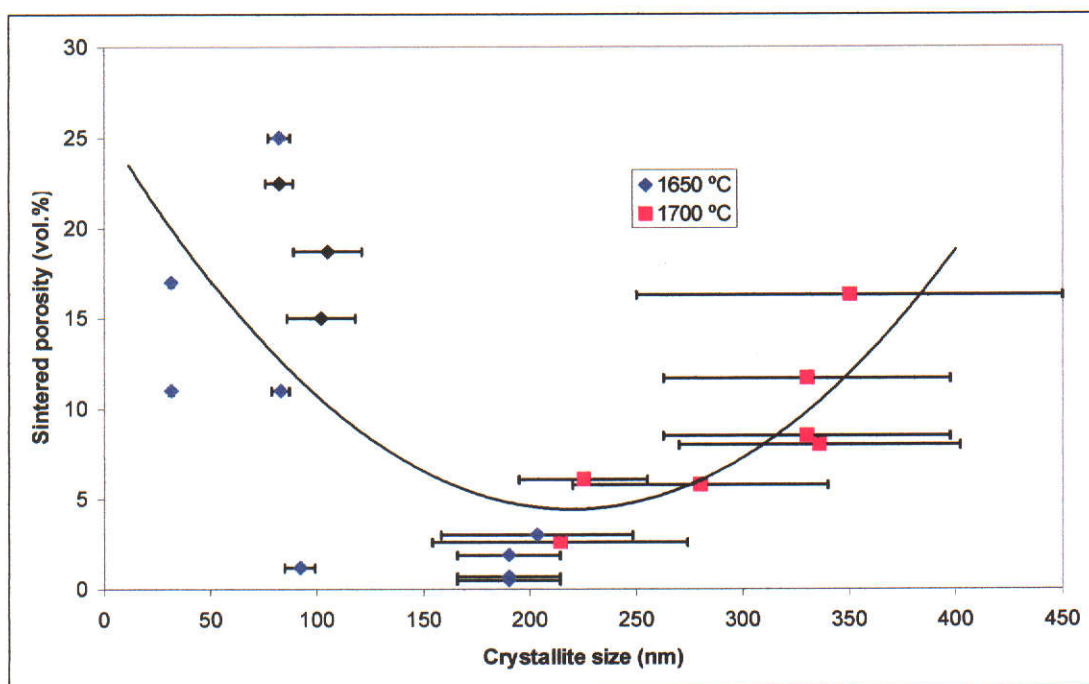


Figure 5.35 Effect of powder crystallite size and sintering temperature on sintered porosity of slip cast BaZrO<sub>3</sub>. Each slip was prepared so as to minimise viscosity by controlling pH and dispersant levels. All points indicated by blue markers contained aluminosilicate contamination either from process water or porcelain crucibles used during calcination. Crystallite size uncertainties are  $\pm 2 \sigma$ .

Improved dispersion is required before slip casting could be routinely employed for high density BaZrO<sub>3</sub> fabrication. Slip casting of BaZrO<sub>3</sub> at the desired stoichiometry for corrosion resistance is very challenging because the inherent particle grain growth resistance of slightly Ba-rich BaZrO<sub>3</sub> powders makes the production of un-agglomerated powders with particle sizes greater than  $\sim 100$  nm quite difficult. As shown in Figure 5.35, poor dispersion of sub  $\sim 100$  nm particles using aqueous ammonium polyacrylate based slips probably precludes routine production of high density ceramics. Slips made from sub  $\sim 100$  nm particles required increased dispersant levels, typically cast slowly and produced soft, plastic castings with high moisture content and high drying shrinkage because of poor particle dispersion. Slips made with large particle sizes cast much more readily and displayed lower drying shrinkage, but did not sinter to acceptable densities.

Investigation of whether a set of slip casting conditions could be established to produce high density ceramics using dispersants and equipment available to this



project proved to be a particularly difficult and ultimately unsuccessful task. Unfortunately, our laboratory had virtually no facilities available for optimisation of slips: development was done merely by visual observation of slip viscosities. Inter-particle attraction causes increased viscosity, and hence viscosities were used as the primary method of comparing dispersion stabilities. Zeta-potential measurements would have greatly aided optimisation of surface charges but instrumentation was not accessible. Due to the high density of  $\text{BaZrO}_3$ , significant quantities of powder are required to produce sufficient volumes of slips at high solids loadings for optimisation of casting and sintering properties. For much of this project, particularly for oxalate precursor development, quantities of powders were at a premium. Also, slip casting optimisation was conducted predominantly using oxalate-derived powders before the strong effect of stoichiometry on processing properties was discovered, and difficulty in reproducing particle sizes and surface areas significantly hampered progress.

Erb stated that use of water during solid-state powder processing must be avoided, and that inert milling fluids such as alcohols should be used (private communication, 2002). For the same reasons as those affecting solid-state powder processing (i.e. hydrolysis), the use of aqueous casting processes may be inherently unsuitable for corrosion resistant crucible fabrication. The inherently low particle size of  $\text{BaZrO}_3$  at the desired stoichiometry for corrosion resistance makes slip casting particularly difficult. This could be countered by increasing calcination temperatures, but increased agglomeration may still render slip casting of high purity  $\text{BaZrO}_3$  unfeasible.

### **5.5.2 Cold isostatic pressing**

Cold isostatic pressing (CIP) is a much simpler process for shape forming than slip casting. High green density can be achieved if the particle size distribution, shape and agglomeration state allow efficient particle packing and if the applied hydrostatic pressure is able to overcome inter-particle friction at the desired level of compaction. Although small particle size may increase inter-particle friction, the effects of ultra-fine particle size are less demanding on CIP than on slip casting. CIP

permitted green forming using particle sizes down to 65 nm (Voigt crystallite size) without obvious problems, whereas slip casting was not feasible for particles of this size (Figure 5.35).

Cetyl alcohol was added as a solid lubricant as described in Section 4.12 to aid compaction by reducing inter-particle friction, and also to serve as a binder to reduce the brittleness of green crucibles. Powders close to the optimum stoichiometry for corrosion resistance required 2.5 - 3.0 wt.% cetyl alcohol for reliable green forming by CIP. The green density of an isostatically pressed oxalate derived powder increased from 55.6 to 57.5 % of theoretical by addition of 5 wt% lubricant (density comparison included correction for the weight of lubricant). Cracked green forms could be re-milled, with additional lubricant if necessary, and re-used. Minor cracking problems persisted at 2.0 wt.% lubricant or below, but were avoided at a 3.0 wt.% addition of cetyl alcohol. The tendency for cracking was increased if the CIP pressure release rate was too high. Any cracks in green forms noticeable after de-moulding persisted after sintering. Given the poor sintering kinetics of this material, it was assumed that any microscopic defects in green bodies remain after sintering. Using slightly too much lubricant was considered to be better than using too little, because percolation through cracks could severely reduce the duration of melt tightness.

Cold isostatic pressing proved to be a far more reliable and simple method of shape forming than slip casting. After the first trial of CIP forming, no powders were subsequently lost during shape forming and only a few crucibles required re-forming because too little lubricant had been used for an initial pressing. CIP also allows crucibles with a wide range of wall thickness to be formed, whereas wall thicknesses in slip casting are limited by the casting and shrinkage properties of slips. Wall sections in crucibles formed by CIP were typically 2 – 3 mm thick, and are only restricted by mould geometry. Wall sections greater than ~2 mm for slip cast crucibles could only be achieved for fast casting slips with low drying shrinkage, but such casting could not be sintered to high density.

## **5.6 Sintering development**

Sintering temperatures were chosen at essentially only two levels considering previous literature and the limitations of available furnace equipment: ~1645 °C and 1700 - 1710°C. The furnaces routinely available to this project were molybdenum disilicide muffle furnaces capable of routine operation at 1650°C. At higher temperature, degradation to elements, refractory linings and Pt-Rh control thermocouples increased rapidly, and 1710 °C was the upper limit beyond which risk of furnace damage was unacceptable. Furnace degradation problems still required the number of firings to be kept to a minimum. One group of samples was sintered at 1750 °C using an alternative furnace, which confirmed that corrosion problems were not simply due to inadequate sintering temperatures.

Table 5.4 shows that sintering temperatures of at least 1700 °C were required to produce adequate density for melt containment. These results are consistent with those of Erb, Walker and Flükiger (1995) and Liang, Bonn and Hardy (1998). Crucibles formed by CIP were easy to sinter to densities higher than 98% at 1750 °C, but such furnace equipment was not regularly available to this project. Sintering at 1650 °C was unsuccessful for all samples free of aluminosilicate contamination.

Table 5.4 Sintered porosities of solid-state derived BaZrO<sub>3</sub> ceramics formed using uniaxial or cold isostatic pressing.

Sintering Time (hours)	Ba : (Zr + Hf) mole ratio (± 0.002)	Wt.% lubricant	Sintering Temperature (°C)	Porosity (vol.%) (± 0.2)
12	0.996	0	1645	21.1 <sup>0</sup>
12	0.996	3.0	1645	19.3 <sup>0</sup>
12	0.998	3.0	1710	5.8 <sup>1</sup>
12	0.998	3.0	1710	1.5 <sup>2</sup>
6	1.002	3.0	1700	2.0 <sup>3</sup>
6	0.998	3.0	1700	2.2 <sup>3</sup>
6	1.001	3.0	1700	2.3 <sup>3</sup>
6	0.999	3.0	1700	3.1 <sup>3</sup>
6	1.006	2.5	1710	0.3 <sup>4</sup>
6	1.013	2.5	1710	-
6	1.003	2.5	1710	-
6	1.003	3.0	1710	1.1 <sup>4</sup>
6	0.995	3.0	1750	0.5 <sup>2</sup>
6	1.005	3.0	1750	0.6 <sup>2</sup>
6	1.015	3.0	1750	0.8 <sup>2</sup>
6	1.025	3.0	1750	0.5 <sup>2</sup>

<sup>0</sup> powder was oxalate-derived. Result included to show sintering temperature effect.

<sup>1</sup> pellet uniaxially pressed at 30 MPa followed by CIP at 200 MPa.

<sup>2</sup> formed by 200 MPa CIP only.

<sup>3</sup> uniaxially pressed at 90 MPa (no CIP).

<sup>4</sup> uniaxially pressed at 150 MPa (no CIP).

Table 5.5 shows sintered densities for oxalate-derived powders. The goal of efficient low temperature sintering using chemically derived powders was not achieved. The use of calcination temperatures below 1300 °C to limit particle size and agglomeration of powders did not result in improved sintered densities, presumably as a result of reduced powder phase purity. Calcination temperatures



below 1300 °C are not recommended, and whether improvement in the sintering properties of oxalate derived powders can be improved using more elevated calcination temperatures requires further experimentation. There was some evidence to suggest that an extended period for lubricant burnout during sintering may improve sintered density, but further experimental confirmation is required.

Table 5.5 Sintered porosities of uniaxially or isostatically pressed oxalate derived powders.

Ba : (Zr + Hf) mole ratio ( $\pm 0.002$ )	Calcination Temperature (°C)	Crystallite Size (Voigt) (nm $\pm 1\sigma$ )	Sintering Temperature (°C)	Sintering Time (hours)	Sintered Porosity (vol.% $\pm 0.2$ )
0.960	1300	190 ( $\pm 12$ )	1650	12	0.7 <sup>1</sup>
0.948	1370	-	1650	10	5.7 <sup>2</sup>
0.986	1300	63 ( $\pm 2$ )	1700	6	5.4
1.005	1000	35 ( $\pm 1$ )	1700	6	9.6
1.005	1150	42 ( $\pm 1$ )	1700	6	10.1
1.005	1300	45 ( $\pm 1$ )	1700	6	5.5
1.005	1300	45 ( $\pm 1$ )	1700 <sup>3</sup>	6	3.6
1.008	1300	53 ( $\pm 2$ )	1700	6	2.6
1.016	1300	59 ( $\pm 2$ )	1700	6	5.5

<sup>1</sup> Slip cast aluminosilicate contaminated sample.

<sup>2</sup> Slip cast sample without aluminosilicate contamination.

<sup>3</sup> Sintering procedure used an extended isothermal treatment at 1000 °C to try to ensure maximum lubricant removal.

Figure 5.36 shows a photograph of a finished ~ 7 mL crucible formed by isostatic pressing. The detailed dimensions of isostatically pressed crucibles are presented in Appendix 4, which can readily be changed by the design of the mould. The insides of crucibles were significantly tapered to allow easy removal from the mould and had very smooth surfaces from the polished steel die used.



Figure 5.36 Sintered solid-state derived crucible ready for single crystal growth.  
Smallest division on ruler is 1 mm.

## CHAPTER 6

# SINTERED CERAMICS, MELT CORROSION AND HIGH PURITY CRYSTALS

---

### 6.1 Introduction

Powder synthesis, forming and sintering development presented in Chapter 5 provided the necessary processing capability with which to develop corrosion resistant ceramics. Chapter 6 presents work done on the development and analysis of corrosion resistant sintered ceramics, describes attributes required for corrosion resistance and discusses aspects of mechanisms of corrosion failure. Basic properties of high purity  $\text{YBa}_2\text{Cu}_3\text{O}_{7-8}$  single crystals grown in a solid-state derived  $\text{BaZrO}_3$  crucible are presented at the end of the chapter.

### 6.2 Basic microstructural analysis

The desired microstructure for maximum corrosion resistance is dense, crack free, phase pure  $\text{BaZrO}_3$  with a fine grain size (Erb, Walker and Flükiger 1995; Liang, Bonn and Hardy 1998). Fine grain size is required for thermal shock resistance and to allow re-use of crucibles for single crystal growth experiments (Liang, Bonn and Hardy 1998). Grain sizes of sintered ceramics were evaluated using optical microscopy and SEM. Fine grain size (approximately 5  $\mu\text{m}$ ) was characteristic throughout the body of all Zr-rich ceramics produced in this study. However, Ba-rich solid-state derived ceramics typically displayed a dramatic increase in grain size within the interior of sintered materials. The dramatic effect of stoichiometry on sintered grain sizes of solid-state derived  $\text{BaZrO}_3$  is shown in Figure 6.1. As shown in Figure 6.2, excessive grain growth did not occur within  $\sim 100 - 200 \mu\text{m}$  of external surfaces in all samples made in this project. Exaggerated grain growth occurred only in Ba-rich solid-state derived samples and did not occur in any oxalate derived samples irrespective of stoichiometry. The typical fine grained microstructure of Ba-rich oxalate derived ceramics is shown in Figure 6.3. The transition in grain size occurred precisely at the phase boundary and required only a very small change in stoichiometry to occur. An increase in Ba : (Zr + Hf) mole ratio



from 0.996 to 1.000 ( $\pm 0.002$ ) caused grain sizes in the interior of samples to increase from a few micrometres to several hundred micrometres. This effect occurred for sintering temperatures of 1700 and 1750 °C.

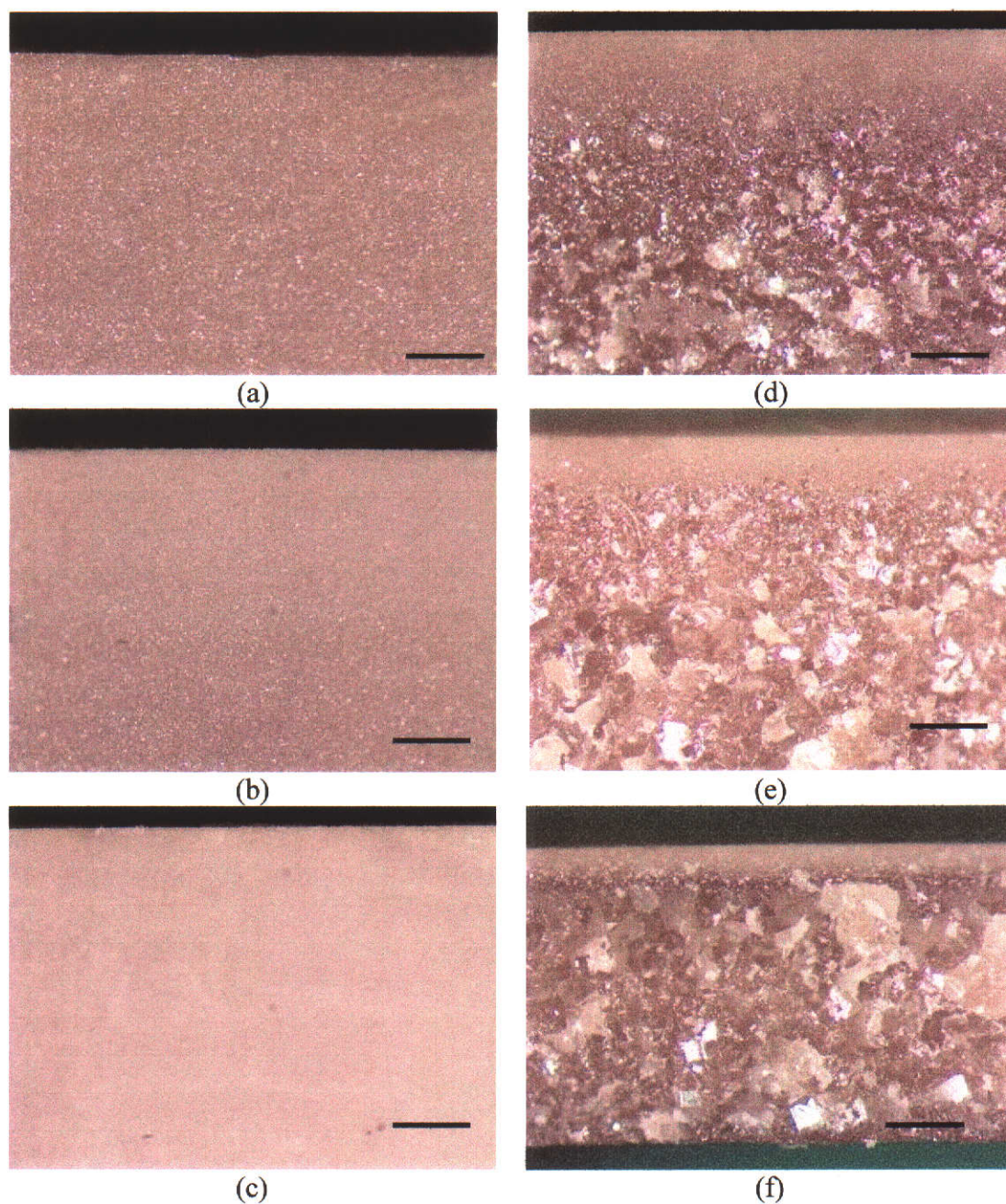


Figure 6.1 Optical micrographs of fractured surfaces of BaZrO<sub>3</sub> pellets with Ba : (Zr + Hf) ratio (a) 0.965, (b) 0.988, (c) 0.996, (d) 1.000, (e) 1.002 and (f) 1.010. Scale bar = 500  $\mu\text{m}$ .



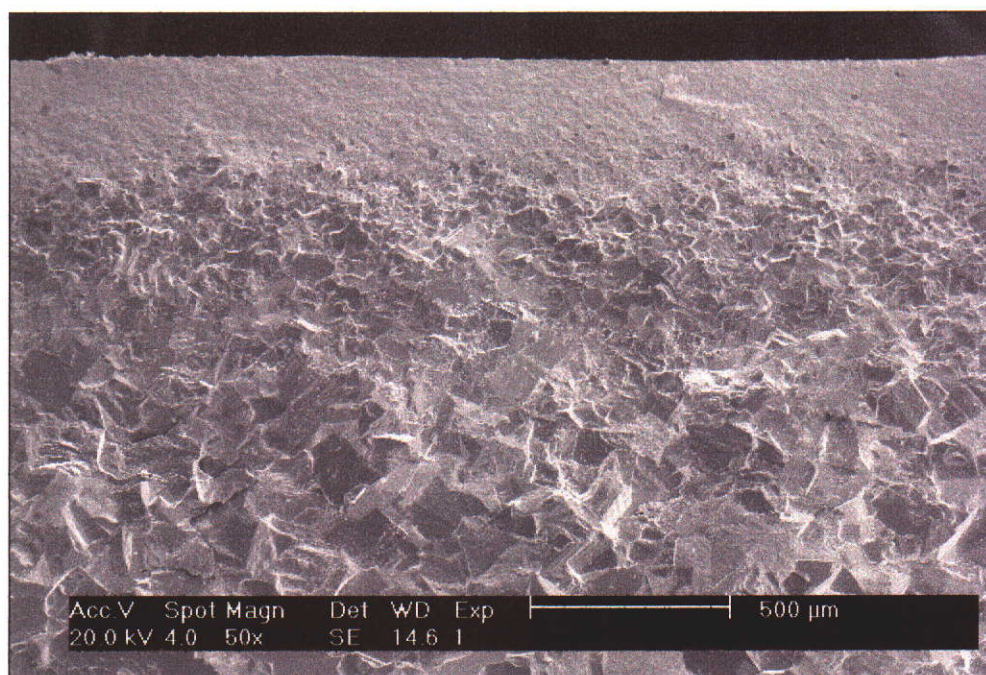


Figure 6.2 Exaggerated grain growth away from external surface (uppermost) in solid-state derived  $\text{BaZrO}_3$  with Ba : (Zr + Hf) mole ratio of  $1.002 \pm 0.002$  (same sample as Figure 6.1 e). Scale bar = 500  $\mu\text{m}$ .

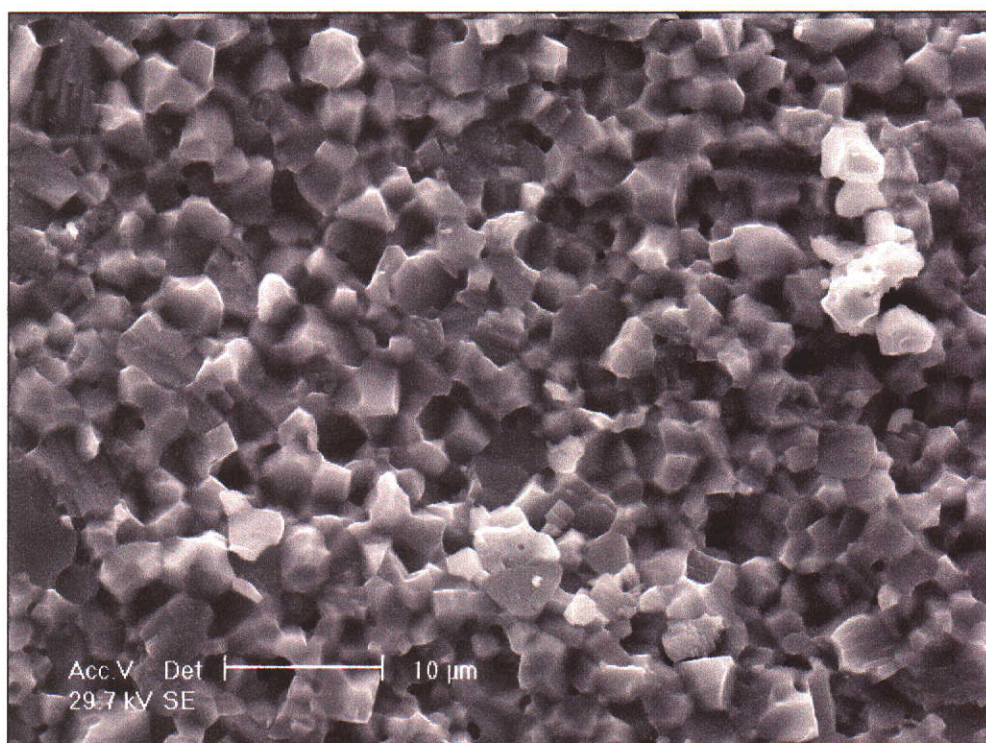


Figure 6.3 SEM micrograph of fracture surface of sintered oxalate-derived  $\text{BaZrO}_3$  with Ba : (Zr + Hf) mole ratio of  $1.015 \pm 0.002$ . Sample isostatically pressed and sintered for 6 hours at 1700 °C. Image taken from centre of cross-section (~ 2 mm from external surface) showing lack of exaggerated grain growth unlike often occurring in Ba-rich solid-state derived ceramics. Scale bar = 10  $\mu\text{m}$ .



Exaggerated grain growth was first observed in sintered crucibles fractured after corrosion exposure for analysis of melt percolation through crucible walls. Initially it was suspected that exaggerated grain growth in Ba-rich ceramics might have been caused by cetyl alcohol used as a lubricant for isostatic pressing. However, the sintered pellets shown in Figure 6.1 were pressed using calcined powder without addition of cetyl alcohol. A light coating of stearic acid was used as a release agent on the surfaces of the die used to press pellets, but this was confirmed as having no effect on grain growth in sintered Ba-rich ceramics. Ba-rich powders with or without cetyl alcohol addition displayed exaggerated grain growth with either cetyl alcohol or stearic acid used in small amounts as a die lubricant for uniaxial pressing.

Excessive grain growth in some Ba-rich ceramics occurred in a thin subsurface layer which did not extend to the centre of sintered sections (Figures 6.4 to 6.7). This thin subsurface layer greatly complicates the explanation of the mechanism of grain growth. If exaggerated grain growth was an intrinsic property of Ba-rich solid-state derived powders (under the powder processing and sintering conditions used in this study), grain growth should occur through the bulk of the ceramic rather than produce only a subsurface layer. There was little observed correlation between process variables (e.g. sintering temperatures, powder and die lubricant use etc.) and the pattern of grain growth occurring either through the interior of sintered samples or as a thin sub-surface layer. Because lubricant use was suspected as a possible cause of grain growth, the sintering procedure was modified to include an isothermal treatment at  $\sim 1000^\circ\text{C}$  during the ramp up to sintering temperature to try to completely remove any effects of lubricant addition. Samples whose sintering procedure included isothermal treatment at  $\sim 1000^\circ\text{C}$  generally produced grain growth as a subsurface layer, whereas heating directly from  $450^\circ\text{C}$  lubricant burnout treatment to full sintering temperature more commonly produced grain growth throughout the interior of samples. However, there was insufficient time to conduct comprehensive experiments to verify these observations. The fact that exaggerated grain growth occurred in some form irrespective of cetyl alcohol addition showed that grain growth was a property of the powder and not caused solely by lubricant addition.



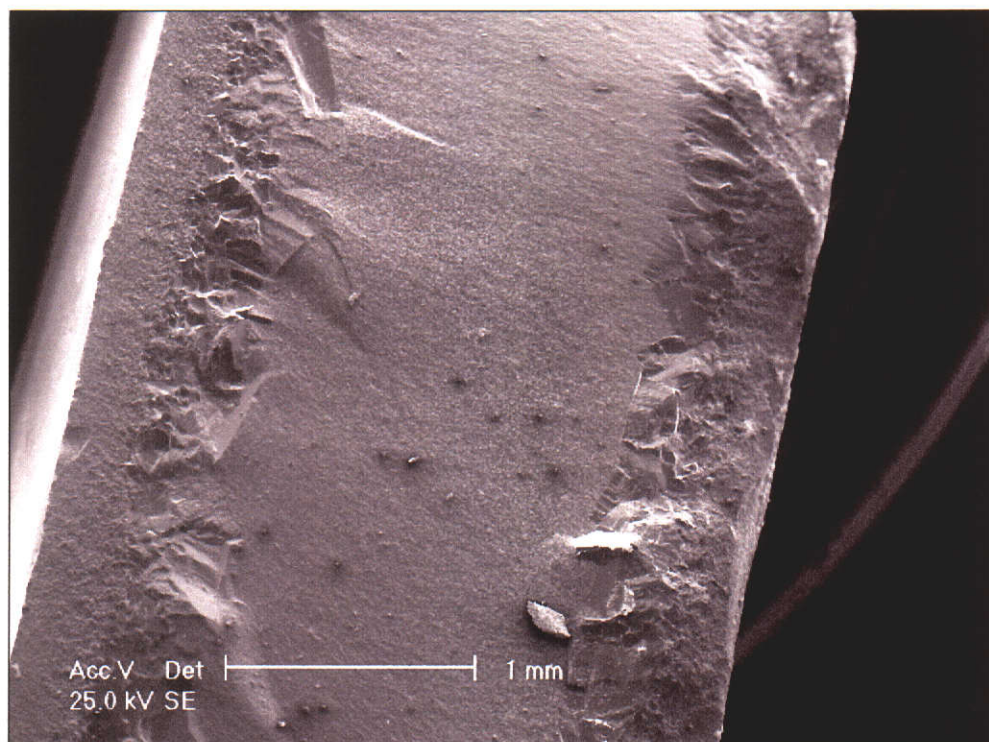


Figure 6.4 Thin sub-surface layer of exaggerated grain growth in solid-state derived BaZrO<sub>3</sub> with Ba : (Zr + Hf) mole ratio of  $1.006 \pm 0.002$ . Scale bar = 1 mm.

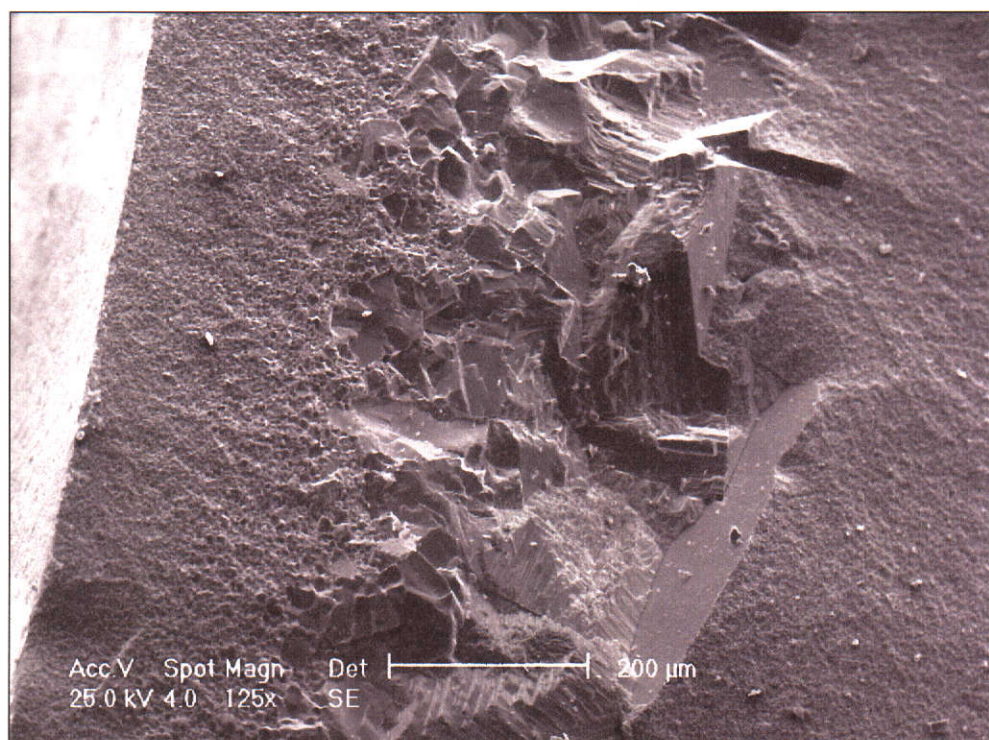


Figure 6.5 SEM micrograph of fracture surface of sintered ceramic made from solid-state derived powder with Ba : (Zr + Hf) mole ratio of  $1.006 \pm 0.002$ . Exaggerated grain growth occurred in subsurface layer between  $\sim 200$  and  $650 \mu\text{m}$  from exterior surfaces, but did not extend to the centre of sintered material. External surface is on left side of image. Scale bar =  $200 \mu\text{m}$ .



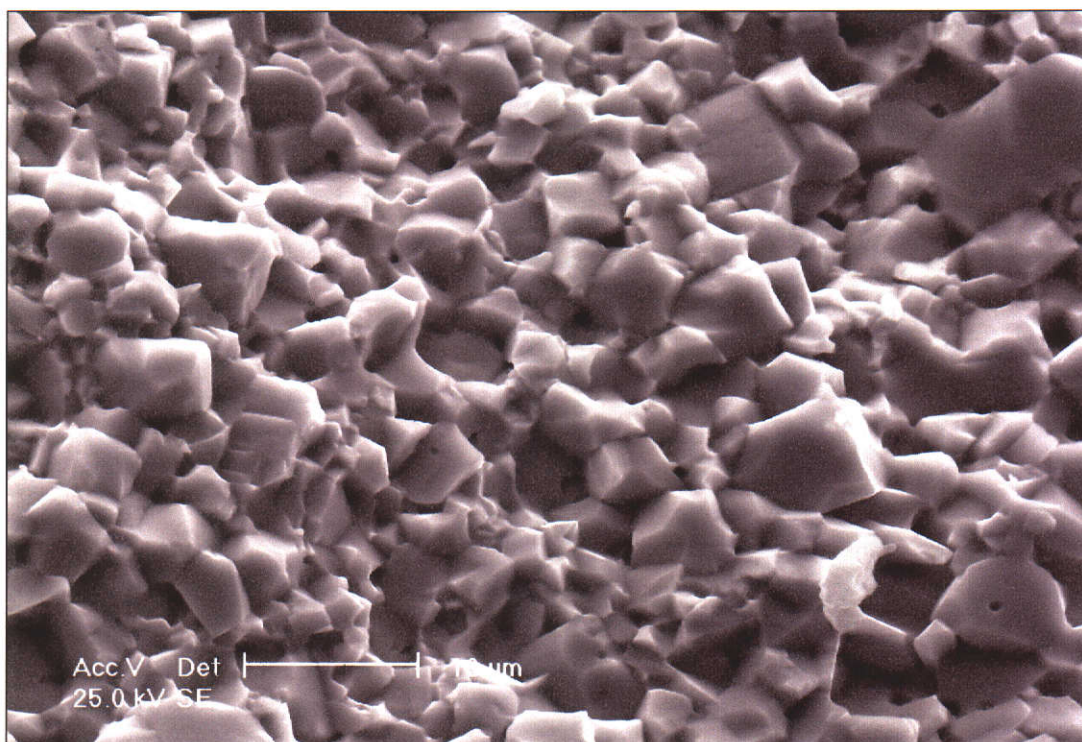


Figure 6.6 Fine grain structure of centre region of sample in Figure 6.5. Scale bar = 10  $\mu\text{m}$ .

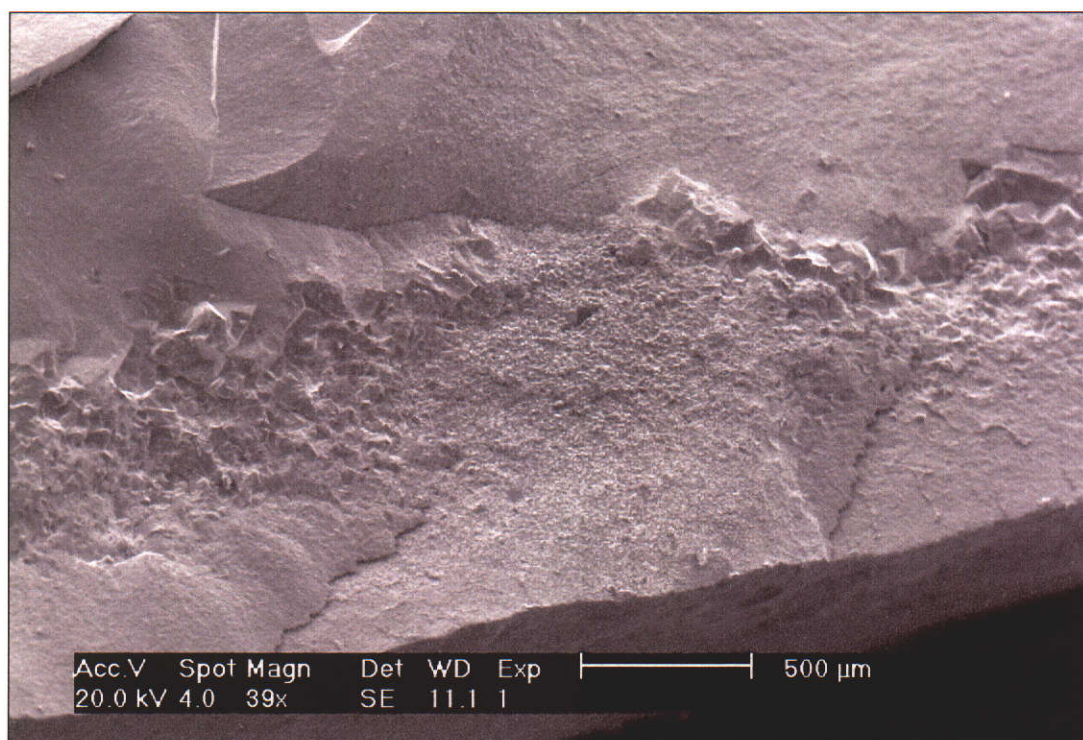


Figure 6.7 Subsurface layer of exaggerated grain growth in solid-state derived  $\text{BaZrO}_3$  with Ba : (Zr + Hf) mole ratio of  $1.003 \pm 0.002$ . External surface is at bottom of image. Scale bar = 500  $\mu\text{m}$ .



Closer examination by SEM showed that very large grains in Ba-rich ceramics were often interspersed amongst very small grains (Figures 6.8 – 6.10). The cause of exaggerated grain growth in Ba-rich solid-state derived ceramics is not apparent from SEM analysis.

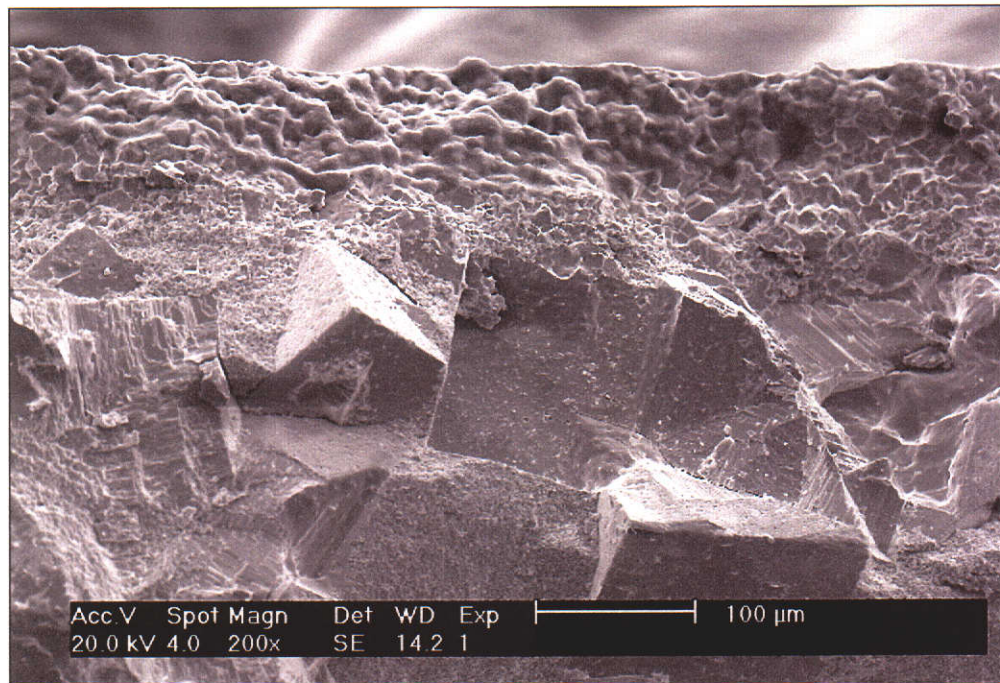


Figure 6.8 Exaggerated grain growth in interior of Ba-rich ceramic mixed with very fine grains. Scale bar = 100 μm.

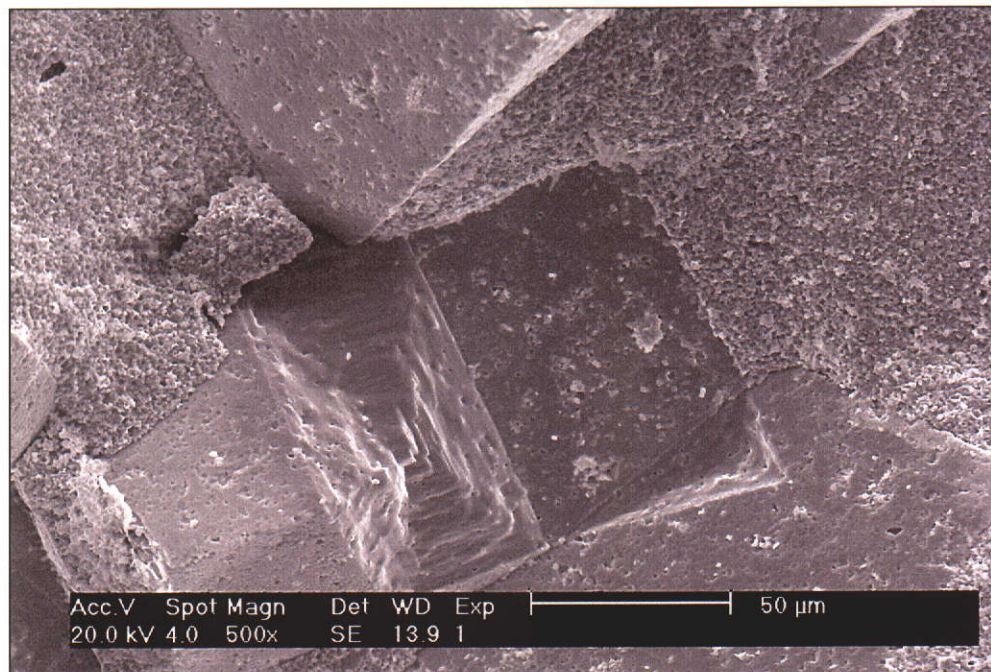


Figure 6.9 Exaggerated grain growth in interior of Ba-rich solid-state derived ceramic mixed with very fine grains. Scale bar = 50 μm.





Figure 6.10 Large  $\text{BaZrO}_3$  grain in fine grained matrix in Ba-rich solid-state derived ceramic where fracture surface has propagated around large grain. Scale bar = 20  $\mu\text{m}$ .

The basic microstructure of Zr-rich ceramics observed by SEM analysis of fractures surfaces is shown in Figures 6.11 to 6.13. Figures 6.11 and 6.12 show the fracture surface of an aluminosilicate contaminated Zr-rich oxalate derived sample. Contamination produced a very high density (99.3 %) at low sintering temperature (1645 °C). The Ba : (Zr + Hf) mole ratio was  $0.960 \pm 0.002$ , and the missing grains in Figures 6.11 and 6.12 were most likely  $\text{ZrO}_2$  lost during fracture rather than porosity. Fracture was largely intra-granular and conchoidal as shown in Figure 6.12. It was suspected that the conchoidal fracture surface may have indicated the presence of glassy grain boundary phases due to aluminosilicate contamination. However, an uncontaminated but otherwise similar sample shown in Figure 6.13 (with Ba : (Zr + Hf) mole ratio of  $0.986 \pm 0.002$  and a density 94.6 % of theoretical) also displayed partly conchoidal fracture.



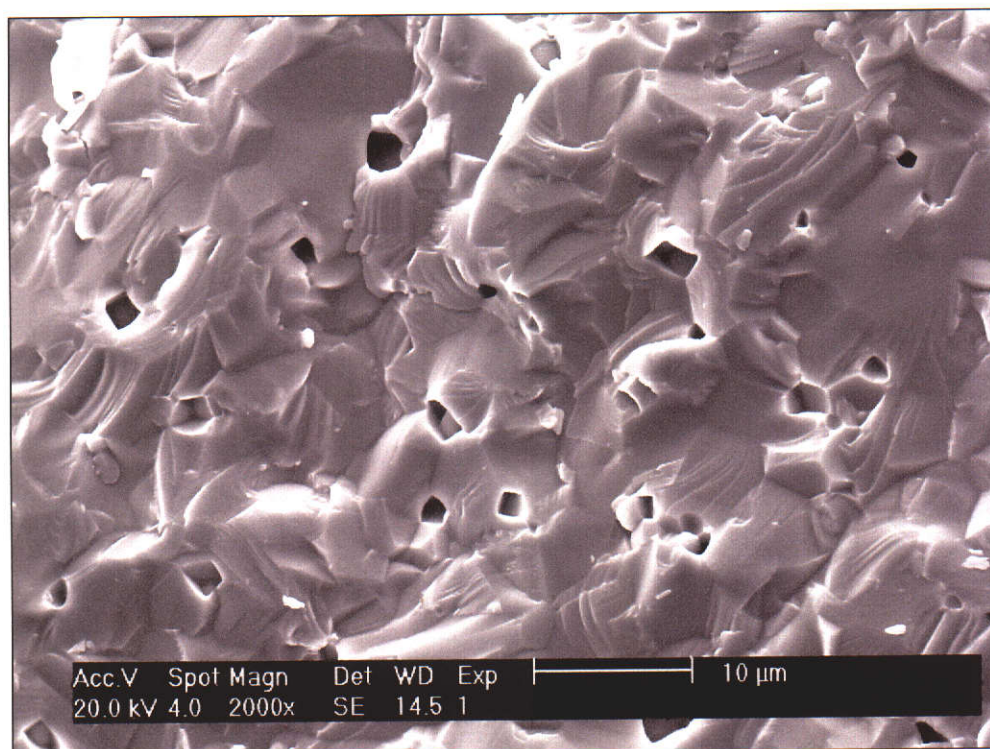


Figure 6.11 SEM micrograph of fracture surface of slip cast Zr-rich oxalate-derived  $\text{BaZrO}_3$  containing aluminosilicate contamination after sintering at  $1650^\circ\text{C}$  for twelve hours. Scale bar =  $10\ \mu\text{m}$ .

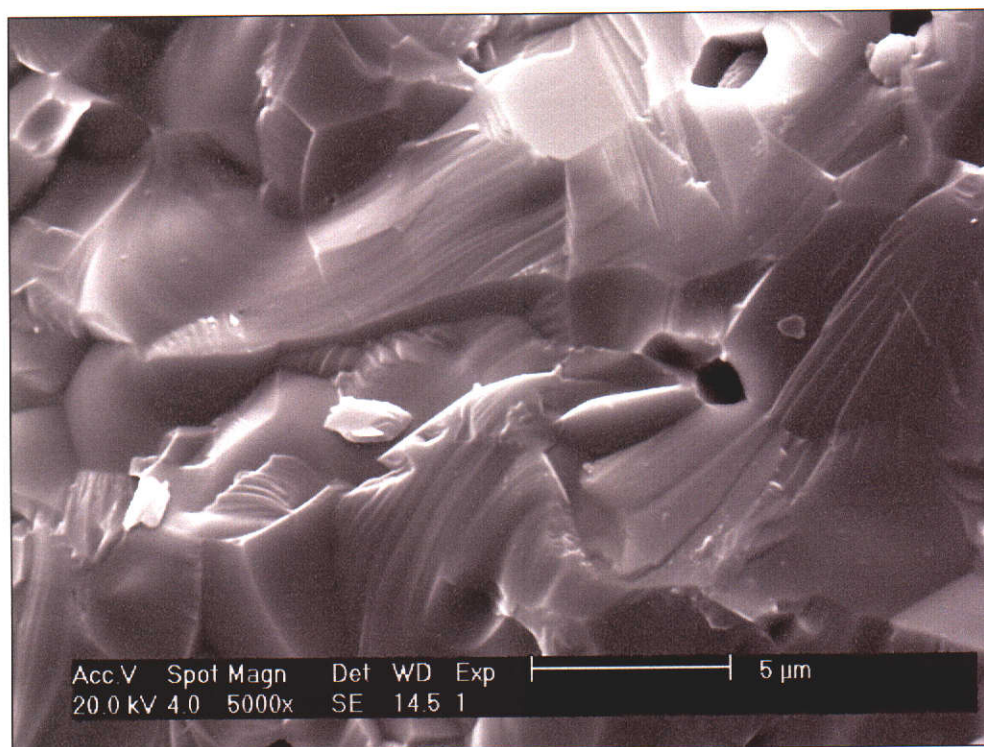


Figure 6.12 Conchoidal fracture surface of same sample as Figure 6.11, i.e. aluminosilicate contaminated oxalate-derived  $\text{BaZrO}_3$  sintered at  $1650^\circ\text{C}$  for twelve hours. Density was 99.3 % and Ba : (Zr + Hf) mole ratio was  $0.960 \pm 0.002$ . Scale bar =  $5\ \mu\text{m}$ .



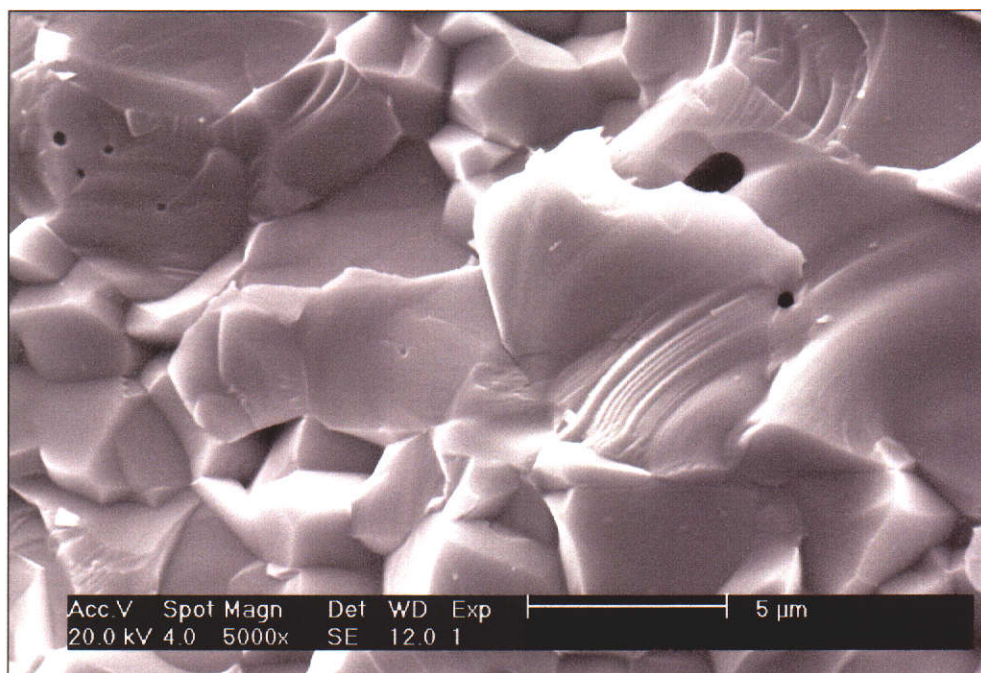


Figure 6.13 Partly conchoidal fracture surface of uncontaminated oxalate-derived BaZrO<sub>3</sub> after sintering at 1700 °C for 6 hours, indicating that conchoidal fracture surface was not caused by aluminosilicate contamination. Sample had Ba : (Zr + Hf) mole ratio of  $0.986 \pm 0.002$  and a density 94.6 % of theoretical. Scale bar = 5 μm.

### 6.3 Bulk analysis

This section presents methods developed for bulk analysis of BaZrO<sub>3</sub> ceramics using XRD and solution analysis. Compared to microscopy, bulk analysis methods allow much larger sampling volumes and are more suited to quantitative analysis if adequate sensitivity can be achieved and the interpretation of results can be verified.

#### 6.3.1 Direct detection of secondary phases by XRD

Figure 6.14 provides information about the detection limits of ZrO<sub>2</sub> for Zr-rich BaZrO<sub>3</sub> close to phase equilibrium. Samples were prepared by triple calcination of BaCO<sub>3</sub> and ZrO<sub>2</sub> at 1300 °C with intermediate re-grinding, sintering to high density at 1700 °C for six hours, followed by ring milling for 30 seconds and bulk phase analysis by powder XRD. The ground powders were exposed to air for several days because they were part of an experiment for determining Ba-rich phase abundances. This method of specimen preparation provided the closest achievable

approximation to thermodynamic phase equilibrium prior to air exposure that was possible with solid-state processing and representative sampling for bulk phase analysis. The most intense  $\text{ZrO}_2$  peaks at  $28.2$  and  $31.5^\circ 2\theta$  are not significantly overlapped by any other secondary phases likely to occur in Zr-rich samples and are the most useful for detection. The other  $\text{ZrO}_2$  peaks at  $24.0$  and  $34.2^\circ 2\theta$  are overlapped by  $\text{BaCO}_3$ , which was present due to reaction of  $\text{BaZrO}_3$  with air.

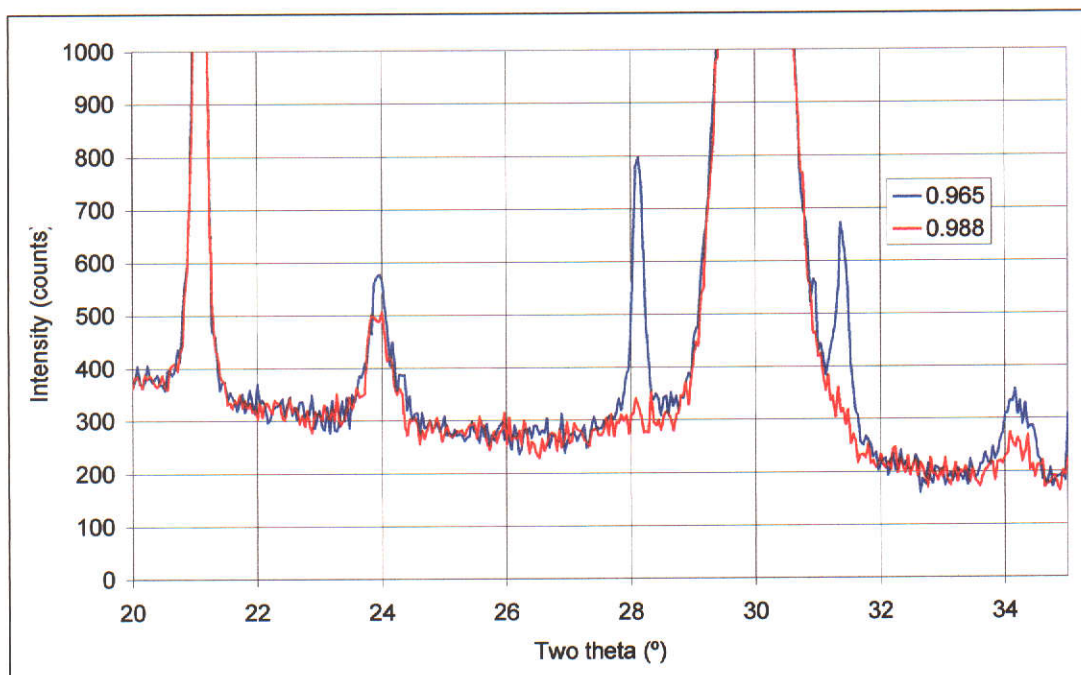


Figure 6.14 Direct detection of  $\text{ZrO}_2$  in Zr-rich  $\text{BaZrO}_3$  close to phase equilibrium at Ba : (Zr + Hf) mole ratios of 0.965 and 0.988.  $\text{ZrO}_2$  could not be detected for solid-state sintered materials ground into powders for analysis with Ba : (Zr + Hf) higher than 0.988.  $\text{ZrO}_2$  peaks not overlapped by other phases are  $28.1$  and  $31.5^\circ$ . Peak height of  $\text{BaZrO}_3$  peak at  $30.0^\circ$  was  $\sim 96\,000$  counts.

$\text{ZrO}_2$  could not generally be detected in samples with a Ba : (Zr + Hf) mole ratios higher than 0.988 using XRD with long counting times of eight seconds per point and maximum tube intensity. At this mole ratio, the detection limit for  $\text{ZrO}_2$  must be at least 0.55 wt.%  $\text{ZrO}_2$  assuming phase equilibrium. This calculation provides a lower bound estimate of the detection limit because the actual  $\text{ZrO}_2$  content would have been higher if thermodynamic equilibrium had not been reached. There is also the effect of particle statistics, where  $\text{ZrO}_2$  may fail to be detected even at phase abundances above the average detection limit due to statistical variation in the amount and particle orientation of  $\text{ZrO}_2$  in the analysed volume. Bulk  $\text{ZrO}_2$  levels



required for corrosion resistance were well beyond reliable detection limits of XRD because acceptable corrosion resistance was not reached for Ba : (Zr + Hf) mole ratios below  $1.002 \pm 0.002$  whereas  $\text{ZrO}_2$  could not generally be detected above  $0.988 \pm 0.002$ .

The XRD pattern of a sample with a Ba : (Zr + Hf) mole ratio of  $1.011 \pm 0.002$  prepared in the same manner as described for the Zr-rich samples above is presented in Figure 6.15. The regions where diffraction from minor secondary phases cannot be detected due to overlap with  $\text{BaZrO}_3$  are shown in red. All but one peak outside these regions are due to  $\text{BaCO}_3$ , and there is a minute peak from  $\text{ZrO}_2$  observable at  $28.2^\circ$ . The detection of this minute peak signifies either contamination of the measured specimen during preparation and/or XRD measurement, or more likely, the occurrence of non-equilibrium  $\text{ZrO}_2$ . The definition of the minute  $\text{ZrO}_2$  peak could be improved by using highly extended counting times (i.e. in excess of 30 seconds per point), because peak overlap is not severe at this angle. However, detection and certainly quantification of this peak is likely to be limited far more by particle statistics than counting statistics. The detection of the minute peak at elevated mole ratio ( $1.011 \pm 0.002$ ) probably occurred because of statistical variation of  $\text{ZrO}_2$  orientation and phase abundance within the analysed volume. Greatly increased counting times would not have any impact on detection limitations due to particle statistics. The minute  $\text{ZrO}_2$  peak in Figure 6.15 is not typical for Ba-rich sintered samples because  $\text{ZrO}_2$  was normally undetectable for samples with Ba : (Zr + Hf) mole ratios higher than 0.988.

Examination of the ICDD cards shows that the only peaks from all other barium zirconates not strongly overlapped by  $\text{BaZrO}_3$  with sufficient relative intensity for any prospect of detection would be from  $\text{Ba}_2\text{ZrO}_4$ , at  $28.98^\circ$  (PDF 77-0944) and/or  $39.85$ ,  $40.54$ , and  $51.14^\circ$  (PDF 22-0105). These peaks are not detectable by laboratory XRD for specimens near phase purity with Ba : (Zr + Hf) mole ratios below  $1.011 \pm 0.002$ . Overlap of all of the major diffraction peaks prevents any prospect of detection of  $\text{Ba}_2\text{ZrO}_4$  from PDF 24-0130 and  $\text{Ba}_3\text{Zr}_2\text{O}_7$  from PDF 24-0131 by conventional laboratory XRD.

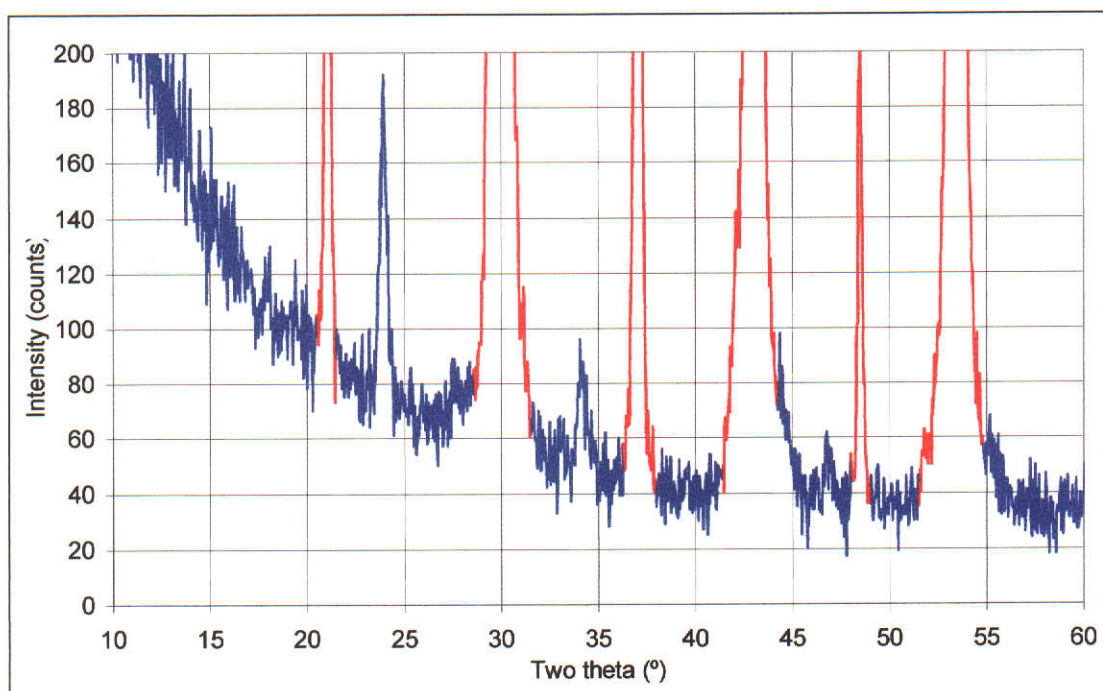


Figure 6.15 Phase analysis of Ba-rich  $\text{BaZrO}_3$  near phase equilibrium at Ba : (Zr + Hf) mole ratio of  $1.011 \pm 0.002$ . Peaks due to  $\text{BaZrO}_3$  are shown in red. Most other diffraction peaks are due to  $\text{BaCO}_3$ . Peak height of  $\text{BaZrO}_3$  at  $30.0^\circ$  was 21 000 counts.

The only secondary phase detectable by laboratory XRD in  $\text{BaZrO}_3$  of sufficient phase purity to be useful for YCBO melt containment is  $\text{BaCO}_3$ . However,  $\text{BaCO}_3$  cannot be present in sintered materials without subsequent exposure to air because  $\text{BaCO}_3$  decomposes to  $\text{BaO}$  above  $\sim 1450^\circ\text{C}$  which would obviously be eliminated through reaction with surrounding zirconate compounds during sintering. As discussed in Section 5.2.2,  $\text{BaCO}_3$  is present in powder samples due to reaction of  $\text{BaZrO}_3$  and Ba-rich zirconates with air, and hence represents the combined effects of Ba-rich secondary phase abundance and  $\text{BaZrO}_3$  surface area. The detection limits for  $\text{BaCO}_3$  are discussed in Appendix 1.

### 6.3.2 Indirect detection of barium rich phases by XRD

As described in Section 5.2.1, Ba-rich powders produced higher levels of  $\text{BaCO}_3$  after exposure to air than Zr-rich powders. The amount of  $\text{BaCO}_3$  formed after air exposure has been shown to be affected by powder surface area but despite this limitation, qualitative comparison of Ba-rich phase abundance in sintered ceramics can still be made. Sintered ceramics with varying Ba : (Zr + Hf) mole ratios were ground in a ring mill and the amount of  $\text{BaCO}_3$  formed after exposure to air is



presented in Figure 6.16. Milling times were kept constant at 30 seconds to attempt to control the effect of  $\text{BaZrO}_3$  surface area. A short milling time was used to minimise the effect of  $\text{BaZrO}_3$  surface area while still exposing Ba-rich phases for reaction with air.

Results showed  $\text{BaCO}_3$  was detected well above background fitting errors in all sintered samples after briefly grinding to a powder. In addition to the explanation given in Section 5.2.2, detection of  $\text{BaCO}_3$  in significantly Zr-rich ceramics supports the conclusion that  $\text{BaZrO}_3$  reacts with air. For constant ring milling times (i.e. roughly constant surface areas), the amount of  $\text{BaCO}_3$  increased above the phase boundary, confirming the presence of Ba-rich phases. If the milling time was increased to several minutes, significantly higher  $\text{BaCO}_3$  levels were observed due to increased  $\text{BaZrO}_3$  surface areas available for reaction with atmospheric  $\text{CO}_2$ . Quantitative comparison of powder and sintered phase purity are not possible from this data because a quantitative correction for the effect of surface area was not feasible within this project. However, Figure 6.16 allows qualitative phase purity comparison for sintered materials after brief ring milling.

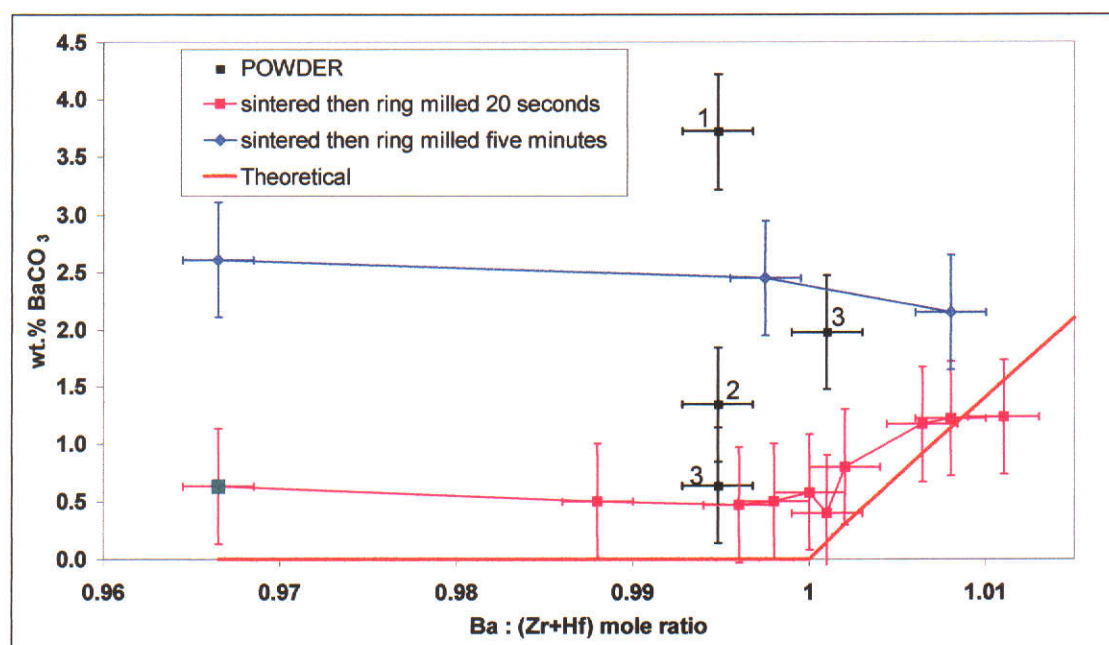


Figure 6.16 Dependence of  $\text{BaCO}_3$  levels after air exposure on stoichiometry and sample preparation. The numbers next to results for powders are the number of calcinations with intermediate regrinding used during powder processing. Theoretical line assumes phase equilibrium and neglects  $\text{BaZrO}_3$  surface area effect. Sintered data at 0.966 includes some overlap from  $\text{ZrO}_2$ .

### 6.3.3 Solution analysis by ICP-MS

As discussed in Section 4.9, strongly Ba-rich ceramics were readily attacked by exposure to water (within hours), whereas Zr-rich ceramics were stable in water for extended periods of time (i.e. at least 12 months). The marked difference in stability in water of Ba-rich and Zr-rich ceramics formed the basis of efforts to develop a method of Ba-rich phase analysis through analysis of supernatant solutions.

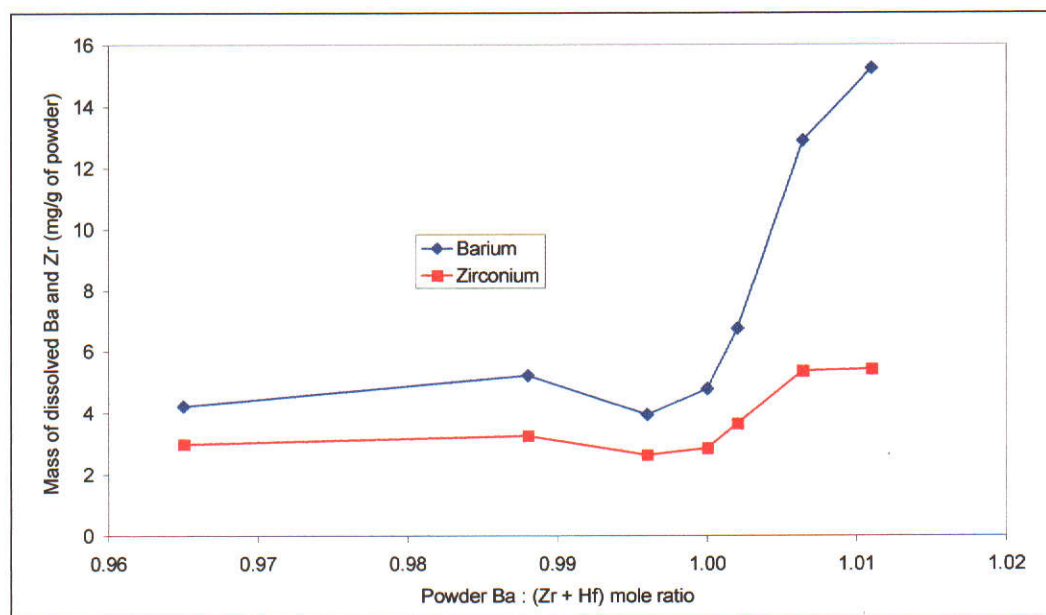


Figure 6.17 Raw data from ICP-MS analysis of ceramic. Error bars due to solution concentration measurements of ICP-MS instrument are too small to show. Scatter in data is primarily due to low levels of particulate material in solutions which could not be removed by filtration or centrifugation.

The amount of barium and zirconium dissolved in dilute HCl from sintered ceramics after briefly grinding to a powder is shown in Figure 6.17. The amount of soluble Ba and Zr remained approximately constant for samples whose Ba : (Zr + Hf) mole ratio was less than or equal to one, but increased rapidly on the Ba-rich side of the phase boundary as expected. The increase in supernatant barium and zirconium concentrations for samples with a bulk Ba: (Zr + Hf) mole ratio greater than one was quantitatively consistent with the presence of Ba-rich secondary phases.

The corrected Ba : (Zr + Hf) mole ratio of the supernatant rose to approximately 2.0 at the highest bulk stoichiometry measured in the specimens

(1.010). Solution concentrations for specimens with  $\text{Ba} : [\text{Zr} + \text{Hf}] > 1$  were corrected for dissolved  $\text{BaZrO}_3$  using the average data of the four specimens with  $\text{Ba} : (\text{Zr} + \text{Hf})$  mole ratios less than one.  $\text{BaZrO}_3$  was assumed to be the only dissolved phase for  $\text{Ba} : (\text{Zr} + \text{Hf})$  mole ratios below one.

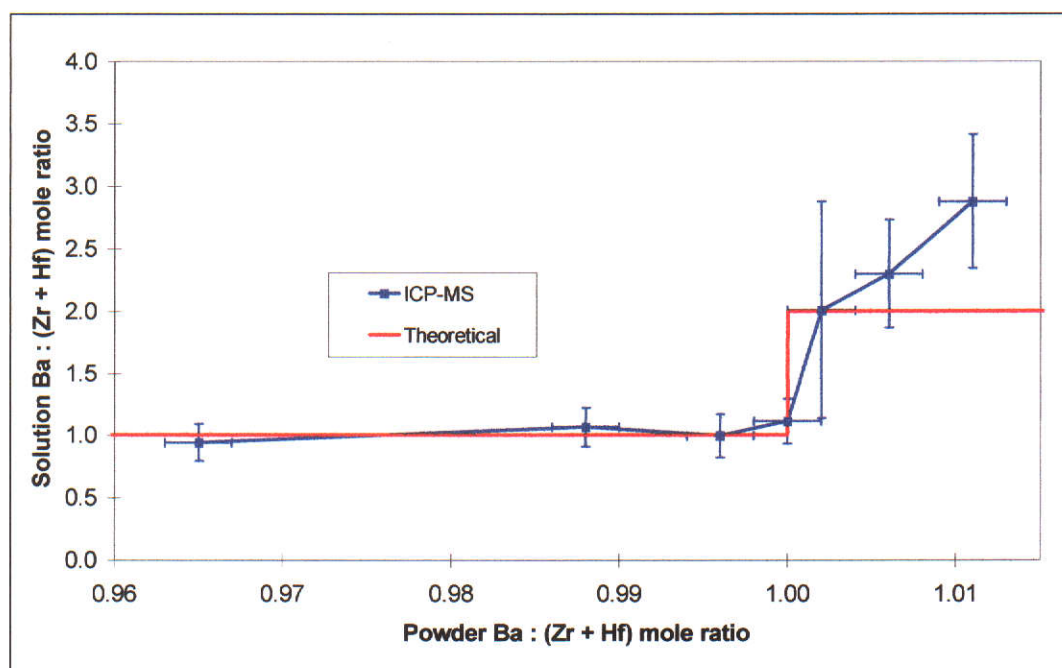


Figure 6.18 Dependence of corrected Ba : (Zr + Hf) ratio of dissolved secondary phases(s) on powder stoichiometry.

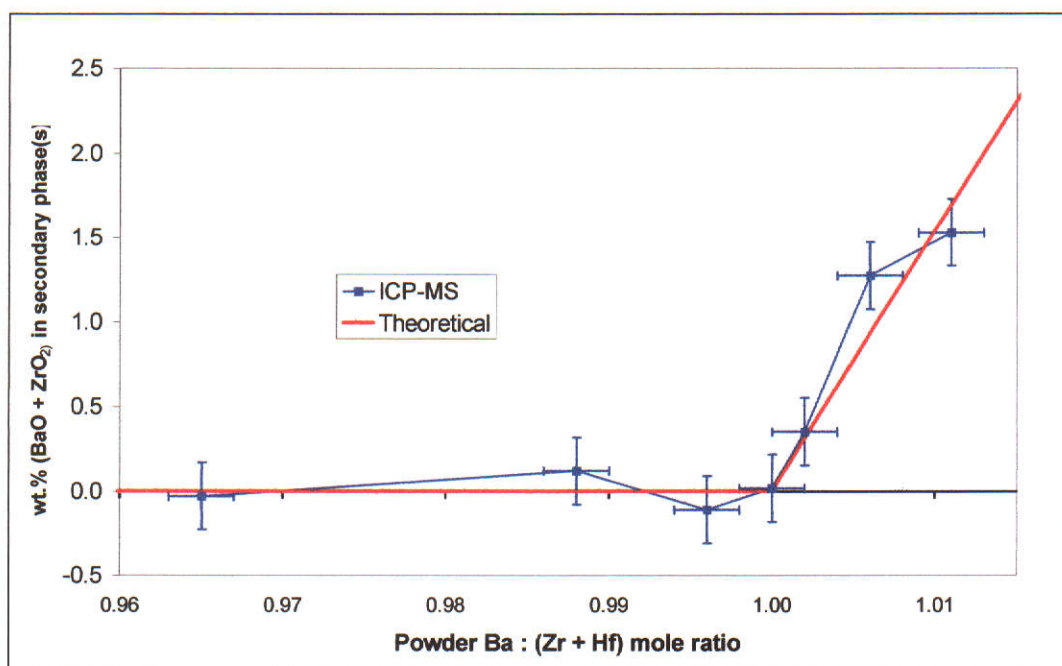


Figure 6.19 Dependence of calculated total weight percentage of secondary phases(s) on powder stoichiometry calculated from measured supernatant solution concentration.

Increased barium and zirconium concentrations compared favourably with equilibrium  $\text{Ba}_2\text{ZrO}_4$  levels as a function of bulk stoichiometry calculated from the phase diagram (Paschoal, Kleykamp & Thuemmler, 1987) as shown in Figure 6.18. Data was corrected for dissolved  $\text{BaZrO}_3$  using the average data of the four specimens with Ba : (Zr + Hf) mole ratio less than one, assuming that Zr-rich samples contained no soluble secondary phases.  $\text{Ba}_2\text{ZrO}_4$  was assumed to be the only dissolved secondary phase for Ba : (Zr + Hf) mole ratios above one.

There are actually three sources of “dissolved” material. In all samples, small amounts of well dispersed un-dissolved powder remained in supernatant solutions and was so fine that it could not be removed by centrifugation. Low levels of particulate contamination could be observed as a faint cloudiness in strong light in the original supernatant solution before subsequent dilution. From the data in Figure 6.17, the average amount of  $\text{BaZrO}_3$  observed in 0.1M HCl can be calculated as 80 mg/L, assuming Zr-rich samples do not contain Ba-rich secondary phases.  $\text{BaZrO}_3$  is itself soluble in HCl, and can be completely dissolved up to at least a few grams per litre in 2M HCl at ambient temperature after prolonged mechanical grinding and after continuous agitation for several days. Apart from particulate material, some of the barium and zirconium in dilute HCl comes from dissolved  $\text{BaZrO}_3$ , and the remainder comes from dissolved or partly dissolved secondary phases.

The solution used for analysing the secondary phase composition needs to be chosen carefully as it has an impact on the results and their interpretation. The initial observation of the solubility of Ba-rich secondary phases was in de-ionised water. Barium solution concentrations were very likely to have remained quantitative. However, zirconium compounds typically have a strong tendency to hydrolyse and zirconium hydroxides have very low solubilities in neutral and especially in alkaline conditions. Zirconium solution concentrations cannot be used to directly estimate secondary phase abundance results under neutral or alkaline conditions, and hence a dilute acid was used to maintain low pH. The extent to which zirconium from secondary phases remained quantitatively in solution in acidic conditions is likely to be considerably higher than under neutral or alkaline conditions, but remains



indeterminate. The acid concentration used to react with the powder could have been increased to attempt to maintain quantitative zirconium dissolution from Ba-rich phases, but this would have resulted in increased dissolution of BaZrO<sub>3</sub>. Consequently, interpretation of the corrected Ba : (Zr + Hf) mole ratio of the supernatant solution is somewhat uncertain, and it may be higher than the expected theoretical composition because some of the zirconium from Ba-rich secondary phases may not have remained in solution. Some of the potentially missing dissolved zirconium may have in fact been the ultra-fine colloid observed in undiluted supernatants (i.e. a zirconium hydroxide), some of which was carried through to final ICP-MS analysis.

The understanding of zirconium solution chemistry gained during oxalate-precursor development was insufficient to devise solution conditions where the solubility of zirconium from Ba-rich phases could be significantly increased without a corresponding increase in BaZrO<sub>3</sub> solubility. Improvement of the method would require improved BaZrO<sub>3</sub> solubility control and particulate removal, which might be considerably aided by addition of an effective flocculant or by performing dissolution at a higher pH near the iso-electric point of BaZrO<sub>3</sub>. Although a higher pH may prohibit quantitative zirconium determination, phase analysis from barium concentrations may be adequate.

Ultimately the supernatant analysis approach may provide an analytical method to quantify secondary phases with sufficient accuracy and precision to quantitatively determine deviation from phase equilibrium. Notwithstanding the current limitations of the method, supernatant analysis provided verification of the position of the phase boundary with respect to XRF results. The position of the apparent phase boundary, as observed by the sharp rise in supernatant concentration, was consistent with XRF results within experimental uncertainty. There was agreement between the secondary phase compositions and phase abundance from solution composition results and those calculated from the phase diagram. For sintered ceramics produced from solid-state derived powders made by multiple calcination with intermediate re-grinding, these results suggested that the phase composition of the ceramic closely approached equilibrium. Further development of the method is needed to reduce experimental errors and provide precise quantitative

phase analysis at the low levels present in these materials. In particular, optimisation of solution chemistry is needed to maximise the difference in solubilities of  $\text{BaZrO}_3$  and Ba-rich phases to lower the detection limits of secondary phases.

The method of supernatant solution analysis also pointed towards an alternative processing method for high quality barium zirconate powders. The main limitation of the solid-state method appears to be poor reaction kinetics between  $\text{BaCO}_3$  and  $\text{ZrO}_2$ . As the reaction of stoichiometric powders proceeds, both the driving force for reaction and diffusion rates reduce, leaving unreacted  $\text{ZrO}_2$  in the product. Instead of mixing the exact amounts of reagents to directly form phase pure  $\text{BaZrO}_3$ , extra driving force to eliminate unreacted  $\text{ZrO}_2$  could be provided by deliberate addition of a substantial excess of  $\text{BaCO}_3$ , deliberately aiming to form a mixture of  $\text{BaZrO}_3$  and barium-rich phases such as  $\text{Ba}_2\text{ZrO}_4$ . It may be easier to remove barium rich secondary phases by chemical extraction than to rely on sluggish solid-state diffusion kinetics to remove  $\text{ZrO}_2$  in stoichiometric mixtures. Secondary extraction of Ba-rich phases may provide increased phase purity whilst maintaining the advantages of solid-state processing.

A brief attempt was made to use this approach on a sample of powder made by repeated calcination with intermediate re-grinding at Ba : (Zr + Hf) mole ratio of 1.15. The powder was washed with dilute HCl and deionised water, which was unsuccessful in quantitatively removing  $\text{Ba}_2\text{ZrO}_4$  because the washed powder was Zr-rich. The main problem in washing chemistry appeared to be complete removal of zirconium from  $\text{Ba}_2\text{ZrO}_3$  in the powder, part of which remained in the washed powder most likely as Zr-rich hydroxide colloids. Under acidic conditions, the relatively stable dispersion of the powder also made washing and filtration rather slow, but improved control of surface chemistry may overcome this difficulty. Through improved solution and surface chemistry in the washing process, an ideal production process may be possible, with several major benefits over chemical precipitation methods. Unfortunately there was insufficient scope in this project to aggressively pursue this possible option. The solid-state system is easy to control and uses inexpensive reagents and processing equipment, has a very high efficiency and can be readily scaled up for large scale industrial production. The use of an excess of barium clearly suppresses grain growth during powder processing, and when

followed by extraction of Ba-rich secondary phases may allow ultrafine powder production of very high phase purity on a large industrial scale. In certain respects this approach is similar to mechanochemical milling for nanopowder production, but requires only thermal treatment to drive the solid-state reaction.

Solution analysis methods were also used to attempt to determine levels of Al and Si contamination in an oxalate powder, which occurred because of use of poor quality deionised water during early development of oxalate processing. Analyses for aluminosilicates by XRF, neutron activation analysis, atomic emission spectroscopy and laser ablation ICP-MS were not able to provide the required detection limits. Solution techniques were severely restricted by the perceived need for fusion dissolution preparation – initial tests did not result in complete dissolution of BaZrO<sub>3</sub> specimens in dilute (e.g. 1 N) mineral acids. Consequently, powders were solubilised by first fusing in a mixture of Li<sub>2</sub>B<sub>4</sub>O<sub>7</sub> and Na<sub>2</sub>CO<sub>3</sub> at 1200°C in Pt crucibles, and then dissolving the bead in 1 M HNO<sub>3</sub>. Standards were made by quantitative addition of SiO<sub>2</sub> and Al<sub>2</sub>O<sub>3</sub> in the fusion of an uncontaminated BaZrO<sub>3</sub> sample. XRF, ICP-MS and flame-AAS (atomic absorption spectroscopy) were not suitable due to inadequate detection limits, either on raw solutions or at the dilution required to keep the total dissolved solid concentrations (most of which was flux) within the limits of the instrument. Graphite furnace AAS (Varian SpectrAA Zeeman220) and ICP-OES (Varian Vista ICP-OES), which can tolerate much higher total dissolved solids concentrations than ICP-MS, were used to determine the Al content as  $320 \pm 85$  ppm and 200 – 380 ppm respectively. The large uncertainties were due to the analysis being conducted close to the detection limit of the instruments and to the effect of the matrix (BaZrO<sub>3</sub>).

During subsequent research it was discovered that BaZrO<sub>3</sub> can in fact be dissolved in mineral acids without requiring prior fusion. A sample of sintered BaZrO<sub>3</sub> was made using an oxalate-derived powder at a mole ratio of  $1.008 \pm 0.002$ . The purpose of this preparation was to produce a sample close to phase equilibrium, with either a zero or very low unreacted ZrO<sub>2</sub> content, so that complete dissolution, if achieved, would prove that BaZrO<sub>3</sub> was soluble. The sintered material was dry ground in a ZrO<sub>2</sub> ring mill for 5 minutes, then 215 mg of the powder was added to 150 mL of 2 M HCl. After three days of gentle stirring on a magnetic stirrer, the



powder had completely dissolved, and remained in solution for at least four months. This shows that  $\text{BaZrO}_3$  is soluble to at least 1.4 g/L in 2 M HCl, although the dissolution rate is very slow at ambient temperature. Microwave digestion may be useful in increasing dissolution rates and may also reduce the need for prolonged mechanical grinding, although the solution stability of zirconium at elevated temperatures at the desired acid concentration would need to be confirmed. Much of the total dissolved solids concentration of fusion dissolved specimens is contributed by the flux. Direct dissolution avoids this limitation and would greatly improve the detection limits, precision and accuracy of light element analysis in  $\text{BaZrO}_3$  by solution analysis methods. Resource limitations prevented further development and use of the direct dissolution method for analysis in this project, but it would clearly be useful to have this knowledge for further research.

#### **6.3.4 Accuracy of stoichiometry measurement by XRF**

The accuracy of XRF analysis was a key concern in this project because of strong effects of stoichiometry on processing and corrosion properties of  $\text{BaZrO}_3$ . Standards for calibration of XRF relied on gravimetric assay of  $\text{BaCO}_3$ , assuming the manufacturer's data for the  $\text{HfO}_2$  used was accurate, and assuming that  $\text{ZrO}_2$  used to make standards was 100 % pure. Minor possible errors in the manufacturer's data for  $\text{HfO}_2$  could not cause significant systematic errors for Ba : (Zr + Hf) measurement because of the low Hf : Zr ratio of reagents used for  $\text{BaZrO}_3$  production.  $\text{ZrO}_2$  was precipitated from high purity  $\text{ZrCl}_4$  using mandelic acid, which was calcined sufficiently strongly to be very likely to produce pure  $\text{ZrO}_2$ . However, no method was available to directly verify the purity of  $\text{ZrO}_2$  used for XRF standards.

The data presented in this Thesis provides substantial support for the accuracy of XRF measurements. The transition of  $\text{BaCO}_3$  levels after air exposure and supernatant solution concentrations for sintered ceramics occurred at  $1.000 \pm 0.005$  (Figures 6.16 and 6.17). The inflection point of the sharp transition of crystallite size with stoichiometry for solid-state derived powders after three calcinations was at 0.995. The upper end of the transition was centred at  $1.000 \pm 0.002$  (Figure 5.12), which represents the phase boundary if Ba-rich phases are

assumed responsible for grain growth suppression in solid-state powder processing. The inflection point for the effect of stoichiometry on non-uniform crystallite strain for solid-state derived powders after three calcinations with intermediate re-grinding was at  $1.000 \pm 0.002$  (Figure 5.11). The consistency of all of these observations is strong evidence that XRF measurements of Ba : (Zr + Hf) mole ratios were accurate within approximately  $\pm 0.002$ .

## 6.4 Colour

Batches in which the furnace was filled with several crucibles (e.g. six) produced darker coloured crucibles than for nearly empty furnace cycles. Several batches of sintered crucibles were slightly whiter in colour on external faces located closest to the furnace door during sintering. This was particularly the case for crucibles that were placed close to the front of the furnace. The poorest seal to the exterior gas environment was the furnace door closure, so crucibles at the front of the furnace may have had more exposure to air. One batch was sintered with all the crucibles upside down because of minor contamination from refractory lining falling from the roof of the furnace. These crucibles were considerably darker on the inner surfaces than on the exterior. This pattern of observations suggested that variation of oxygen partial pressure may affect the colour of sintered materials. To test this hypothesis, several batches of crucibles were held for several hours at 1000 °C before reaching full sintering temperature for extended burnout of lubricant, which resulted in slightly whiter colouration of sintered crucibles. Materials which did not sinter to greater than  $\sim 90\%$  density were generally markedly whiter in colour than those above 97 % density.

The interiors of sintered materials were generally darker in colour than areas close to external surfaces. The colour of the crucibles, while not important in itself, may point towards a highly significant issue: oxygen vacancies. It is well known that zirconia ceramics turn a darker colour (e.g. grey) when sintered in reducing environments due to oxygen vacancies (Richerson 1992, p. 541). By analogy, discolouration of BaZrO<sub>3</sub> might also indicate oxygen vacancies, which may play a critical role in melt corrosion by increasing diffusion rates or in the formation of

intra-crystalline defects. Erb noticed that a piece of BaZrO<sub>3</sub> sintered under a reducing atmosphere, 5 % H<sub>2</sub> in N<sub>2</sub> had a much lighter colour than normal (Erb 2002, pers. comm., 18 March). However, the current observations suggest the opposite, that is, reducing atmospheres cause dark discolouration.

All crucibles produced in this study showed evidence of melt percolation reaching the external surfaces of crucibles within a few days of melt exposure despite the development work conducted on stoichiometry, density, phase purity and to a lesser extent grain size. Clearly at least one significant mechanism of mass transport was still operating. Mass transport clearly occurred along grain boundaries despite no evidence of grain boundary defects by TEM analysis. It is suspected that defect diffusion, particularly along grain boundaries, may contribute to mass transport during corrosion. Chemical impurities may cause crystallographic defects, so the highest purity reagents within the resources of the project were used for all experiments. To avoid the possibility of oxygen vacancies, sintering in elevated oxygen pressures (i.e. pure oxygen) would have been attempted if the furnace equipment had gas injection capabilities. This experiment is strongly recommended for future research, and other than using very high purity reagents (i.e. 99.99 %+), and avoiding the use of a lubricant for CIP, there appears to be little scope for improvement of corrosion properties of solid-state derived materials using the techniques and equipment available to this project.

## **6.5 Detailed structural analysis**

The basic analysis presented in Section 6.2 was extended using more detailed SEM, TEM and XRD measurement for structural analysis at the nano and crystallographic scale. Detailed analysis was performed to support the understanding of microstructure formation, exaggerated grain growth, effects of chemical contamination and melt corrosion processes.

### 6.5.1 SEM

Fracture surfaces propagated both through and around large grains as shown in Figure 6.8. The fracture surfaces of large grains showed a distinctive geometrical relationship between the apparent crystal habit of large cubic grains and the propagation of the fracture along apparent crystal planes. As shown in Figures 6.20 – 6.24, there was a distinctive relationship between the cubic crystal structure of  $\text{BaZrO}_3$  and the geometry of fractures surfaces inside large grains. Fracture surfaces having characteristic  $90^\circ$  angles between local fracture planes may indicate a strong tendency for fracture along  $\langle 100 \rangle$  planes. There were also distinctive fractures at  $45^\circ$  and other angles characteristic of fracture along minor zone axes of the cubic system. Apparent intra-crystalline fracture produced steps in fracture surfaces ranging from much less than  $\sim 100$  nm up to several micrometres. Figure 6.23 shows the fracture surface at a boundary between two large grains.

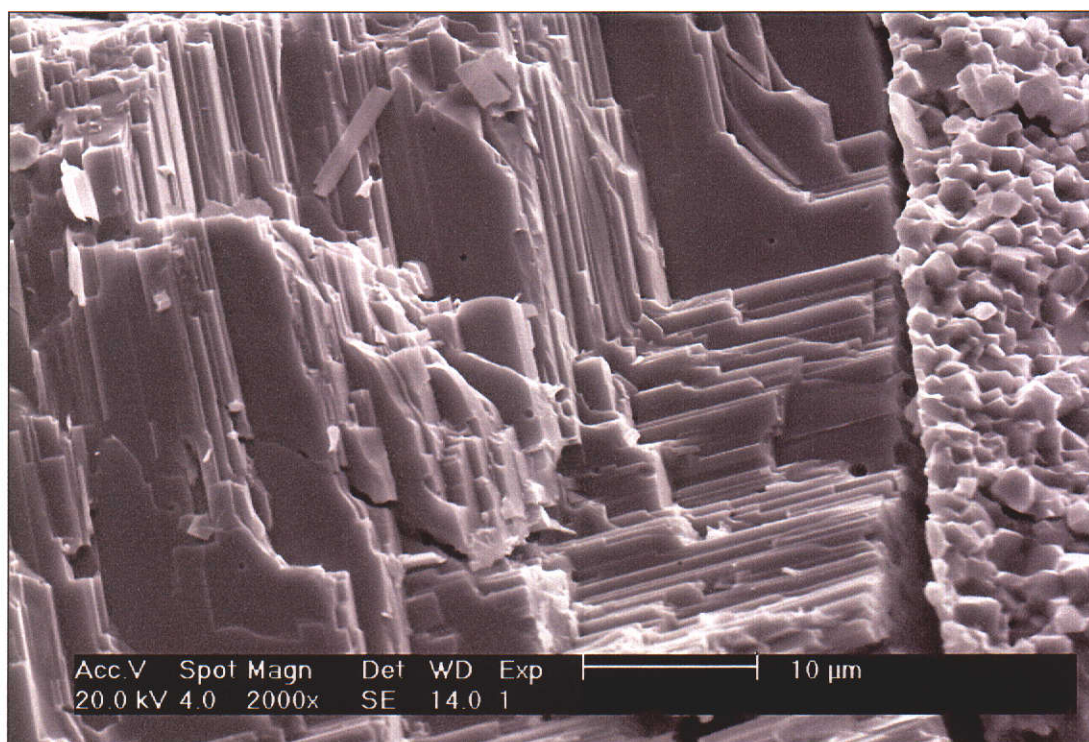


Figure 6.20 Fracture surface of large grain where fracture has propagated through large grain. Scale bar =  $10\ \mu\text{m}$ .



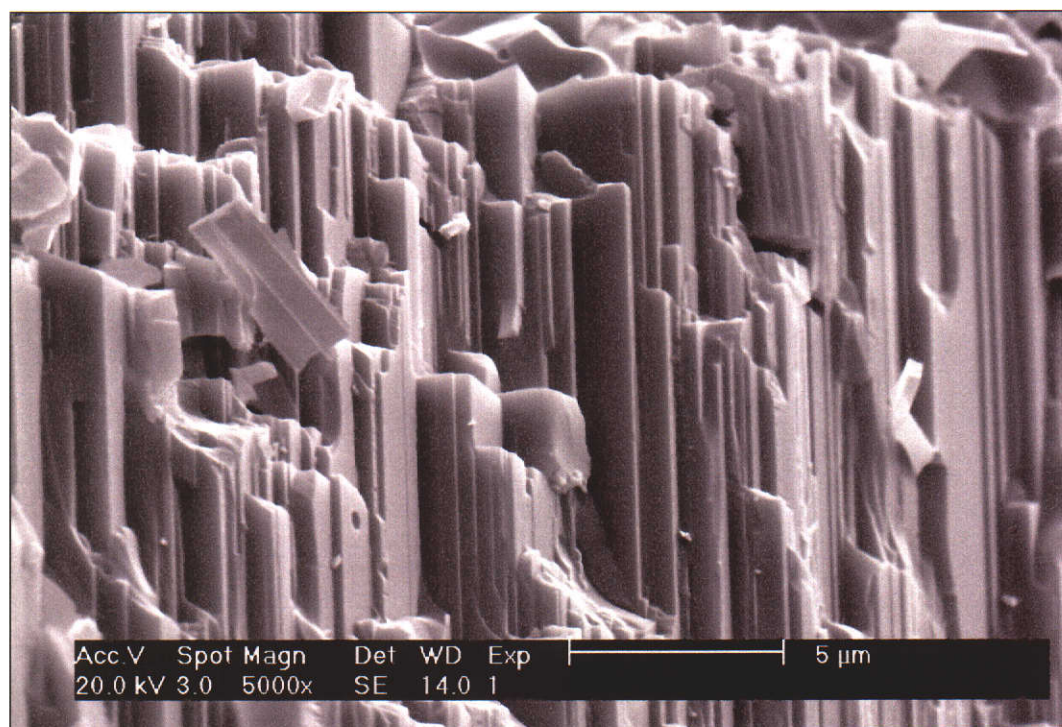


Figure 6.21 Fracture surface of large grain where fracture has propagated through large grain. Scale bar = 5 μm.

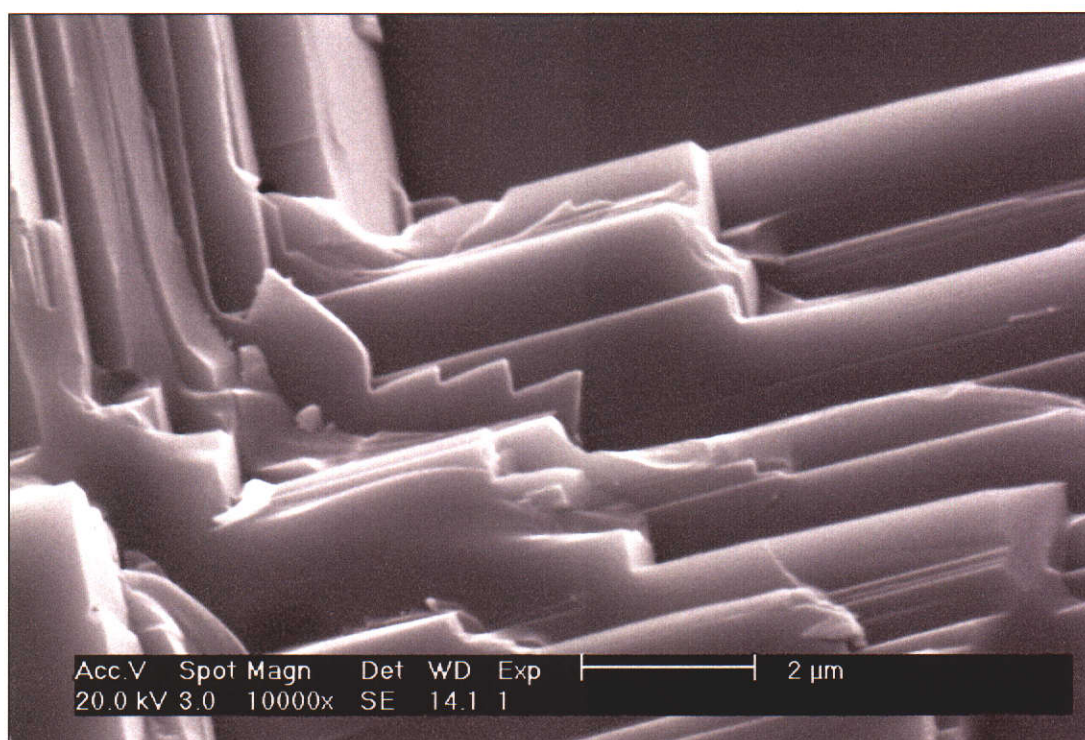


Figure 6.22 Intragranular fracture surface within large grain of Ba-rich solid-state derived ceramic. Image is a higher magnification of the central region of Figure 6.20. Scale bar = 2 μm.



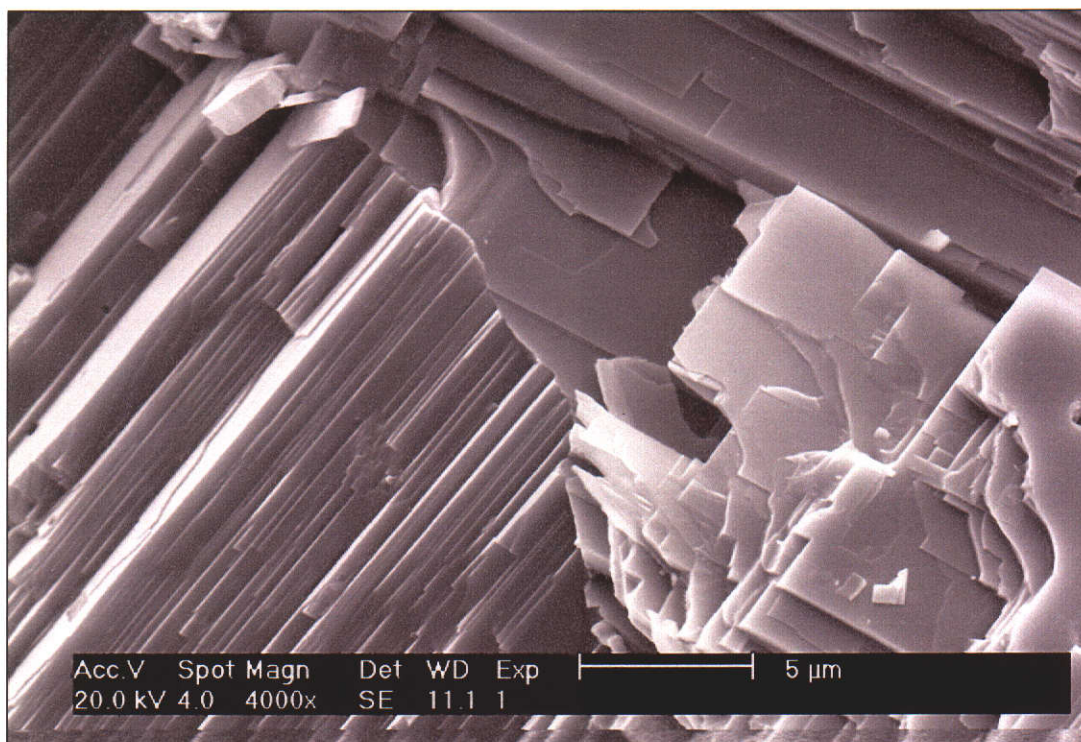


Figure 6.23 Intragranular fracture in Ba-rich solid-state derived ceramic including a grain boundary between two large grains. Scale bar = 5  $\mu\text{m}$ .

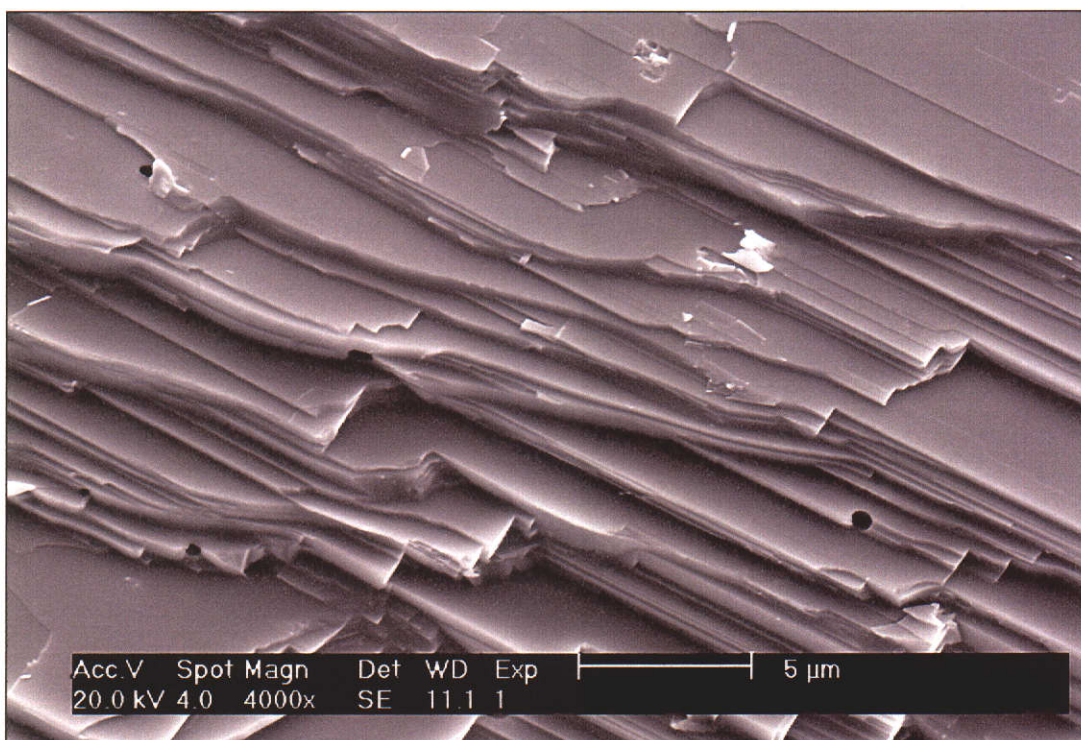


Figure 6.24 Intragranular fracture in Ba-rich solid-state derived ceramic showing fracture morphology which appears to closely conform to an underlying cubic crystal structure. Scale bar = 5  $\mu\text{m}$ .



Large grains were either single crystals, or at least structures where the local fracture geometry was consistent across the fracture surface of each large grain and with their external habits. Whether or not large cubic grains were single crystals, they contained defects at a microstructural level and possibly at a crystallographic level. Figure 6.25 shows detail of a large grain containing a large number of near spherical defects which may have been either trapped pores or secondary phase(s) lost during fracture. Close inspection of Figures 6.10 shows similar defects which were common in most large grains. The residual material on the surfaces of these defects shown in Figure 6.26 suggests they may have been secondary phase(s) lost during fracture. Such residual phases if present, would almost certainly be Ba-rich. Figure 6.26 also shows that the surface of these defects were not always spherical but bounded by short straight segments conforming to the cubic crystal structure of  $\text{BaZrO}_3$ .

TEM analysis showed that these defects were most likely to be pores rather than secondary phases. Had these defects been due to Ba-rich phases of similar density to  $\text{BaZrO}_3$ , they would have appeared darker than  $\text{BaZrO}_3$  in brightfield images because of increased mass thickness (assuming they were milled to the same thickness) and consistently given a higher Ba : Zr ratio in EDS analysis. However, in brightfield TEM imaging, these defects appeared as bright circular spots compared to the surrounding material. EDS analysis did not show a consistent difference in composition of these spots compared to the adjacent material, and so increased transmission was most likely caused by reduced mass-thickness contrast, i.e. small pores trapped within grains during densification. Trapped porosity within grains commonly occurs during exaggerated grain growth of alumina (Richerson 1992, p. 529). The same probably occurred for  $\text{BaZrO}_3$ .

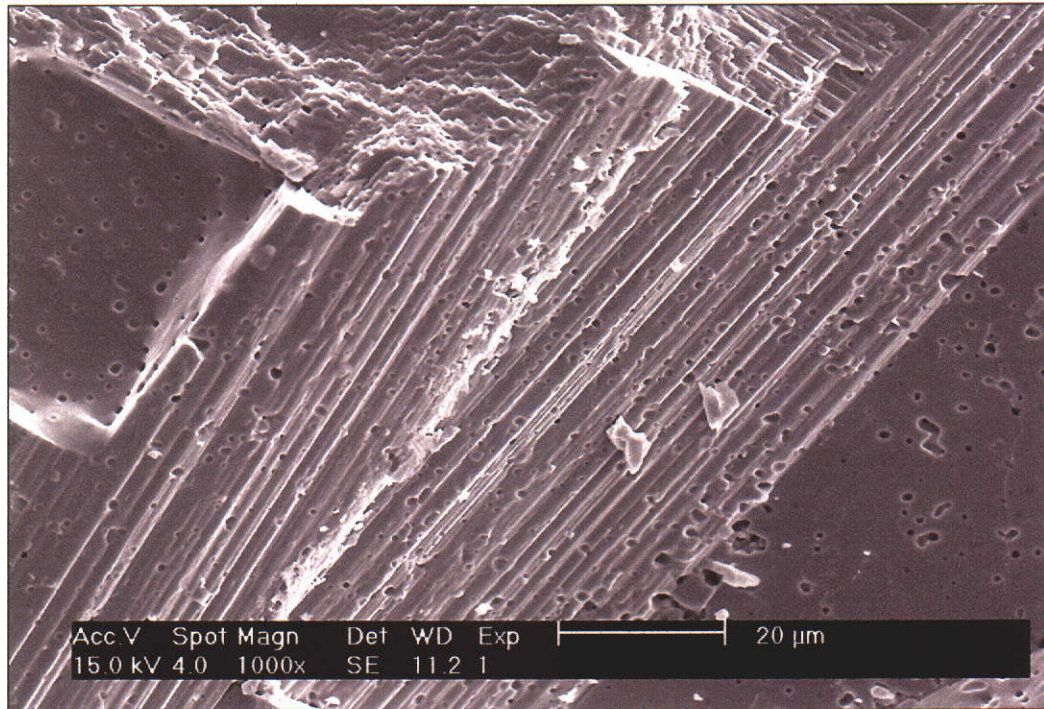


Figure 6.25 Intragranular fracture surface of large grain in Ba-rich solid-state derived ceramic showing large number of small ( $\sim 1 \mu\text{m}$ ) circular defects. Orientation of steps in fracture surface shows a rotation about half way through the large grain. Scale bar =  $20 \mu\text{m}$ .

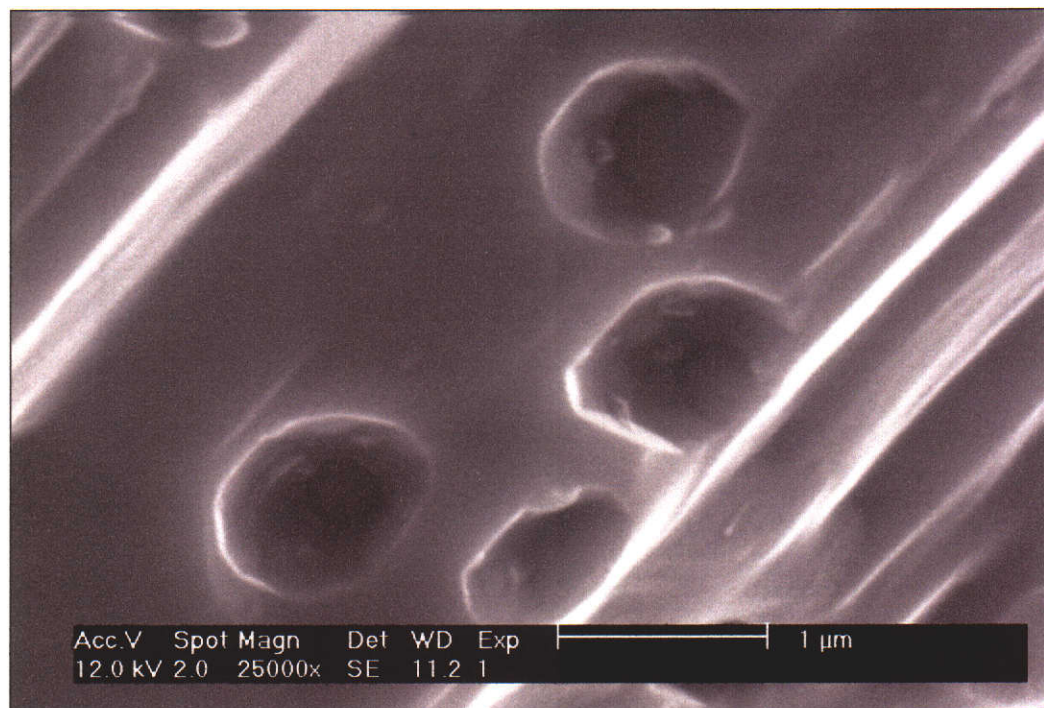


Figure 6.26 SEM of small circular defects within large grains in Ba-rich solid-state derived ceramics. Image is higher magnification of sample shown in Figure 6.25. Scale bar =  $1 \mu\text{m}$ .



Exaggerated grain growth is considered to reduce the mechanical strength and thermal shock resistance of crucibles (Liang, Bonn and Hardy 1998). Erb observed that a grain size of up to  $\sim 20\text{ }\mu\text{m}$  is tolerable (Erb 2002, pers. comm., 6 Nov.) whereas many of the Ba-rich ceramics produced in this study had grain sizes very much larger than desirable. Crucibles at the optimum stoichiometry for corrosion resistance were more corrosion resistant if exaggerated grain growth occurred in a thin subsurface layer rather than throughout the interior of the ceramic (Section 6.6.2). Controlling grain size should be an important means of significantly improving the corrosion resistance of solid-state derived ceramics at the optimum stoichiometry.

### 6.5.2 XRD

Detailed analysis and verification of the origin of exaggerated grain growth was beyond the scope of this study, but the results of brief experiments and discussion of mechanisms that have been considered are presented as an initial guide to assist future research in this area.

One possible explanation for exaggerated grain growth in barium-rich samples is partial melting of Ba-rich secondary phases during sintering leading to grain growth. The phase diagram (Figure 1.1) shows that non-equilibrium barium-rich regions with Ba : (Zr + Hf) mole ratios greater than two would temporarily form a eutectic melt at  $1335\text{ }^{\circ}\text{C}$  (Paschoal, Kleykamp and Theummler 1987). The presence of a liquid phase would clearly affect mass transport during sintering. Evaporation of BaO may eliminate this effect close to external surfaces during sintering. However, the likelihood of barium-rich phases with a Ba : Zr mole ratio of greater than two persisting for a long period of time above  $1335\text{ }^{\circ}\text{C}$  is very low. Powders used in this study were of relatively high phase purity, and hence there is a great deal of BaZrO<sub>3</sub> surface area to rapidly remove any such non-equilibrium Ba-rich phases in the earliest stages of sintering. The lowest phase purity powder used to produce a sintered pellet was an oxalate derived powder with a Ba : (Zr + Hf) mole ratio of  $1.005 \pm 0.002$  calcined at only  $1000\text{ }^{\circ}\text{C}$ , and this sample produced a fine grained microstructure although of relatively low sintered density (Table 5.5). The extraordinarily rapid increase in grain size (two orders of magnitude) with a very

minor change in stoichiometry (from only 0.996 to 1.000) for solid-state derived samples solely because of non-equilibrium melt formation seems most improbable.

A brief study was undertaken to investigate the possible relationship between fracture properties and crystal structure using XRD. Powder patterns were taken for sintered ceramics after dry grinding in a ring mill for two to three minutes and are presented in Figures 6.27 to 6.29. The differences in XRD patterns between samples with and without exaggerated grain growth can be accounted for by preferred orientation and do not require changes in crystal structural parameters to produce Rietveld models which adequately match the measured data. XRD patterns from samples with exaggerated grain growth throughout their interior showed strong preferred orientation in the  $\langle 100 \rangle$  axis, whereas preferred orientation from samples without exaggerated grain growth was much weaker. Preferred orientation in powder samples was related only to grain growth in sintered samples and was independent of stoichiometry. Ba-rich samples with exaggerated grain growth only in a thin subsurface layer did not display strong preferred orientation in powder XRD patterns after grinding. SEM analysis of ground powders showed that preferred orientation was not an artifact of inadequate particle size reduction, because all samples ring milled for more than two minutes had particle sizes less than  $\sim 1 \mu\text{m}$ . Because all samples were ground to particle sizes significantly less than the grain sizes of the corresponding sintered ceramic, the difference in XRD patterns between samples with and without exaggerated grain growth shows that structural differences exist on a scale smaller than the grain size. Large grains have substructure and/or crystallographic defects (such as point defects and/or dislocations) which affect fracture properties resulting in oriented powder XRD patterns. All other specimens analysed, including all processed powders and ground sintered ceramics without exaggerated grain growth, produced XRD patterns with significantly less or no preferred orientation.

Measurement of crystallographic defect structure, particularly using XRD, is beyond the scope of this project and would require careful experimental design and high quality data for reliable conclusions. Increased diffusion rates caused by crystallographic defects could explain the origin of exaggerated grain growth which requires greatly increased crystal growth rates compared to the fine grained structure

more typical of BaZrO<sub>3</sub> produced in this and other research (Richerson 1992, p. 529). By analogy to ZrO<sub>2</sub> which turns a dark grey colour if sintered in a sufficiently reducing atmosphere, the apparent dependence of the colour of BaZrO<sub>3</sub> on oxygen partial pressure during sintering is inferred as indicating oxygen vacancies. The most likely crystallographic defect in Ba-rich ceramics is hypothesised to be substitution of Ba<sup>2+</sup> for Zr<sup>4+</sup> ions in the BaZrO<sub>3</sub> structure, with an adjacent oxygen vacancy for charge conservation and to provide space for the large Ba ion in the crystal lattice. Without oxygen vacancies, there is simply no space for the substitution of the very large Ba<sup>2+</sup> ion for the much smaller Zr<sup>4+</sup> ion within the BaZrO<sub>3</sub> crystal lattice. This paired defect would be expected to provide weakness in <100> planes and give rise to the typically orthogonal surfaces shown in Figures 6.20 to 6.24 and perhaps the defect structures observed in TEM although this is not certain. The requirement of oxygen vacancies for the possibility of Ba substitution may explain why exaggerated grain growth was not observed at external surfaces where oxygen partial pressures would be highest during sintering.

The effect of oxygen partial pressure during sintering is rather contentious because grain growth occurred with and without addition of organic lubricants, and therefore oxygen partial pressures higher than in air would be needed to investigate this possibility. Exaggerated grain growth was not observed for Zr-rich ceramics, possibly because they lack excess of Ba for substitution into the BaZrO<sub>3</sub> lattice and therefore do not produce the possible crystallographic defects that lead to grain growth. The substitution of Zr<sup>4+</sup> into the BaZrO<sub>3</sub> lattice would be most unlikely because of the high 4<sup>+</sup> valency (Richerson 1992, p. 41), which is consistent with the lack of defects observed by TEM within BaZrO<sub>3</sub> grains in Zr-rich specimens, and the segregation of off stoichiometric Zr as ZrO<sub>2</sub> (Section 6.5.3).

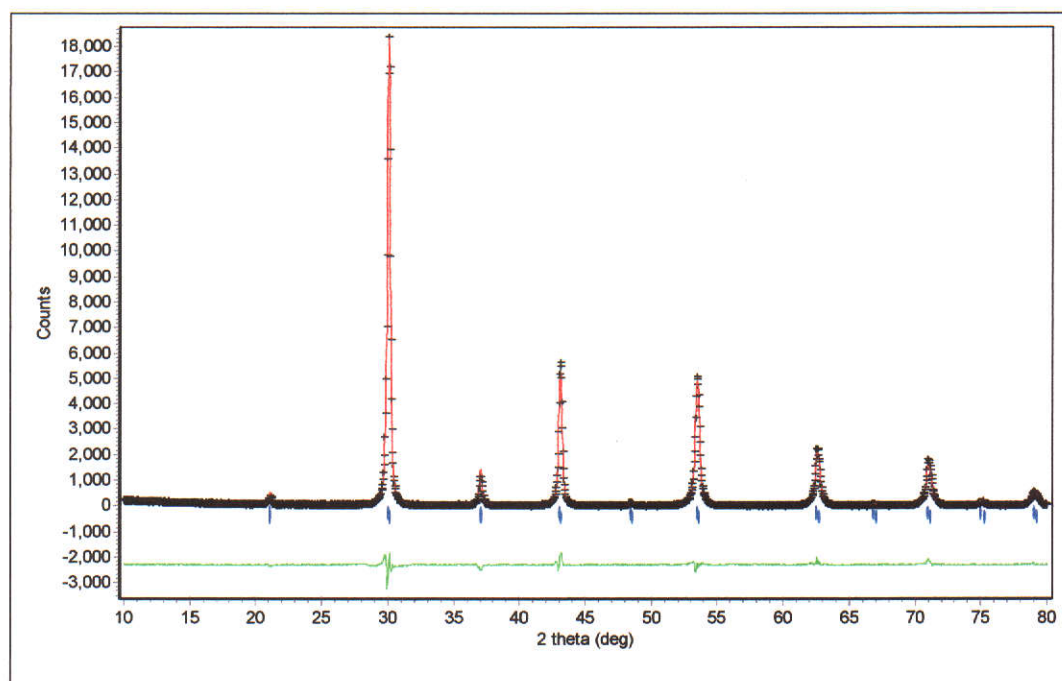


Figure 6.27 XRD pattern of solid-state derived sintered ceramic without exaggerated grain growth after brief milling. Ba : (Zr + Hf) mole ratio =  $0.988 \pm 0.002$ . Black points are measured data, red and green lines are calculated and difference plots of Rietveld model. Preferred orientation was minimal.

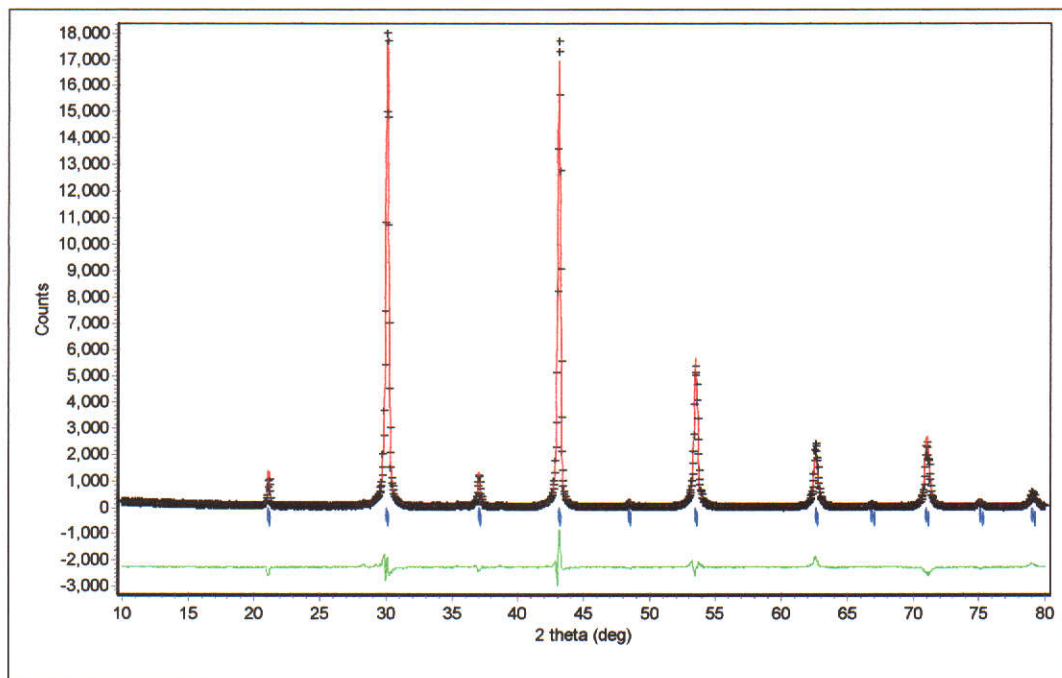


Figure 6.28 XRD pattern of solid-state derived sintered ceramic with exaggerated grain growth showing strong preferred orientation in powder pattern after brief milling: peaks at 21 and 43 ° are much larger than standard patterns from random crystallite orientation. Ba : (Zr + Hf) mole ratio =  $1.015 \pm 0.002$ .



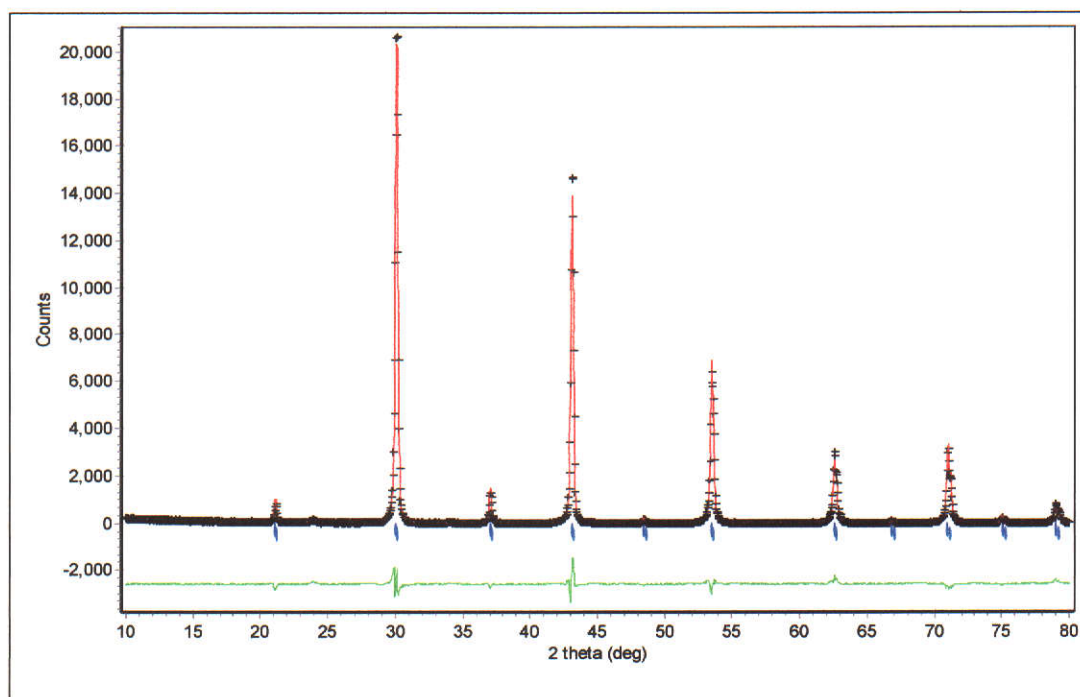


Figure 6.29 XRD pattern of solid-state derived ground sintered ceramic with exaggerated grain growth showing strong preferred orientation in powder pattern after brief ring milling (20 seconds). Ba : (Zr + Hf) mole ratio =  $1.011 \pm 0.002$ .

Microstructural considerations affecting sintered grain sizes cannot be ignored. Fine grain size in Zr-rich ceramics may be due to grain boundary pinning of  $\text{ZrO}_2$  grains present as a secondary phase, which according to the phase diagram are insoluble in  $\text{BaZrO}_3$  and have been observed in Zr-rich ceramics as discrete grains. The lack of exaggerated grain growth in Ba-rich oxalate derived ceramics may simply be due to grain boundary pinning by residual  $\text{ZrO}_2$  caused by poor phase purity.

Time and resources prevented further development to devise a means of preventing exaggerated grain growth in Ba-rich oxalate powders. Before commencing a detailed mechanistic study, some simple experiments at a constant, slightly Ba-rich stoichiometry are suggested which may provide a solution or help understand the mechanism of exaggerated grain growth. The first experiment is to investigate the effect of powder phase purity on sintered grain growth by sintering powders produced using one to three calcinations with intermediate regrinding. Grain size may be increased by reduced powder phase purity if Ba-rich phases cause grain growth, or may be reduced if  $\text{ZrO}_2$  causes grain boundary pinning. Grain boundary

pinning should be able to be observed by electron microscopy if suitable specimen preparation facilities are available.  $\text{ZrO}_2$  pinning would not be an effective solution for grain growth because of its strong effect on corrosion resistance shown in Table 6.1 (p. 205). The second experiment is to sinter under very oxidizing conditions (i.e. pure  $\text{O}_2$ ) and reducing conditions (e.g.  $\text{H}_2$  in  $\text{N}_2$ ) to observe whether sintering atmospheres affect grain growth. This could not be attempted in this project because sintering atmosphere control was not available.

### 6.5.3 TEM

The fracture surfaces of very large grains in solid-state derived Ba-rich ceramics and strong preferred orientation of (h00) peaks of these samples ground into powders and analysed by XRD implied the existence of defects on a scale significantly smaller than the size of the large grains. The size of steps in fracture surfaces appearing to conform to the cubic crystal structure observed by SEM ranged from several micrometres down to only a few tens of nanometres. Defects did not result in changes in lattice parameters, and whether defects were present within the crystal structure was not resolved from XRD measurements.

The existence of nanoscale defects within  $\text{BaZrO}_3$  grains in Ba-rich samples was directly confirmed by TEM analysis. The need to avoid all contact with water for sectioning of Ba-rich ceramics severely restricted the number of specimens that could be prepared for TEM analysis. Few samples were available for analysis because most were needed for Archimedes density measurement, during which water exposure renders them inappropriate for microstructural examination. Detailed examination of the internal structure of very large grains was difficult because only relatively small areas of electron transparent material could be produced using the preparation method available. However, intra-crystalline defects were observed in Ba-rich ceramics both with and without exaggerated grain growth. Two types of defect morphologies were observed in Ba-rich ceramics. As shown in Figures 6.30 and 6.31 quite large scale defects were observed within a very large grain which ran in straight lines  $45^\circ$  apart. The curved edges of the grain shown in Figure 6.30 were due to perforation from ion beam thinning, and are caused mostly by the circular geometry of the ion beam rather than the properties or structure of the specimen.

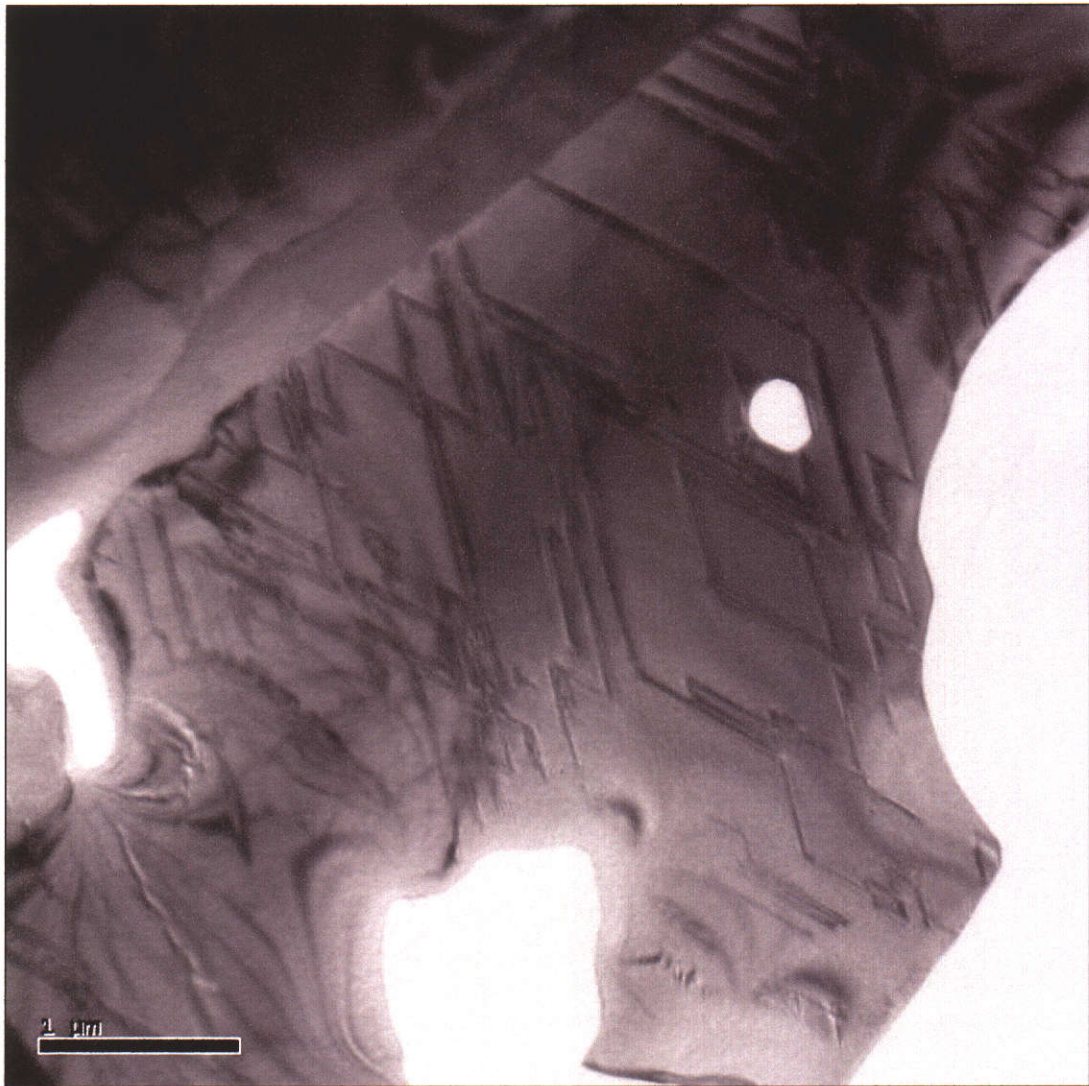


Figure 6.30 TEM of defect structure in a large BaZrO<sub>3</sub> grain in Ba-rich solid-state derived ceramic showing consistent defect orientation over a large area of the grain, and characteristic 45 ° angles between defects which may be related to the crystal structure of BaZrO<sub>3</sub>. Scale bar = 1 μm.



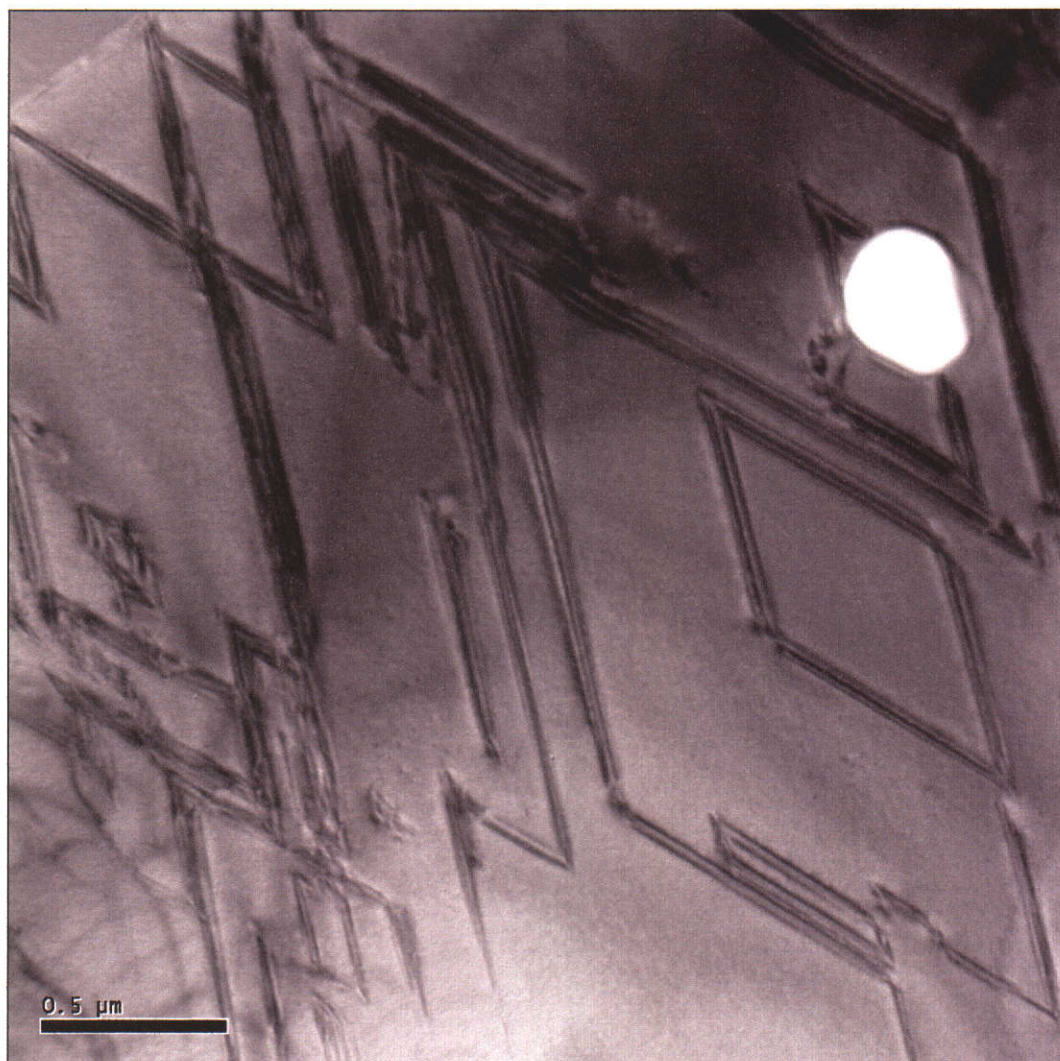


Figure 6.31 Higher magnification TEM image of Figure 6.30 showing defect structure in more detail. Defect orientation was maintained across the pore shown in the top right of image. Scale bar = 0.5  $\mu\text{m}$ .

TEM was used to analyse the fine grained interior of another solid-state derived specimen with a Ba : (Zr + Hf) mole ratio of  $1.006 \pm 0.002$  which produced exaggerated grain growth only in a thin subsurface layer. The vast majority of grains in this sample contained high levels of defects as shown in Figures 6.32 and 6.33. Defects were either very sharply defined almost perfect squares or rectangles as shown in the grain towards the bottom right of Figure 6.32, or more commonly very small cubic shaped defects as shown in Figure 6.33. The orthogonal geometry of these defects suggests they are closely associated with the cubic crystal structure of  $\text{BaZrO}_3$ . Some of these defects appear to be associated with strain contrast, which in a few locations propagated across grain boundaries.

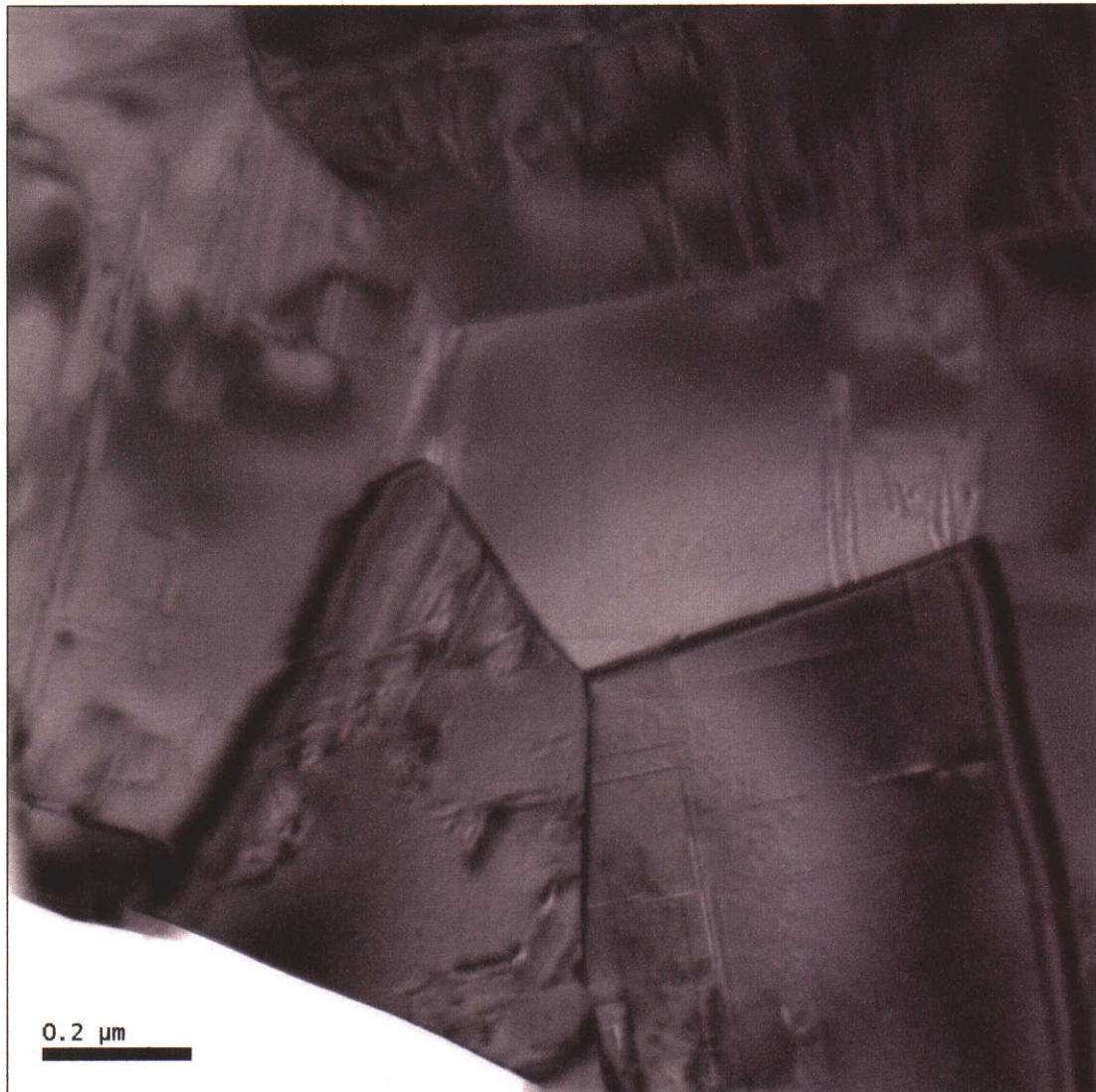


Figure 6.32 Defect structure in a fine grained Ba-rich solid-state derived ceramic. Defects were rectangular with sharply defined edges (grain in bottom right of image) or had a more diffuse, banded morphology (grain at top of image).



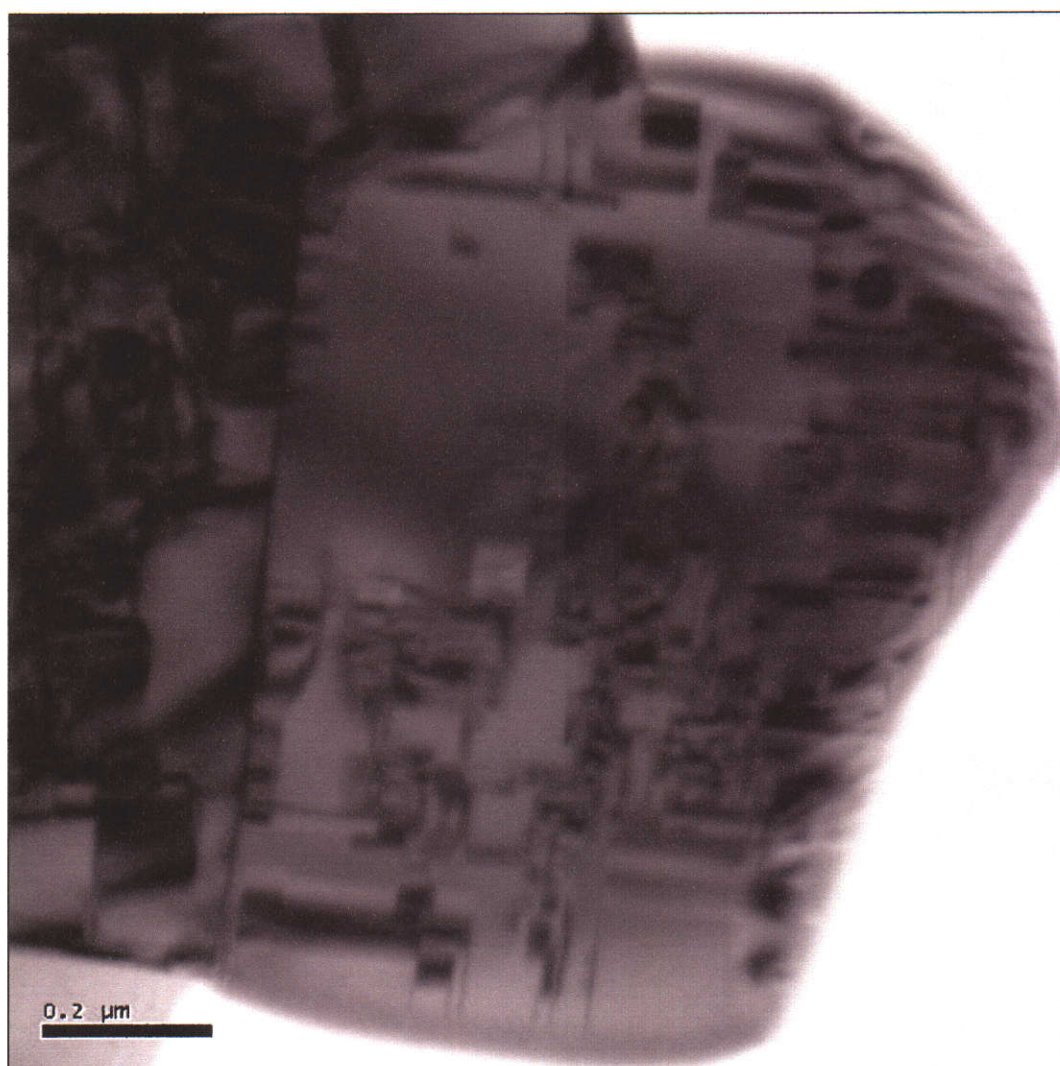


Figure 6.33 Detail of typical defect structure in fine grained Ba-rich solid-state derived ceramic. Defects show contrast reversal, rectangular geometry, and some are associated with strain contrast across grain boundaries. Scale bar = 200 nm.

The orientation of defects was strikingly constant within each grain in Ba-rich solid-state derived specimens, although this was difficult to confirm for very large grains because of limited transparent area. This suggested grains were single crystals, which contained defects on a nano or crystallographic scale for Ba-rich solid-state derived ceramics.

The intra-crystalline defect structures observed for Ba-rich solid-state derived specimens were not observed for Zr-rich specimens. Defects within grains in Zr-rich ceramics were not observed using brightfield TEM imaging. The microstructure of an oxalate derived Zr-rich specimen with Ba : (Zr + Hf) mole ratio is shown in



Figures 6.34 - 6.38 . Excess zirconium segregated as discrete  $\text{ZrO}_2$  grains between  $\sim 50 - 1000 \text{ nm}$  in size, which consistently had a twinned structure consistent with monoclinic  $\text{ZrO}_2$ .  $\text{ZrO}_2$  grains were typically at the grain boundaries of  $\text{BaZrO}_3$  grains, however small amounts of intragranular  $\text{ZrO}_2$  was also observed as shown in Figure 6.35.

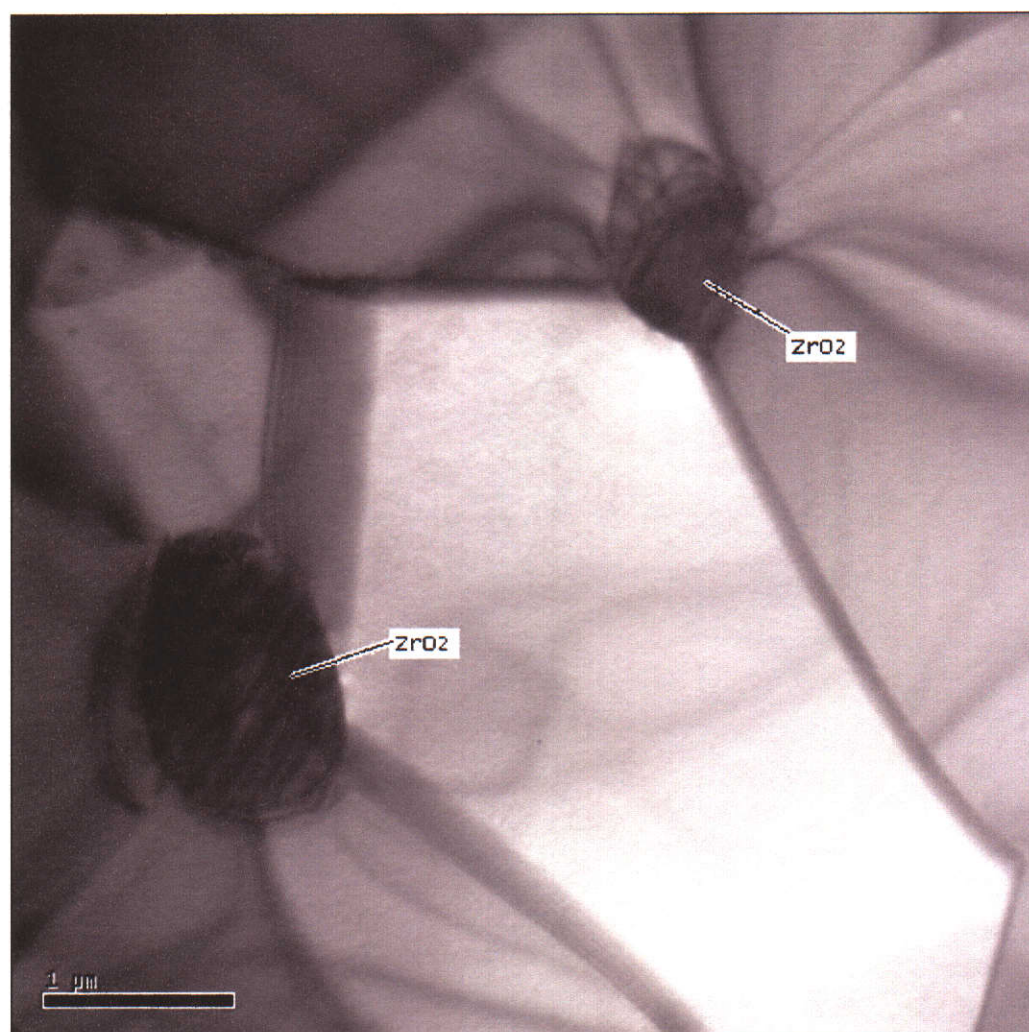


Figure 6.34 TEM micrograph of Zr-rich oxalate derived ceramic showing lack of defects within  $\text{BaZrO}_3$  grains and segregation of Zr as  $\text{ZrO}_2$  grains. Bands across central grain are thickness fringes and not crystal defects. Scale bar =  $1 \mu\text{m}$ .

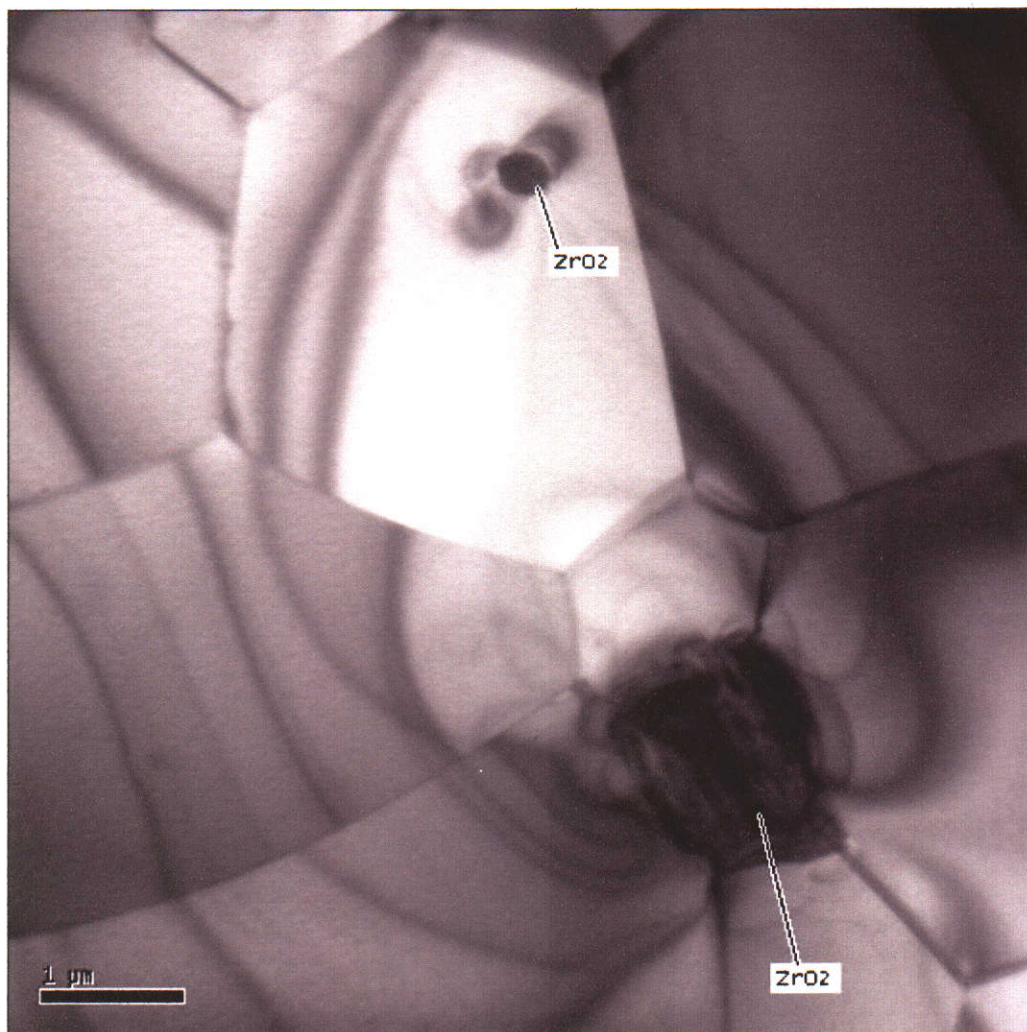


Figure 6.35 Brightfield TEM showing inter- and intragranular  $\text{ZrO}_2$  in Zr-rich oxalate derived  $\text{BaZrO}_3$ . Strain fields around  $\text{ZrO}_2$  are clearly visible. Other dark bands are thickness fringes and not crystallographic defects.

There was no evidence of Zr-rich films along grain boundaries, either continuous or otherwise. Figures 6.34 – 6.36 show there was good image contrast between  $\text{ZrO}_2$  and  $\text{BaZrO}_3$ . The apparent cross sectional widths of grain boundaries such as in Figures 6.34, 6.36 and 6.37 are due to the orientation of the grain boundary relative to the plane of analysis. The greater is the angle between the grain boundary and the axis of projection, the wider is the projected width of the grain boundary. The width of grain boundaries was negligible after tilting the grain boundary parallel to the projection axis. Grain boundary films thicker than 5 nm would have been readily observed with the instruments used in this study, and with careful analysis films as thin as 2 nm would have been detected, but such grain



boundary films were not found. Many hours were spent searching for Zr segregation along grain boundaries because of SEM observation of grain boundary films of YBCO melt after corrosion exposures. This included several hours of STEM analysis using a Jeol 3000 FEGTEM, one of the most powerful TEM instruments available for analysing fine scale segregation to less than  $\sim 2$  nm. Despite very high beam intensities and small probe sizes there was no indication of Zr segregation other than in discrete  $\text{ZrO}_2$  grains.

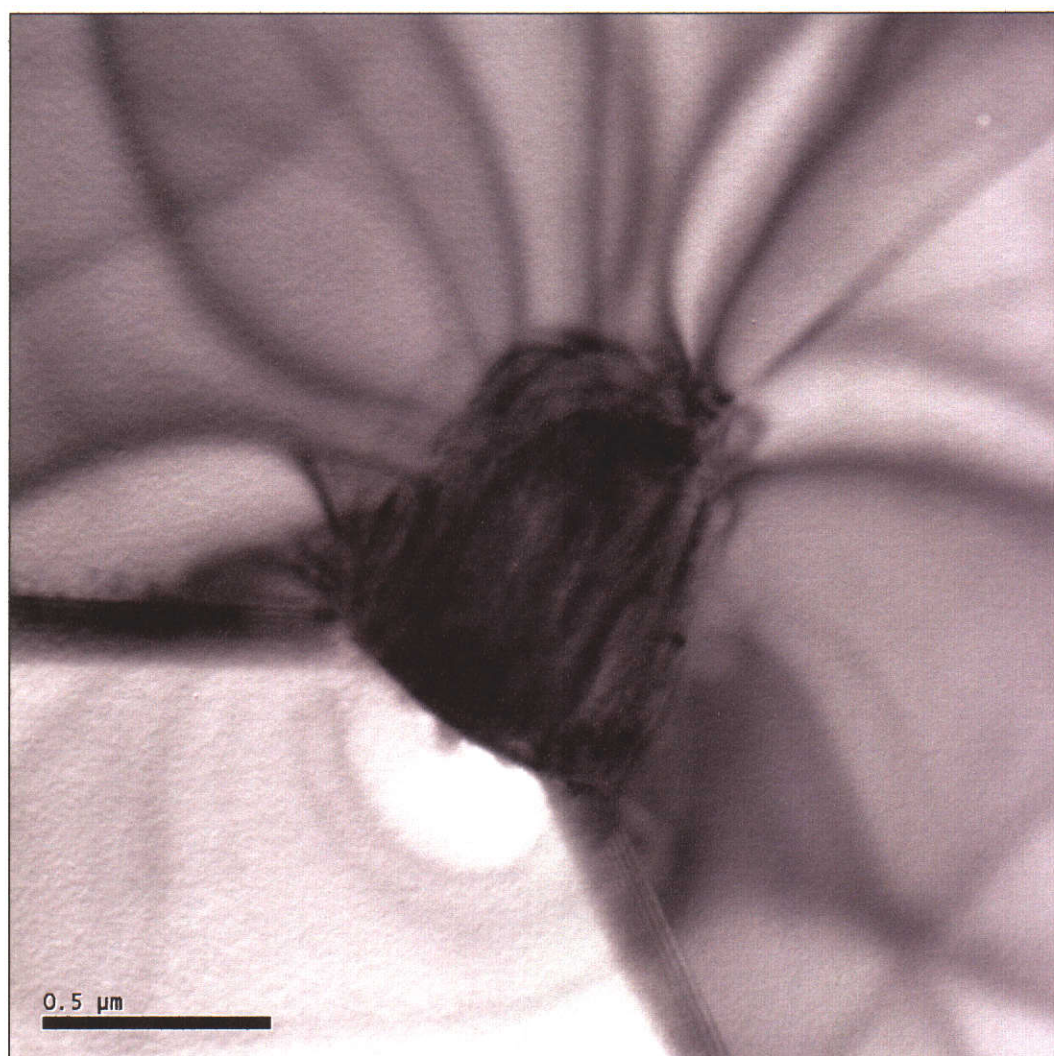


Figure 6.36 Bands across  $\text{BaZrO}_3$  grains are thickness fringes and strain contours due to  $\text{ZrO}_2$  particle. Grain boundaries show Moire fringes due to lattice orientation mismatch between grains but no evidence of grain boundary films. Scale Bar =  $0.5 \mu\text{m}$ .

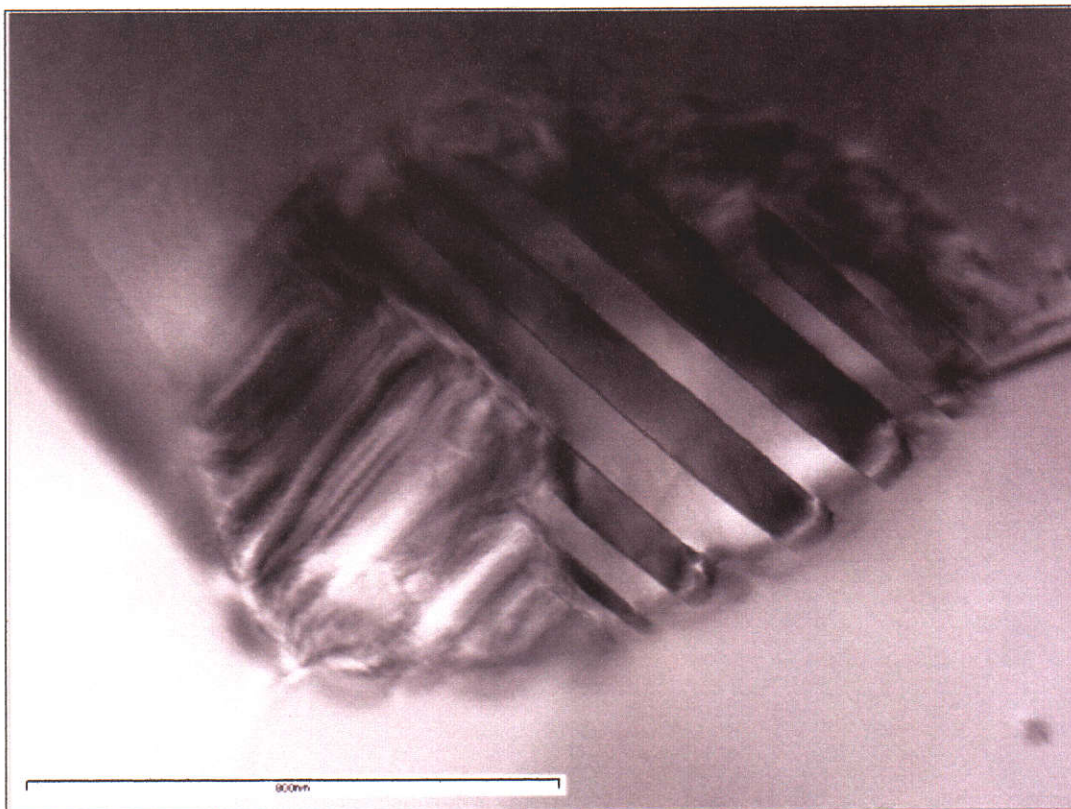


Figure 6.37 Brightfield STEM image of ZrO<sub>2</sub> grain in sintered Zr-rich ceramic. Scale Bar = 800 nm.

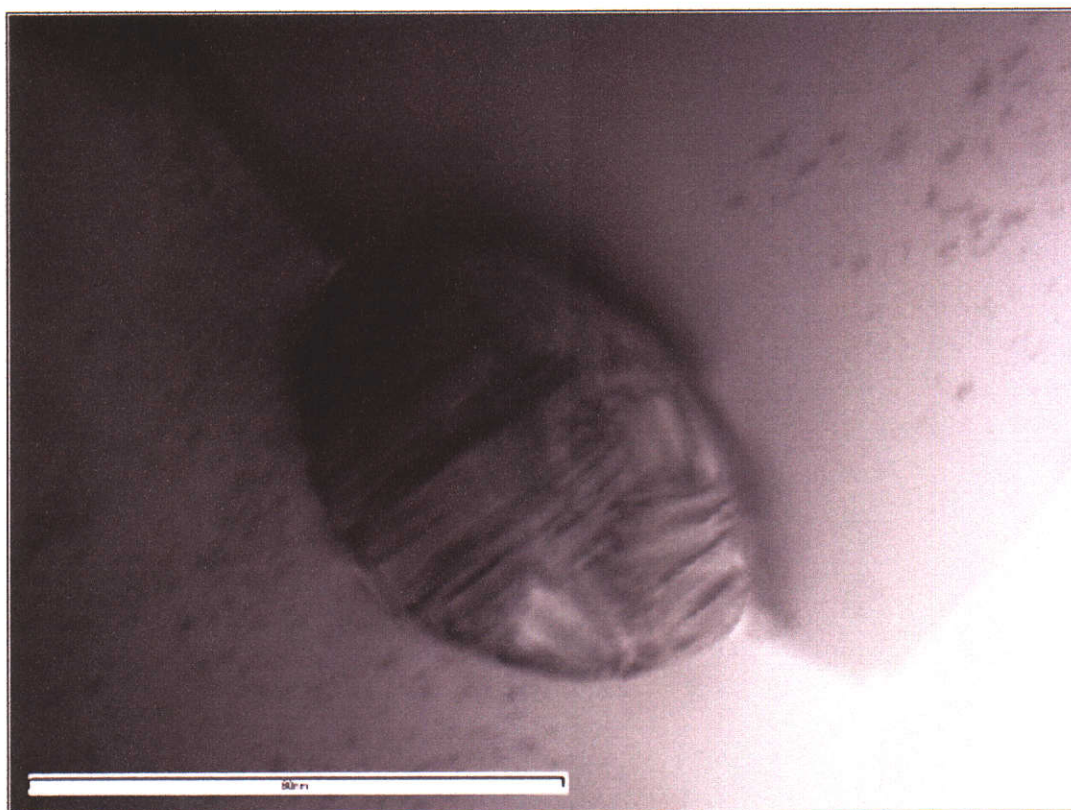


Figure 6.38 Brightfield STEM image of ZrO<sub>2</sub> grain in sintered Zr-rich ceramic. Scale Bar = 80 nm.



#### 6.5.4 Chemical contamination in oxalate processing

Deionised water used during initial oxalate processing experiments was found to be contaminated by aluminosilicate particles using SEM to analyse residues collected on 0.2  $\mu\text{m}$  polymer membrane filters. Aluminosilicate contamination artificially assisted sintering to high density, and when contamination was removed by changing to high purity deionised water, the difficulty of achieving high sintered densities for oxalate derived ceramics greatly increased. TEM was used to determine the location of aluminosilicate contamination.

A sintered specimen containing 0.5 wt.% kaolin was prepared to determine the suitability of TEM for locating aluminosilicate contamination. Figures 6.39 to 6.41 show that aluminosilicate contamination resulted in barium aluminosilicate secondary phases, which were readily detected to below  $\sim 50$  nm in size. These secondary phases could be visually located by brighter intensity due to reduced mass-thickness, and then confirmed by EDS analysis. Although spot sizes as low as 2 nm were used, a significant proportion of the x-ray signal for small precipitates was due to  $\text{BaZrO}_3$  and hence quantitative analysis of the composition of contaminants smaller than  $\sim 30$  nm was not feasible. Cu detection in spectra was due to the mounting of thin sections of Cu slot grids. However, the detection of Al and Si in spectra was sufficient to confirm the identity of secondary phases due to contamination.

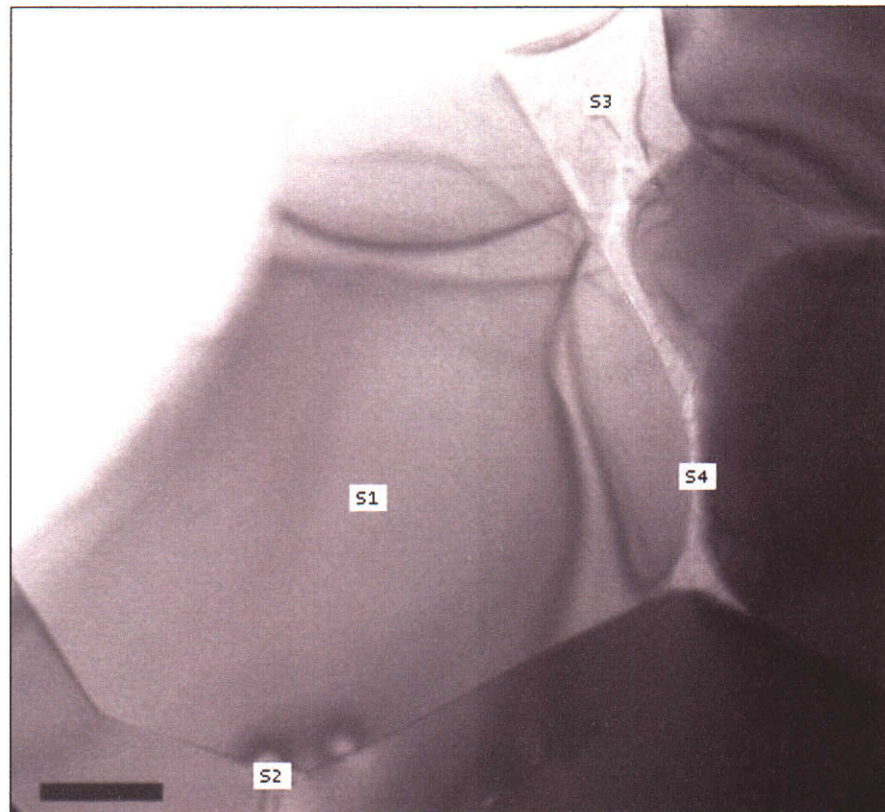


Figure 6.39 Bright-field TEM image of grain boundary in kaolin doped sample (Trang 2002). S1 – S4 are sites where EDS analysis was performed. Scale bar = 1  $\mu\text{m}$ .

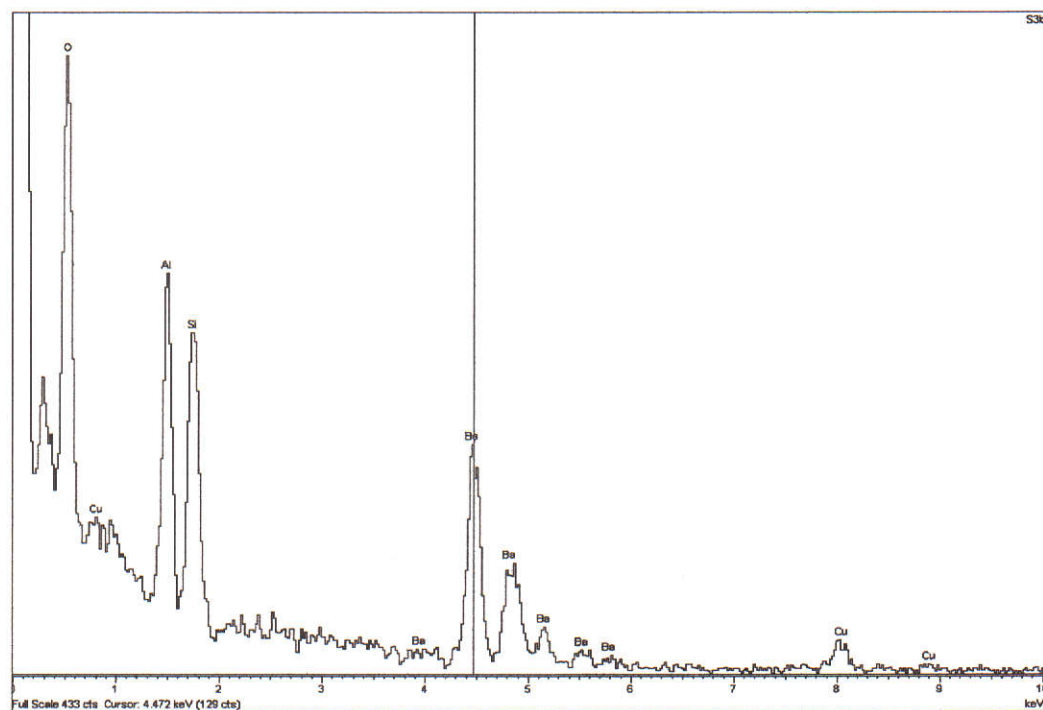


Figure 6.40 EDS spectrum from site 3 in Figure 6.39 showing aluminosilicate contamination resulted in barium aluminosilicate secondary phases that did not contain zirconium (Trang 2002).



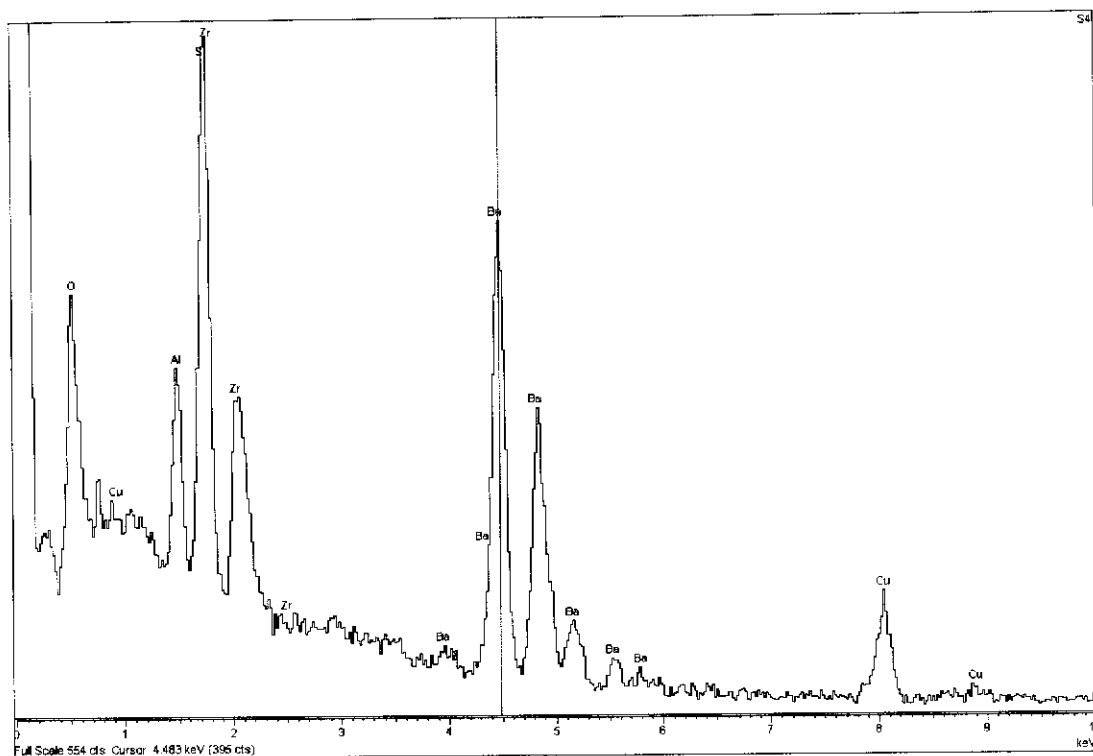


Figure 6.41 EDS spectrum from site 4 in Figure 6.39 confirming detection of barium aluminosilicate phases below  $\sim 50$  nm in size. Zirconium and part of the barium peaks are due to excitation of  $\text{BaZrO}_3$  (Trang 2002).

Figures 6.42 to 6.45 show TEM results for a sintered  $\text{BaZrO}_3$  sample contaminated by process water rather than by deliberate kaolin addition. Barium aluminosilicate phases typically occurred as very small ( $\sim 5 - 50$  nm) triple point phases in a small fraction ( $\sim 5\%$ ) of the observed triple points. There was no evidence of extended grain boundary films due to contamination. Aluminosilicate contaminants were not observed within  $\text{BaZrO}_3$  grains.

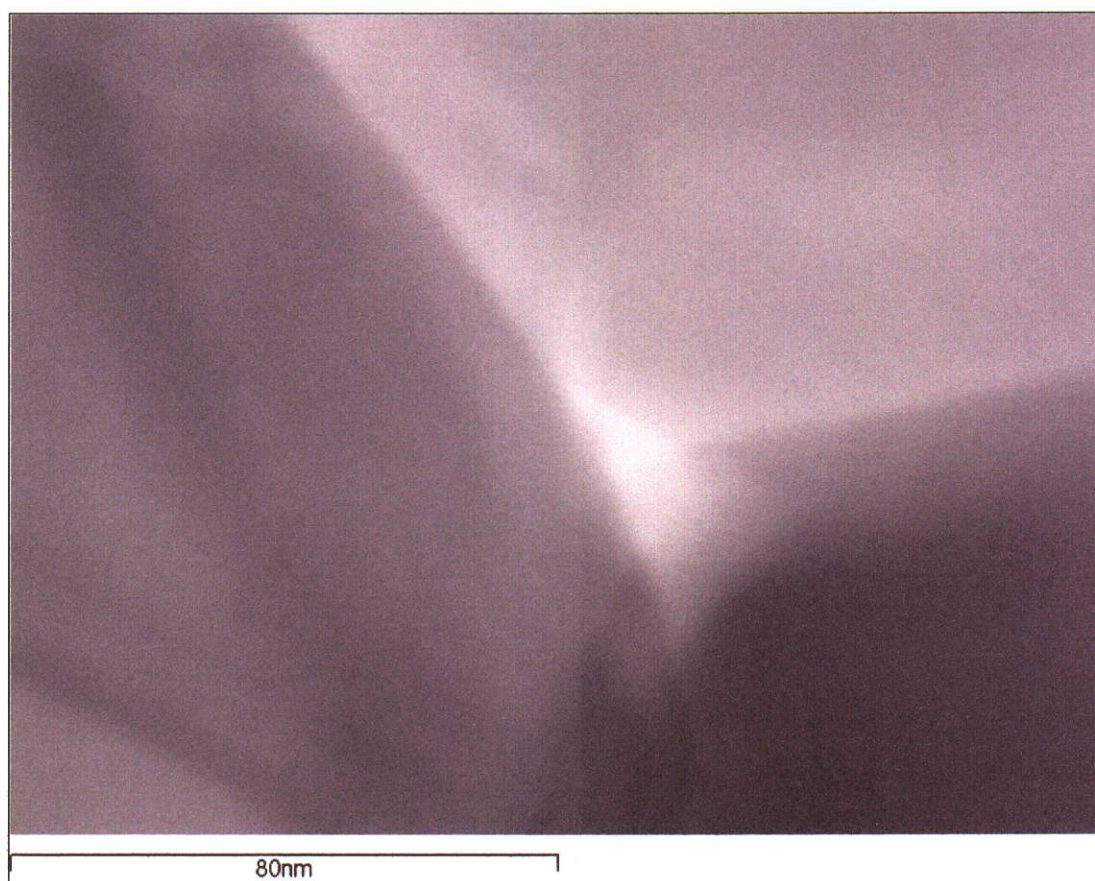


Figure 6.42 Brightfield STEM image of a  $\sim 5 - 10$  nm barium aluminosilicate precipitate at triple point of contaminated sample. Scale bar = 80 nm.

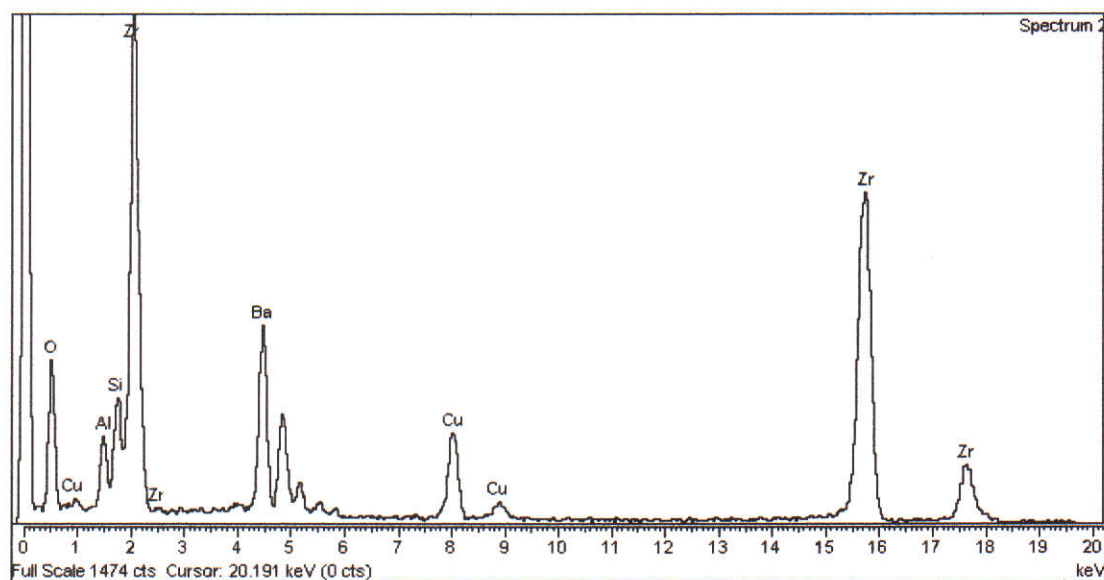


Figure 6.43 EDS Spectrum from triple point shown in Figure 6.42. Cu was due to slot grid on which thin section was mounted (Trang 2002).

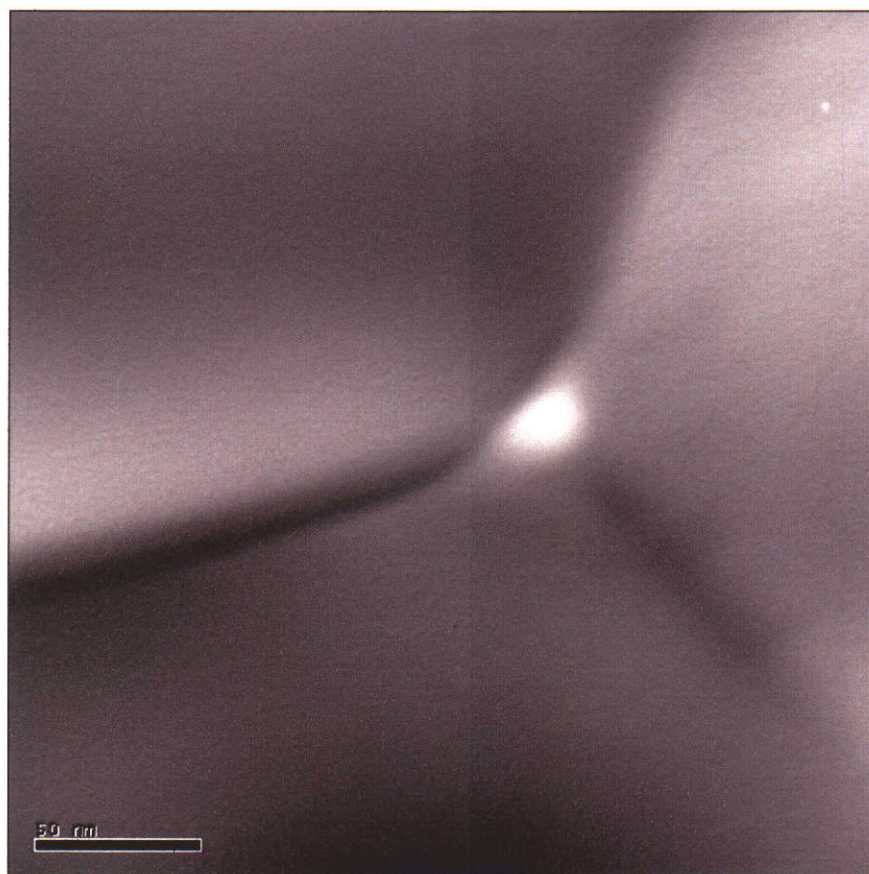


Figure 6.44 Brightfield TEM image of a  $\sim 20$  nm barium aluminosilicate precipitate in a triple point of a contaminated sample. Scale bar = 50 nm.

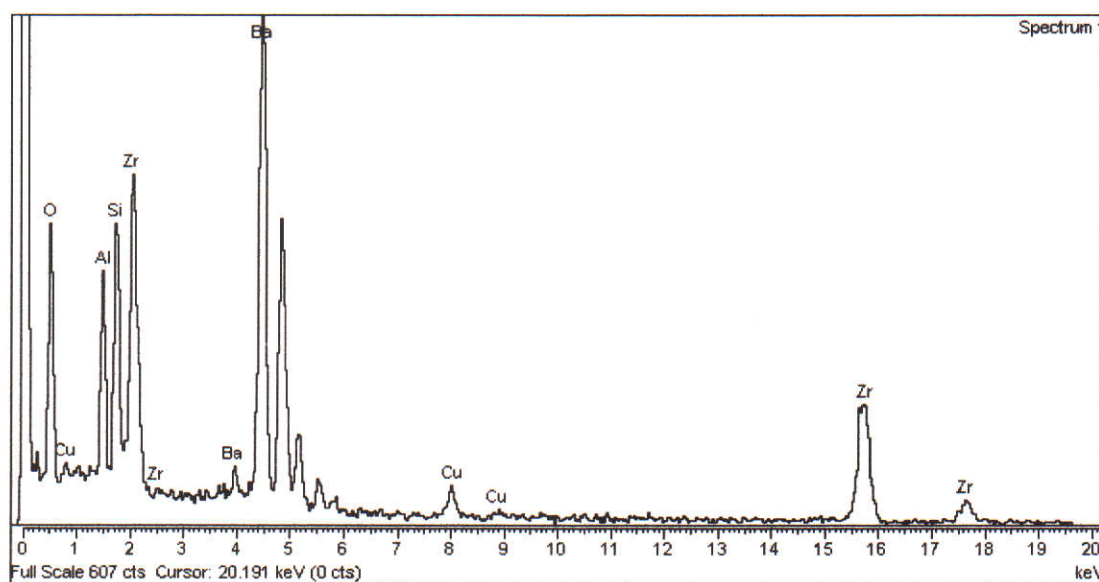


Figure 6.45 EDS Spectrum from triple point shown in Figure 6.44. Cu was due to slot grid on which thin section was mounted.

### 6.5.5 Conclusions

Results presented in Section 6.5 showed that exaggerated grains in Ba-rich solid-state derived ceramics were not perfect single crystals but contained a larger number of defects at a nano and/or crystallographic scale which produced fracture surfaces which conformed closely with an underlying cubic crystal structure. The exact nature of these defects was not determined, such as whether they were dislocations and if so of what type and crystallographic orientation etc., or whether they were due to very small scale phase separation possible due to excess Ba that may have been in solid solution at the sintering temperature but segregated during cooling. Whether these defects play an important role in mass transport during sintering and/or melt corrosion was beyond the scope of this project and could require substantial research to properly address this issue. Lack of time, difficulties in specimen preparation for electron microscopy and the more detailed nature of the microstructure prevented adequate assessment of the microstructural distribution of Ba-rich phases in Ba-rich ceramics.

The microstructure of Zr-rich ceramics was determined in considerable detail. Excess Zr clearly segregated as  $\text{ZrO}_2$  grains, most of which were intergranular with respect to  $\text{BaZrO}_3$ . Excess  $\text{ZrO}_2$  did not lead to grain boundary films. Apart from strain fields surrounding  $\text{ZrO}_2$  grains,  $\text{BaZrO}_3$  grains were essentially free of observable defects. Aluminosilicate contamination lead to very small barium aluminosilicate grains at a small fraction of observed triple points rather than grain boundary films.

## 6.6 Melt corrosion

### 6.6.1 Corrosion properties

Table 6.1 shows the effect of stoichiometry on the corrosion resistance of solid-state derived crucibles. Maximum corrosion resistance was observed in a narrow range of Ba : (Zr + Hf) mole ratios between approximately 1.002 – 1.010. All crucibles with Ba : (Zr + Hf) mole ratios lower than 1.001 failed rapidly during corrosion exposure and would not be useful for single crystal growth experiments, which typically take at least 36 hours at ~1000 °C. Crucibles with a slight barium excess of up to ~ 1.010 Ba : (Zr + Hf) mole ratio were considerably more corrosion resistant than crucibles with any measurable excess of zirconium.

Table 6.1 Effect of stoichiometry on corrosion resistance of solid-state derived crucibles.

Ba : (Zr + Hf) Mole Ratio	Time melt remained above 2/3 original level (days)	Time melt remained above ½ original level (days)	Time melt remained above ¼ original level (days)
0.961	0.5*	1.0	1.0
0.961	0.5*	1.0	1.0
0.995	0.5*	1.0	1.7
0.996	2.4	2.7	3.3
0.997	0.5*	0.9*	1.5
1.002	2.7	3.0	3.3
1.002	2.7	3.0	3.3
1.003	3.3	X	X
1.003	3.4	4.4	7.1
1.005	2.8	3.7	5.8
1.008	2*	2*	3.4
1.014	2*	2*	3.4
1.015	1.7	2.0	2.8

\* = estimation based on observation of sample at a later time in corrosion exposure.

X = corrosion exposure stopped early

The relationship between corrosion resistance and stoichiometry of oxalate-derived crucibles is presented in Table 6.2. As for solid-state derived crucibles, Zr-rich oxalate derived crucibles were not suitable for single crystal growth due to complete melt leakage within one to two days. Leakage was typically associated with macroscopic crack formation, particularly at the front surface where thermal shock exposure was most severe.

The number of oxalate derived crucibles that could be produced for corrosion resistance testing was impeded by the very large experimental program required to develop the oxalate process and slightly increased difficulty in sintering oxalate derived samples to high density. The corrosion resistance of Ba-rich oxalate derived crucibles was more difficult to reproduce than solid-state derived crucibles, but in most cases was at least as good as solid-state derived crucibles. One oxalate derived crucible failed prematurely during single crystal growth, but the density of this crucible was not determined. One oxalate derived crucible did not show macroscopic cracking after 7.5 days melt exposure and was topped up to half full with melt from other crucibles being tested at the same time. The rate of leakage during a second week of melt exposure was very low, suggesting that with further process optimisation and better sintering, the oxalate process may have the potential to supersede the solid-state process. However, there was insufficient experimental evidence to adequately demonstrate whether the solid-state process had been superseded at the current state of oxalate process development.



Table 6.2 Effect of stoichiometry on corrosion resistance of oxalate derived crucibles.

Ba : (Zr + Hf) Mole Ratio	Porosity (vol. %) $\pm 0.1$	Time melt remained above 2/3 original level (days)	Time melt remained above 1/2 original level (days)	Time melt remained above 1/4 original level (days)
0.950	5.5	< 0.5	0.5	< 1
0.986	5.4	< 1	1	< 2
1.005 <sup>1</sup>	< 9 <sup>2</sup>	< 4.5	4.5	7.5 <sup>3</sup>
1.015	2.7	4	5.5	6.5

<sup>1</sup> Estimated, based on measurement of other batch of powder precipitated under the same conditions.

<sup>2</sup> Test pellet used for density measurement had numerous cracks, whereas crucible was free of cracks and was expected to be significantly less porous.

<sup>3</sup> Crucible was topped up to half full with melt from other crucibles after 7.5 days exposure. Melt leakage was very slow after 7.5 days, taking another 7 days for the melt height to drop to one third full.



Figure 6.46 Solid-state derived crucible with Ba : (Zr + Hf) mole ratio of 1.008 after four days corrosion exposure at 1050 °C. The front surface in the photograph was at the front of the furnace during exposure. Smallest division on ruler is 1 mm.



Figure 6.47 Solid-state derived crucible with Ba : (Zr + Hf) mole ratio of  $1.002 \pm 0.002$  after four days corrosion exposure at 1050 °C. Smallest division on ruler is 1 mm.



Figure 6.48 Oxalate derived crucible with Ba : (Zr + Hf) mole ratio of  $\sim 1.005$  after eight days corrosion exposure at 1050 °C. Smallest division on ruler is 1 mm.

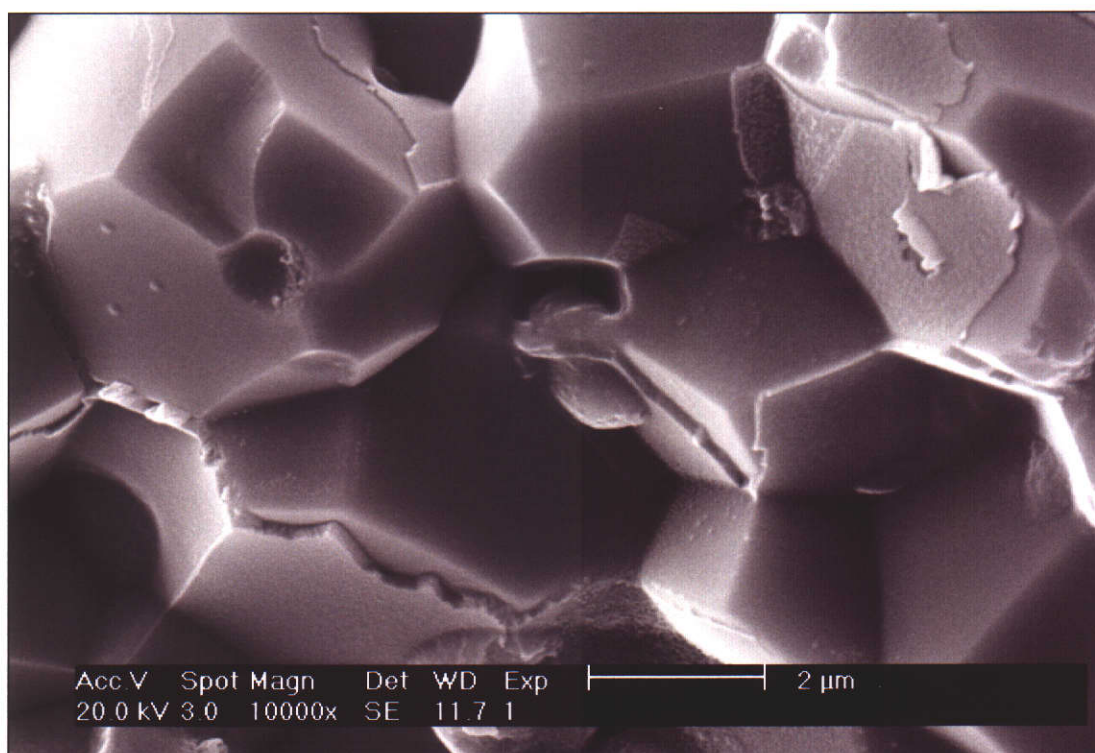


### 6.6.2 Mechanisms of corrosion processes

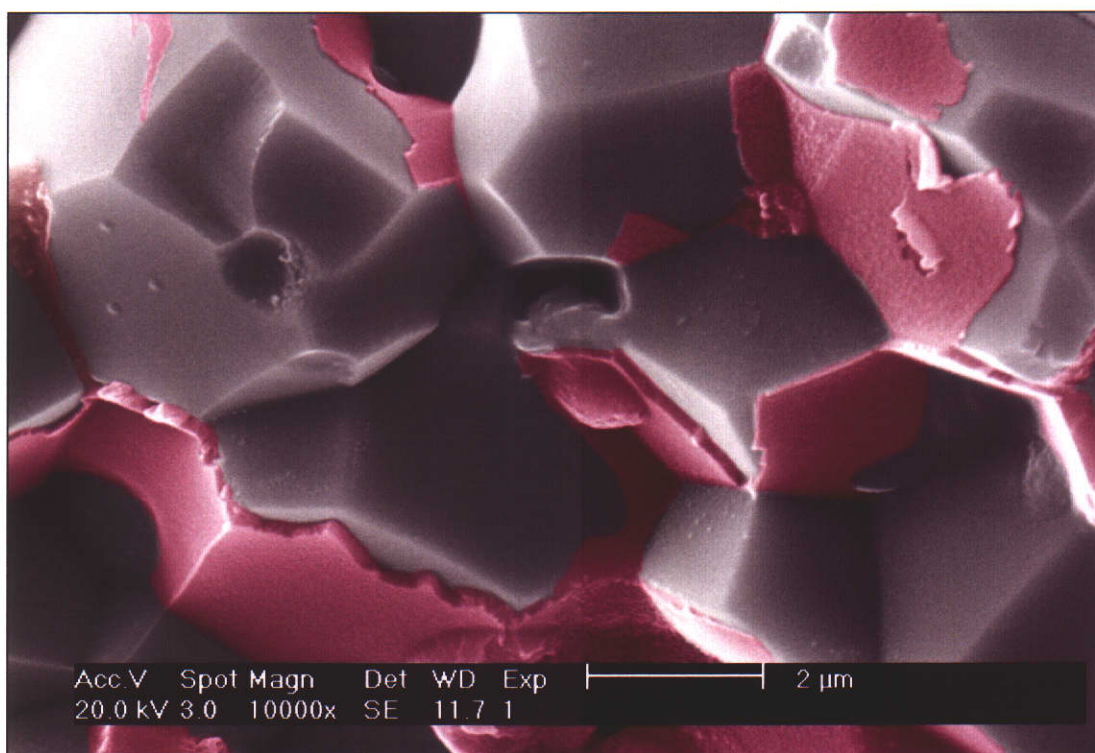
The most probable explanation for the acute sensitivity of crucibles to residual  $\text{ZrO}_2$  almost certainly lies in the very large volume expansion of  $\text{ZrO}_2$  after reaction with  $\text{BaO}$  from the melt to form  $\text{BaZrO}_3$ . The molar volumes of monoclinic  $\text{ZrO}_2$  and  $\text{BaZrO}_3$  are 21.4 mL and 44.4 mL respectively (calculated from ICDD 6-399 and 37-1484), and the  $\sim 100\%$  volume expansion of  $\text{ZrO}_2$  after reaction with the melt causes severe localised strains which cannot be accommodated elastically, hence cracking is inevitable. No brittle material has the capacity to absorb  $100\%$  localised volumetric expansion without at least localised cracking. As shown in Figures 6.49 to 6.50,  $\text{ZrO}_2$  rich ceramics displayed distinctive grain boundary films of YBCO melt after corrosion exposures, which were readily observed using secondary electron imaging and confirmed by EDS analysis. These grain boundary films can be nearly continuous (e.g. at 0.95 Ba : (Zr + Hf) mole ratio) and occupy far more volume than any observable grain boundary structures in the un-corroded ceramic.

TEM analysis conclusively showed that  $\text{ZrO}_2$  was not present as grain boundary films in any detectable form (i.e. continuous or fragmented, and above  $\sim 2$  nm in thickness).  $\text{ZrO}_2$  was present only as discrete grains between a few tens to a few hundred nanometres in diameter (Section 6.5.3). It is clear that cracking from  $\text{ZrO}_2$  reacting with the melt causes localised expansion along grain boundaries, providing space for melt to flow through a progressively corroding body. The detailed mechanisms of other possible mass transport processes along grain boundaries remained unknown because defect structures such as crystallographic vacancies at grain boundaries were not observed. Initiation of grain boundary cracking by melt reaction with  $\text{ZrO}_2$  at external surfaces might be sufficient to lead to complete corrosion failure without requiring other mass transport mechanisms along grain boundaries such as vacancies or other defects. As shown in Figures 6.46 to 6.48, macroscopic cracking during corrosion was also frequently observed. Macroscopic cracking was exacerbated by thermal shock exposure, but was more pronounced in Zr-rich than Ba-rich ceramics.

Crucibles were exposed to significant thermal shock during corrosion resistance evaluation because of limitations of available equipment. Observing the crucibles during exposure required the door of the muffle furnace to be completely opened, for approximately two seconds on each occasion. To minimise thermal shock damage caused by exposing a relatively brittle ceramic to up to 1000 °C temperature difference, inspection times were kept as brief as possible and only a few inspections were conducted during each day of exposure. Despite this, thermal shock clearly contributed to premature failure, because the initial and most severe macroscopic cracking occurred on the side closest to the door of the furnace, on every crucible tested (e.g. Figure 6.46). Damage due to thermal shock was almost certainly exacerbated by internal stresses from crystallographic transformations of  $\text{ZrO}_2$ , reactions of secondary phases with the melt, and large grain sizes for Ba-rich solid-state derived crucibles. Brittle failure due to thermal shock may have contributed significantly to the variability of corrosion resistance observed in this project. Thermal shock exposure is not present during single crystal growth because temperatures and temperature gradients are precisely controlled, so the suitability of crucibles for melt containment for single crystal growth might be slightly extended.

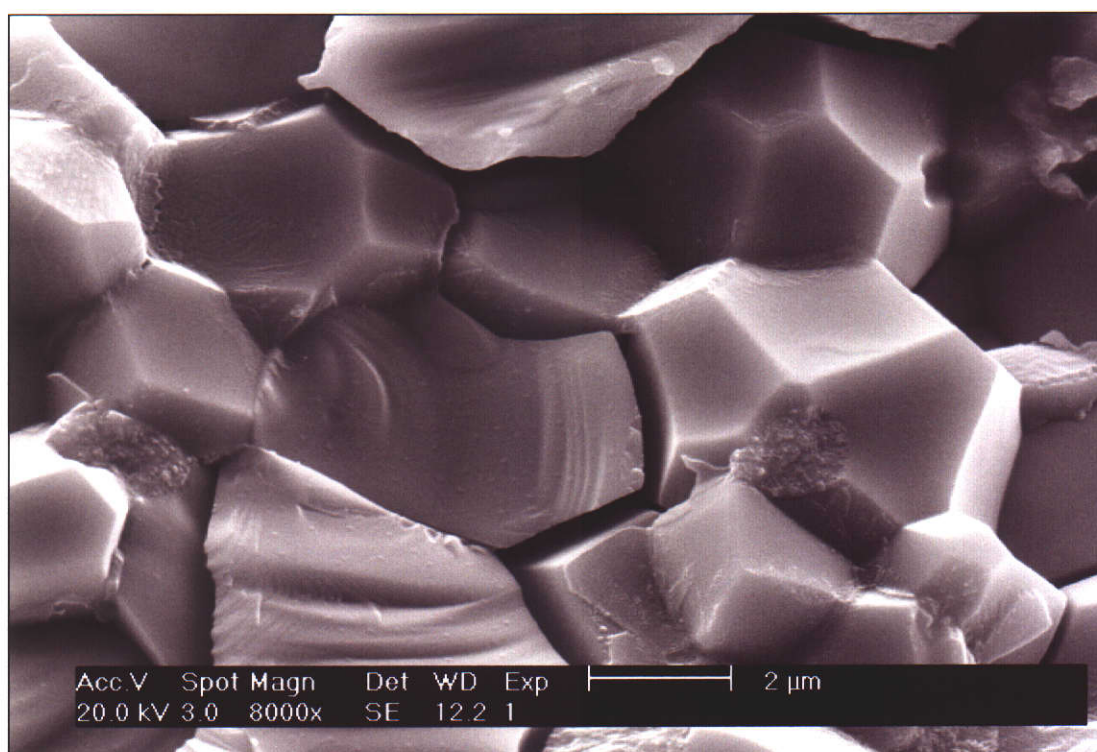


(a)

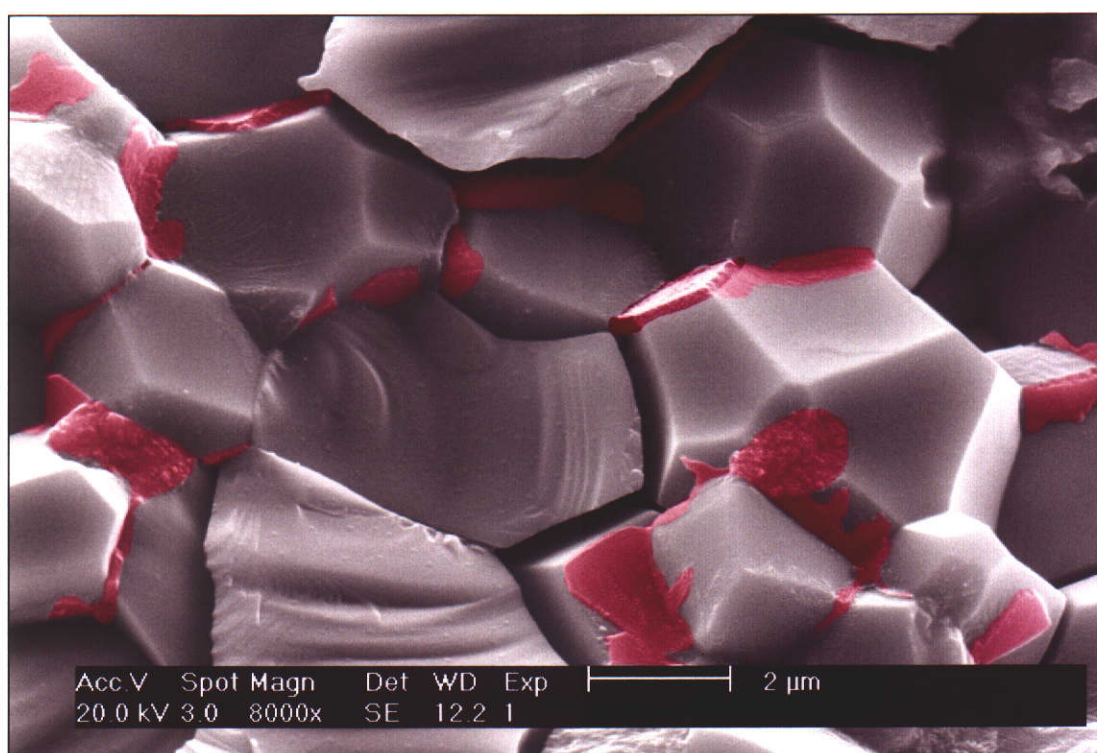


(b)

Figure 6.49 SEM micrograph showing YBCO grain boundary films after melt corrosion of Zr-rich ceramic. Original SE image (a) and false coloured image (b) indicating locations where YBCO was confirmed by EDS analysis. Scale bar = 2  $\mu\text{m}$ .



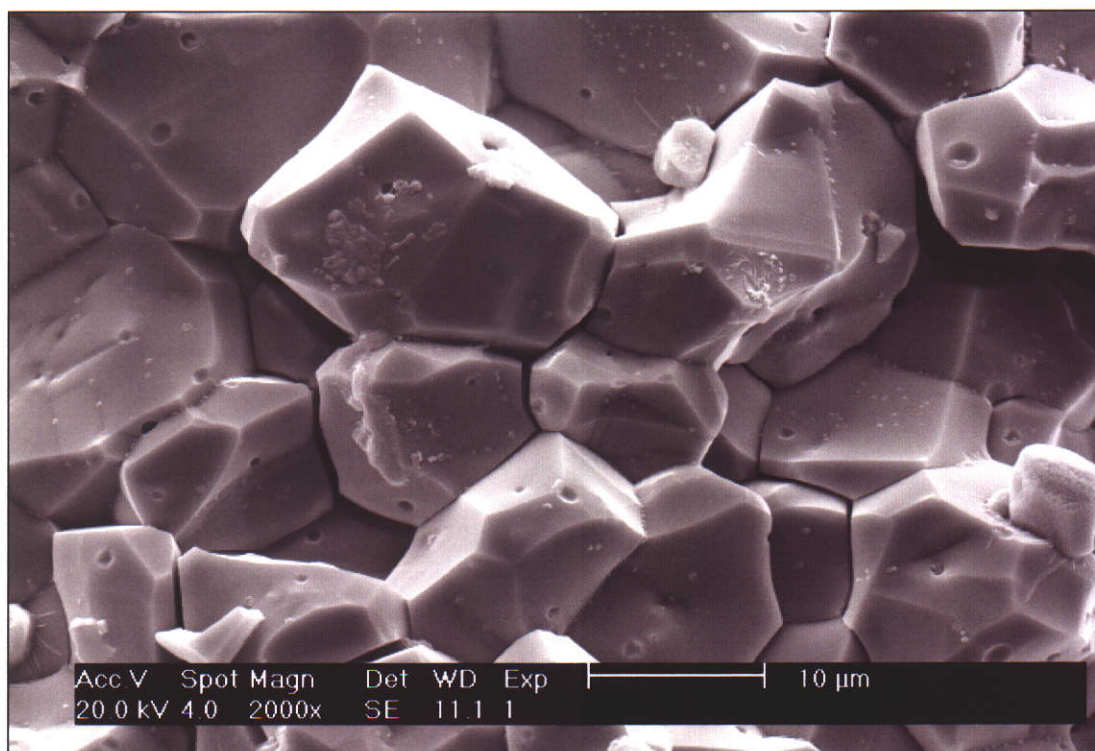
(a)



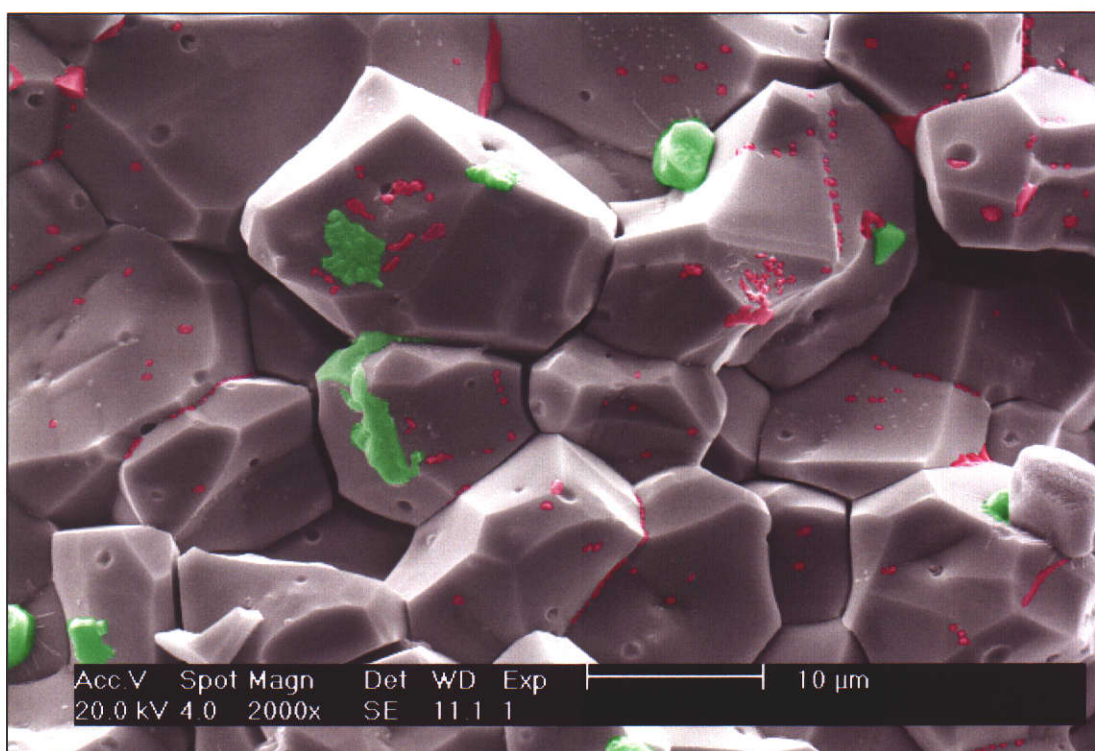
(b)

Figure 6.50 SEM micrograph confirming YBCO grain boundary films were observed extensively throughout Zr-rich ceramics after melt corrosion. Original SE image (a) and false coloured image (b) indicating locations where YBCO was confirmed by EDS analysis. Scale bar = 2  $\mu\text{m}$ .



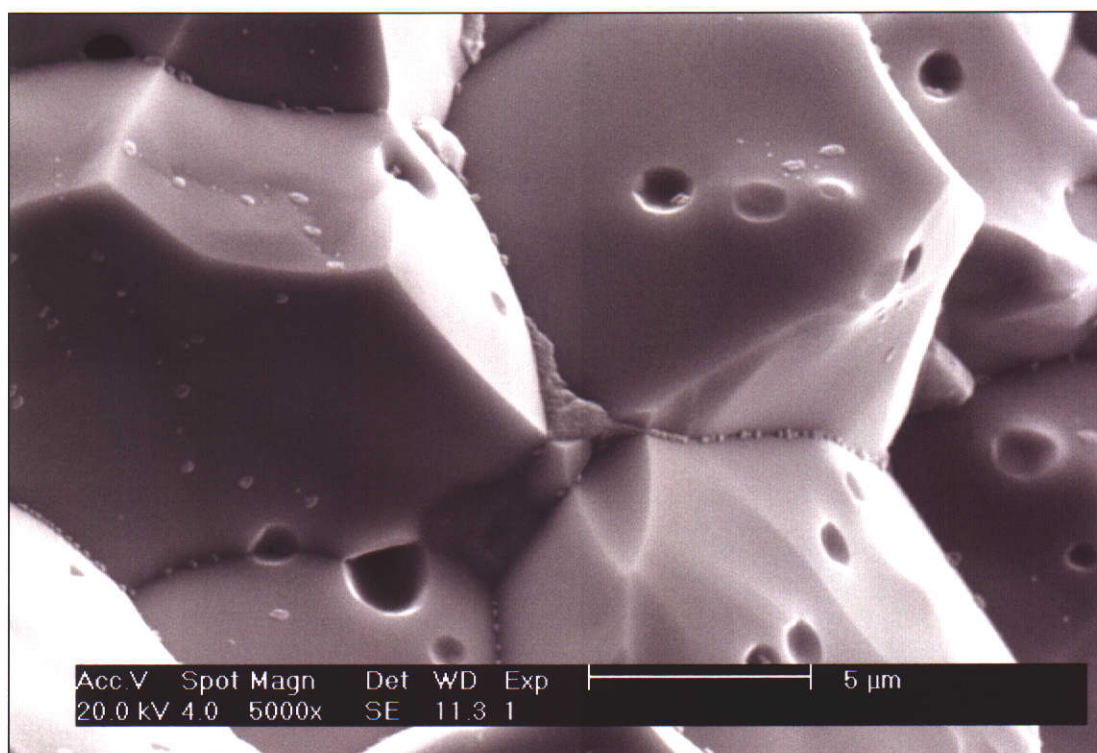


(a)

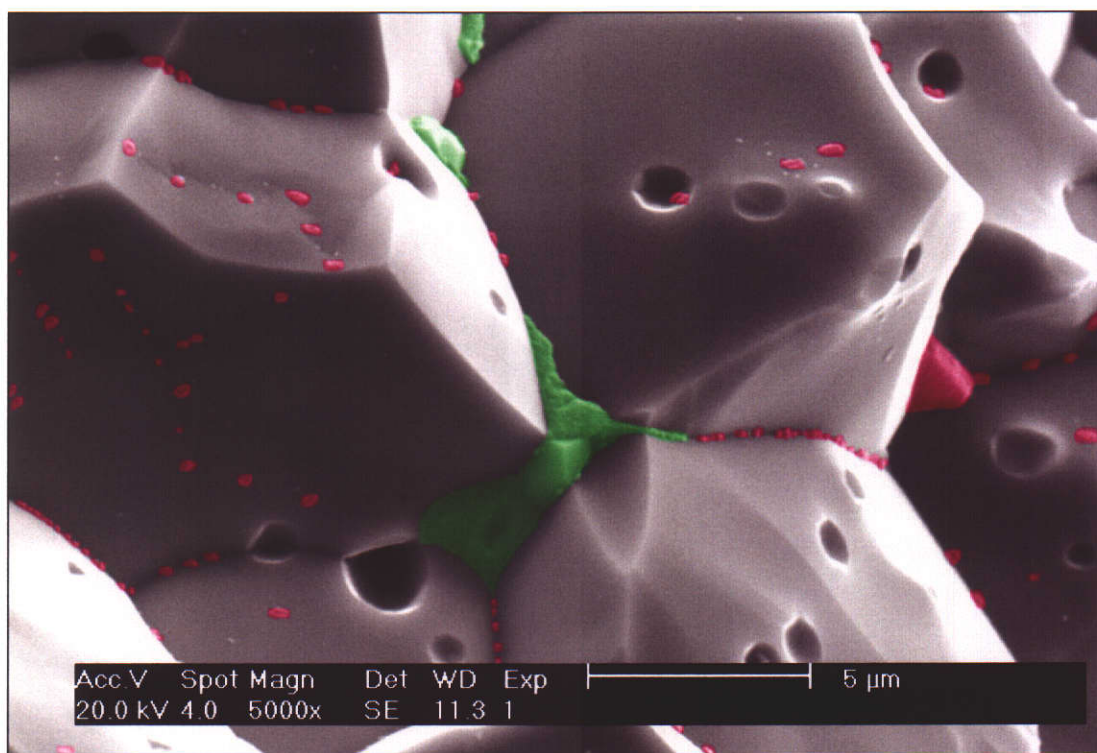


(b)

Figure 6.51 Distribution of YBCO melt in Ba-rich ceramic in region without exaggerated grain growth. Green regions readily allowed Cu identification by EDS. Red areas with similar morphology and distribution were considered to be YBCO melt even though they were too small and/or not accessible to EDS detector to permit Cu identification by EDS. Scale bar = 10  $\mu\text{m}$ .



(a)



(b)

Figure 6.52 Distribution of YBCO melt in Ba-rich ceramic in region without exaggerated grain growth: confirmation that observations made in Figure 6.51 were representative of the sample. Scale bar = 5  $\mu\text{m}$ .

Figures 6.51 and 6.52 show that the distribution of YBCO melt in Ba-rich ceramics was quite different to Zr-rich ceramics. Grain boundary YBCO melt films were readily observed in Zr-rich ceramics and were often close to continuous. However, YBCO melts in Ba-rich ceramics were rarely observed as continuous films. In regions without exaggerated grain growth in Ba-rich ceramics, YBCO melts were most easily observed at triple points. The larger areas of YBCO identified by EDS detection of Cu are highlighted in green in Figures 6.51 and 6.52. There were large numbers of small round features embedded in grain boundaries and attached to grain surfaces which were considered to be YBCO melt (highlighted in red in Figures 6.51 and 6.52). The largest of these allowed detection of Cu by EDS analysis, but most were too small to provide sufficient Cu intensity for detection by EDS. However their similar morphology and distribution strongly suggested they were YBCO melt.

The difference in YBCO distribution in Ba-rich ceramics compared to Zr-rich ceramics suggests the mechanism of corrosion differs on each side of the phase boundary. The local expansion from the reaction of residual  $\text{ZrO}_2$  grains with YBCO melt appears to open large numbers of intergranular cracks and cause rapid melt percolation in Zr-rich ceramics. Ba-rich phases appear much more likely to partly dissolve in YBCO melts, and if so the distribution of YBCO after melt percolation would simply match the original distribution of Ba-rich secondary phases. Ba-rich phases are unable to completely dissolve in barium cuprate melts because the solubility of Zr is very low. The most likely cause of corrosion appears to be the dissolution of the excess Ba from Ba-rich phases into the melt (until they revert to  $\text{BaZrO}_3$ ) and the reduced volume of solid allows space for melt percolation.

The distribution of YBCO melt through regions of exaggerated grain size was not able to be determined by SEM analysis of fracture surfaces. Unlike areas with intergranular fractures, it was difficult to associate patterns of melt distribution with visual information such as morphology or secondary electron image contrast. Backscattered electron imaging did not provide useful image contrast to differentiate the melt from the ceramic. EDS mapping did not have sufficient resolution to determine melt distributions.



TEM and optical microscopy analysis provided some information on the location of YBCO melt after corrosion exposure of Ba-rich specimens, but there was considerable ambiguity in results compared to the very clear patterns observed for Zr-rich samples from SEM. The stoichiometry result for the sample shown in Figure 6.53 was very slightly below one, probably because of random measurement error. Exaggerated grain size suggests that the actual stoichiometry was towards the upper end of XRF uncertainty, i.e. at or slightly above unity. Figure 6.53 shows a TEM thin section inspected by optical microscopy. The light colour of very large grains observed optically indicated low penetration of melt into these grains, because YBCO melt is black in colour due to CuO and provides strong colour contrast with BaZrO<sub>3</sub>. Most of the rest of the material was dark coloured, and there were very dark areas which looked like cracks filled with YBCO melt, although this was not able to be confirmed.

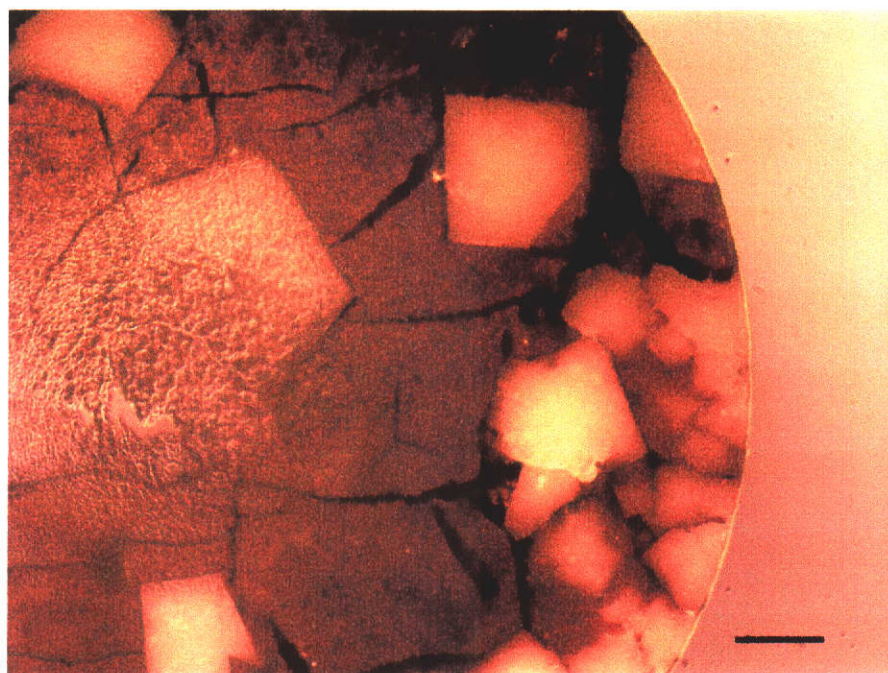


Figure 6.53 Optical micrograph of TEM specimen of solid-state derived ceramic with Ba : (Zr + Hf) mole ratio of  $0.999 \pm 0.002$  after melt exposure. Scale bar = 100  $\mu\text{m}$ .

Basic TEM analysis was conducted on this specimen in the region immediately adjacent to the perforation on the left side of Figure 6.53. There was insufficient time or number of available samples for comprehensive analysis of the

Cu distribution of Ba-rich ceramics with exaggerated grain size in the interior of crucibles after melt exposure, and the need for specimen preparation in kerosene impeded sample preparation. However, the preliminary results presented in Figures 6.54 to 6.55 show Cu was not generally detected within grains but was typically intergranular. Although continuous grain boundary films were not clearly observed, some grain boundaries without obvious grain boundary YBCO presence still showed detectable Cu in EDS analysis. YBCO melt was most easily detected as discrete phases of up to a few hundred nanometres in size as shown in the EDS map in Figure 6.55. Considerably more experimentation would be required to accurately determine the distribution of melt penetration through regions of very large grain size in solid-state derived ceramics. The effort necessary to take such measurements was not made because there was insufficient time, and because the need to solve the grain growth problem in solid-state derived ceramics would be of higher priority for future research than the analysis of these non-ideal materials.

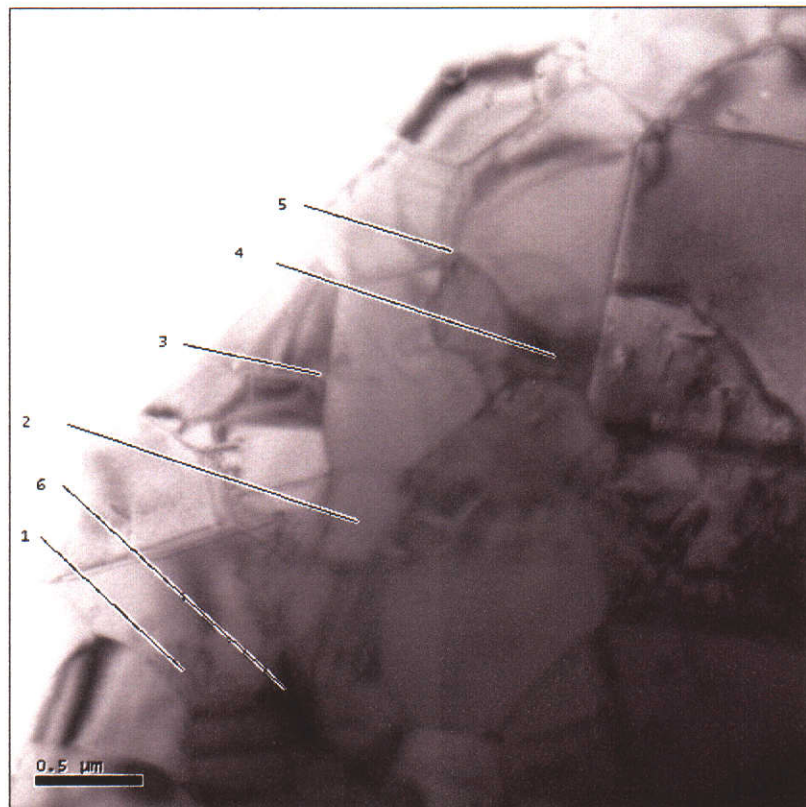
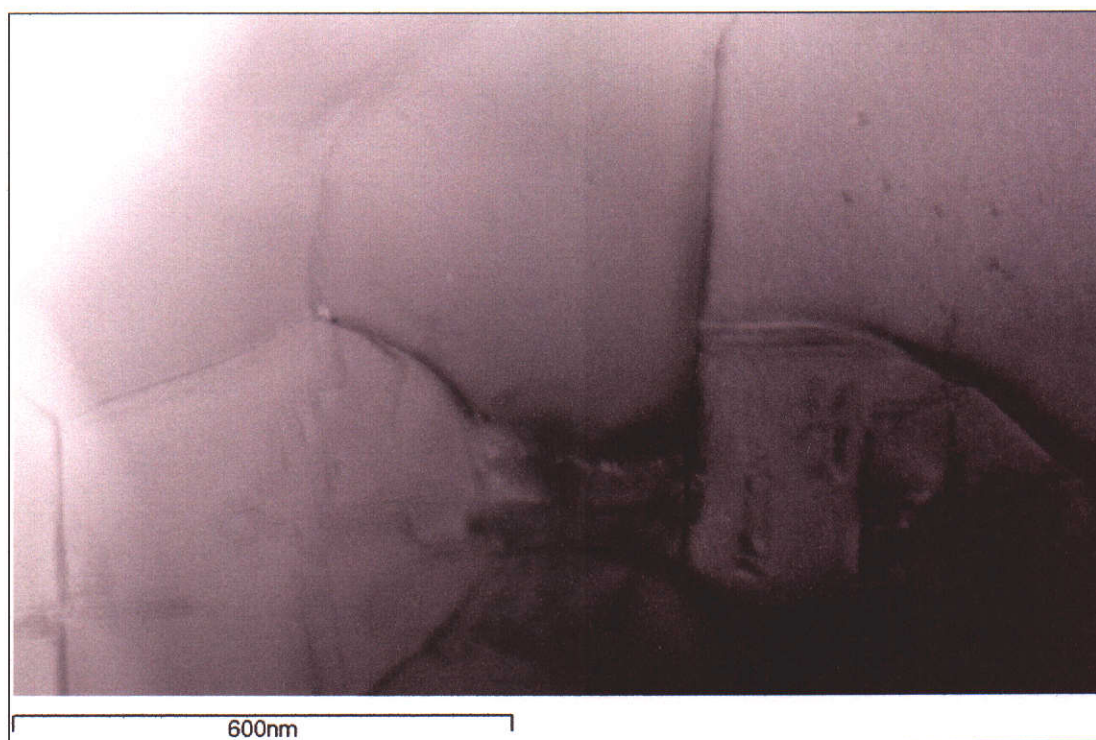
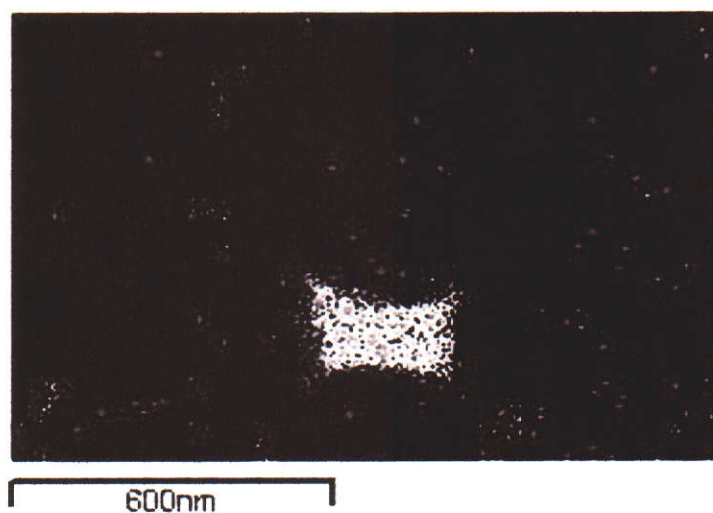


Figure 6.54 Cu detection within a sample with exaggerated grain growth with a Ba : (Zr + Hf) mole ratio of  $0.999 \pm 0.002$ . Features 1 and 2 had very low Cu levels, the grain boundary at site 3 had moderate Cu levels, and sites 4 – 6 were clearly YBCO melt with very high Cu levels. Scale bar = 0.5  $\mu\text{m}$ .





(a)



(b)

Figure 6.55 TEM images of the corroded Ba-rich ceramic from Figure 6.53. (a) is a brightfield STEM image and (b) is the corresponding Cu K $\alpha$  x-ray map. Scale bar = 600 nm.



## 6.7 High purity YBCO single crystals

High purity  $\text{YBa}_2\text{Cu}_3\text{O}_{7-\delta}$  single crystals were grown and measured by the Interdisciplinary Research Centre in Superconductivity at the University of Cambridge using solid-state derived  $\text{BaZrO}_3$  crucibles made during this research at Curtin. After growth over approximately three days, crystals were annealed in pure oxygen for 10 days at 420 °C, then for 72 hours at 350 °C to 550 °C. Re-annealing was conducted using 3 hours at 920 °C followed by 10 days at 420 °C (marked as 420r in Figure 6.56). Crystals were also annealed in air at 525 – 555 °C. SQUID magnetometry measurements on single crystals presented in Figure 6.57 show the maximum  $T_C$  of a high purity  $\text{YBa}_2\text{Cu}_3\text{O}_{7-\delta}$  single crystal grown in a solid-state derived crucible was 93.32 K (Cooper 2003, pers. comm., 5 August).

This compares favourably with 93.7 K of Liang, Bonn and Hardy (1998) and is higher than the maximum  $T_C$  of 91.4 K of Breit *et al.* (cited in Liang, Bonn and Hardy 1998). The width of the superconducting transition (10 to 90 %) was approximately 0.8 K, whereas Liang, Bonn and Hardy achieved a transition width of 0.2 K (1998). The relationship between  $T_C$  and oxygen loss is shown in Figure 6.58. The preliminary results available at the time of completion of this Thesis showed that crystals produced using these crucibles were of good quality, but more detailed measurements are still needed to fully assess crystal quality. The properties of superconductors are well known to be affected by chemical contamination, and if further improvements in crystal properties are required, the use of higher purity reagents for crucible fabrication may produce crystals of even higher quality.

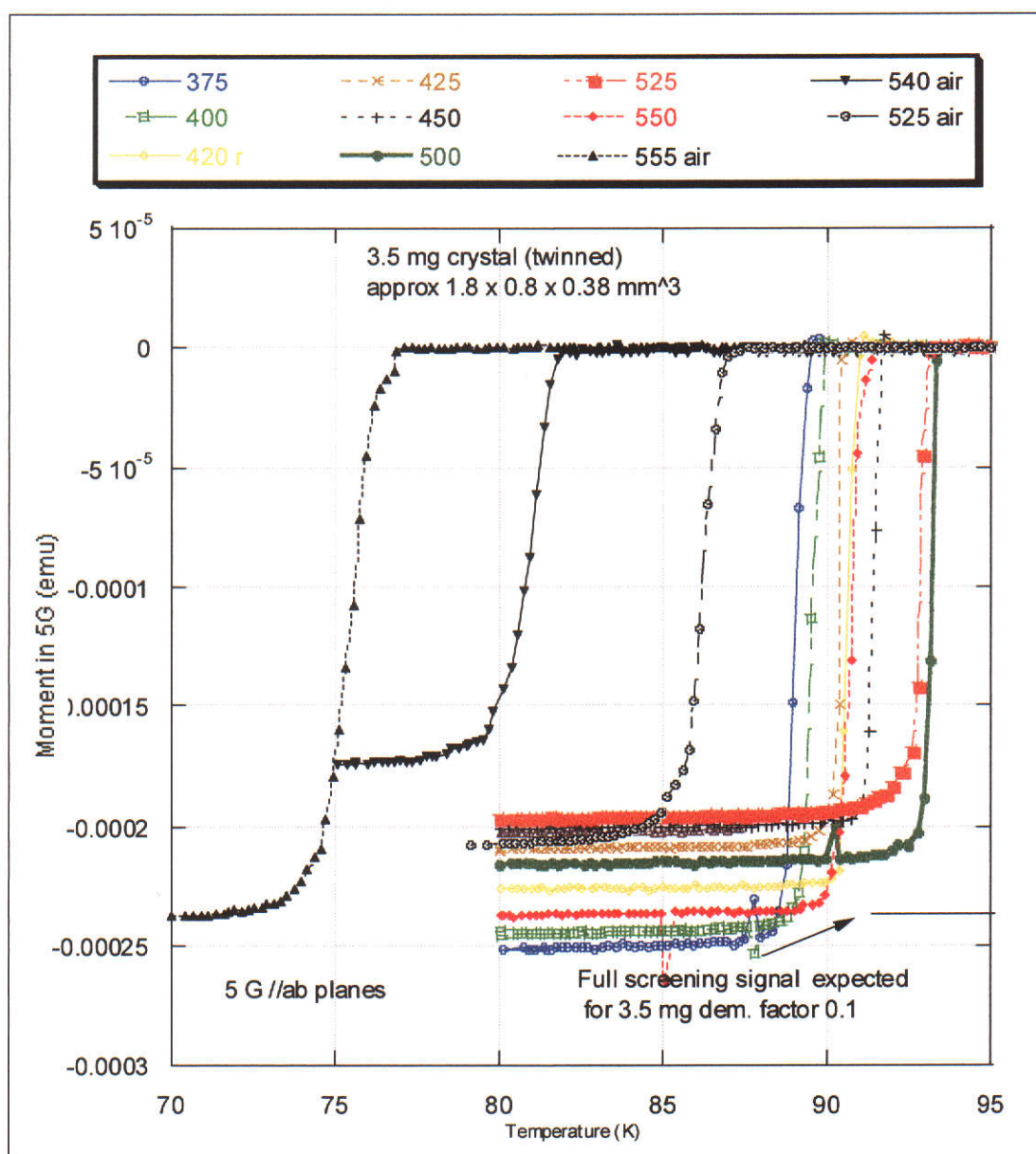


Figure 6.56 The effect of annealing temperature in high purity oxygen and in air on second magnetic moment of a high purity 3.5 mg twinned  $\text{YBa}_2\text{Cu}_3\text{O}_{7-\delta}$  single crystal annealed in high purity oxygen by SQUID magnetometry.

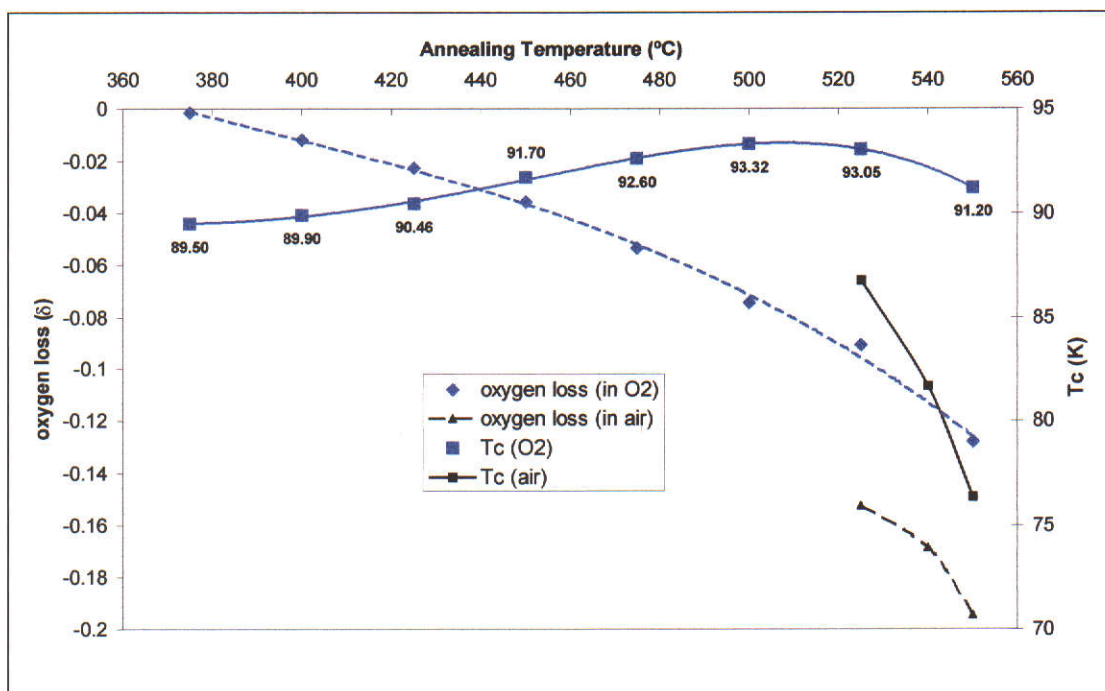


Figure 6.57 Relationship between annealing temperature, critical superconducting temperature by SQUID magnetometry and oxygen loss for annealing a high purity 3.5 mg twinned  $\text{YBa}_2\text{Cu}_3\text{O}_{7-\delta}$  single crystal annealed in high purity oxygen and in air. (Oxygen loss =  $\delta$  in crystal formula  $\text{YBa}_2\text{Cu}_3\text{O}_{7-\delta}$ ).

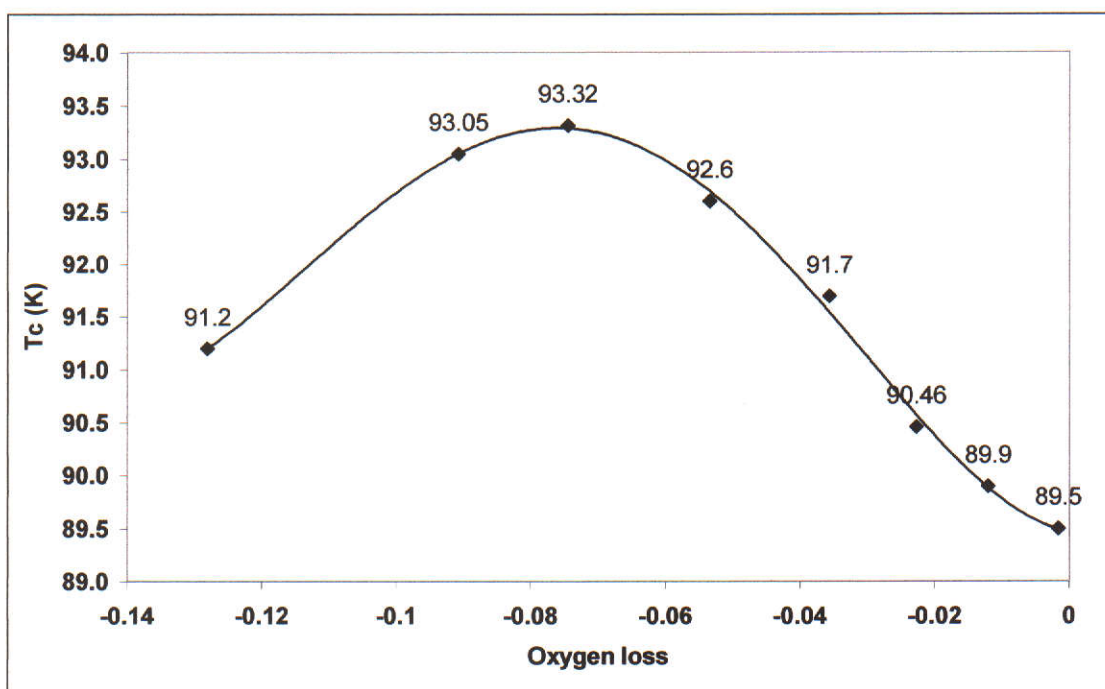


Figure 6.58 Relationship between  $T_c$  and oxygen loss for annealing in pure oxygen.

## 7.0 CONCLUSIONS

---

The development of superconductors with properties suitable for widespread application requires further scientific and technical advances. High temperature superconductors and current knowledge of the physics of high temperature superconductivity are still largely based on barium cuprates. Particularly when processed in the molten state, barium cuprates are very corrosive to substrate materials, and these corrosion products normally contaminate the superconductor. Chemical contamination degrades superconducting properties and hinders efforts to understand the physics of high temperature superconductivity. The progress of physical research into high temperature superconductivity, not just of barium cuprates, depends in part on the availability of high quality single crystals. High purity single crystal growth is in turn dependent on substrate and crucible technology.

Molten barium cuprates are corrosive to all but one known crucible material including noble metals and their alloys and all common ceramics. Crucible corrosion products normally contaminate the molten  $\text{BaCuO}_2$  -  $\text{CuO}$  flux used to grow  $\text{YBa}_2\text{Cu}_3\text{O}_{7-\delta}$  single crystals, and often the single crystals as well. Pure  $\text{BaZrO}_3$  is the only material known to be inert to molten barium cuprates, but is acutely sensitive to defects and secondary phases that degrade its performance.  $\text{BaZrO}_3$  of adequate quality is difficult to produce and its use has not proliferated to date.

$\text{BaZrO}_3$  is in principle a simple binary ceramic, whose crystal structure and equilibrium phase diagram has been known for a long time. Production of moderate quality  $\text{BaZrO}_3$  can be readily accomplished by solid-state reaction of  $\text{BaCO}_3$  and  $\text{ZrO}_2$  at  $\sim 1000 - 1500$  °C. However,  $\text{BaZrO}_3$  suitable for containment of molten barium cuprates requires very high levels of phase purity and density that are difficult to achieve. Phase purity is restricted by kinetic limitations of solid-state reaction and it is a difficult material to sinter to high density. Characterisation of powders and ceramics of suitable quality has numerous practical difficulties and is very demanding of current analytical technology.

Although much basic information is available in published literature, further research was required to provide quantitative information on powder processing and ceramic characteristics. This project was conducted in order to:

- investigate processing properties of BaZrO<sub>3</sub> using the traditional solid-state process
- develop a new production process attempting to exploit the numerous potential benefits of solution based chemical processing
- develop analytical methods to support BaZrO<sub>3</sub> development at the high quality required for melt processing of barium cuprates
- determine key characteristics required for corrosion resistant BaZrO<sub>3</sub>
- understand corrosion mechanisms.

## **7.1 Analytical development**

Development of high quality BaZrO<sub>3</sub> required the development of analytical methods able to provide useful information at the high quality of materials required for this application. There are numerous practical difficulties in the characterisation of high quality BaZrO<sub>3</sub> powders, particularly in the assessment of phase purity.

Perhaps the most important measurement for powders is that of Ba : (Zr + Hf) mole ratios. After considerable refinement, XRF provided an accuracy and precision of  $\pm 0.002$  which was adequate for this application. This level of accuracy and precision requires careful attention to the preparation of standards and specimens, and careful optimisation of the analytical method (e.g. intensity ratios) and operation of the spectrometer. The quality of results achieved on a modern spectrometer using the method developed in this project are limited as much by the repeatability of manual specimen preparation as by the instrumentation. The position of the apparent phase boundary as indicated by sharp transitions in the properties of powders and sintered ceramics was in very close agreement with XRF measurements. XRF provided a combination of precision, accuracy, reliability and convenience for stoichiometry control of BaZrO<sub>3</sub> unequalled by any other common laboratory technique. Apart from quantification of measurement precision, it was one of the few measurements in this project that provided absolute results requiring little interpretation.



Of the techniques used in this study, XRF was the most effective for the assessing of the suitability of powders for production of corrosion resistant materials. The results of this study showed that a narrow range of stoichiometry is required to produce corrosion resistant ceramics, and XRF may be used to screen out powders of unsuitable stoichiometry. Other techniques such as XRD may be used to determine other powder properties such as phase purity and particle size, which although important are secondary to stoichiometry.

Assessment of the phase purity of powders and sintered ceramics by XRD required considerable development and interpretation, and has significant limitations. The sensitivity of XRD to secondary phases such as  $\text{ZrO}_2$ ,  $\text{Ba}_3\text{Zr}_2\text{O}_7$  and  $\text{Ba}_2\text{ZrO}_4$  is far too low for detection at levels relevant to corrosion resistant materials.  $\text{BaCO}_3$  was the only secondary phase directly detectable by XRD in processed powders, and in sintered ceramics with Ba : (Zr + Hf) mole ratios higher than  $\sim 0.97$  after being ground into powders. The level of  $\text{BaCO}_3$  in powders increased after exposure to air, reaching a maximum after  $\sim 24$  hours for processed powders. A positive relationship between high  $\text{BaCO}_3$  levels after air exposure with increased Ba : (Zr + Hf) mole ratios and/or with limited calcination suggested  $\text{BaCO}_3$  levels might provide a useful indirect method of measuring Ba-rich phase impurities. However, further analysis provided strong evidence that  $\text{BaZrO}_3$  reacts with  $\text{CO}_2$  at ambient humidity to produce  $\text{BaCO}_3$ , so  $\text{BaCO}_3$  detected in powders after air exposure cannot be attributed only to Ba-rich phases. After completion of the reaction between  $\text{BaZrO}_3$  and humid air, the level of  $\text{BaCO}_3$  depended on the surface area of the powder. Accurate quantitative correction for the effect of surface area was not feasible within the resources of this project, and hence variations in surface areas partially interfered with measurements of phase purity by XRD.

Reliable quantitative assessment of powder phase impurities at levels relevant to corrosion resistant materials using bulk techniques was found to be a nearly impossible task. XRD has inadequate sensitivity to directly determine secondary phases other than  $\text{BaCO}_3$  and interpretation of  $\text{BaCO}_3$  levels is complicated by reaction of  $\text{BaZrO}_3$  with air. Synchrotron radiation diffraction may offer useful improvements in secondary phase detection limits but not when using glass capillaries due to high background intensities. Infrequent access to synchrotron

radiation diffraction rendered its use inappropriate during this project. However, the current body of research provides sufficient information to support the design of experiments where the benefits of synchrotron radiation diffraction could now justify its use.

Quantitative analysis of residual  $\text{ZrO}_2$  in processed powders could be attempted by dissolving  $\text{BaZrO}_3$  in mineral acids followed by analysis of undissolved  $\text{ZrO}_2$ . However this would be very difficult because it requires quantitative collection and/or determination of small amounts of ultra-fine  $\text{ZrO}_2$  particles from acidic suspensions, and verification of the solubility of ultrafine  $\text{ZrO}_2$  in the acid used.

Microscopy, especially TEM, was the most effective method for detecting secondary phases in sintered ceramics. The suitability of SEM and TEM for microstructural analysis is significantly affected by specimen preparation, which must take account of the potential for secondary phases to be removed during preparation such as dissolution of Ba-rich phases in water and mechanical removal of  $\text{ZrO}_2$ . These practical difficulties and the time consuming nature of specimen preparation impeded the application of electron microscopy during this project. However, the results obtained showed that electron microscopy was far more sensitive than bulk methods of analysis and revealed structural information not possible with other techniques, such as the intra-granular defects observed by TEM. Extensive use of TEM analysis will be of substantial benefit for further development of corrosion resistant  $\text{BaZrO}_3$ .

Voigt function profile fitting of the  $\text{BaZrO}_3$  (110) XRD peak with the instrument profile determined using  $\text{LaB}_6$  provided crystallite size measurements that were clearly of sufficient precision and accuracy for process control and development in this project. Voigt profile crystallite size results were closely supported by TEM observations of primary particle sizes and BET  $\text{N}_2$  adsorption measurements of surface area. Crystallite sizes from XRD patterns calculated using the Scherrer equation were somewhat less accurate than Voigt function results because of the presence of non-uniform strain. However, Scherrer equation results were included in parts of this thesis because despite their inaccuracy, they are still useful for process development and control where more sophisticated peak shape analysis software is not accessible.

## 7.2 Powder processing

BaZrO<sub>3</sub> powders were produced using either solid-state reaction of BaCO<sub>3</sub> and ZrO<sub>2</sub>, or from oxalate precursors precipitated from aqueous solution. The key parameters requiring control were Ba : (Zr + Hf) mole ratio, phase purity, particle size and level of agglomeration. Powders were analysed by XRF, XRD, DTA/TGA, TEM and BET N<sub>2</sub> adsorption.

### 7.2.1 Solid-state powder processing

Solid-state powder processing is in principle a very simple method, but there are significant practical limitations depending on the quality of the product required and the processing and analytical equipment available.

Despite its limitations, XRD was able to provide information useful in optimisation of calcination procedures for solid-state processing. BaCO<sub>3</sub> levels in powders after two or more calcinations for one hour at 1300 °C with intermediate regrinding were not detectable by XRD immediately after calcination, whereas levels in powders calcined for at least three hours at 1300 °C without intermediate regrinding were substantially higher. The increase in BaCO<sub>3</sub> content of all powders after exposure to air was significantly reduced by intermediate regrinding during powder processing. Accurate corrections for surface area effects on BaCO<sub>3</sub> levels after air exposure were not feasible. However, the small number of BET measurements that were available supported the conclusion that intermediate regrinding resulted in increased phase purity and not reduced powder surface areas alone.

Results showed that the solid-state reaction of BaCO<sub>3</sub> and ZrO<sub>2</sub> powders at 1300 °C does not proceed at a useful rate after 60 minutes, and that regrinding between calcinations is much more effective in promoting reaction than increasing calcination times. Solid-state derived powders for ceramic fabrication were produced using two calcinations for three hours followed by calcination for one hour, all at 1300 °C with intermediate regrinding. This protocol was selected primarily to maximise apparent phase purity as estimated by XRD. The third calcination time was restricted to one hour to attempt to minimise grain growth and agglomeration in powders.

Ubaladini *et al.* (2003) proposed a shrinking core model for the solid-state reaction, in which reaction kinetics are controlled by diffusion of reactants through  $\text{BaZrO}_3$  that forms at the surface of  $\text{ZrO}_2$  particles. The current results suggest regrinding was therefore effective in exposing  $\text{ZrO}_2$  particles for further reaction. Kinetic limitations due to  $\text{ZrO}_2$  reactivity have important implications for  $\text{ZrO}_2$  particle size distributions of reagents and on optimisation of precipitation in solution chemical processes.

The crystallite size of process powders decreased sharply with increasing Ba : (Zr + Hf) mole ratio at the phase boundary, i.e.  $1.000 \pm 0.002$  by XRF. The surface areas of powders increased correspondingly with barium content. This transition was observed after two or more calcinations with intermediate regrinding but not for the first calcination within the stoichiometry range studied. The strong dependence of crystallite size, surface area and particle morphology on bulk Ba : (Zr + Hf) mole ratios after near completion of the solid-state reaction suggests that local variations in stoichiometry (e.g. due to imperfect mixing) would lead to heterogeneous powder structure.

Grain growth in slightly Ba-rich powders was strongly suppressed at 1300 °C, and high calcination temperatures (i.e. 1500 °C) were required to increase crystallite sizes of Ba-rich powders above ~ 60 nm as estimated by XRD. Primary particles in Ba-rich powders were distinctly cubic in morphology and were often single crystals as observed by HRTEM. Grain growth readily occurred in Zr-rich powders, which displayed more obvious agglomeration than Ba-rich powders. Zr-rich powders had large particles with a distinctly rounded shape after three calcinations with intermediate regrinding. Powders very close to the phase boundary contained a mixture of these morphologies and particle sizes, presumably as a result of very minor localised stoichiometry variation. Qualitative TEM observations of primary sizes were in good agreement with crystallite sizes calculated by Voigt function profile fitting of XRD patterns over a wide size range.

Powders with Ba : (Zr + Hf) mole ratios well above one must contain Ba-rich secondary phases if the phase equilibrium diagram is correct. If so, Ba-rich phases do not cause grain growth in Ba-rich powders at 1300 °C, and they may even suppress grain growth of  $\text{BaZrO}_3$  under the conditions used. Grain growth in Zr-rich powders

may be caused by residual  $\text{ZrO}_2$ , but the observation that it did not occur during initial calcination suggests that grain growth in powders first requires almost complete removal of Ba-rich phases.

The effect of stoichiometry on powder crystallite and particle size does not appear to have been previously reported in the literature and has important implications for processing properties. The benefit of the resistance of slightly Ba-rich powders to grain growth has been overlooked in the existing processing literature, and can be used to partially offset some of the reputed disadvantages of solid-state processing for ultra-fine powder production. Particle size control is required for shape forming and sintering properties. Slightly Ba-rich  $\text{BaZrO}_3$  powders are very difficult to use for slip casting and tape casting, because stable dispersions at high solids contents are difficult to maintain at such small particle sizes. Agglomeration inherent to solid-state reactions may also impede efficient particle packing, further hindering shape forming and sintering processes.

### **7.2.2 Oxalate precursor processing**

Solution based processing was developed in an attempt to overcome the reputed limitations of the solid state process and provide ceramics with superior processing and corrosion properties. Development was focussed on oxalate precursors after consideration of processing equipment, reagent costs, and the level of process development reported in the literature. The initial aim was to implement a mature process directly from information available in existing literature, but it soon became apparent that considerable further research was needed to develop a viable process.

The barium chloride, zirconium oxychloride, oxalic acid system can produce stoichiometric precursors and is more efficacious at elevated temperature (i.e.  $\sim 95^\circ\text{C}$ ) than at ambient temperature. The excess of oxalic acid required ( $\sim 30\%$ ) depends on the temperature used for precipitation and levels of residual HCl in the zirconium salt. The system does not behave as reported by Reddy and Mehrotra (1979) and their method for producing stoichiometric precursors does not work as claimed. Rapid addition of reagents caused significant difficulty in washing and



recovering the precipitate and therefore difficulty in reproducing product stoichiometry and scale up of production quantities. Requirements for slow addition of reagents, elevated temperatures, instability of acidic zirconium oxalate solutions at elevated temperatures, and the sensitivity of product stoichiometry to solution mole ratios of all three reagents makes the barium chloride, zirconium oxychloride, oxalic acid system unsuitable for routine production of high quality  $\text{BaZrO}_3$ . Dissolution of zirconium may result in Ba-rich precipitates if the level of oxalic acid addition is too high. The instability of acidic zirconium oxalate solutions at elevated temperatures suggested that phase segregation may occur for barium zirconium oxalate precipitation under such conditions.

Precipitation of near stoichiometric oxalate precursors can be conducted much more favourably at neutral pH than under acid conditions. The barium acetate, zirconium oxychloride, ammonium oxalate system can readily produce nearly stoichiometric precipitates at ambient temperature, using reasonably high solution concentrations without requiring large excesses or slow addition of reagents. The barium acetate, zirconium oxychloride, ammonium oxalate system does not inherently produce a single compound of invariant stoichiometry, but allows variation of stoichiometry by adjustment of solution mole ratios. The crystallite size of oxalate derived  $\text{BaZrO}_3$  was dependent on bulk stoichiometry and could be adjusted by variation of calcination temperatures between  $\sim 1000$  and  $1500^\circ\text{C}$ .

The relationship between solution and precipitate mole ratios was favourable for stoichiometric precipitation because only the barium acetate to zirconium oxychloride ratio required precise control and product stoichiometry was insensitive to oxalate levels above a critical level. With increasing ammonium oxalate addition, the  $\text{Ba} : (\text{Zr} + \text{Hf})$  mole ratio of the precipitate asymptotically approached a limit close to unity that can be adjusted by variation of the  $\text{Ba} : (\text{Zr} + \text{Hf})$  solution mole ratio. Unlike under acid conditions, an excess of ammonium oxalate in this system of up to at least 50% did not solubilize Zr to cause a Zr deficient precipitate. Near stoichiometric precipitation required only a small excess of barium acetate ( $\sim 2\%$ ) and a 20 % excess of ammonium oxalate, and hence reagent efficiency may be high. The crystallite size of powders can be adjusted within certain limits by varying

calcination temperatures. A tenfold scale up of precipitation volume caused a minor reduction in precipitate Ba : (Zr + Hf) mole ratio, but barium acetate addition can simply be increased slightly to maintain stoichiometry control. The system can be affected by possible processing variations in residual acid concentrations in zirconium salts, and so industrial application may require further process controls than were required in the laboratory.

The most important and complex consideration for oxalate process development was control over zirconium solution speciation. Direct analysis of zirconium speciation was beyond the scope of this research, but useful conceptual models of zirconium oxalates as molecular or colloidal solutions were proposed based on observations of solution stabilities and precipitate stoichiometry. Processing performance appears to depend on control of the molecular or colloidal structure of zirconium during processing, which can be adjusted according to thermal history, solution concentrations and ratios, ligand complexing properties, and in particular, pH. The optimal conditions for oxalate processing are likely to be those which minimise zirconium colloid formation, permitting molecular scale mixing of barium and zirconium.

### **7.3 Forming and sintering**

Powders were formed into green crucibles by aqueous slip casting using an ammonium polyacrylate dispersant, or by CIP. Slip casting was a difficult and ultimately unsuccessful approach to shape forming for the production of high density crucibles. Sintered porosities below 5 % were not reproducible, which was inadequate for prolonged melt tightness. The principle difficulty of slip casting was in maintaining sufficiently stable particle dispersions at high solids content with the very fine particle sizes inherent to barium zirconate of the optimal stoichiometry required for corrosion resistance. Larger particles ( $> 200$  nm crystallite sizes by XRD) which can be produced using Zr-rich powders were suitable for slip casting but Zr-rich ceramics have very poor corrosion resistance.

CIP was an effective and reliable process for green forming and is recommended where facilities are available. Cetyl alcohol was used as a lubricant to avoid cracking and to slightly improve packing densities. There is a possibility that organic lubricants may reduce corrosion resistance based on the fact that Erb does not use them. Isothermal treatments during heating to sintering temperatures were used to burn out the lubricant, so problems due to lubricant use, though possible, are not expected. Grain growth observed in Ba-rich ceramics occurred with or without lubricant addition.

BaZrO<sub>3</sub> is a highly refractory material requiring high sintering temperatures for densification. Sintering temperatures required for densities sufficient for melt tight ceramics have been previously reported as 1730 °C or higher, although high sintered densities using powders derived using novel chemical processes have been claimed using temperatures as low as 1400 °C. Solid-state and oxalate derived powder produced in this study could not be adequately sintered below 1700 °C. Solid-state derived powders sintered at 1700 –1710 °C for six hours in air reproducibly produced porosities below 3 %, whereas oxalate derived powders calcined at 1300 °C were somewhat more difficult to sinter and produced porosities ranging from 2.5 to 5.5 %. Densification occurred more readily at 1750 °C than 1700 °C. Molybdenum disilicide furnaces capable of operation at 1750 °C require specialised grades of refractories and elements, but are highly recommended unless the sintering properties of BaZrO<sub>3</sub> can be significantly improved.

#### **7.4 Microstructure**

The microstructure of sintered ceramics was analysed by optical and electron microscopy. Zr-rich solid-state derived ceramics, and both Zr- and Ba-rich oxalate derived ceramics had fine grained microstructure with grains typically around 5 µm in size. Highly exaggerated grain growth up to several hundred micrometres occurred in Ba-rich solid-state derived ceramics, either throughout their interior or as a thin subsurface layer, and in both cases a fine grain size occurred within ~200 µm of exterior surfaces. Large grains were clearly visible to the naked eye on cross section fracture surfaces. For solid state-derived ceramics, the transition from fine

grained microstructure to exaggerated grain growth occurred over a narrow range of stoichiometry at the phase boundary, i.e. between 0.996 and  $1.000 \pm 0.002$  measured by XRF. Control of excessive grain growth would be required for improved corrosion performance, and although the mechanism of grain growth was not identified, the effect of oxygen partial pressure during sintering is recommended for further investigation.

Intragranular fractures surfaces of large grains had a distinctive morphology suggestive of underlying defect structures in the cubic  $\text{BaZrO}_3$  crystal system. XRD analysis of sintered ceramics performed after grinding into powders showed no significant changes in crystallography (such as lattice parameters) but samples with excessive grain growth displayed much stronger  $\langle 100 \rangle$  preferred orientation than present in all other samples. TEM analysis showed that intragranular defects were prevalent in Ba-rich ceramics whereas grains in Zr-rich ceramics were relatively free of defects. These defects may have an important role in ceramic processing and melt corrosion properties and warrant further analysis.

Excess zirconium segregated as discrete  $\text{ZrO}_2$  grains between  $\sim 50 - 1000$  nm in size, which consistently had a twinned structure.  $\text{ZrO}_2$  grains were typically at the grain boundaries of  $\text{BaZrO}_3$  grains, but small amounts of intragranular  $\text{ZrO}_2$  were also observed.  $\text{ZrO}_2$  grain boundary films were not observed by detailed TEM analysis. Contamination of certain oxalate derived samples by aluminosilicate particles in process water lead to  $\sim 30$  nm barium aluminosilicate precipitates at a small fraction of triple points, which would be expected to react with YBCO melt if accessible via mass transport processes along grain boundaries. The microstructural distribution of Ba-rich phases was not adequately determined because of specimen preparation difficulties and the complexity of fracture surfaces of Ba-rich ceramics. Although an effective method for TEM preparation of Ba-rich ceramics was devised, time limitations prevented its extensive use. Despite practical difficulties and its time consuming nature, TEM was the most effective technique for characterisation of sintered ceramics because of high spatial resolution and much higher sensitivity to secondary phases than bulk methods of analysis.

## 7.5 Corrosion properties

The corrosion properties of high density BaZrO<sub>3</sub> for YBCO melt containment are strongly dependent on the levels and types of phase impurities in the ceramic. Phase impurities are strongly dependent on the stoichiometry of the material and may also be caused by processing artefacts.

Maximum corrosion resistance of solid-state derived crucibles was observed in the narrow stoichiometry range of  $1.003 \pm 0.003$ . All crucibles tested in this study with Ba : (Zr + Hf) mole ratios below  $1.001 \pm 0.002$  failed in less than two days of melt exposure and were unsuitable for single crystal growth experiments. The acute corrosion sensitivity of BaZrO<sub>3</sub> to ZrO<sub>2</sub> was attributed to cracking caused by the 100 vol.% localised expansion caused by reaction of ZrO<sub>2</sub> with YBCO melt to form BaZrO<sub>3</sub>. Cracking along grain boundaries allowed melt to percolate through the ceramic. No ceramic has the ability to withstand such extreme localised expansion, so the phase abundance residual of ZrO<sub>2</sub> must be suppressed as much as possible to maximise corrosion resistance. Corrosion resistance decreased above  $\sim 1.010$ , but the effect of excess barium was less severe than excess ZrO<sub>2</sub>. The mechanism of corrosion of Ba-rich ceramics does not appear to involve localised expansion but simply partial dissolution of Ba-rich secondary phases. Crucibles with Ba : (Zr + Hf) mole ratios above  $1.015 \pm 0.002$  were readily attacked by exposure to water (such as for Archimedes density measurement) and therefore not tested for corrosion resistance.

Oxalate derived crucibles showed potential for improved corrosion resistance over solid-state derived crucibles, but further improvement of sintering properties is required to produce crucibles capable of sustained melt containment more reproducibly. Oxalate derived crucibles produced useful corrosion resistance at Ba : (Zr + Hf) mole ratios as high as  $1.015 \pm 0.002$ , which was not expected and not clearly understood. The fine grained microstructure of Ba-rich oxalate derived ceramics was one factor which may have aided their corrosion performance. Further development of processes for chemical synthesis of BaZrO<sub>3</sub> appears to be the most likely means of obtaining substantial improvements in processing and corrosion performance. Information provided by this Thesis will significantly reduce the complexity of such development.

Optimal corrosion resistance was observed in slightly barium-rich rather than apparently stoichiometric ceramics. The apparent requirement for a slight Ba excess for optimal corrosion resistance could be an artefact of processing limitations, that is, a small Ba excess may have been required to adequately suppress  $\text{ZrO}_2$  left over from incomplete phase formation. The difference between the observed and ideal optimum corrosion resistance was slightly higher than the measurement uncertainty of XRF. If a production process were able to reach thermodynamic equilibrium, there would be little reason not to expect optimal corrosion resistance at unity Ba : (Zr + Hf) mole ratio. What is certain is that residual  $\text{ZrO}_2$  must be strictly avoided.

Probably the most important conclusion of this research was quantification of the limits of stoichiometry over which corrosion resistance was observed, and by inference the limits within which corrosion resistance would appear to be possible. Such information can directly assist other researchers to fabricate potentially useful crucibles and could save a great deal of unproductive research, particularly for the development of processes for the chemical synthesis of powders intended for this application. Had this information been available to this project, the quantity of process development could have been substantially reduced. It appears futile to pursue research or development on corrosion resistant materials outside of the Ba : (Zr + Hf) mole ratio range of  $1.005 \pm 0.005$ . Although stoichiometry is a critical factor affecting corrosion resistance, the effects of grain size and processing artefacts still play an important role. The closer a production process can approach thermodynamic equilibrium, the closer the Ba : (Zr + Hf) mole ratio can be set to unity and the greater the corrosion resistance may be.

High purity  $\text{YBa}_2\text{Cu}_3\text{O}_{7-\delta}$  single crystals were synthesised by the Interdisciplinary Research Centre in Superconductivity (University of Cambridge) using solid-state derived crucibles produced at Curtin during this research. Preliminary results showed these crystals had good superconducting properties. There are currently very few research groups able to produce  $\text{BaZrO}_3$  crucibles suitable for high quality single crystal growth experiments, and the development presented in this Thesis would allow other interested researchers to more readily develop this capability.

## **7.6 Overall conclusions**



Fabrication of BaZrO<sub>3</sub> with high resistance to YBCO melt corrosion is at the limits of conventional processing technology. Particularly stringent quality requirements necessitate careful attention to all aspects of ceramic processing and place substantial demands on analytical methods. Although BaZrO<sub>3</sub> may be inherently resistant to YBCO melt corrosion, it is acutely sensitive to defects and secondary phases which degrade its performance. Optimum corrosion resistance was observed over a narrow range of Ba : (Zr + Hf) mole ratios ( $1.003 \pm 0.003$ ) and future development substantially outside this range appears futile. For optimal corrosion resistance, residual ZrO<sub>2</sub> must be strictly avoided, and the phase abundance of Ba-rich secondary phases must be minimised within the approximation of phase equilibrium provided by the production process.

The development of processes for BaZrO<sub>3</sub> synthesis from solution chemistry appears to be a key option for significant improvement over conventional solid-state powder synthesis. This research produced the first chemically derived precursor process demonstrated to produce a ceramic of adequate quality for sustained BaCuO<sub>2</sub>-CuO melt containment. Although BaZrO<sub>3</sub> produced from oxalate precursors showed some signs of improvement over solid-state processing, improvement of sintering properties to reproducibly produce crucibles with sustained melt tightness is still required. An alternative approach to further improving the BaZrO<sub>3</sub> system is the addition of dopants to improve phase formation and sintering kinetics, but this was beyond the scope of this research.

Processing development revealed strong effects of stoichiometry on powder processing properties near the phase boundary. This information was not available in the literature and has important implications on the suitability of powders for subsequent processing stages. The observation of reaction between BaZrO<sub>3</sub> and atmospheric CO<sub>2</sub> at ambient humidity and the limitations of techniques for bulk analysis greatly restricted measurement of phase purity of powders and ceramics. The most sensitive method for secondary phase and defect analysis of BaZrO<sub>3</sub> ceramics used was TEM, and its further use is recommended despite the effort required for specimen preparation.

Crucibles suitable for research applications were produced during this study, but the widespread application of BaZrO<sub>3</sub> for melt processing of barium cuprates requires further development. BaZrO<sub>3</sub> is a system fraught with numerous practical and analytical challenges, but the background provided by this Thesis will significantly reduce the complexity and difficulty of further development

## **7.7 Outlook and recommendations for future research**

Considerable effort has gone into this research on processing and optimisation of BaZrO<sub>3</sub> and progress has been made in numerous areas of the BaZrO<sub>3</sub> binary system. Crucibles suitable for research applications have been produced and tested during this study. However, further development is needed before BaZrO<sub>3</sub> is suitable for widespread routine application in superconductor research and manufacturing. Although the aims of ceramic fabrication have become substantially and quantitatively clearer through this research, production of crucibles and substrates suitable for melt processing of barium cuprates remains difficult. This research has established the stoichiometry limits required to make corrosion resistance possible, but further improvement of corrosion properties is desirable. There are two aspects to the existing limitations of corrosion resistance: what are the intrinsic limitations of the BaZrO<sub>3</sub> binary system, and how closely was this approximated experimentally during this study? Staying within the BaZrO<sub>3</sub> binary system, one can only attempt to remove processing artefacts by further processing improvement. Alternately, one may consider departing from a binary system.

There was insufficient time to investigate the cause of reduced densification of oxalate derived powders, but it could be associated with lower phase purity compared to fully processed solid-state derived powders. A simple experiment that could be conducted to test this possibility is to test the sintering properties of solid-state derived powders after only one calcination, because the surface areas measured by BET and phase purity measured by XRD are quite similar. There was limited time within this project to produce samples which were not intended to work.

Because of the difficulty in measuring phase purity, it was difficult to estimate how closely the materials produced in this study approximated the full

potential of BaZrO<sub>3</sub>. Electron microscopy was most useful in obtaining useful information on secondary phases in sintered ceramics. There appears to be little chance of improved phase purity after three calcinations with intermediate re-grinding in the solid-state system. Some progress was made using oxalate derived ceramics, but difficulties remained and a new chemical process to supersede oxalates is still required. The effect of stoichiometry is such that novel processes must maintain very precise control over stoichiometry (ideally better than  $\pm 0.001$ ) to have a good chance of superseding the solid-state process, and must not leave residual ZrO<sub>2</sub> in the ceramic.

It could be that improved corrosion resistance is not possible without improving the quality of reagents used, hence other areas of development might remain unproductive without improved reagent purity. Exploring this possibility was prohibitively expensive and would have been premature before this body of research had been assembled. Perhaps the use of organic lubricants for shape forming of powder has an unforeseen effect on corrosion resistance despite the efforts to burn out the lubricant during sintering. Other researchers (e.g. Erb) do not use a lubricant but this was unavoidable with the processing equipment available to this project. Given their nearly identical chemical properties, there seems to be no reason to attribute limited corrosion resistance to substitution of Zr by Hf. However, the experience in this project has been that BaZrO<sub>3</sub> has a remarkable habit of producing unexpected results, so assumptions must be recognised and verified wherever possible.

Perhaps the gas environment in the furnace could be changed to O<sub>2</sub> to completely remove the binder and possibly reduce crystallographic defects in Ba-rich ceramics. This is an experiment strongly recommended in the earliest stages of any future research. Perhaps for some unseen reason a reducing atmosphere (such as H<sub>2</sub> in N<sub>2</sub>) may improve corrosion resistance. In principle these are relatively simple experiments to conduct given the background on powder processing and ceramic design requirements provided in this Thesis.

One has to question the potential of the BaZrO<sub>3</sub> binary system for routine production of corrosion resistant materials. No matter how much development is put

into this system, production may be intrinsically too difficult for routine application. An alternative may either be required or more desirable. The major problems in  $\text{BaZrO}_3$  fabrication are kinetic limitations of phase formation and densification during sintering. Perhaps the most obvious way to mitigate these problems is to depart from the binary system and deliberately introduce small amounts of dopants to increase diffusion kinetics during powder processing and sintering. The levels and type of additives(s) may have to take into consideration  $\text{BaZrO}_3$  crystal defect chemistry, phase relationships (i.e. avoidance of secondary phases due to additives), leaching of additives during corrosion and potential contamination of the melt and/or single crystals. Use of sintering aids was avoided during this project and has previously been shown to cause problems in Y-stabilised  $\text{ZrO}_2$ , but the possible benefits from very low levels of additives that may remain in solid solution in  $\text{BaZrO}_3$  are certainly worth considering. Perhaps alternatively, controlled sintering atmospheres (esp. reducing atmospheres) might be useful in producing desirable defect structures for improving reaction and sintering kinetics without requiring chemical additives.

The great benefits obtainable from routine application of superconductivity may still lie some way off, but any contribution of inert  $\text{BaZrO}_3$  substrates and crucibles to what lies between present developments and future possibilities in this field make it a material worthy of further endeavour.

## 8.0 REFERENCES

---

- Alecu, I.D., Stead, R.J., Phillips, D.N., and van Bruchem, S. (1999) "Barium Zirconate and Calcium Zirconate Ceramic Materials Slip Cast from Non-Aqueous Suspensions", *Proceedings of the 6<sup>th</sup> European Ceramic Society Conference*, pp. 279-80.
- Arendt, R.H. (1981) "Molten Salt Synthesis of Alkaline Earth Titanates, Zirconates and their Solid Solutions", *US Patent No. 4293534*, General Electric Company, Schenectady N.Y. USA, Issued 6/10/81.
- Arendt, R.H. (1983) "Preparation of Ultrafine BaZrO<sub>3</sub>", *US Patent No. 4374117*, General Electric Company, Schenectady N.Y. USA, Issued 15/2/83.
- Azad, A-J. and Subramaniam, S. (2002) "Synthesis of BaZrO<sub>3</sub> by a Solid State Reaction Technique using Nitrate Precursors", *Materials Research Bulletin*, vol. 37, pp. 85-97.
- Azad, A-J., Subramaniam, S., and Dung, T.W. (2002) "On the Development of High Density Barium Metazirconate (BaZrO<sub>3</sub>) Ceramics", *Journal of Alloys and Compounds*, vol. 334, pp. 118-30.
- Babko, A.K. and Gridchina, G.I. (1961) "Investigation of the Polymerisation of Zirconium Ions by Dialysis", *Russian Journal of Inorganic Chemistry*, vol. 6, no. 6, pp. 680-3.
- Babko, A.K. and Gridchina, G.I. (1962) "Influence of the Constitution of Zirconium in Solution on its Reaction with Organic Reagents", *Russian Journal of Inorganic Chemistry*, vol. 7, no. 4, pp. 458-62.
- Bertin, E.P. (1970) *Principles and Practice of X-ray Spectrometric Analysis*, Plenum Press, New York.
- Bind, J.M., Dupin, T., Schafer, J., and Titeux, M. (1987) "Industrial Synthesis of Coprecipitated BaTiO<sub>3</sub> Powders", *Journal of Metals*, vol. 39, pp.60-1.

- Blanco López, M.C., Rand, B., and Riley, F.L (2000a) "Polymeric Stabilisation of Aqueous Suspensions of Barium Titanate. Part I: Effect of pH", *Journal of the European Ceramic Society*, vol. 20, pp. 1579-86.
- Blanco López, M.C., Rand, B., and Riley, F.L (2000b) "Polymeric Stabilisation of Aqueous Suspensions of Barium Titanate. Part II: Effect of Polyelectrolyte Concentration", *Journal of the European Ceramic Society*, vol. 20, pp. 1587-94.
- Brzezinska-Miecznik, J., Haberko, K., and Bucko, M.M. (2002) "Barium Zirconate Ceramic Powder Synthesis by the Coprecipitation-Calination Technique", *Materials Letters*, vol. 56, pp. 273-8.
- Britton, H.T.S. (1925) "Electrometric Studies of the Precipitation of Hydroxides. Part II. The Precipitation of the Hydroxides of Zinc, Chromium, Beryllium, Aluminium, Bivalent Tin and Zirconium by Use of the Hydrogen Electrode, and their Alleged Amphoteric Nature", *Journal of the Chemical Society*, vol. 127, part II, pp. 2120-41.
- Cima, M.J., Schneider, J.S., and Peterson, S.C. (1988) "Reaction of  $\text{Ba}_2\text{YCu}_3\text{O}_{6.9}$  Films With Ytria-Stabilised Zirconia Substrates", *Applied Physics Letters*, vol. 53, no. 8, pp. 710-2.
- Clabaugh, W.S., Swiggard, E.M., and Gilchrist, R. (1956) "Preparation of Barium Titanyl Oxalate for Conversion to Barium Titanate of High Purity", *Journal of the National Bureau of Standards*, vol. 56, no. 5, pp. 289-91.
- Clearfield, A. (1956) "The Crystal Structure of Zirconyl Chloride Octahydrate and Zirconyl Bromide Octahydrate", *Acta Crystallographica*, vol. 9, pp. 555-8.
- Clearfield, A. (1964) "Structural Aspects of Zirconium Chemistry", *Reviews of Pure and Applied Chemistry*, vol. 14, pp. 91-108.
- Connick, R.E. and McVey, W.H., (1949) "The Hydrolysis and Polymerisation of Zirconium in Perchloric Acid Solution", *Journal of the American Chemical Society*, vol. 73, pp. 1171-6.



- Connick, R.E. and Reas, W.H., (1951) "The Aqueous Chemistry of Zirconium", *Journal of the American Chemical Society*, vol. 71, pp. 3182-91.
- Chaput, F. and Boilot, J.P. (1987) "Chemical Processing of (Ba,Sr)(Ti,Zr)O<sub>3</sub> Perovskite Ceramics", *Journal of Materials Science Letters*, vol. 6, pp.1110-2.
- Dierickx, D., Houben, I., Lapin, J., Delannay, F., and van der Biest, O. (1996) "Dense Polycrystalline BaZrO<sub>3</sub> Substrates for YBa<sub>2</sub>Cu<sub>3</sub>O<sub>7-x</sub> Melt Processing", *Journal of Materials Science Letters*, vol. 15, pp. 1573-6.
- Elert, G. (2003), *Superconductivity* [Online], Available:  
[\[http://hypertextbook.com/physics/modern/superconductivity/index.shtml\]](http://hypertextbook.com/physics/modern/superconductivity/index.shtml)  
 (February 25, 2003).
- Elinson, S.V. and Petrov K.I. (1969) *Analytical Chemistry of Zirconium and Hafnium*, Ann Arbor-Humphrey Science Publishers, London.
- Enomoto, Y., and Yamaji, A. (1981) "Preparation of Uniformly Small-Grained BaTiO<sub>3</sub>", *Ceramic Bulletin*, vol, 60, no. 5, pp. 566-70.
- Erb, A. (1994) "Untersuchungen zum Phasendiagramm und Kristallzüchtung im System YBa<sub>2</sub>CuO<sub>7-δ</sub> - BaCuO<sub>2</sub> - CuO" Ph.D. Dissertation, Universität Karlsruhe, FRG.
- Erb, A. (1999) "The Impact of Crystal Growth, Oxygenation and Microstructure on the Physics of the Rare Earth (123) Superconductors", Thèse d'habilitation, Université de Genève.
- Erb, A., Biernath, T., and Müller-Vogt, G (1993) "YBa<sub>2</sub>Cu<sub>3</sub>O<sub>7-δ</sub> - BaCuO<sub>2</sub> - CuO: Investigations on the Phase Diagram and Growth of Single Crystals", *Journal of Crystal Growth*, vol. 132, pp. 389-95.
- Erb, A., Manuel, A.A., Dhalle, M., Marti, F., Genoud, J-Y., Revaz, B., Junod, A., Vaumathi D., Ishibashi, S., Shukla, A., Walker, E., Fischer, Ø., Flükiger, R., Pozzi, R., Mali, M., and Brinkmann, D. (1999) "Experimental Evidence for Fast Cluster Formation of Chain Oxygen Vacancies in YBa<sub>2</sub>Cu<sub>3</sub>O<sub>7-δ</sub> as the Origin of the Fishtail Anomaly", *Solid State Communications*, vol. 112, pp. 245-9.

- Erb, A., Walker, E., and Flükiger, R. (1995) "BaZrO<sub>3</sub>: The Solution for the Crucible Corrosion Problem During The Single Crystal Growth Of High T<sub>c</sub> Superconductors REBa<sub>2</sub>Cu<sub>3</sub>O<sub>7-d</sub>; RE=Y, Pr", *Physica C*, vol. 245, pp. 245-51.
- Erb, A., Walker, E., and Flükiger, R. (1996) " The Use of BaZrO<sub>3</sub> Crucibles in Crystal Growth of High-T<sub>c</sub> Superconductors - Progress in Crystal Growth as well as in Sample Quality", *Physica C*, vol. 258, pp. 9-20.
- Erb, A., Walker, E., Genoud, J-Y, and Flükiger, R. (1997) "Improvements in Crystal Growth and Crystal Homogeneity and its Impact on Physics", *Physica C*, vol. 282-7, pp. 89-92.
- Etienne, J., Larbot, A., Julbe, A., Guizard, C., and Cot, I. (1994) "A Microporous Zirconia Membrane Prepared by the Sol-Gel Process from Zirconyl Oxalate", *Journal of Membrane Science*, vol. 86, pp. 95-102.
- Fang, J., Wang, J., Ng, S-C., Chew C-H., and Gan, L-M.. (1997) "Ultrafine Zirconia Powders via Microemulsion Processing Route", *NanoStructured Materials*, vol. 8, no. 4, pp. 499-505.
- Fisher, G. (1988) "Superconducting Mysteries Unravel as Developments Proceed", *Ceramic Bulletin*, vol. 67, no. 4, pp. 725-35.
- Flaschen, S.S. (1955) "An Aqueous Synthesis of Barium Titanate", *Journal of the American Chemical Society*, vol. 77, p. 6197.
- Flood, H., and Förland, T. (1947) "The Acidic and Basic Properties of Oxides", *Acta Chemica Scandinavica*, vol. 1, pp. 592-604.
- Gallagher, P.K. and Schrey F. (1963) "Thermal Decomposition of Some Substituted Barium Titanyl Oxalates and its Effect on the Semiconducting Properties of the Doped Materials", *Journal of the American Ceramic Society*, vol. 46, no. 12, pp. 567-73.
- Gangadevi, T., Subba Rao, M., and Kutty, T.R.N. (1980) "Thermal Decomposition of Zirconyl Oxalates. I - Barium Zirconyl Oxalate", *Journal of Thermal Analysis*, vol. 19, pp. 321-32.

- Gautier-Picard, P., Chaud, X., Beaugnon, E., and Tournier, R. (1997) "Growth Kinetic of Top-Seeded YBCO Single Domains", *Physica C*, vol. 282-287, pp. 461-2.
- Genoud, J.-Y., Erb, A., Revaz, B., and Junod, A. (1997) "Growth of High Purity  $\text{YBa}_2\text{Cu}_3\text{O}_8$  and  $\text{Y}_2\text{Ba}_4\text{Cu}_7\text{O}_{15-8}$  Single Crystals in  $\text{BaZrO}_3$  Crucibles under High Oxygen Pressure, and Absence of Magnetic Fishtail Effect", *Physica C*, vol. 282-287, pp. 457-8.
- Gladysz, G.M. and Chawla, K.K. (2001) "Coefficients of Thermal Expansion of Some Laminated Ceramic Composites", *Composites: Part A*, vol. 32, pp. 173-8.
- Goretta, K.C., Park, E.T., Koritala, R.E., Cuber, M.M., Pascual, E.A., Nan Chen, de Arellano-Lopez, A.R., and Routbort, J.L. (1998) "Thermomechanical Response of Polycrystalline  $\text{BaZrO}_3$ ", *Physica C*, vol. 309, pp. 245-50.
- Gregory, J. (1993) "Stability and Flocculation of Suspensions" in *Processing of Solid-Liquid Suspensions*, P. Ayazi Shamlou (ed.), Butterworth-Heinemann, Oxford.
- Grinberg, A.A. and Astapovich V.I. (1961) "Complex Zirconium Oxalates", *Russian Journal of Inorganic Chemistry*, vol. 6, no. 2, pp. 164-7.
- Hennings, D., and Schreinemaker H.J, (1991) "Method of Manufacturing Barium Titanate  $\text{BaTiO}_3$ " *US Patent No. 5009876*, US Philips Corp, New York, USA, Issued 23 April 1991.
- Hérard, C., Faivre, A. and Lemaître, J. (1995a) "Surface Decontamination Treatments of Undoped  $\text{BaTiO}_3$  – Part I: Powder and Green Body Properties", *Journal of the European Ceramic Society*, vol. 15, pp. 135-43.
- Hérard, C., Faivre, A. and Lemaître, J. (1995b) "Surface Decontamination Treatments of Undoped  $\text{BaTiO}_3$  – Part II: Influence on Sintering", *Journal of the European Ceramic Society*, vol. 15, pp. 145-53.

- Huang, Y.B., Witz, G., Giannini, E., Erb, A., Shlyakhtin, O.A., and Flükiger, R. (1999) "Interaction of Bi, Pb(2223) Precursors with Metal Zirconates", *Superconductor Science and Technology*, vol. 12, pp. 411-6.
- Inoue, O., and Kawashima, S. (1989) "Method for Producing Crystalline Complex Perovskite Compounds", *US Patent No. 4853199*, Matsushita Electric Industrial Co, Ltd Japan, Issued 1/8/1989.
- Jenkins, R., and Snyder, R.L. (1996) *Introduction to X-ray Powder Diffraction*, John Wiley & Sons Inc., New York.
- Ju, X., Huang, P., Xu, N., and Shi., J. (2000) "Influences of Sol and Phase Stability on the Structure and Performance of Mesoporous Zirconia Membranes", *Journal of Membrane Science*, vol. 166, pp. 41-50.
- Karlesheva, K.F. and Sheka, I.A. (1962) "Composition of the Zirconium and Hafnium Derivatives of Cupferron", *Russian Journal of Inorganic Chemistry*, vol. 7, no. 6, pp. 666-70.
- de Keijser, Th.H., Langford, J.I., Mittemeijer, E.J. and Vogels A.B.P. (1982) "Use of the Voigt Profile in a Single-Line Method for the Analysis of X-ray Diffraction Line Broadening", *Journal of Applied Crystallography*, vol. 15, p. 308-14.
- Kolthoff, I.M., Sandell, E.B., Meehan E.J., and Bruckenstein S. (1969) *Quantitative Chemical Analysis*, The MacMillan Co., New York.
- Kovalenko, P.N., and Bagdasarov, K.N (1961) "The Solubility of Zirconium Hydroxide", *Russian Journal of Inorganic Chemistry*, vol. 6, no. 3, pp. 272-5.
- Kuznetsov, V.I. and Fang Ming-o (1962) "Extraction of Zirconium in the Presence of Weak Complexing Agents", *Russian Journal of Inorganic Chemistry*, vol. 7, no. 2, pp. 215-7.
- Kutty, T.R.N., Vivekanandan, R., and Philip, S. (1990) "Precipitation of Ultrafine Powders of Zirconia Polymorphs and their Conversion to  $MZrO_3$  (M=Ba, Sr, Ca) by the Hydrothermal Method", *Journal of Materials Science*, vol. 25, pp. 3649-58.

- Kraus, K. and Johnson, J. (1953) *Journal of the American Chemical Society*, vol. 75, p. 5769.
- Lewis, J.A. (2000) "Colloidal Processing of Ceramics", *Journal of the American Ceramic Society*, vol. 83, no. 10, pp. 2341-59.
- Liang, R., Bonn, D.A., and Hardy, W.N. (1998) "Growth of High Quality YBCO Single Crystals Using BaZrO<sub>3</sub> Crucibles", *Physica C*, vol. 304, pp. 105-11.
- Lilley, E., and Wusirika, R.R. (1988) "Method for the Production of Mono-Size Powders of Barium Titanate", *US Patent No. 4764493*, Corning Glass Works, Corning N.Y. USA, Issued 16/8/1988.
- Malmsten, M. (ed), (1998) *Biopolymers at Interfaces*, Marcel Dekker, Inc., New York.
- Marov, I.N. and Ryabchikov, D.I (1962) "Complex Formation of Zr<sup>IV</sup> and Hf<sup>IV</sup> with Chloride, Nitrate and Oxalate Ions", *Russian Journal of Inorganic Chemistry*, vol. 7, no. 5., pp. 533-9.
- Matijevic, E., and Her, Y-S. (1999) "Process for the Synthesis of Crystalline Powders of Perovskite Compounds", *US Patent No. 5900223*, Chon Int. Co. Ltd, Seoul, Rep of Korea, Issued 4 May 1999.
- Mazdiasni, K.S. (1984) "Fine Particle Perovskite Processing", *Ceramic Bulletin*, vol. 63, no. 4, pp. 591-4.
- Mazdiasni, K.S., Dolloff, R.T., and Smith, J.S. (II) (1969) "Preparation of High-Purity Submicron Barium Titanate Powders", *Journal of the American Ceramic Society*, vol. 52, no. 10, pp. 523-6.
- Mohanty, S.R., Singh, D., and Murty, J.G.K (1955) "Estimation and Complexes of Zirconium with Oxalates", *Current Science*, no. 7, p.229.
- Mukherji, A.K (1970) *Analytical Chemistry of Zirconium and Hafnium*, Pergamon Press, Oxford.

- Muha, G.M. and Vaughan, P.A. (1960) "Structure of the Complex Ion in Aqueous Solutions of Zirconyl and Hafnyl Oxalates", *Journal of Chemical Physics*, vol. 33, no. 1, pp. 194-9.
- Mulder, B.J. (1970) "Preparation of BaTiO<sub>3</sub> and Other Ceramic Powders by Coprecipitation of Citrates in an Alcohol", *Ceramic Bulletin*, vol. 49, no. 11, pp. 990-3.
- Nabivanets, B.I. (1961) "Electromigration of Zirconium Ions in Perchloric, Hydrochloric and Nitric Acids", *Russian Journal of Inorganic Chemistry*, vol. 6, no. 5, pp. 586-90.
- Norlund Christensen, A. (1970) "Hydrothermal Preparation of Barium Titanate by Transport Reactions", *Acta Chemica Scandinavica*, vol. 24, pp. 2477-52.
- Norrish, K., and Hutton, J.T. (1969) "An Accurate X-Ray Spectrographic Method for the Analysis of a Wide Range of Geological Samples", *Geochimica et Cosmochimica Acta*, vol. 33, pp. 431-53.
- Paschoal, J.O.A., Kleykamp, H., and Thuemmler, F. (1987) *Journal of Nuclear Materials*, vol. 151, no. 1, pp. 10-21.
- Pfaff, G. (1995) "A Novel Reaction Path to Barium Zirconates by the Decomposition of Peroxide Precursor", *Materials Letters*, vol. 24, pp. 393-7.
- Phulé, P.P., and Risbud, S.H. (1989) "Low Temperature Synthesis and Dielectric Properties of Ceramics Derived from Amorphous Barium Titanate Gels and Crystalline Powders", *Materials Science and Engineering B*, vol. 3, pp. 241-7.
- Phulé, P.P., and Grundy, D.C. (1994) "Pathways for the Low Temperature Synthesis of Nano-Crystalline Barium Zirconate", *Materials Science and Engineering B*, vol. 23, pp. 29-35.
- Phulé, P.P., and Risbud, S.H. (1990) "Review: Low Temperature Synthesis and Processing of Electronic Materials in the BaO-TiO<sub>2</sub> System", *Journal of Materials Science*, vol. 25, pp. 1169-83.



- Potdar, H.S., Deshpande, S.B., Godbole, P.D., and Date, S.K. (1993) "Synthesis of Microcrystalline BaZrO<sub>3</sub> via Molecular Precursor Route", *Journal of Materials Research*, vol. 8, no. 5, pp. 948-50.
- Reddy, V.B., and Mehrotra, P.N. (1979) "Preparation, Characterisation and Thermal Decomposition of Barium Zirconyl Oxalate", *Thermochimica Acta*, vol. 31, pp. 31-7.
- Resnitskii, L.A. and Guzei, A.S. (1978) "Thermodynamic Properties of Alkaline Earth Titanates, Zirconates and Hafnates", *Russian Chemical Reviews*, (English translation of Uspekhi Khimii), vol. 47, no. 2, pp. 99-119.
- Richerson, D.W. (1992) *Modern Ceramic Engineering*, Marcel Dekker Inc., New York.
- Robertz, B., Boshini, F., Cloots, R., and Rulmont, A. (2001) "Importance of Soft Solution Processing for Advanced BaZrO<sub>3</sub> Materials", *International Journal of Inorganic Materials*, vol. 3, pp. 1185-7.
- Roosen, A., and Hausner, H., (1988) "Techniques for Agglomeration Control During Wet-Chemical Powder Synthesis", *Advanced Ceramic Materials*, vol. 3, no. 2, pp. 131-7.
- Schneemeyer, L.F., Waszczak, J.V., Siegrist, T., van Dover, R.B., Rupp, L.W., Batlogg, B., Cava, R.J., and Murphy, D.W. (1987) "Superconductivity in YBa<sub>2</sub>Cu<sub>3</sub>O<sub>7</sub> Single Crystals", *Nature*, vol. 328, no. 13, pp. 601-2.
- Shadow: A system for X-ray Powder Diffraction Pattern Analysis* (1998), Materials Data Inc., Livermore CA, USA.
- Sin, A., El Montaser, B., and Odier, P. (2002) "Synthesis and Sintering of Large Batches of Barium Zirconate Nanopowders", *Journal of the American Ceramic Society*, vol. 85, pp. 1928-32.
- Singh, R.P., and Banerjee, N.R. (1961) "Electrometric Studies on the Precipitation of Hydrous Oxides of Some Quandrivalent Cations. Part I. Precipitation of

- Zirconium Hydroxide from Solutions of Zirconium Salts”, *Journal of the Indian Chemical Society*, vol. 38, no. 11, pp. 865-70.
- Smith, D.K. (1992) “Particle Statistics and Whole-Pattern Methods in Quantitative X-ray Powder Diffraction Analysis”, *Advances in X-ray Analysis*, vol. 35A, pp. 1-15.
- Solovkin, A.S., and Tsvetkova, S.V. (1962) “The Chemistry of Aqueous Solutions of Zirconium Salts (Does the Zirconyl Ion Exist?)”, *Russian Chemical Reviews*, (English translation of *Uspekhi Khimii*), vol. 31, no. 11, pp. 655-69.
- Stenstrop, G., and Engell J., (1990) “BaZrO<sub>3</sub>: Synthesis, Properties and Compatibility with Ba<sub>2</sub>YCu<sub>3</sub>O<sub>7-x</sub>”, *Journal of Less-Common Metals*, vol. 164-5, pp. 200-7.
- Tagami, M., Sumida, M., Krauns, Ch., Yamada, Y., Umeda, T., and Shiohara, Y. (1995) “Fabrication and Growth Rate Estimation of PrBa<sub>2</sub>Cu<sub>3</sub>O<sub>7-δ</sub> Single Crystals by the Modified Top Seeded Crystal Pulling Method”, *Physica C*, vol. 250, pp. 240-6.
- Taglieri, G., Tersigni, M., Villa, P.L., and Mondelli, C. (1999) “Synthesis by the Citrate Route and Characterisation of BaZrO<sub>3</sub>, a High Tech Ceramic Oxide: Preliminary Results”, *International Journal of Inorganic Materials*, vol. 1, pp. 103-10.
- Trang, A. (2002) “Development of Barium Zirconate Crucibles for the Growth of Ultra-Pure High Temperature Superconductor Single Crystals”, Honours Dissertation, Curtin University of Technology, Australia.
- Ubal dini, A., Buscaglia, V., Uliana, C., Costa, G. and Ferretti, M. (2003) “Kinetics and Mechanism of Formation of Barium Zirconate from Barium Carbonate and Zirconia Powders”, *Journal of the American Ceramic Society*, vol. 86, no. 1, pp. 19-25.
- Uedaira, S., Suzuki, M., Yamanoi, H., and Tamura, H. (1986) “Method for Manufacturing Fine Powder Barium Zirconate”, *US Patent No. 4595580*, Sony Corp, Tokyo, Japan., Issued 17 June 1986.

- Vinogradov, A.V., and Sphinel, V.S. (1961) "Composition and Properties of Quinolinatozirconium from an Oxalae Medium", *Russian Journal of Inorganic Chemistry*, vol. 6, no. 6, pp. 687-8.
- Wu, M.K., Ashburn, J.R., Torng, C.J., Hor, P.H., Meng, R.L., Gao, L., Huang, Z.J., Wang, Y.Q., and Chu, C.W. (1987) "Superconductivity at 93 K in a new mixed-phase Yb-Ba-Cu-O compound system at ambient pressure", *Physical Review Letters*, vol. 58, no. 9, pp. 908-10.
- Yatsimirskii, K.B., and Raizman, L.P. (1961) "Complex Formation in Solution of Zirconium with Anions of Organic Acids", *Russian Journal of Inorganic Chemistry*, vol. 6, no. 11, pp. 1263-7.
- Young, R.A. (1993) *The Rietveld Method*, International Union of Crystallography Monographs, Oxford University Press, Oxford.
- Yuranova, L.I., Komissarova, L.N., and Plyuschchev V.E. (1962) "Solubility and Thermal Stability of Zirconium and Hafnium Oxide Nitrate Hexahydrates", *Russian Journal of Inorganic Chemistry*, vol.7, no. 5, pp 546-8.
- Zaitsev, L.M., and Bochkarev, G.S., (1962a) "Peculiarities in the Behaviour of Zirconyl in Solutions", *Russian Journal of Inorganic Chemistry*, vol. 7, no. 4, pp. 411-4.
- Zaitsev, L.M., and Bochkarev, G.S., (1962b) "Preparation of Some Oxalato-Compounds of Zirconyl", *Russian Journal of Inorganic Chemistry*, vol. 7, no. 7, pp. 802-6.

## **9.0 APPENDICES**

---

## **9.1 Appendix 1 - Development and assessment of quantitative x-ray analysis methods**

### **9.1.1 XRF analysis using a Siemens SRS200 spectrometer**

XRF was the primary method used to measure the stoichiometry (Ba : Zr + Hf mole ratio) of powders, which as shown in Section 6.6 was a critical parameter affecting the processing and corrosion properties of BaZrO<sub>3</sub>. The tolerances on stoichiometry for optimum corrosion resistance are so narrow that optimisation and assessment of the accuracy and precision of measurement required careful attention. Considerable effort was required to produce measurements of acceptable accuracy and precision using the instrument available for the bulk of this project (a ~20 years old Siemens SRS200). Appendix 1 presents salient considerations in development of the measurement and detailed analysis of its precision. More modern instruments suffer the same problems as the SRS200 only to reduced extent, and the rigorous attention to detail needed for the SRS200 can be applied to other instruments to deliver results of the highest quality.

The performance of the SRS200 instrument under carefully optimised acquisition conditions is shown in Table A1.1 and Figures A1.1 and A1.2. Optimisation of acquisition parameters took into account the specific properties of the instrument, such as the linearity of the counting system, repeatability of positioning of optical components (crystals and collimators) and stability of tubes, detectors and associated electronics. A long start-up time at full tube power (at least 6 hours) was necessary to produce useful measurements.

Two key parameters controlling instrument performance were temperature control and errors due to specimen holders. The instrument had a temperature controller (containing an air-conditioner and heater system) originally specified to maintain the spectrometer to a fixed temperature within  $\pm 0.5$  °C. Due to the age of the temperature controller and its loss of refrigerant, the performance of the controller steadily deteriorated and it became inoperable by mid-way through the project. Consequently, frequent re-calibration or drift correction (i.e. every seven unknowns), was needed to minimise drift effects on observed intensities, particularly

from the flow counter. Temperature control problems also required a flow counter energy window wider than desirable, slightly reducing signal to noise ratios. Intensity errors due to specimen holder variation were apparent by analysing a fused bead and a powder specimen in all 10 specimen holders. Figure A1.3 shows the effects of specimen holders on Zr intensities, which would occur similarly for any other element.

The intensity ratio method provided significantly more repeatable results than using raw intensities because of effects of a number of instrument errors including specimen holder errors, detector and instrument stability problems. The observation that barium and zirconium intensities often varied simultaneously suggested incident intensity instability, because the detection efficiency of zirconium by a scintillation detector would be expected to be quite stable. The period of intensity variation (~24 hours, Figure A1.1) approximately matched the period of cooling water temperature variation from a central chilled water plant operating on off-peak electricity at night. Using the intensity ratio method, all intensities were arbitrarily normalised to the observed Zr-K $\alpha$  intensity, because Zr had the highest observed intensity. Incidentally, Zr also had the most reliable raw intensities because of the stability and reliability of the scintillator detector. For the entire project, intensity ratios were used for calibrations rather than raw intensities.



Table A1.1 Example of a calibration and analysis of residuals from SRS200. Residuals are the deviation of measured points from the fitted calibration plane and provide an effective basis for determining measurement precision.

BaL <sub>α1</sub> : ZrK <sub>α</sub> Observed Intensity Ratio	HfL <sub>β1</sub> : ZrK <sub>α</sub> Observed Intensity Ratio	Actual BaO : ZrO <sub>2</sub> Mole Ratio	Actual HfO <sub>2</sub> : ZrO <sub>2</sub> Mole Ratio	BaO : ZrO <sub>2</sub> Mole Ratio		HfO <sub>2</sub> : ZrO <sub>2</sub> Mole Ratio	
				Calculated	Residual	Calculated	Residual
0.32137	0.00054	0.8994	0.00000	0.8988	0.0006	-0.0002	0.0002
0.32361	0.00475	0.9028	0.00589	0.9042	-0.0013	0.0059	0.0000
0.32440	0.00878	0.9080	0.01177	0.9055	0.0025	0.0116	0.0001
0.32802	0.01358	0.9139	0.01835	0.9147	-0.0008	0.0185	-0.0001
0.32964	0.01800	0.9173	0.02470	0.9183	-0.0009	0.0248	-0.0001
0.35775	0.00056	1.0023	0.00000	1.0016	0.0007	0.0000	0.0000
0.35926	0.00473	1.0039	0.00584	1.005	-0.0011	0.0059	-0.0001
0.36185	0.01001	1.0108	0.01359	1.0111	-0.0003	0.0135	0.0001
0.36387	0.01408	1.0159	0.01901	1.0159	0.0000	0.0193	-0.0003
0.36619	0.01755	1.0218	0.02428	1.0217	0.0001	0.0242	0.0000
0.40235	0.00063	1.1273	0.00000	1.1277	-0.0004	0.0002	-0.0002
0.39384	0.00421	1.1060	0.00521	1.1029	0.0032	0.0053	-0.0001
0.39928	0.00878	1.1132	0.01197	1.1172	-0.0040	0.0118	0.0001
0.39835	0.01230	1.1119	0.01694	1.1138	-0.0019	0.0169	0.0001
0.40140	0.01704	1.1251	0.02380	1.1213	0.0037	0.0236	0.0002

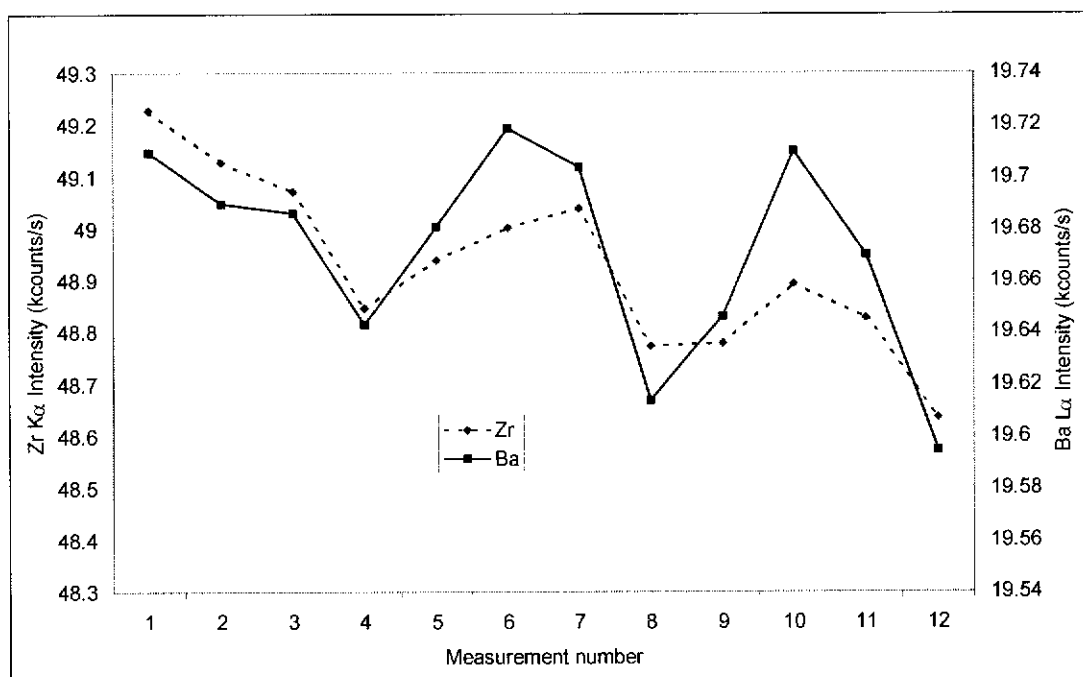


Figure A1.1 Intensity stability on the SRS200 spectrometer. Measurements were taken six to twelve hours apart over four days.

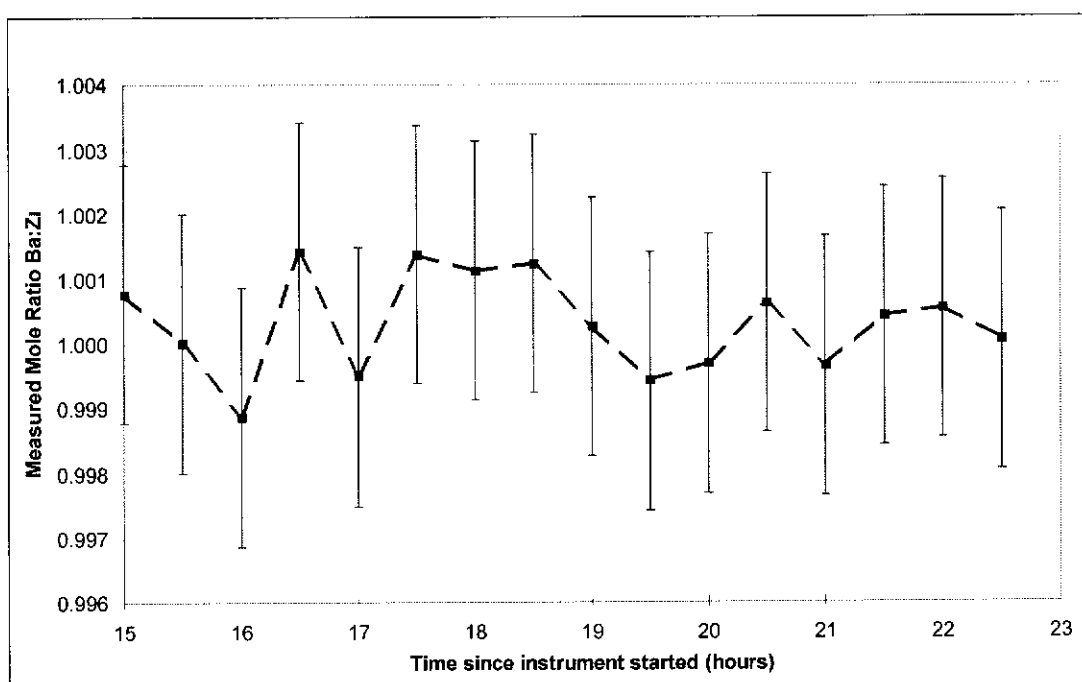


Figure A1.2 Typical repeatability of Ba : (Zr + Hf) mole ratios for a sample with a nominal mole ratio of 1.000 on a single specimen holder in the SRS200 spectrometer. Uncertainties are  $\pm 2\sigma$ .

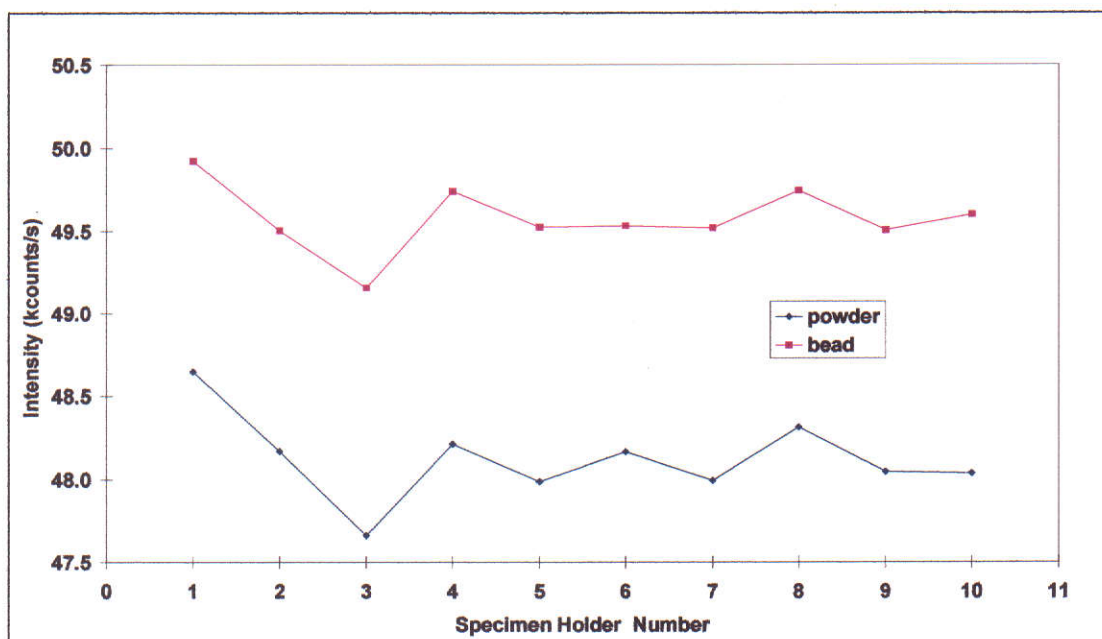


Figure A1.3 The effect of specimen holders on Zr  $K_{\alpha}$  intensities of a single powder and fused bead specimen in the SRS200 spectrometer. The acquisition parameters were fixed for each type of specimen, but the powder and fused specimens were analysed using different instrument settings to produce similar intensities. Error bars from counting statistics are too small to plot: the correlation between the two sets of data shows that the effect of specimen holders was real.

Figure A1.2 shows the repeatability of Ba : Zr mole ratio measurement on the XRF after a long warm-up time on the SRS200. The standard deviation of the 16 measurements shown in Figure A1.2 is 0.00076, hence the two standard deviation repeatability was observed as  $\pm 0.0015$ . Errors are stated as  $\pm 0.002$  because although many specimens were analysed using multiple specimens and/or repeated analysis, some were analysed using one specimen and one acquisition.

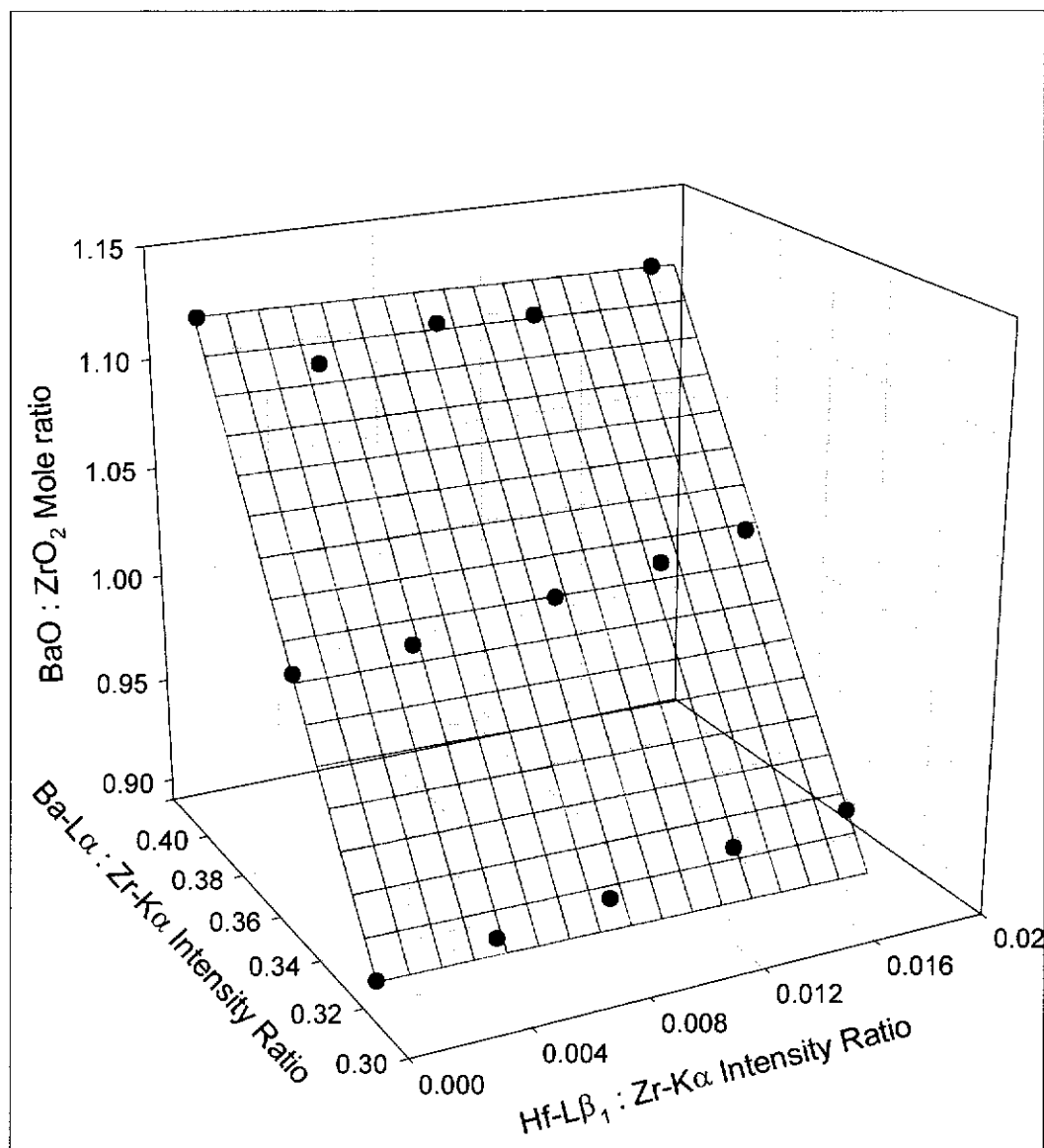


Figure A1.4 BaO : ZrO<sub>2</sub> mole ratio full calibration on SRS200.

Figure A1.4 shows that the observed Ba-La $\alpha_1$  : Zr-K $\alpha$  intensity ratio was dependent on the BaO : ZrO<sub>2</sub> mole ratio and nearly independent of HfO<sub>2</sub> content. Though small, the inter-element effect of HfO<sub>2</sub> on the observed intensity ratio was just resolved above statistical errors in these measurements. Figure A1.5 shows the small effect of BaO : ZrO<sub>2</sub> ratios on observed Hf-L $\beta_1$  : Zr-K $\alpha$  intensity ratios. The small correction for the effect of HfO<sub>2</sub> should be applied for accurate measurement of BaO : ZrO<sub>2</sub> mole ratios, but may be ignored for approximate measurements. The Ba : (Zr + Hf) mole ratio can be calculated from observed intensity ratios using Equations A1.1 and A1.2. Calibration constants need to be re-determined when changing instruments or any parameter affecting intensity ratios.

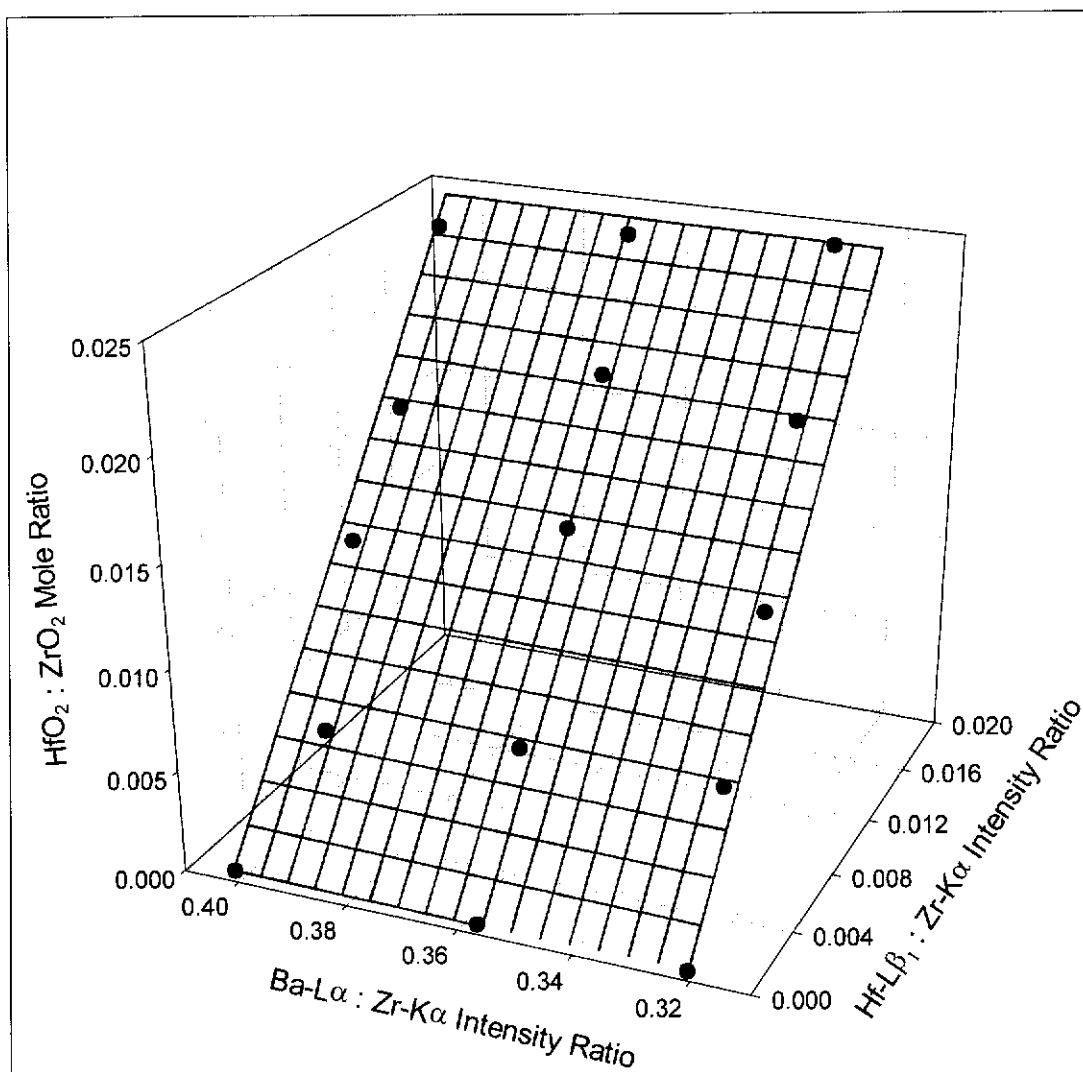


Figure A1.5 HfO<sub>2</sub> : ZrO<sub>2</sub> mole ratio full calibration on SRS200.

Equation A1.1

$$\text{BaO: ZrO}_2 = [-0.0096 (0.0067)] - [0.2241 (0.0919) X] + [2.8271 (0.0184) Y]$$

where:

X = Observed intensity ratio of Hf-L<sub>α1</sub> : Zr-K<sub>α1</sub>

Y = Observed intensity ratio of Ba-L<sub>α</sub> : Zr-K<sub>α1</sub>

figures in parentheses are 1 standard error.

Equation A1.2

$$\text{HfO}_2: \text{ZrO}_2 = [-0.0018 (0.0005)] + [1.4273 (0.0065) X] + [0.0027 (0.0013) Y]$$

where:

X = Observed intensity ratio of Hf-L<sub>α1</sub> : Zr-K<sub>α1</sub>

Y = Observed intensity ratio of Ba-L<sub>α</sub> : Zr-K<sub>α1</sub>

figures in parentheses are 1 standard error.

The uncertainties shown in Equations A1.1 and A1.2 are 1 standard error estimates of the planar regressions fitted using Sigmaplot® v7.101. The constant term in Equation A1.1 represents the intersection of the fitted plane with both the X and Y planes, and its uncertainty was relatively large because of extrapolation in the Y axis (Ba : Zr intensity ratio). The extrapolation was rather large because calibrations were performed only above a Ba : (Zr + Hf) mole ratio of  $\sim 0.9$ . Uncertainties in Equation A1.1 are of very limited use in calculating actual measurement uncertainties, which are better represented by the residuals in the composition range of interest (the distances of measured points above and below the fitted plane) as shown in Table A1.1. The small constant term in Equation A1.2 represents minor errors in background correction of Hf-L $\alpha_1$  intensities. The substantial relative uncertainty in the inter-element correction term in Equation A1.2 (i.e.  $0.0027 \pm 0.0013$  Y) indicates that statistical confidence in correcting the observed HfO $_2$  : ZrO $_2$  mole ratio for the effect of BaO : ZrO $_2$  ratios was relatively low, and could be ignored for approximate measurements.

Fifteen standards were used to cover complete variation of BaO : ZrO $_2$  : HfO $_2$  ratios over the composition range of interest. Figures A1.4 and A1.5 show that intensity ratios can be accurately fitted to planar surfaces within this range. In practice, the number of samples required for calibration can be reduced to four to allow rapid calibration, one in each corner of the surfaces fitted in Figures A1.4 and A1.5. Furthermore if the HfO $_2$  content is known and constant, a linear calibration may be performed using standards of constant ZrO $_2$  : HfO $_2$  ratio equivalent to the samples, and in fact this was done for the vast majority of samples because the Zr : Hf ratio of most samples was fixed by using a single supply of zirconium.

Regular monitoring over time may be needed to control instrument drift as shown in Figure A1.6. Zr-K $\alpha$  was measured by the scintillation counter, whereas Ba-L $\alpha$  and Hf-L $\beta_1$  were measured using a gas flow counter which is sensitive to temperature and pressure variation. Factors affecting instrument sensitivity influence the calibrations reported here (such as Equations A1.1 and A1.2), but new calibrations may be readily measured and monitored with as few as three calibration standards.



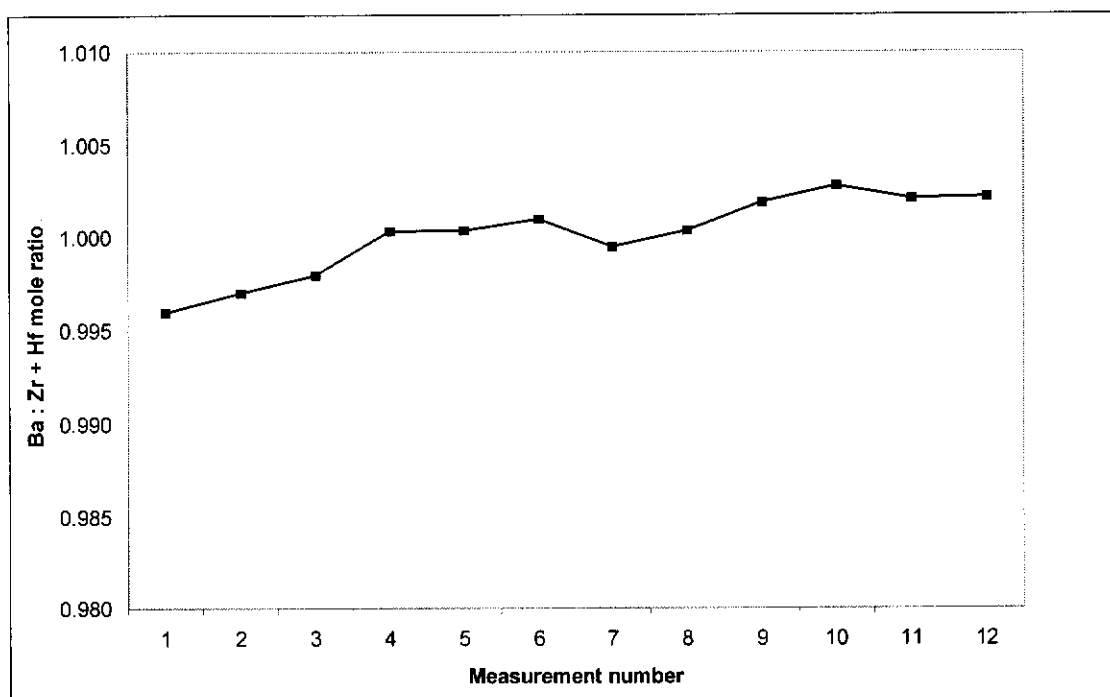


Figure A1.6 Stability of apparent BaO : ZrO<sub>2</sub> mole ratio of 0.9972 standard without applying new calibrations during a long series of measurements, demonstrating the need for drift correction or frequent re-calibration of the SRS200. Measurements were taken six to twelve hours apart over four days.

Table A1.1 shows the quality of the calibrations achieved on the SRS200. The residuals (vertical deviations from the planar surfaces fitted in Figures A1.4 and A1.5) allowed the BaO : (ZrO<sub>2</sub>+HfO<sub>2</sub>) mole ratio to be determined to a two standard deviation uncertainty of  $\pm 0.002$ . Most specimens analysed on the SRS200 were measured several times so that two standard errors of Ba : (Zr + Hf) mole ratio measurements were maintained below  $\pm 0.002$ .

### 9.1.2 XRF analysis using a Philips PW1404 spectrometer

Calibration of the PW1404, as for later samples on the SRS200, was performed using only three calibrations standards with HfO<sub>2</sub> : ZrO<sub>2</sub> ratios matching those of unknowns since HfO<sub>2</sub> : ZrO<sub>2</sub> ratios of unknowns were fixed by use of a single supply of raw materials. The method was optimised to suit the response of the instrument, which was an easy task with the instrument in much better condition than the SRS200. The main requirement was to avoid use of the LiF220 crystal with a fine collimator, which reduced intensity repeatability to  $\pm \sim 0.5\%$  due to mechanical wear of either the goniometer or a problem with collimator positioning. This problem was

avoided by simply switching to a coarser collimator. The procedure of leaving the tube on a standby setting (low current and voltage) after operation provided high stability within one hour of restoring full power to the tube. Table A1.2 shows the intensity ratio repeatability of standards on the PW1404 spectrometer over a four hour period.

Net intensities also had excellent stability, i.e. 0.026 % and 0.018 % standard errors (three measurements) for Ba  $L_{\alpha}$  and Zr  $K_{\alpha}$  over a three hour period, which from Table 4.5 can readily be shown as verging on counting statistic errors alone. The quality of the data allowed confident analysis of each specimen using a single measurement, which was necessary in many cases because of limited access to the instrument. To ensure quality of results, specimens were run in batches of 10 - 15 including three calibration standards used for calibration of each group of specimens. The analysis time was five minutes per specimen (Table 4.5), hence calibration was checked every one to three hours despite the high stability of the instrument.

Table A1.2 Calibration data from PW1404. Four calibrations were performed over a four hour period and were applied to corresponding batches of unknowns.

<b>Intensity Ratio Ba <math>L_{\alpha}</math> : Zr <math>K_{\alpha}</math></b>	<b>Ba : Zr + Hf Mole Ratio of Standard</b>		
	<b>0.8997</b>	<b>1.0019</b>	<b>1.1008</b>
Calibration 1	0.23201	0.25818	0.28477
Calibration 2	0.23080	0.25728	0.28330
Calibration 3	0.23079	0.25722	0.28342
Calibration 4	0.23091	0.25704	0.28311
<b>All Calibrations</b>			
Average	0.2311	0.2574	0.2836
Standard Deviation	0.00059	0.00051	0.00076
Standard Error of Mean	0.00030	0.00026	0.00038
% Standard Deviation	0.26	0.20	0.27
% Standard Error of Mean	0.13	0.10	0.13
<b>Excluding Calibration 1</b>			
Average	0.23083	0.25718	0.28328
Standard Deviation	0.00007	0.00012	0.00016
Standard Error of Mean	0.00003	0.00006	0.00008
% Standard Deviation	0.03	0.05	0.06
% Standard Error of Mean	0.01	0.02	0.03

### 9.1.3 BaCO<sub>3</sub> determination by quantitative x-ray diffraction

Quantitative determination of BaCO<sub>3</sub> was an important measurement required for optimisation of powder processing and assessment of phase purity. XRD was the most effective technique available to determine BaCO<sub>3</sub> levels in the bulk. Assessment of the accuracy and precision of the measurement was required because analysis was required close to detection limits. Quantitative analysis was required at levels that would often be below the detection limits when using routine measurement conditions for basic phase identification. Careful selection of instrument parameters were required to maximise data quality, specifically selection of step size and scan rate, and also adjustment of the secondary monochromator to completely remove spurious diffraction peaks due to Cu-K $\beta$  and W-L lines from the tube.

The masses of powders used to prepare BaCO<sub>3</sub> in BaZrO<sub>3</sub> standards are shown in Table A1.3. Weighing uncertainties for standard preparation were negligible compared to other sources of error. Counting statistic uncertainties shown in Table A1.4 are  $\pm 3$  standard deviations. The magnitude of the x-intercept in Figure A1.7 represents the amount of BaCO<sub>3</sub> in the powder used to make the standards (i.e. 1.66 wt.%), and its uncertainty is  $\pm 0.16$  (1 standard error) based on regression statistics.

Table A1.3 Weights of powders used to produce standards for BaCO<sub>3</sub> in BaZrO<sub>3</sub> for quantitative XRD. Weighing uncertainties were  $\pm 0.2$  mg, which contributed a negligible amount to the total measurement uncertainty.

Wt. Sample (g)	Wt. BaCO <sub>3</sub> Added (g)	Wt.% BaCO <sub>3</sub> Added
-	-	0
3.9871	0.0390	0.978
3.9780	0.0815	2.049
3.9772	0.1608	4.043
3.6898	0.3201	8.675
3.6042	0.5096	14.14

Absolute BaCO<sub>3</sub> contents of standards (Figure A1.8) were calculated from the BaCO<sub>3</sub> in the original powder (Figure A1.7) and the amount subsequently added. Uncertainties in absolute BaCO<sub>3</sub> weight percentages were primarily due to the uncertainty of the BaCO<sub>3</sub> content of the starting powder used to make the standards as calculated from the x-intercept in Figure A1.7. The calibration slope ( $m = 132$ ) has an uncertainty of  $\pm 2$  from regression statistics.

Table A1.4 Intensities of x-ray diffraction peaks from BaCO<sub>3</sub> standards. Standard deviations in this table only include counting statistical errors. All intensities are integrated peak areas.

	Weight Percent BaCO <sub>3</sub> Added					
	0	0.987	2.049	4.043	8.675	14.14
<b>Peak Intensity - BaCO<sub>3</sub></b>						
Total Peak Area (counts)	20132	23536	27036	34659	48159	63382
Background Area (counts)	14650	14650	14650	14650	14650	14650
Net Peak Area (counts)	5482	8886	12386	20009	33509	48732
Standard Deviations						
Total Peak Area (counts)	137	153	164	186	219	252
Background Area (counts)	121	121	121	121	121	121
Net Peak Area (counts)	183	195	204	222	251	279
<b>Peak Intensity - BaZrO<sub>3</sub></b>						
Total Peak Area (counts)	502253	499833	479452	486067	479359	475133
Background Area (counts)	23228	23228	23228	23228	23228	23228
Net Peak Area (counts)	479025	476605	456224	462839	456131	451905
Standard Deviations						
Total Peak Area (counts)	709	707	692	697	692	689
Background Area (counts)	152	152	152	152	152	152
Net Peak Area (counts)	725	723	709	714	709	706
<b>Net Peak Area Ratio</b>	<b>0.0110</b>	<b>0.0186</b>	<b>0.0271</b>	<b>0.0432</b>	<b>0.0735</b>	<b>0.1078</b>
Standard Deviation ( $\sigma$ )	0.00038	0.00041	0.00045	0.00048	0.00056	0.00064
3 $\sigma$	<b>0.00114</b>	<b>0.00123</b>	<b>0.00135</b>	<b>0.00145</b>	<b>0.00168</b>	<b>0.00192</b>
% 3 $\sigma$	<b>10.4</b>	<b>6.6</b>	<b>5.0</b>	<b>3.4</b>	<b>2.3</b>	<b>1.8</b>

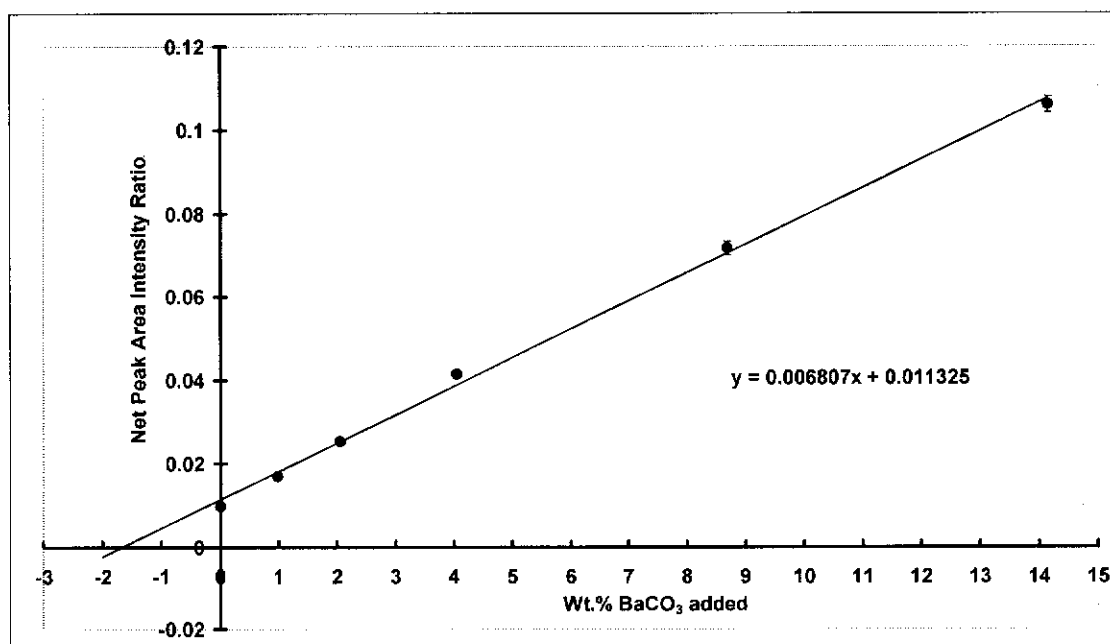


Figure A1.7. Preliminary calibration graph for BaCO<sub>3</sub> assay by quantitative XRD.

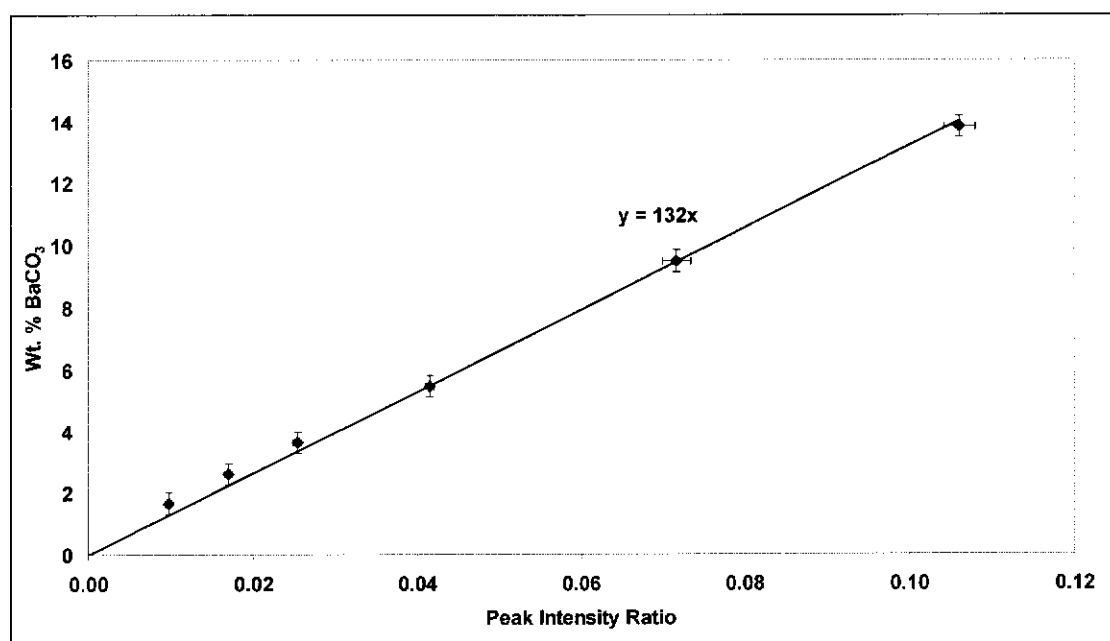


Figure A1.8. Final calibration graph for absolute BaCO<sub>3</sub> assay by quantitative XRD in BaZrO<sub>3</sub>. Uncertainties are  $\pm 2\sigma$ .

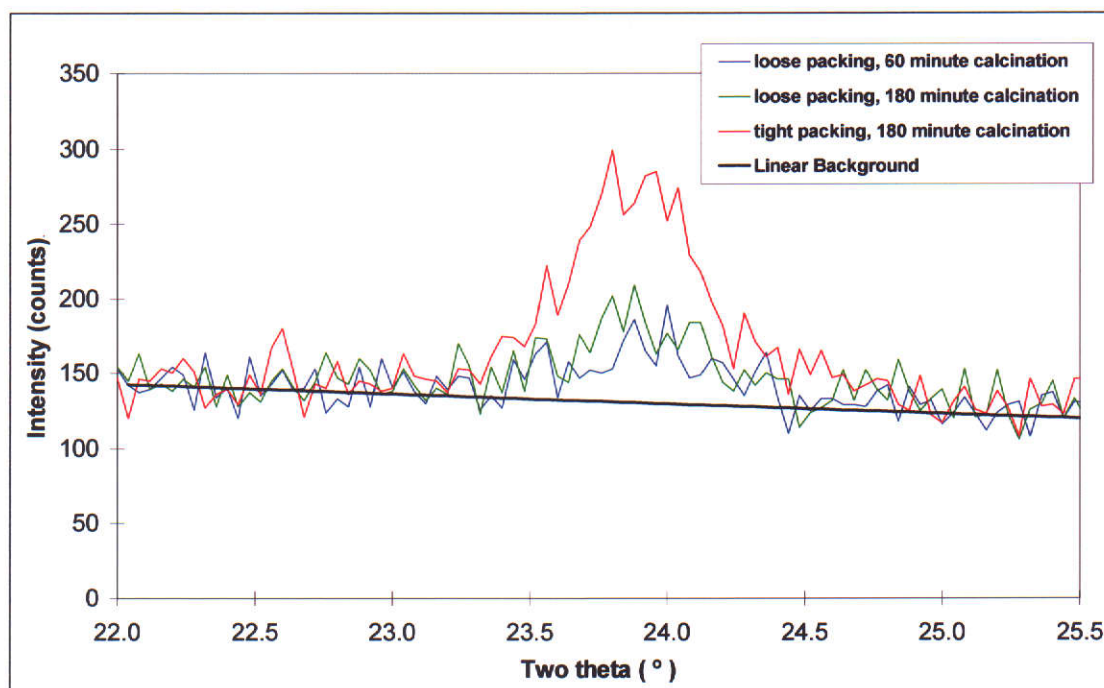


Figure A1.9 Typical weak  $\text{BaCO}_3$  diffraction peaks requiring analysis.

Figure A1.9 shows  $\text{BaCO}_3$  diffraction peaks for solid-state derived powders at low levels of  $\text{BaCO}_3$ . Although the diffraction peaks are very small, between 0.15 and 0.7 % of the largest  $\text{BaZrO}_3$  diffraction peak, all three peak areas are larger than counting statistical error ( $3\sigma = 0.15 \text{ wt.\% BaCO}_3$ ) and therefore  $\text{BaCO}_3$  has definitely been detected in these specimens. The  $\text{BaCO}_3$  peak for the solid-state derived powder packed tight into a crucible and calcined for 180 minutes (Section 5.1) clearly appears visibly larger than the others. Sampling and particle statistical errors also contribute to the total measurement uncertainty. As shown in Figure 5.1, there is slight overlap in the error bars of all three results, hence the chance of all three results being statistically equivalent are still significant at 95 % confidence levels. The confidence intervals of these measurements could have been reduced by repeated measurement, but this was impractical given the long acquisition times required to accumulate adequate counting statistics for each specimen.

The results of this calibration show that quantitative XRD can be used to analyse the  $\text{BaCO}_3$  content of  $\text{BaZrO}_3$  powders at quite low levels, certainly down to  $\sim 1 \text{ wt.\%}$ . The detection limit is difficult to estimate accurately from the data in Table A1.4 and Figure 5.1 alone because the total measurement uncertainty includes



contributions from several sources. Counting uncertainties are readily calculated and have been included in Table A1.4. Random errors dominate the estimation of the  $\text{BaCO}_3$  of the powder used to make standards, which in turn contribute significantly to absolute errors for unknowns. Errors due to particle statistics are likely to dominate the total error of the measurement close to the detection limit. The high attenuation coefficient of  $\text{BaZrO}_3$  at  $1.5418 \text{ \AA}$  ( $\sim 217 \text{ cm}^2/\text{g}$ ) restricts the total mass of analysed material to  $\sim 4 \text{ mg}$ , of which only  $\sim 40 \text{ }\mu\text{g}$  is  $\text{BaCO}_3$  for samples close to the detection limit. Sampling variation may be significant because of the low effective specimen mass. Furthermore, very little of the  $\sim 40 \text{ }\mu\text{g}$  of  $\text{BaCO}_3$  contributes to the diffracted intensity because only a very small fraction of particles are correctly oriented to produce diffraction within the geometry of the diffractometer optics.

Particle statistic errors are difficult to calculate theoretically. Using the approximate estimate of Smith (1992), only  $\sim 200$  crystallites contribute to the most intense  $\text{BaCO}_3$  diffraction peak at  $24^\circ$  in samples with 1 wt.%  $\text{BaCO}_3$  whose average crystallite size is  $1 \text{ }\mu\text{m}$ , with the optical configuration used in this project. This calculation ignores the effect of sample spinning. Since the number of particles contributing to the observed diffraction peak varies with the cube of their volume averaged particle size, the errors in estimation of particle statistic uncertainties are inherently large. An increase in average  $\text{BaCO}_3$  crystallite size to  $\sim 3 \text{ }\mu\text{m}$  would reduce the number of crystallites contributing to an average of only  $\sim 8$ , hence quantitative diffraction analysis would be impossible at 1 wt.%  $\text{BaCO}_3$ .

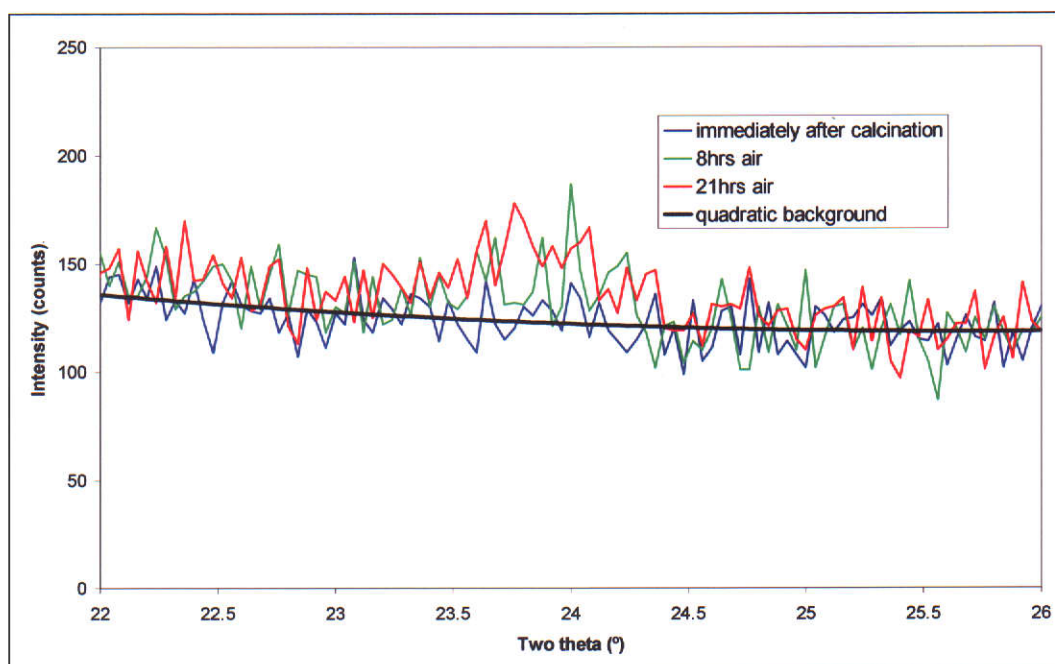


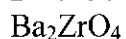
Figure A1.10  $\text{BaCO}_3$  diffraction peaks in solid-state derived powders produced with intermediate re-grinding, at and below the detection limits of the method.

Empirical methods may provide a more reliable estimate because very few assumptions are required. The repeatability of  $\text{BaCO}_3$  in the original starting powder for standards (with 1.6 wt.%  $\text{BaCO}_3$ ) was  $\pm 0.53$  (2 standard errors of 4 samples). Total measurement uncertainties were considerably larger than counting statistical errors, presumably because of sampling and particle statistic limitations. Specimens that produce a larger  $\text{BaCO}_3$  diffraction peak than attributable to uncertainties of counting statistics are considered to definitely contain  $\text{BaCO}_3$ . This corresponds to greater than 0.15 wt.%  $\text{BaCO}_3$ . The  $\text{BaCO}_3$  diffraction peak near the detection limit of counting errors is illustrated by the largest of the peaks shown in Figure A1.10. Specimens with uniform particle mixing and random crystallite orientation cannot produce a detectable  $\text{BaCO}_3$  diffraction peak with  $\text{BaCO}_3$  contents below 0.15%. The probability of failing to detect  $\text{BaCO}_3$  (due to effects including particle statistics and sampling variation) remains statistically significant up to approximately 0.6 wt.%. Specimens with observed  $\text{BaCO}_3$  contents between 0.15 and 0.6 wt.% are considered to definitely contain  $\text{BaCO}_3$ , but measurement uncertainties are too large to provide useful quantification. Samples containing greater than 0.6 wt.%  $\text{BaCO}_3$  allow quantitative analysis with useful accuracy and precision, and the risk of failing to detect  $\text{BaCO}_3$  in any one specimen becomes statistically acceptable.

## 9.2 Appendix 2 – Crystallographic data

### 9.2.1 ICDD cards of barium zirconates and related phases

#### 24-0130



Barium Zirconium Oxide

Radiation : Cu Ka  
 $\lambda$  : 1.5418 Å  
 Filter : Ni  
 d-sp :  
 Intensity : Diffract.  
 I/Icor :  
 Reference : Appenino,  
 Ramonda,  
 Ann.Chim.  
 (Rome), 61, 61  
 (1971)  
 System : Tetragonal  
 S.G. : I4/mmm (139)  
 a : 4.181  
 b :  
 c : 13.475  
 A :  
 C : 3.2229  
 Z : 2  
 Dx : 6.061  
 Dm :  
 SS/FOM :  $F_{30} = 11$  (0.07,39)  
 Comments : to replace 22-0105  
 Mwt = 429.88

Wavelength = 1.54184 Å

2 $\theta$	Int	h	k	l
13.175	10	0	0	2
22.281	5	1	0	1
26.528	10	0	0	4
29.184	100	1	0	3
29.832	90	1	1	0
33.067	1	1	1	2
39.819	7	1	0	5
40.205	15	0	0	6
40.678	10	1	1	4
43.334	30	2	0	0
49.198	1	2	1	1
51.113	20	1	1	6
51.484	3	2	0	4
52.371	7	1	0	7
53.124	30	2	1	3
54.425	8	0	0	8
60.295	4	2	1	5
60.556	20	2	0	6
62.926	8	2	2	0
63.647	2	1	1	8
66.395	4	1	0	9
70.850	7	3	0	3
71.407	12	3	1	0
72.036	2	2	0	8
77.117	2	3	0	5
77.325	3	2	2	6
78.000	2	1	1	10
82.091	1	1	0	11
82.605	1	2	1	9
85.287	2	3	1	6

**22-0105****Ba<sub>2</sub>ZrO<sub>4</sub>****Barium Zirconium Oxide****Quality Mark: i**

Radiation : Cu Ka  
 $\lambda$  : 1.5418 Å  
 Filter : Ni  
 d-sp :  
 Intensity : Diffract.  
 I/I<sub>cor</sub> :  
 Reference : Scholde, Rade,  
                   Schwartz, Z.  
                   Anorg. Allg.  
                   Chem., 362, 149  
                   (1968)  
  
 System: Tetragonal  
 S.G. :  
 a : 4.187  
 b :  
 c : 13.48  
 A :  
 C : 3.2195  
 Z :  
 Dx : 6.040  
 Dm : 5.980  
 SS/FOM : F<sub>28</sub> = 5 (0.052,101)  
 Comments : Deleted by  
                   24-0130  
                   Mwt = 429.88

Wavelength = 1.54184 Å

2θ	Int	h	k	l
13.254	5	0	0	2
29.184	95	1	0	3
30.131	85	1	1	0
39.853	35	1	0	5
40.186	100	0	0	6
40.544	35	1	1	4
43.226	60	2	0	0
51.144	30	1	1	6
52.243	15	1	0	7
53.025	45	2	1	3
54.489	20	0	0	8
60.469	20	2	0	6
62.784	15	2	2	0
63.550	10	1	1	8
66.289	10	1	0	9
69.825	10	0	0	10
70.667	15	3	0	3
71.220	10	3	1	0
72.036	10	2	0	8
77.251	5	2	2	6
77.699	5	1	1	10
81.837	10	1	0	11
82.433	5	2	1	9
85.102	10	3	1	6
85.660	5	2	0	10
86.608	10	3	2	3
94.837	5	4	0	0
97.548	5	2	1	11

**24-0131** $\text{Ba}_3\text{Zr}_2\text{O}_7$ 

Barium Zirconium Oxide

Quality Mark: i

Radiation : Cu Ka  
 $\lambda$  : 1.5418 Å  
 Filter : Ni  
 d-sp :  
 Intensity : Diffract.  
 I/Icor :  
 Reference : Appenino,  
 Ramonda,  
 Ann.Chim.  
 (Rome), 61, 61  
 (1971)

System : Tetragonal  
 S.G. : I4/mmm (139)  
 a : 4.188  
 b :  
 c : 21.722  
 A :  
 C : 5.1867  
 Z :  
 Dx : 6.040  
 Dm : 5.980  
 SS/FOM :  $F_{26} = 11$  (0.036,65)  
 Comments : Mwt = 706.43

Wavelength = 1.54184 Å

2 $\theta$	Int	h	k	l
8.263	5	0	0	2
16.385	3	0	0	4
21.516	6	1	0	1
24.523	3	1	0	3
29.579	85	1	0	5
30.162	100	1	1	0
32.980	6	0	0	8
35.996	2	1	0	7
39.310	8	1	1	6
41.539	8	0	0	10
43.226	55	2	0	0
48.805	1	2	1	1
50.359	3	2	0	6
52.211	10	1	1	10
53.291	35	2	1	5
59.610	1	0	0	14
61.490	10	2	0	10
62.784	13	2	1	9
68.261	3	1	1	14
68.488	3	2	2	6
69.237	2	0	0	16
70.973	6	3	0	5
71.158	12	3	1	0
78.228	5	1	0	17
84.643	1	2	1	15
86.036	2	3	1	10

**06-0399**BaZrO<sub>3</sub>

Barium Zirconium Oxide

Quality Mark: \*

Radiation : Cu Ka1  
 $\lambda$  : 1.5405 Å  
 Filter : Ni  
 d-sp :  
 Intensity: Diffract.  
 I/I<sub>cor</sub> :  
 Reference : Swanson et al., Natl. Bur. Stand.  
 (US) Circ. 539, V, 8 (1955)

System : Cubic  
 S.G. : Pm $\bar{3}$ m (221)  
 a : 4.193  
 b :  
 c :  
 A :  
 C :  
 Z : 1  
 Dx : 6.229

Dm :  
 SS/FOM : F<sub>17</sub> = 152  
 (0.0048 , 23)

Comments : Colourless.  
 Pattern taken at 26C.  
 Sample prepared by heating BaCO<sub>3</sub>  
 and ZrO<sub>2</sub> at 1550C for an hour.  
 Spect. Analysis,  
 <1.0% Hf Sn;  
 <0.1%, Al, Ca, Fe, Mg, Si;  
 <0.001% Mn, Sr.  
 Perovskite, CaTiO<sub>3</sub> type  
 Mwt = 276.55

Wavelength = 1.54184 Å

2 $\theta$	Int	h	k	l
21.184	10	1	0	0
30.141	100	1	1	0
37.136	10	1	1	1
43.139	35	2	0	0
48.555	2	2	1	0
53.540	40	2	1	1
62.671	20	2	2	0
71.109	18	3	1	0
75.158	2	3	1	1
79.124	6	2	2	2
86.937	16	3	2	1
94.694	4	4	0	0
102.530	10	3	3	0
110.617	8	4	2	0
119.180	6	3	3	2
128.504	6	4	2	2
139.277	12	5	1	0



**74-1299**BaZrO<sub>3</sub>

Barium Zirconium Oxide

Quality Mark: C

Radiation : Cu Ka1  
 $\lambda$  : 1.54060 Å  
 Filter :  
 d-sp : Calculated  
 Cut off : 17.7  
 Intensity: Calculated.  
 I/I<sub>cor</sub> : 14.89  
 Reference : Calculated from ICSD using  
 POWD-12++  
 Megaw, H.D., Proc. Phys. Soc.,  
 London, 58, 133 (1946)

System : Cubic  
 S.G : P23(195)  
 a : 4.1815(1)  
 b :  
 c :  
 A :  
 C :  
 Z : 1  
 Dx : 6.281  
 Dm :  
 ICSD # : 027048  
 Comments : Peak height intensity.  
 R-factor :0.000  
 Mwt: 276.55

Wavelength = 1.54184 Å

2 $\theta$	Int	h	k	l
21.248	18	1	0	0
30.227	999	1	1	0
37.245	65	1	1	1
43.275	282	2	0	0
48.693	9	0	1	2
53.693	314	2	1	1
62.861	137	2	2	0
67.159	4	3	0	0
71.325	111	0	1	3
75.391	12	3	1	1
79.383	37	2	2	2
83.324	2	0	2	3
87.233	109	1	2	3

**77-0944**Ba<sub>2</sub>ZrO<sub>4</sub>

Barium Zirconium Oxide

Quality Mark: C

Radiation : Cu Kα1  
 λ : 1.54060 Å  
 Filter :  
 d-sp : Calculated  
 Cut off : 8.25  
 Intensity: Calculated.  
 I/I<sub>cor</sub> : 14.89  
 Reference : Calculated from ICSD using  
 POWD-12++ (1997)  
 Shpanchenko, R.V., Antipov, E.V.,  
 Kovba, L.M., Zh. Neorg. Khim.,  
 38, 599, (1993)

System : Tetragonal  
 S.G : I4/mmm (139)  
 a : 4.2045(8)  
 b :  
 c : 13.587(4)  
 A :  
 C :  
 Z : 2  
 Dx : 5.944  
 Dm :  
 ICSD # : 039707  
 Comments : Peak height intensity.  
 R-factor : 0.120  
 Mwt: 429.88

Wavelength = 1.54184 Å

2θ	Int	h	k	l
13.032	39	0	0	2
22.131	60	1	0	1
26.236	73	0	0	4
28.977	999	1	0	3
30.058	610	1	1	0
32.885	9	1	1	2
39.485	70	1	0	5
39.807	117	0	0	6
40.315	108	1	1	4
43.026	241	2	0	0
45.147	3	2	0	2
48.901	10	2	1	1
50.674	118	1	1	6
51.095	19	2	0	4
51.886	33	1	0	7
52.709	227	2	1	3
53.991	12	0	0	8
59.812	25	2	1	5
60.050	80	2	0	6
62.478	45	2	2	0
63.035	13	1	1	8
64.130	1	2	2	2
65.718	16	1	0	9
67.144	1	3	0	1
68.957	5	2	2	4
69.138	4	0	0	10
69.616	17	2	1	7
70.312	30	3	0	0
70.876	37	3	1	0
71.400	13	2	0	8
72.431	1	3	1	2
76.475	4	3	0	5
76.685	24	2	2	6
77.021	12	3	1	4
77.194	11	1	1	10
81.160	13	1	0	11
81.821	11	2	1	9
83.139	1	3	2	1
84.502	20	3	1	6
85.00	3	2	0	10
85.449	3	3	0	7
85.824	2	0	0	12
86.104	23	3	2	3
87.134	5	2	2	8

**37-1484**ZrO<sub>2</sub>

Zirconium Oxide

Baddeleyite, syn

Quality Mark: \*

Radiation : Cu Kα1

λ : 1.540598 Å

Filter : Graph Mono

d-sp : Diff.

Cut off : 17.7

Intensity: Diffract.

I/I<sub>cor</sub> : 2.6Reference : McMurdie, H. et al.,  
Powder Diffraction, 1, 275 (1986)

System : Monoclinic

S.G : P2<sub>1</sub>/a (14)

a : 5.3129(4)

b : 5.2125(4)

c : 5.1471(5)

A : 1.0193

C : 0.9875

a :

b : 99.218(8)

Z : 4

Dx : 5.817

Dm :

SS/FOM : F<sub>30</sub> = 111(0.0073 , 37)

Comments : Colourless.

Peak height intensity.

Sample heated to 1300° for 48 hrs,  
data collected at 25.5°C

To replace 13-0307 and 36-0420.

See also ICSD 18190, 15983,

26488, 60903.

Mwt: 123.22

Wavelength = 1.54184 Å

2θ	Int	h	k	l
17.433	3	0	0	1
24.068	14	1	1	0
24.461	10	0	1	1
28.198	100	$\bar{1}$	1	1
31.494	68	1	1	1
34.188	21	2	0	0
34.412	11	0	2	0
35.338	13	0	0	2
38.428	1	$\bar{2}$	1	0

Wavelength = 1.54184 Å

2θ	Int	h	k	l
35.930	2	$\bar{2}$	0	1
38.573	4	1	2	0
39.444	<1	0	1	2
40.024	<1	$\bar{2}$	1	1
40.759	12	$\bar{1}$	1	2
41.185	5	2	0	1
41.409	5	$\bar{1}$	2	1
44.864	7	2	1	1
45.561	6	$\bar{2}$	0	2
48.991	2	$\bar{2}$	1	2
49.309	18	2	2	0
50.159	22	0	2	2
50.603	13	$\bar{2}$	2	1
51.237	5	$\bar{1}$	2	2
54.728	11	0	0	3
54.728	<1	2	2	1
55.319	11	1	2	2
55.449	11	3	1	0
55.619	9	$\bar{3}$	1	1
55.932	6	0	3	1
57.218	7	$\bar{1}$	1	3
57.912	4	$\bar{1}$	3	1
58.319	3	$\bar{2}$	2	2
59.828	8	1	3	1
60.108	7	$\bar{2}$	0	3
61.422	5	3	1	1
62.040	5	$\bar{3}$	1	2
62.895	8	1	1	3
64.137	1	3	2	0
64.308	2	2	3	0
65.023	<1	0	3	2
65.443	2	$\bar{2}$	3	1
65.760	6	0	2	3
65.944	4	$\bar{1}$	3	2
68.975	1	2	3	1
69.684	<1	3	2	1
70.255	<1	$\bar{3}$	2	2
71.137	2	$\bar{2}$	2	3
71.366	4	$\bar{4}$	0	1
72.017	1	4	0	0
72.171	1	$\bar{2}$	3	2
72.517	<1	0	4	0
etc.				

**45-1471**BaCO<sub>3</sub>

Barium Carbonate

Witherite, syn

Quality Mark: \*

Radiation : Cu Kα1

λ : 1.540598 Å

Filter : Ge Mono

d-sp : Diff.

Cut off : 17.7

Intensity: Diffract.

I/I<sub>cor</sub> : 3.4Reference : Kern, A. Geyer, A., Eysel,  
W., Miner.Petrog. Inst. U.  
Heidelberg Germany, ICDD  
Grant in aid (1993)

System : Orthorhombic

S.G : Pnma (62)

a : 6.4330(1)

b : 5.3148(1)

c : 8.9036(2)

A : 1.2104

C : 1.6752

a :

Z : 4

Dx : 4.306

Dm :

SS/FOM : F<sub>30</sub> = 255(0.0031 , 38)

Comments : White.

Integrated intensities.

Aldrich 99.9%

determination based on

profile fit (Split Pearson

VII). Aragonite group.

To replace 44-1487. See

ICSD 15196 and 26718.

Mwt: 197.37.

Wavelength = 1.54184 Å

2θ	Int	h	k	l
19.454	8	0	1	1
19.943	4	0	0	2
23.911	100	1	1	1
24.317	50	1	0	2
27.736	20	2	0	0
29.528	6	2	0	1
29.634	2	1	1	2

Wavelength = 1.54184 Å

2θ	Int	h	k	l
32.538	4	2	1	0
33.246	<1	1	0	3
33.731	18	0	2	0
34.103	30	2	1	1
34.395	16	2	0	2
34.616	40	0	1	3
37.997	1	1	2	1
39.493	12	0	2	2
40.525	4	0	0	4
42.012	50	1	2	2
42.997	20	1	0	4
44.209	18	2	2	0
44.920	40	2	1	3
46.438	<1	1	1	4
46.809	30	3	1	1
47.035	14	3	0	2
48.080	1	1	2	3
48.942	6	2	2	2
49.816	3	2	0	4
50.233	<1	3	1	2
52.676	3	0	3	1
53.375	<1	1	0	5
53.716	3	0	2	4
54.334	2	0	1	5
54.722	12	1	3	1
55.738	14	1	2	4
56.333	12	1	1	5
57.288	3	4	0	0
57.813	<1	1	3	2
58.302	<1	4	0	1
59.121	6	3	2	2
59.892	2	3	0	4
60.568	3	2	3	1
60.900	7	0	3	3
61.094	5	4	1	1
61.283	2	4	0	2
61.516	3	2	2	4
62.081	3	2	1	5
62.598	3	0	0	6
68.184	12	2	3	3
68.690	10	4	1	3
69.799	14	2	0	6
70.530	7	3	2	4
etc.				

### 9.2.2 ICSD data for BaZrO<sub>3</sub>

**Coll Code** 90049  
**Rec. Date** 18/12/2001  
**Chem. Name** Barium zirconate  
**Structured** Ba (Zr O3)  
**Sum** Ba1 O3 Zr1  
**ANX** ABX3  
**D(calc)** 6.21  
**Formula Wt** 276.557  
**Title** A neutron diffraction study of BaCe<sub>x</sub>Zr<sub>1-x</sub>O<sub>3</sub>  
**Author(s)** Pagnier, T., Charrier-Cougoulic, I., Ritter, C., Lucazeau, G.  
**Reference** The European Journal of Applied Physics (2000), 9, 1-9  
**Unit Cell** 4.19729(4), 4.19729(4), 4.19729(4), 90, 90, 90  
**Vol** 73.94  
**Z** 1  
**Space Group** P m -3 m  
**SG** PM3-M  
**SG Number** 221  
**Cryst. Sys.** cubic  
**Pearson** cP5  
**Wyckoff** d b a  
**R value** 0.017  
**Red. Cell** P 4.197, 4.197, 4.197, 90, 90, 90, 73.945  
**Trans Red.** 1.000 0.000 0.000 / 0.000 1.000 0.000 / 0.000 0.000 1.000  
**Comments** Neutron diffraction (powder)  
Rietveld profile refinement applied

Atom	#	Ox	Site	x	y	z	SOF.	H	ITF (B)
Ba	1	+2	1b	0.5	0.5	0.5	1	0	0.86(2)
Zr	1	+4	1a	0	0	0	1	0	0.75(2)
O	1	-2	3d	0.5	0	0	1	0	1.19(3)

### 9.3 Appendix 3 – Rietveld Refinement Results

Appendix 3 presents the results of Rietveld refinements of powder XRD patterns presented in Figures 6.27 – 6.29. The purpose of these Rietveld refinements was to illustrate the differences between XRD patterns of samples of sintered ceramic with and without exaggerated grain growth were due to preferred orientation when analysed as powders after brief milling. Rietveld refinements were based on the Zr-rich specimen shown in Figure 6.27. Acceptable refinements for other specimens were readily obtained by largely fixing all parameters other than preferred orientation.

Table A3.1 Parameters fixed for all Rietveld refinements of solid-state derived sintered ceramics analysed as powders after brief ring milling

Space group	P23
Attenuation coefficient	216 cm <sup>2</sup> /g
Lattice parameter	4.1899 Å
Atom coordinates, B, n	x, y, z, B, n
Ba	0.5, 0.5, 0.5, 0.6, 0.08333
Zr	0, 0, 0, 0.6, 0.08333
O	0.5, 0, 0, 0.6, 0.25
Wavelength 1	1.54051 Å
Wavelength 2	1.54433 Å
Ratio	0.5
Profile	Voigt profile (Rietveld asymmetry)
Base width	7
Histogram weighting	1
Polarisation	0.8
Zero offset	-0.100
Asymmetry 1	0.0056

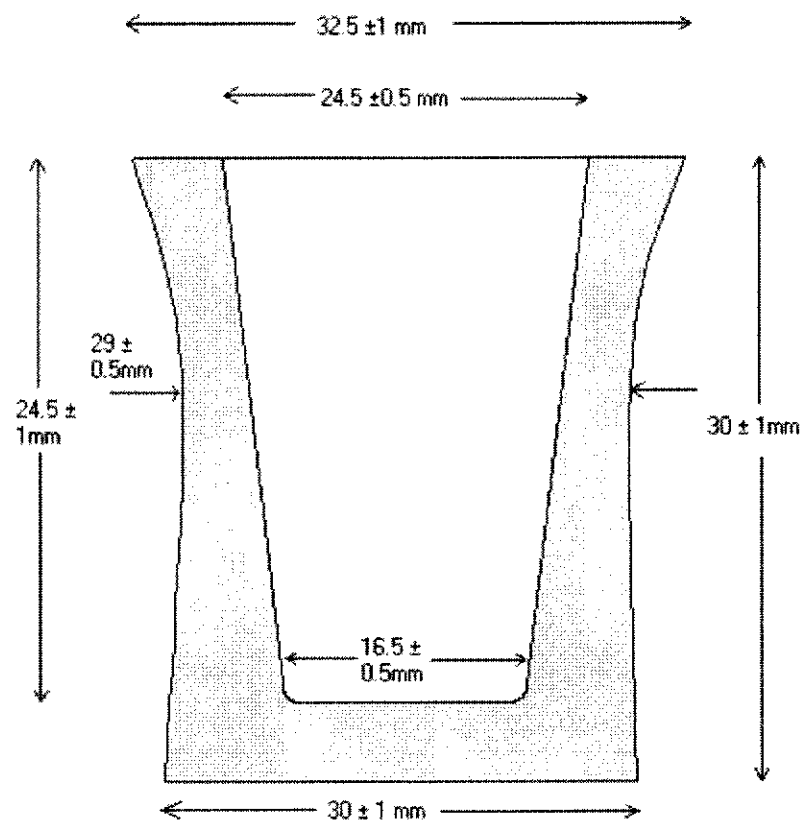


Table A3.2 Results of Rietveld refinements of XRD patterns of solid-state derived sintered ceramics analysed as powders after brief ring milling.

	Figure 6.27	Figure 6.28	Figure 6.29
Exaggerated grain growth?	no	yes	yes
Ba : (Zr + Hf) mole ratio ( $\pm$ 0.002)	0.988	1.015	1.011
Phase Scale	0.00589(2)	0.00668(7)	0.00648(2)
Specimen displacement	0.0581(9)	0.019(1)	0.0014(8)
Background -1	2914(46)	2350(78)	2815(57)
Background 0	-49(2)	10(5)	-56(3)
Background 1	0.71(3)	0.31(6)	0.70(4)
U	0.04(4)	0.06(4)	0.059(2)
V	-0.05(3)	-0.09(3)	-0.098(2)
W	0.036(7)	-0.035(3)	0.042(4)
Size (Å)	2500(376)	2600(380)	2218(236)
<b>March preferred orientation parameter, &lt;100&gt;</b>	<b>0.866(7)</b>	<b>0.568(2)</b>	<b>0.613(2)</b>
Rp	6.71	8.68	8.94
Rwp	9.29	11.4	12.4
$\chi^2$	2.48	4.37	4.31

#### 9.4 Appendix 4 - Crucible Dimensions

Dimensions of sintered crucibles formed by CIP produced in this study



## **9.5 Appendix 5 - Raw Materials Suppliers' Data**

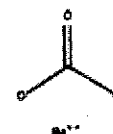
FLUKA-11729

Barium carbonate  
puriss. p.a. ACS 299.0% (KT)

Packages	Availability			
11729-50G	Inquire		25.90	<a href="#">Comments</a>
11729-250G	Inquire		57.60	<a href="#">Comments</a>
11729-1KG	Yes		191.40	<a href="#">Comments</a>

**Product Identifier**

Molecular Formula  $\text{CBaO}_3$   
Molecular Weight 197.3  
CAS Number 513-77-9  
EG/EC Number 2081673  
MDL number MFCD00003448

[Zoom In](#)**Product Properties**

Substances not precipitated by  $\text{H}_2\text{SO}_4$  (as  $\text{SO}_4$ )  $\leq 0.2\%$

Chloride (Cl)  $\leq 20$  mg/kg

Sulfide (S)  $\leq 10$  mg/kg

Cas 50 mg/kg

Cd  $\leq 5$  mg/kg

Co  $\leq 5$  mg/kg

Cr  $\leq 5$  mg/kg

Cu  $\leq 5$  mg/kg

Fe  $\leq 5$  mg/kg

K  $\leq 50$  mg/kg

Mg  $\leq 5$  mg/kg

Mn  $\leq 5$  mg/kg

Na  $\leq 50$  mg/kg

Ni  $\leq 5$  mg/kg

Pb  $\leq 5$  mg/kg

Sr  $\leq 7000$  mg/kg

Zn  $\leq 5$  mg/kg

**References**

null



Rockingham Plant  
PO Box 283 Rockingham WA 6168  
1 Ward Road Rockingham WA 6168  
Australia  
Tel. (08) 9439 9000  
Fax (08) 9439 1055  
[www.millenniumchem.com](http://www.millenniumchem.com)

Version Date 13 August 2001  
Page 1 of 1

## DPS3005 Certificate of Analysis Monoclinic Zirconia Millennium Z0.5

Date: 20 MAY 2002

Batch No: 0479

### Chemical Analysis

Element	Unit	Standard Specification	Batch Result
Al <sub>2</sub> O <sub>3</sub>	ppm	< 100	<20
CaO	ppm	< 100	<20
Fe <sub>2</sub> O <sub>3</sub>	ppm	< 100	<20
SiO <sub>2</sub>	ppm	< 100	<20
TiO <sub>2</sub>	ppm	< 100	<20
ZrO <sub>2</sub> (+HfO <sub>2</sub> )	wt%	> 99.9	> 99.0

### Particle Size Distribution (by Coulter LS230 – laser diffraction)

		Unit	Standard Specification	Batch Result
After ultrasonic dispersion	10% less than	micron	-	0.41
	50% less than	micron	0.3 – 0.5	
	90% less than	micron	-	

### Other Physical Properties

	Unit	Standard Specification	Batch Result
Surface Area (by BET)	m <sup>2</sup> /g	20.0 – 30.0	23.25
Loss on Ignition (at 1000°C)	wt%	< 2.0	1.0

Millennium Inorganic Chemicals Ltd, a Millennium Chemicals company  
Registered in Australia A.B.N. 50 008 683 627



**ZIRCONIUM CHLORIDE SOLUTION**

**Millennium-ZOCL**

**Certificate of Analysis**

**Date: 16 August, 2000**

**BATCH: C246**

**ZR NO: 10511**

ZrO <sub>2</sub> %:	36.1%
---------------------	-------

**Chemical Analysis:**

(ppm, except where noted)

SiO <sub>2</sub>	144
Fe <sub>2</sub> O <sub>3</sub>	<20
TiO <sub>2</sub>	<20
CaO	<20
Al <sub>2</sub> O <sub>3</sub>	80
Y <sub>2</sub> O <sub>3</sub>	97
K <sub>2</sub> O	<20
NiO	<20
Cr <sub>2</sub> O <sub>3</sub>	<20
U <sub>3</sub> O <sub>8</sub>	<20
ThO	<20

*This delivery has met required specifications prior to bulk storage.*

A Millennium Chemicals Company

Millennium Performance Chemicals (Advanced Ceramics) Pty Ltd  
is registered in Australia ACN 091 009 504





RIEDEL-32305

Barium acetate  
puriss. p.a. Reag. ACS >99%

Packages	Availability		
32305-1KG-R	Inquire	133.70	
32305-100G-R	Inquire	29.90	
32305-250G-R	Yes	42.60	
32305-6X100G-R	Inquire	162.00	
32305-6X1KG-R	Inquire	722.40	

### Product Identifier

**Molecular Formula**  $C_4H_6BaO_4$   
**Molecular Weight** 255.4  
**CAS Number** 543-80-6  
**Beilstein Registry Number** 3693411  
**EG/EC Number** 2088490  
**MDL number** MFCD00012447

[Zoom In](#)

### Product Properties

Heavy metals (as Pb)  $\leq 0.0005\%$   
 $KMnO_4$  red. matter (as  $HCOOH$ )  $\leq 0.025\%$   
pH 7-8.5 (20°C, 5%)  
Chloride (Cl)  $\leq 5$  mg/kg  
Nitrate ( $NO_3$ )  $\leq 20$  mg/kg  
Ca  $\leq 20$  mg/kg  
Fe  $\leq 5$  mg/kg  
K  $\leq 30$  mg/kg  
Mg  $\leq 10$  mg/kg  
Na  $\leq 50$  mg/kg  
Sr  $\leq 2000$  mg/kg

### References

null  
null

### Safety Information

**Safety Statements** 28  
**Risk Statements** 20/22  
**Hazard Codes** Xn  
**RTECS** AF4550000  
**SWISS** 2  
**SWISS** 2

RIEDEL-31670

Zirconium(IV) oxychloride octahydrate  
puriss. p.a. >99.5%

Packages	Availability			
31670-25G-R	Inquire	33.20	<a href="#">Comments</a>	
31670-100G-R	Yes	85.70	<a href="#">Comments</a>	
31670-6X25G-R	Inquire	179.40	<a href="#">Comments</a>	
31670-6X100G-R	Inquire	463.20	<a href="#">Comments</a>	

### Product Identifier

**Synonyms** Zirconyl chloride octahydrate  
Zirconium(IV) oxide chloride

**Molecular Formula**  $\text{Cl}_2\text{OZr} \cdot 8\text{H}_2\text{O}$

**Molecular Weight** 322.2

**CAS Number** 13520-92-8

**EG/EC Number** 2317179

**MDL number** MFCD00149898

[Zoom In](#)

### Product Properties

Heavy metals (as Pb) ≤ 0.001%

Sulfate ( $\text{SO}_4$ ) ≤ 50 mg/kg

Fe ≤ 10 mg/kg

Ti ≤ 50 mg/kg

passes test for Suitability as micro reagent

### References

null

### Safety Information

**Safety Statements** 26-27-36/37/39

**Risk Statements** 34

**Hazard Codes** C

**RTECS** ZH7250000

**RIDADR** UN 3260 8/PG 2

**SWISS** 4

**SWISS** 4

RIEDEL-32304

## Ammonium oxalate monohydrate

puriss. p.a. Reag. ACS, Reag. ISO, Reag. Ph. Eur. 99.5-101.0%

Packages	Availability		
32304-1KG	Inquire	133.70	
32304-250G	Inquire	45.00	
32304-500G	Inquire	74.70	
32304-6X250G	Inquire	243.00	
32304-2.5KG	Inquire	288.10	
32304-6X500G	Inquire	403.80	
32304-5KG	Inquire	499.60	
32304-6X1KG	Inquire	722.40	
32304-6X2.5KG	Inquire	1,555.80	
32304-4X5KG	Inquire	1,798.80	

## Product Identifier

Synonyms Oxalic acid diammonium salt

Molecular  $C_2H_8N_2O_4 \cdot H_2O$ 

Formula

Molecular 142.1

Weight

CAS 6009-70-7

Number

Bellstein 3759830

Registry

Number

EG/EC 2381354

Number

MDL MFCD00149694

number



Zoom In

## Product Properties

In water insoluble matters  $\leq 0.005\%$ Residue on ignition  $\leq 0.02\%$  (as  $SO_4$ )

pH 6-7 (20°C, 2.5%)

Chloride (Cl)  $\leq 5$  mg/kgNitrate ( $NO_3$ )  $\leq 5$  mg/kgSulfate ( $SO_4$ )  $\leq 20$  mg/kgCa  $\leq 10$  mg/kgCd  $\leq 5$  mg/kgCu  $\leq 5$  mg/kgFe  $\leq 2$  mg/kgK  $\leq 10$  mg/kgMg  $\leq 10$  mg/kgNa  $\leq 10$  mg/kgPb  $\leq 5$  mg/kgZn  $\leq 5$  mg/kg

## References

null

null

## PRODUCT SPECIFICATION

Product	:	<b>BARIUM CHLORIDE Dihydrate AR</b>
Code	:	BA027
Formula	:	$\text{BaCl}_2 \cdot 2\text{H}_2\text{O}$
Molecular Weight	:	244.27
Appearance	:	Colourless/ white crystalline powder
Loss on drying (@150°C)	:	14.0-16.0
pH of a 5% solution (@25°C)	:	5.2-8.2

<b>Maximum Levels of Impurities</b>	<b>%</b>
Insoluble matter	0.005
Oxidising substances (as $\text{NO}_3$ )	0.005
Substances not precipitated by $\text{H}_2\text{SO}_4$	0.05
Calcium	0.05
Heavy metals (as Pb)	0.0005
Iron	0.0002
Strontium	0.1
CONFORMS TO ACS	

Chem-Supply Pty Ltd does not warrant that this product is suitable for any use or purpose. The user must ascertain the suitability of the product for any intended purpose. Preliminary testing of the product before use or application is recommended. Any reliance or purported reliance upon Chem-Supply Pty Ltd with respect to any skill or judgement or advice in relation to the suitability of this product for any purpose is disclaimed. Except to the extent prohibited at law, any condition implied by any statute as to the merchantable quality of this product or fitness for any purpose is hereby excluded. This product is not sold by description. Where the provisions of Part V, Division 2 of the Trade Practices Act apply, the liability of Chem-Supply Pty Ltd is limited to the replacement or supply of equivalent goods or payment of the cost of replacing the goods or acquiring equivalent goods.

Printed on: 21/07/00

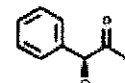
BA027.TDS

FLUKA-63470

DL-Mandellic acid

puriss. p.a. for gravimetric determination (of Zr) ≥99.0% (T)

Packages	Availability		
63470-100G-F	Inquire	22.60	
63470-500G-F	Inquire	66.90	

**Product Identifier****Synonyms** (±)-α-Hydroxyphenylacetic acid**Molecular Formula** C<sub>8</sub>H<sub>8</sub>O<sub>3</sub>**Molecular Weight** 152.2**CAS Number** 90-64-2**Beilstein Registry Number** 510011**EG/EC Number** 2020076**MDL number** MFCD00064250[Zoom In](#)**Product Properties**

Residue on Ignition 0.05%

bp

mp 117-120 °C

**References**

null

null

**Safety Information****Safety Statements** 22-24/25**RTECS** 006300000**SWISS** 4**SWISS** 4



**SIGMA-ALDRICH**

**Certificate of Analysis**

**Product Name**  
**Product Number**  
**CAS Number**  
**Molecular Formula**  
**Molecular Weight**

Zirconium(IV) chloride  
22,188-0  
10026-11-6  
Cl<sub>4</sub>Zr  
233.0

**TEST**

**APPEARANCE**

**TITRATION**

**TRACE ANALYSIS, ICP**

**ICP ASSAY**

**PURITY**

**QUALITY CONTROL ACCEPTANCE DATE**

**SPECIFICATION**

WHITE POWDER

60.2% - 61.5% CL (WITH SILVER NITRATE)

5000 PPM (MAXIMUM) TOTAL METALLIC IMPURITIES

CONFIRMS ZIRCONIUM COMPONENT.

**LOT 10231KU RESULTS**

WHITE POWDER

60.3% CL (WITH SILVER NITRATE)

SN 25 PPM MN 6.7 PPM FE 3.3 PPM NA 1.8 PPM

CONFIRMS ZIRCONIUM COMPONENT

99.995+ % BASED ON TRACE METAL ANALYSIS

SEPTEMBER 1999



ALDRICH-221880 Zirconium(IV) chloride  
99.5+%

Packages	Availability		
221880-5G	Inquire	38.30	
221880-100G	Inquire	53.60	
221880-500G	Yes	184.60	

### Product Identifier

**Synonyms** Zirconium tetrachloride

**Molecular Formula**  $\text{Cl}_4\text{Zr}$

**Formula**

**Molecular Weight** 233.0

**CAS Number**

10026-11-6

**EG/EC Number**

2330582

**MDL number**

MFCD00011306



[Zoom In](#)

### Product Description

**Features and Benefits** Suitable for nuclear reactor applications.

**Citations** for Denton, S.M. Wood, A.Synlett1999,55.

**Attributes**

**Citation** Activates pyrrolidines for improved conversion, via a modified Bouveault reaction, to the corresponding  $\alpha$ -dimethylamines.

### Product Properties

Density 2.803 g/mL (lit.)

### References

null

null

### Safety Information

**Safety Statements** 26-36/37/39-45

**Risk Statements**

14-22-34

**Hazard Codes**

C

**RTECS**

ZH7175000

**RIDADR** UN 2503 8/PG 3

**RIDADR** UN 2503 8/PG 3

ALDRICH-202118 Hafnium(IV) oxide  
powder 98%

Packages	Availability		
202118-25G	Yes	87.40	
202118-100G	Inquire	255.20	

### Product Identifier

Molecular Formula  
 $\text{HfO}_2$   
Molecular Weight  
210.5  
CAS Number  
12055-23-1  
EG/EC Number  
2350132  
MDL number  
MFCD00003565



[Zoom In](#)

### Product Properties

Density 9.68 g/mL (lit.)

### References

null

### Safety Information

Safety Statements  
22-24/25  
Safety Statements  
22-24/25



National Institute of Standards & Technology

## Certificate

### Standard Reference Material® 660a

#### Lanthanum Hexaboride Powder Line Position and Line Shape Standard for Powder Diffraction

This Standard Reference Material (SRM) is intended for use as a standard for calibration of diffraction line position and line shapes determined through powder diffractometry. A unit of SRM 660a consists of approximately 6 g of lanthanum hexaboride powder bottled under argon.

**Material Description:** The SRM material was prepared via a solid state process, jet milled, and annealed. The powder was de-agglomerated with a kneading operation using a mortar and pestle, then fractionated. The coarse fraction was removed by passing the material through a 15  $\mu\text{m}$  sieve using isopropanol as a suspending agent. The powder was then dried and bottled under argon. An analysis of X-ray powder diffraction data indicated that the SRM material is homogeneous with respect to diffraction properties.

**Certified Value and Uncertainty:** The certified lattice parameter for a temperature of 22.5 °C is

$$0.41569162 \text{ nm} \pm 0.00000097 \text{ nm}$$

The intervals defined by a value and its uncertainty in this certificate are 95 % confidence intervals for the true value of the mean in the absence of systematic error [1].

**Expiration of Certification:** The certification of this SRM is deemed to be indefinite within the stated uncertainties, provided the SRM is stored and handled in accordance with the instructions given in this certificate (see Storage section). This material degrades slowly with exposure to humidity. If excessive exposure is suspected, discontinue use.

**Storage:** SRM 660a was bottled under argon to protect against humidity. When not in use, store the unused portion of this powder tightly capped in the original bottle or in a manner with similar or greater protection against humidity.

This SRM was prepared and certified by J.P. Cline of the NIST Ceramics Division, R.D. Deslattes, J.L. Staudenmann, L.T. Hudson, and A. Henins of the NIST Atomic Physics Division, and R.W. Cheary of the University of Technology, Sydney, Australia.

Statistical analysis was provided by J.J. Filkiben of the NIST Statistical Engineering Division.

The support aspects involved in the preparation, certification, and issuance of this SRM were coordinated through the NIST Standard Reference Materials Program by R.J. Gettings and N.M. Trahey.

Stephen W. Freiman, Chief  
Ceramics Division

Gaithersburg, MD 20899  
Certificate Issue Date: 13 September 2000

Nancy M. Trahey, Chief  
Standard Reference Materials Program

## 9.6 Appendix 6 – Publications Arising from Thesis

### Refereed Papers

- Kirby, N.M., van Riessen, A., Buckley, C.E., Wittorff, V.W. (2003) “Oxalate-Precursor Processing for High Quality BaZrO<sub>3</sub>”, Submitted to *Journal of Materials Science*.

### Conference Papers

- Kirby, N.M., Buckley, C.E., van Riessen, A., (2003) “BaZrO<sub>3</sub> Crucibles for Melt Processing of Barium Cuprate Superconductors”, in "Proceedings of the 2003 Joint AXAA(WA) and WASEM Conference", ISBN 0-9586039-3-6.
- Kirby, N.M., van Riessen, A., Buckley, C.E. (2002) “BaO:[ZrO<sub>2</sub>+HfO<sub>2</sub>] Stoichiometry of BaZrO<sub>3</sub> by X-ray Fluorescence Spectroscopy”, AXAA 2002 National Conference and Exhibition Program and Abstracts, p. 93. (Awarded Student Prize for XRF Section.)
- Kirby, N.M., van Riessen, A., Buckley, C.E., Wittorff, V.W. “An Oxalate-Precursor Process For BaZrO<sub>3</sub> Ceramics”, Austceram 2002 Proceedings, 29<sup>th</sup> Sept - 4<sup>th</sup> October 2002, Perth, W.A. p235.
- Kirby, N.M., van Riessen, A., Buckley, C.E., Wittorff, V.W. (2001) “Development of an Oxalate-Precursor Process for the Production of High Quality BaZrO<sub>3</sub> Crucibles” in "Proceedings of the 2001 Joint Conference - AXAA(WA) and WASEM", ISBN 0-9586039-2-8.
- Kirby, N.M., van Riessen, A., Buckley, C.E. (2001) “Measurement of BaO:[ZrO<sub>2</sub>+HfO<sub>2</sub>] Stoichiometry of BaZrO<sub>3</sub> Powders by X-ray Fluorescence Spectroscopy” in "Proceedings of the 2001 Joint Conference - AXAA(WA) and WASEM", ISBN 0-9586039-2-8.